EPFL

Active sites on copper-based catalysts for electrochemical CO_2 reduction selectively to C_{2+} products

Présentée le 11 janvier 2022

Faculté des sciences de base
Laboratoire des matériaux pour les énergies renouvelables
Programme doctoral en chimie et génie chimique

pour l'obtention du grade de Docteur ès Sciences

par

Jie ZHANG

Acceptée sur proposition du jury

Prof. B. Smit, président du jury
Prof. A. Züttel, Prof. W. Luo, directeurs de thèse
Prof. P. Broekmann, rapporteur
Prof. H. Jónsson, rapporteur
Prof. K. Sivula, rapporteur

École
polytechnique
fédérale
de Lausanne

2022

Acknowledgements

My four years of PhD study is like my recent hiking in Nüschenstock, a mountain of the Glarus Alps in Switzerland. I began the trip by strolling the grassland trail in the valley, with limitless confidence to conquer the upcoming hiking path at an altitude of 2400 m, which, even although, we had heard is quite difficult. The seeming infinite circuitous climbing route, however, frustrated us many times when we thought we reached the top which was actually another turn. Like trudging up the bumpy tortuous uphill path, this PhD thesis cannot be accomplished without the guidance, support, help, and encouragement from my supervisor, director, colleagues, friends, and family. I really thank them and appreciate what they have done to help me finish the thesis. Especially, here I would like to mention the following people for their indispensable help and contributions.

Andreas Züttel, Professor, EPFL

I would like to thank my supervisor, Prof. Züttel, for the scientific support and guidance. I am very grateful that Andreas offered me this precious opportunity to conduct my PhD study in his lab, which is equipped with the most advanced facilities and resourceful support from the EPFL. I appreciate that he continuously shaped my scientific thinking, especially the starting point – that is, to elucidate the scientific issues we are going to solve when we propose a project. He gave me the most freedom to explore any interesting research topics and methods. He provided us a pleasant research atmosphere and also taught us to relax from the intensive research work by organizing the summer and winter excursions in the beautiful resorts. I thank him for supporting me to attend several summer schools and international conferences, where I got the chance to meet and communicate with the experts and colleagues in my field from all around the world.

Wen Luo, Scientist in EPFL and then Professor in Shanghai University

I would like to express my deep appreciation to my co-director, Prof. Luo, for the scientific support, guidance, and daily supervision. I appreciate that he encouraged me to delve deeper into certain research topics and let me roam around to try some ambitious ideas in the meanwhile. He has given me valuable advices about my proposing research topics, designing experiments, revising and polishing papers, and preparing presentations. I admire that he is always so efficient in revising my manuscript and gives the feedback so quick. It was a precious time that we were working together to design, modify, and repair the experimental setup and instruments. I am grateful for his help in my daily life and the great time we had together in skiing, hiking, biking, and parties.

Ms. **Thi Ha My PHAM** (PhD student, EPFL) helped me analyse the catalyst samples with the high resolution transmission electron microscopy (HRTEM) and energy dispersive X-ray (EDX) to obtain the information of crystal structures and elemental distribution about the catalysts. Dr. **Mo Li** (PhD student, EPFL) helped me analyse the catalyst samples with the X-ray photoelectron spectroscopy to obtain the valence of the elements in the copper phthalocyanine catalysts. I also thank him for his

Abstract

Renewable energy is being used to replace fossil fuels to mitigate global environmental problems (e.g., global warming) and to reduce the risk connected with the depletion of fossil fuels. Renewable energy (e.g., solar energy and wind energy), however, is produced intermittently and thus requires storage systems to ensure its constant supply. Electrochemical CO_2 reduction (eCO_2RR) towards value-added chemicals, powered by renewable electricity, is a promising technology for storing the intermittent renewable energy in the form of chemical bonds. Among the various products of eCO_2RR, multi-carbon (C_{2+}) molecules, such as ethylene and ethanol, are particularly interesting because they can be either important commodity chemicals or liquid fuels compatible with the current storage and transport facilities.

Production of C_{2+} molecules from eCO_2RR still suffers from low selectivity, reactivity, and stability, mainly due to the lack of proper catalysts and optimal reaction conditions. To develop proper catalysts for C_{2+} products from eCO_2RR, it is necessary to understand the reaction pathways and the key properties of the catalysts that determine the performance. Among the various catalysts that have been investigated, copper-based materials can catalyze eCO_2RR to C_{2+} products with a substantial selectivity. Therefore, the main objective of this thesis is to develop advanced copper catalysts for and understand the eCO_2RR process. The specific objectives are as follows: (1) revealing the active sites of different copper catalysts for C_{2+} products, (2) designing advanced copper-silver bimetallic catalysts to enhance C_{2+} production, (3) understanding the effects of mass transfer and pH on the activity and selectivity of eCO_2RR to C_{2+} products, and (4) investigating the transport of liquid products from eCO_2RR in a flow cell.

First, to reveal the active sties on monometallic copper catalysts for eCO_2RR to C_{2+} products, we used copper phthalocyanine as a precursor, which contains a single copper atom in each molecule, allowing us to observe the evolution of single copper atoms to nanoclusters to nanoparticles. We found that the average size of the copper nanoparticles was correlated to the selectivity of the C_{2+} products and identified the grain boundaries as the active sites for C_{2+} products. In addition, the reaction intermediates, such as CO, were found to accelerate the reconstruction of the copper nanoparticles.

Next, we investigated the active sites of copper-based bimetallic catalysts. We designed and synthesized Ag@Cu and Ag@C@Cu core-shell nanoparticles to control the interface formation between silver and copper, making it possible to distinguish between the tandem and interface effects. By using this specially designed bimetallic catalysts, we found that the high local concentration of CO, generated by the eCO_2RR on silver, suppressed the production of ethylene but improved the selectivity of ethanol compared with that on monometallic copper. These results indicate that the

tandem effect in bimetallic catalysts for eCO$_2$RR has the potential to switch the dominant C$_{2+}$ product from ethylene to ethanol.

Afterwards, we developed self-supported copper-based gas diffusion electrodes and achieved a current density up to 300 mA cm^{-2} with a high selectivity for C$_{2+}$ products (> 40%). The self-supported gas diffusion electrodes also allowed us to compare the selectivity and activity of eCO$_2$RR directly on the same catalysts in the batch and flow cells. This comparison revealed that the copper catalyst in the batch cell was limited by the mass transfer of CO$_2$. Thus, this cell had low current density (< 20 mA cm^{-2}) and C$_{2+}$ products selectivity (< 19%). However, the Cu catalyst in the flow cell produced a much higher selectivity (> 40%) of C$_{2+}$ products at a higher current density (> 100 mA cm^{-2}) due to the fast CO$_2$ diffusion and high pH. The electrode design strategies and the experimental findings presented in this section are valuable for the development of other self-supported electrodes for practical applications.

Finally, we found that more than 30% of the liquid products from eCO$_2$RR passed through the gas diffusion electrode and anion exchange membrane (AEM) at commercial current densities from 50 mA cm^{-2} to 300 mA cm^{-2}. Volatile products (e.g., ethanol, propanol) pass through the gas diffusion electrode mainly by evaporation, and the migration rate increases linearly with the applied current density and CO$_2$ flow rate. Non-volatile products (e.g., formate ions) prefer to cross the AEM through electromigration, and the migration rate is affected by the current density and the flow rate of the catholyte.

To sum up, we developed different types of copper-based catalysts for eCO$_2$RR and identified their active sites for producing C$_{2+}$ products (mainly ethylene and ethanol). We also demonstrated the effects of mass transfer and pH on the selectivity and activity of C$_{2+}$ products. These findings open up new directions for the design of new catalysts and for optimizing the reaction environments to selectively produce ethylene or ethanol. We also highlighted the importance of considering product crossover in eCO$_2$RR in order to adequately assess catalytic performances in a flow reactor.

Keywords

Résumé

Les énergies renouvelables sont utilisées pour remplacer les combustibles fossiles afin d'atténuer les problèmes environnementaux mondiaux (par exemple, le réchauffement climatique) et de réduire le risque lié à l'épuisement des combustibles fossiles. En comparaison, les énergies renouvelables (par exemple, l'énergie solaire et l'énergie éolienne) sont produites par intermittence et nécessitent donc des systèmes de stockage pour assurer un approvisionnement constant en énergie. La réduction électrochimique du CO_2 (eCO_2RR) vers des produits chimiques à valeur ajoutée, alimentée par de l'électricité renouvelable, est une technologie prometteuse pour le stockage de l'énergie renouvelable intermittente sous forme de liaisons chimiques. Parmi les différents produits de l'eCO_2RR, les molécules multi-carbonées (C_{2+}), telles que l'éthylène et l'éthanol, sont particulièrement intéressantes car elles constitutent des produits chimiques de base importants ou des carburants liquides compatibles avec les installations de stockage et de transport actuelles.

La production de molécules C_{2+} à partir d'eCO_2RR souffre toujours d'une faible sélectivité, réactivité et stabilité, principalement en raison du manque de catalyseurs appropriés et de conditions de réaction optimales. Pour développer des catalyseurs appropriés pour les produits C_{2+} à partir d'eCO_2RR, il est nécessaire de comprendre les chemins réactionels et les propriétés clés des catalyseurs qui déterminent les performances. Parmi les différents catalyseurs étudiés, les matériaux à base de cuivre peuvent catalyser le CO_2 en produits C_{2+} par eCO_2RR avec une sélectivité substantielle. Par conséquent, l'objectif principal de cette thèse est de développer des catalyseurs en cuivre avancés et de comprendre le processus d'eCO_2RR. Les objectifs spécifiques sont les suivants: (1) révéler les sites actifs de différents catalyseurs à base de cuivre pour les produits C_{2+}, (2) concevoir des catalyseurs bimétalliques cuivre-argent avancés pour favoriser les produits C_{2+}, (3) comprendre les effets du transfert de masse et du pH sur la l'activité et la sélectivité de l'eCO_2RR par rapport aux produits C_{2+}, et (4) l'étude du transport des produits liquides de l'eCO_2RR dans une cellule à écoulement.

Tout d'abord, pour révéler les sites actifs sur les catalyseurs monométalliques en cuivre pour les produits d'eCO2RR C_{2+}, nous avons utilisé la phtalocyanine de cuivre comme précurseur, qui contient un seul atome de cuivre dans chaque molécule, nous permettant d'observer l'évolution des atomes de cuivre uniques en nanoclusters, puis en nanoparticules. Nous avons trouvé que la taille moyenne des nanoparticules de cuivre corréla avec la sélectivité des produits C_{2+}, et identifié les joints de grains comme sites actifs pour les produits C_{2+}. De plus, les intermédiaires de réaction, tels que le CO, se sont avérés accélérer la reconstruction des nanoparticules de cuivre.

Ensuite, nous avons étudié les sites actifs de catalyseurs bimétalliques à base de cuivre. Nous avons conçu et synthétisé des nanoparticules noyau-coque Ag@Cu et Ag@C@Cu pour contrôler la formation de l'interface entre l'argent et le cuivre, permettant de distinguer les effets tandem et d'interface. En utilisant ces catalyseurs bimétalliques spécialement conçus, nous avons constaté que la concentration

locale élevée de CO, générée par l'eCO$_2$RR sur l'argent, supprimait la production d'éthylène mais améliorait la sélectivité de l'éthanol par rapport à celle du cuivre monométallique. Ces résultats indiquent que l'effet tandem dans les catalyseurs bimétalliques pour l'eCO$_2$RR a le potentiel de faire basculer le produit C$_{2+}$ dominant de l'éthylène vers l'éthanol.

Par la suite, nous avons développé des électrodes à diffusion gazeuse autoportées à base de cuivre et atteint une densité de courant jusqu'à 300 mA cm^{-2} avec une sélectivité élevée pour les produits C$_{2+}$ (> 40 %). Les électrodes à diffusion gazeuse autoportées nous ont également permis de comparer la sélectivité et l'activité de l'eCO$_2$RR sur les mêmes catalyseurs avec une cellule discontinue et à écoulement. Cette comparaison a révélé que le catalyseur au cuivre dans la cellule discontinue était limité par le transfert de masse de CO$_2$. Ainsi, cette cellule avait une faible densité de courant (< 20 mA cm^{-2}) et sélectivité pour les produits C$_{2+}$ (< 19%). Cependant, le catalyseur Cu dans la cellule à écoulement a produit une sélectivité beaucoup plus élevée (> 40 %) des produits C$_{2+}$ à une densité de courant plus élevée (> 100 mA cm^{-2}) en raison de la diffusion rapide du CO$_2$ et du pH élevé. Les stratégies de conception des électrodes et les résultats expérimentaux présentés dans cette section sont précieux pour le développement d'autres électrodes autoportées pour des applications pratiques.

Enfin, nous avons constaté que plus de 30% des produits liquides peuvent traverser l'électrode à diffusion gazeuse et la membrane échangeuse d'anions (AEM) à des densités de courant commerciales de 50 mA cm^{-2} à 300 mA cm^{-2}. Les produits volatils (par exemple, l'éthanol, le propanol) traversent l'électrode à diffusion gazeuse principalement par évaporation, et le taux de migration augmente linéairement avec la densité de courant appliquée et le débit de CO$_2$. Les produits non volatils (par exemple, les ions formiate) préfèrent traverser l'AEM par électromigration, et le taux de migration est affecté par la densité de courant et le débit du catholyte.

En résumé, nous avons développé différents types de catalyseurs à base de cuivre pour l'eCO$_2$RR et identifié leurs sites actifs pour la production de produits C$_{2+}$, principalement l'éthylène et l'éthanol. Nous avons également démontré les effets du transfert de masse et du pH sur la sélectivité et l'activité des produits C$_{2+}$. Ces découvertes peuvent aider à la conception de nouveaux catalyseurs et optimiser les environnements de réaction pour produire sélectivement de l'éthylène ou de l'éthanol. Nous avons également souligné l'importance de considérer le croisement des produits dans l'eCO$_2$RR afin d'évaluer adéquatement les performances catalytiques dans un réacteur à flux.

Mots-clés

List of publications

Publications included in this thesis

1. **Jie Zhang**, Thi Ha My Pham, Mo Li, Youngdon Ko, Loris Lombardo, Wen Luo, Andreas Züttel, Bottom-up unveiling the size effect of copper nanoparticles on electrochemical CO_2 reduction to C_{2+} products by using phthalocyanine demetalation, *in preparation*.

2. **Jie Zhang**, Thi Ha My Pham, Youngdon Ko, Shuliang Yang, Cedric David Koolen, Wen Luo, Andreas Züttel, Ag@C@Cu core-shell nanoparticles reveal tandem effect for electrochemical CO_2 reduction, *in preparation*

3. **Jie Zhang**, Wen Luo, Andreas Züttel, Crossover of liquid products from electrochemical CO_2 reduction through gas diffusion electrode and anion exchange membrane, *Journal of Catalysis* 2020, 385 140.

4. **Jie Zhang**, Wen Luo, Andreas Züttel, Self-supported copper-based gas diffusion electrodes for CO_2 electrochemical reduction, *Journal of Materials Chemistry A* 2019, 7, 26285 (cover highlighted)

Publications not included in this thesis

1. Shuliang Yang[#], **Jie Zhang**[#], Li Peng, Mehrdad Asgari, Dragos Stoian, Ilia Kochetygov, Wen Luo, Emad Oveisi, Olga Trukhina, Adam Hugh Clark, Daniel T Sun, Wendy Lee Queen, A metal-organic framework/polymer derived catalyst containing single-atom nickel species for electrocatalysis, *Chemical Science* 2020, 11, 10991 (# equally contribution)

2. Xin Zong[#], **Jie Zhang**[#], Jinqiu Zhang, Wen Luo, Andreas Züttel, Yueping Xiong, Synergistic Cu/CeO_2 carbon nanofiber catalysts for efficient CO_2 electroreduction, *Electrochemistry Communications* 2020, 114, 106716 (# equally contribution)

3. Wen Luo, Qin Zhang, **Jie Zhang**, Emanuele Moioli, Kun Zhao, Andreas Züttel, Electrochemical reconstruction of ZnO for selective reduction of CO_2 to CO, *Applied Catalysis B: Environmental* 2020, 273, 119060

4. Wen Luo, **Jie Zhang**, Mo Li, Andreas Zuttel, Boosting CO production in electrocatalytic CO_2 reduction on highly porous Zn catalysts, *ACS Catalysis* 2019, 5, 3783

5. Wen Luo, Wei Xie, Mo Li, **Jie Zhang**, Andreas Züttel, 3D Hierarchical Porous Indium Catalyst for Highly Efficient Electroreduction of CO_2, *Journal of Materials Chemistry A* 2019, 7, 4505

Contents

List of Figures

Chapter 1 Introduction

1.1 Background: What electrochemical CO_2 reduction can do

Rapidly increasing global energy consumption has been sustaining the ever-growing global population and increasing standards of living, to the point that the 28 terawatt (TW) global energy production rate predicted for 2050 is two times that (14TW) for 2010 (Figure 1.1a).[1] Fossil fuels (coal, oil, and natural gas) have been the main energy sources since Industrial Revolution, which will likely continue in the near future. To maintain the high-speed development of our economy and society, the use of fossil fuels has skyrocketing from 20, 000 TWh (1950) to 136, 000 TWh (2019) in the past seventy years (Figure 1.1b). Our reliance on fossil fuels has given rise to two main problems: (1) an energy crisis due to the non-renewability and limited reserves of fossil fuels,[2] and (2) high levels of atmospheric CO_2 concentrations due to CO_2 emissions (Figure 1.2a).[3] CO_2 emissions have resulted in a sharp increase in atmospheric CO_2 concentrations (Figure 1.2a), giving rise to global problems, such as the global warming, climate change, ocean acidification, and so on.[4-7] Therefore, it is urgent to end our dependence on fossil fuels by using renewable energy.
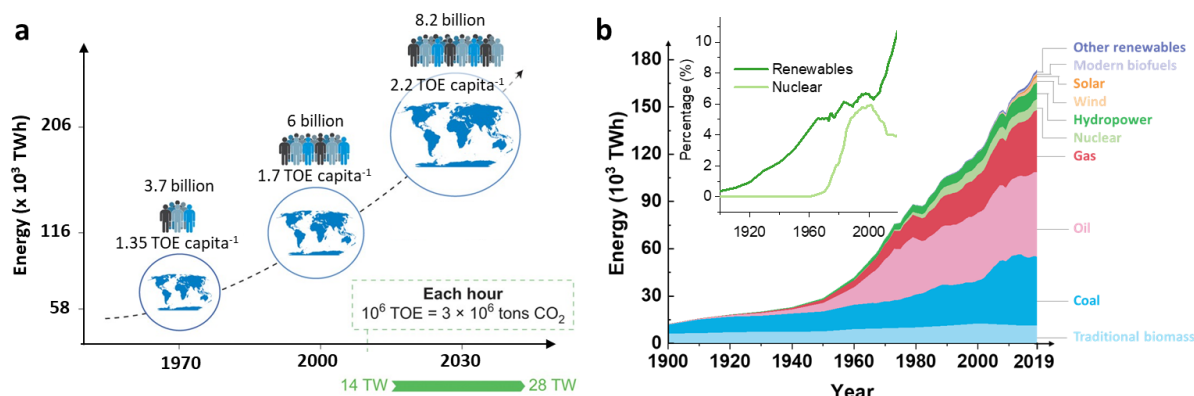
Figure 1.1 Global energy consumption and distribution in the past century. (a) Forecast of the world's energy needs up to 2050, in which our energy demand will double from 14 TW (2010) to 28 TW (2050). TW = terawatts (10^{12} watts), TOE = ton of oil equivalent, and 1 TOE = 1.163×10^{-5} TWh. (b) Distribution of the global primary energy consumption by sources in the past two hundred years. The data comes from Our World in Data.[8] (a) Reproduced with permission from Larcher et al.,[1] copyright 2015, Springer Nature.

The technologies used to harvest energy from renewable sources (e.g., wind, solar, and hydropower) have been progressing rapidly, resulting in a significant increase in the percentage of renewable energy consumption, i.e., from 3.08% (1950) to 10.68% (2019) relative to the global energy consumption (see the inset in Figure 1.1b).[8] However, all the renewable energy sources that have been developed are inherently intermittent (Figure 1.2b) and generally disperse, making energy storage systems essential.[9] Renewable energy can be stored with various strategies, among which the particularly attractive technologies are based on hydrogen cycle and carbon cycle, involving water splitting and CO_2 reduction powered by renewable electricity, respectively.[9, 10]

1
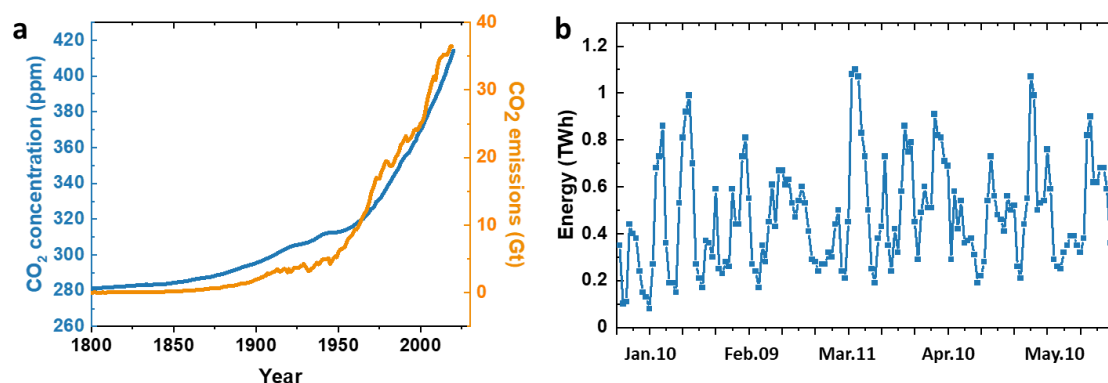
Figure 1.2 Correlation of the atmospheric CO$_2$ concentration and global CO$_2$ emissions and an example showing the intermittency of renewable energy. (a) Evolution of the atmospheric CO$_2$ concentration and global CO$_2$ annual emissions in the past two hundred years. Atmospheric CO$_2$ data comes from NOAA.[3, 11] CO$_2$ emissions data from Our World in Data.[12, 13] (b) Total daily production of wind and solar energy in Germany in the first five months in 2021. The data is from the Fraunhofer Institute for Solar Energy Systems ISE.[14]

Electrochemical CO$_2$ reduction (eCO$_2$RR) is one of the most promising approaches for storing renewable energy. Using CO$_2$, water, and renewable electricity, eCO$_2$RR can produce various value-added chemicals, such as CO, hydrocarbons, and oxygenates. As shown in Figure 1.3, this technology not only can store intermittent renewable energy as liquid fuels (e.g., formate, methanol, and ethanol) but also produce commodity chemical feedstocks (CO and C$_2$H$_4$), thus allowing it to mitigate the global warming problem caused by high atmospheric CO$_2$ concentrations and help release our heavy dependence on fossil fuels.[15] However, the current eCO$_2$RR technology, especially to produce C$_{2+}$ products, is far from being usable in industrial scale, leading to our interest in investigating the eCO$_2$RR to C$_{2+}$ products from the fundamental aspects in this thesis, including the active catalytic sites, the effects of the local reaction environments, and the transport of the products in the flow reactor.
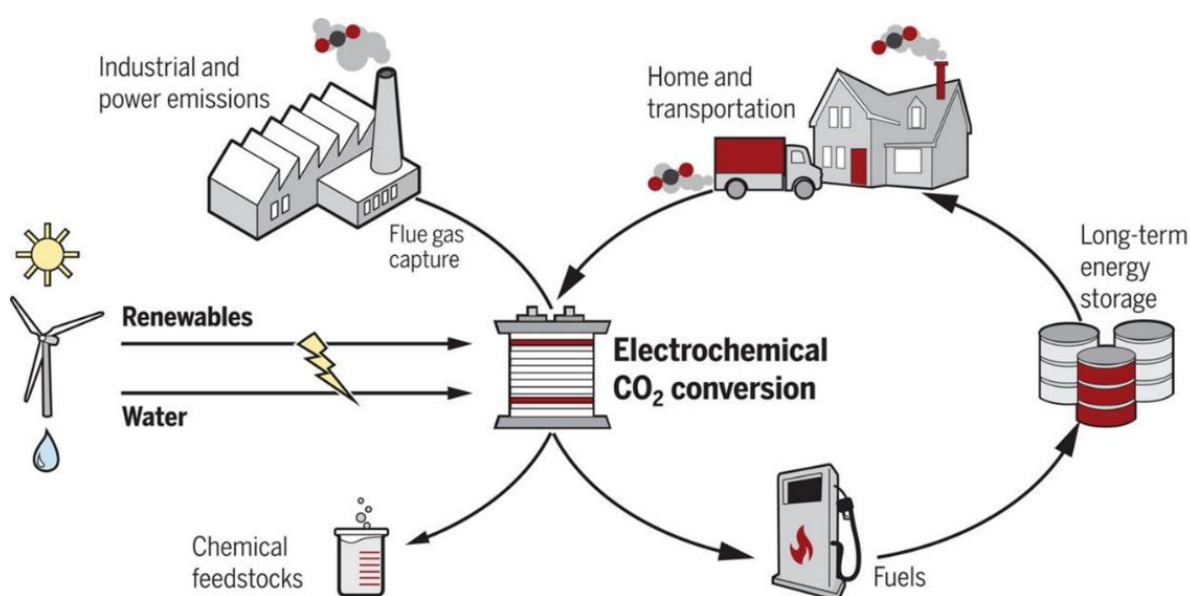
Figure 1.3 Schematics of the carbon cycle employing electrochemical CO$_2$ reduction. Electrochemical CO$_2$ reduction converts CO$_2$ and water into fuels or commodity chemical feedstocks by using renewable electricity. Reproduced with permission from Luna et al.,[15] copyright 2019, The American Association for the Advancement of Science.

2

1.2 General introduction for electrochemical CO_2 reduction

1.2.1 Thermodynamics and economics

eCO_2RR in aqueous solution can produce more than 16 products,[16] with the commonly reported products including CO, formate, CH_4, methanol, C_2H_4, ethanol, acetate, and n-propanol, primarily because their relatively high selectivity allows for easy quantification. In Figure 1.4, the standard equilibrium potentials of eCO_2RR to the commonly reported products are compared with the hydrogen evolution reaction (HER) and oxygen evolution reaction (OER).[17] Notably, electrolysis of CO_2 in aqueous solution requires potentials comparable to that of HER (Figure 1.4); thus, the inhibition of the evolution of H_2 is one of the key issues in eCO_2RR. OER in aqueous solution is one of the best anodic reactions because water is renewable and scalable.[17] Other reactions can also be coupled with eCO_2RR, such as the electro-oxidation of glycerol.[18]

E / V vs RHE				
	$CO_2 + 2H^+ + 2e^-$	$HCOOH_{(aq)}$	−0.12 V	Formic acid
	$CO_2 + 2H^+ + 2e^-$	$CO_{(g)} + H_2O$	−0.10 V	Carbon monoxide
−0.0	$2H^+ + 2e^-$	H_2	0.00 V	Hydrogen evolution
	$CO_2 + 6H^+ + 6e^-$	$CH_3OH_{(aq)} + H_2O$	+0.03 V	Methanol
	$CO_2 + 4H^+ + 4e^-$	$CH_3CHO_{(aq)} + H_2O$	+0.06 V	Acetaldehyde
	$2CO_2 + 12H^+ + 12e^-$	$C_2H_{4(g)} + 4H_2O$	+0.08 V	Ethylene
0.5	$2CO_2 + 12H^+ + 12e^-$	$CH_3CH_2OH_{(aq)} + 3H_2O$	+0.09 V	Ethanol
	$3CO_2 + 18H^+ + 18e^-$	$C_3H_7OH_{(aq)} + 5H_2O$	+0.10 V	n-propanol
	$2CO_2 + 8H^+ + 8e^-$	$CH_3COOH_{(aq)} + 2H_2O$	+0.11 V	Acetic acid
	$CO_2 + 8H^+ + 8e^-$	$CH_{4(g)} + 2H_2O$	+0.17 V	Methane
1.0				
	$O_2 + 4H^+ + 4e^-$	$2H_2O$	+1.23 V	Oxygen evolution

Energy stored

Figure 1.4 Standard equilibrium potentials vs reversible hydrogen electrode of eCO_2RR to its common products. The data is from Thomas F. Jaramillo and coworker's review paper, in which they use Gibbs free energy of the reactions to calculate the standard potentials when CO_2 is in its gas phase and water is in its liquid phase.[17]

The 1.23 V potential difference between eCO_2RR and OER, together with the number of transferred electrons, measures the minimum energy input for a given product and thus can be used to estimate the economic viability of that product. Figure 1.5a compares the market prices of the selected products with the corresponding minimum costs (dashed lines) to produce those products via eCO_2RR powered by photovoltaic electricity and using OER as the electron and proton source.[17] Formic acid, propanol, ethanol, C_2H_4, and methanol have a market price higher than their minimum costs, indicating that it is possible to profit from producing them via eCO_2RR, especially in the future when the price of renewable electricity drops. These minimum costs, however, only consider the cost of capturing CO_2 and the minimum electricity. In practice, a large overpotential is needed for both eCO_2RR and OER to reach a certain reaction rate. At the same time, the Faradaic efficiency, CO_2 conversion, separation of the products, and infrastructures also affect the cost.[15] By assuming a 90% Faradaic efficiency, pure CO_2 at a price of $30 ton^{-1}, and a 30 years lifetime for the infrastructure, Sargent and coworkers calculated the cost of producing CO, C_2H_4, and ethanol as a function of energy

conversion efficiency and the cost of electricity, as shown in Figure 1.5b for ethanol.[15] They found that CO, C$_2$H$_4$, and ethanol produced from eCO$_2$RR under the assumed optimistic conditions are competitive with the products from fossil fuel sources in terms of price. Taking ethanol as an example (Figure 1.5b), it can be produced profitably via eCO$_2$RR when its energy conversion efficiency is above 60% and the price of electricity is below 4 cents per kWh. The energy conversion efficiency here is determined by the overpotential, which, together with Faradaic efficiency, activity, and stability, further determines the production cost from the aspect of eCO$_2$RR.

Overall, to make eCO$_2$RR commercially available, it is essential to decrease the required overpotential and to increase the reaction activity, product selectivity, and reaction stability. The key to achieving them is to develop advanced catalysts and optimize the reaction conditions.
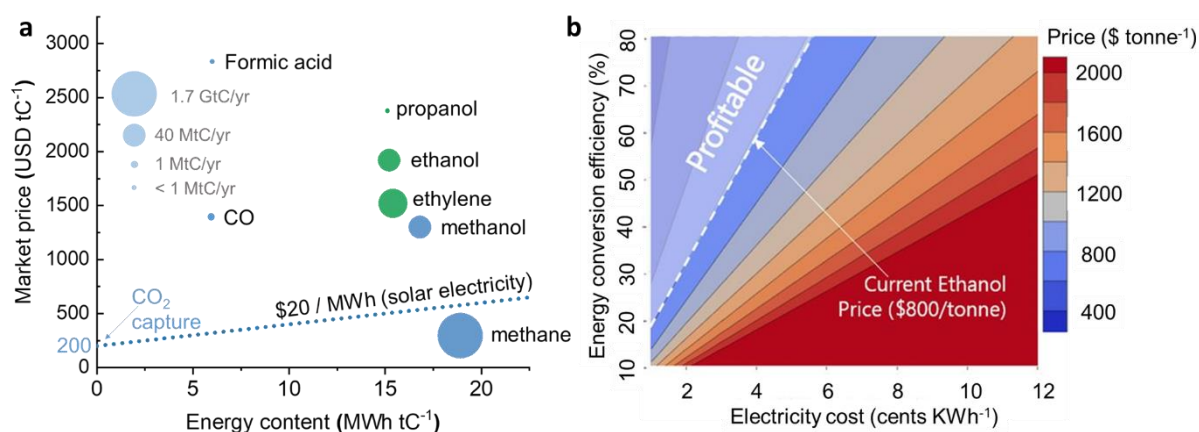
Figure 1.5 Economic analysis of electrochemical CO$_2$ reduction to common products using renewable electricity. (a) Comparison of the current market prices of the selected common products with the minimum costs (dashed lines) necessary to produce these products via eCO$_2$RR assuming that the CO$_2$ capture cost is 200 USD tC^{-1}, both the selectivity and energy conversion efficiency are 100%, and no capital costs are included. The size of the marker shows the logarithmic sizes of the global market for these products, apart from formic acid, propanol, and CO. Data is from Thomas F. Jaramillo and coworker's review paper.[17] (b) Comparison of the costs of ethanol derived from eCO$_2$RR with the current market price of ethanol when considering the capital costs and operating costs under assumed optimum conditions. Reproduced with permission from Luna et al.,[15] copyright 2019, The American Association for the Advancement of Science.

1.2.2 Catalyst materials

The most-investigated electrocatalysts for eCO$_2$RR can be classified into three categories: metal-based catalysts, carbon-based catalysts, and metal-complex catalysts. This thesis will mainly focus on metallic catalysts, especially copper-based catalysts. Thus, carbon-based catalysts and metal-complex catalysts will be introduced briefly.

Pure carbon materials usually lack active sites for eCO$_2$RR and thus require doping of nitrogen and/or metal atoms to obtain decent activity and selectivity. Figure 1.6a shows the typical structure of a carbon doped with nitrogen and metal atoms together, in which each metal atom is anchored by nitrogen atoms that are bonded with carbon atoms. This type of material is often referred to as a single-atom catalyst. Most single-atom catalysts catalyze eCO$_2$RR to produce CO with high selectivity.[19] Copper single-atom catalysts are special in that they can produce other products, such

as C_2H_4 and CH_4; however, they are unlikely to remain stable during CO_2 reduction.[20] Metal complexes, such as metal phthalocyanine, are similar in structure to single-atom catalyst, in that they have a center metal atom anchored by four nitrogen atoms in a carbon matrix (Figure 1.6b). Thus, metal complex catalysts also almost exclusively produce CO.[21] Similar to copper single-atom catalysts, copper complexes are not stable and can demetallize to form copper clusters during eCO_2RR, accounting for their ability to produce C_2H_4 and CH_4.[22] Thus, we are inspired to use the demetallization of copper phthalocyanine to demonstrate the evolution of copper catalysts from isolated atoms to clusters to nanoparticles during eCO_2RR.

a

b

● Carbon ● Nitrogen ● Metal

M = Fe, Co, Ni, Cu
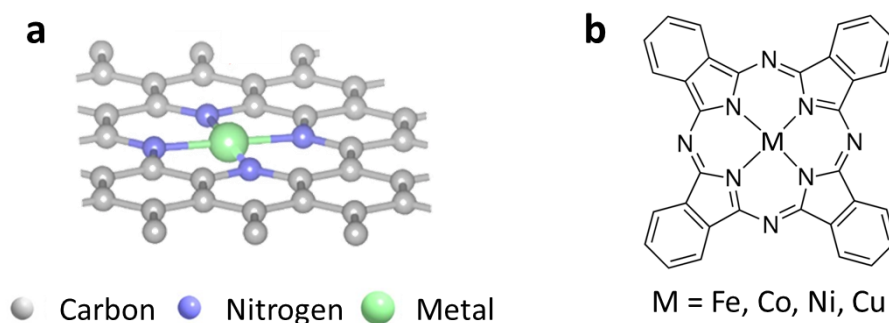
Figure 1.6 Typical structures of the carbon-based single metal-atom catalysts and metal complex catalysts. (a) Schematics of the metal-and-nitrogen atom-doped carbon (metal single-atom catalyst). Reproduced with permission from Yang et al.,[23] copyright 2018, Springer Nature. (b) Molecular formula of a metal phthalocyanine.

Metal catalysts have been classified into four groups according to their product selectivity.[24] Group 1, including indium, tin, bismuth, lead, cadmium, mercury, and thallium, mainly catalyzes eCO_2RR to formate; group 2, including gold, silver, zinc, palladium, and gallium, preferentially produces CO; group 3, containing only copper, can catalyze eCO_2RR beyond CO and formate to produce various hydrocarbons and oxygenates, as shown in Figure 1.4; group 4, consisting of nickel, iron, platinum, and titanium, prefers HER over eCO_2RR.

The different product preferences of different metals can be explained by the different adsorption energies of the key reaction intermediates, including *H, *OCHO (bound through O), *COOH (bound through C), and *CO, on the metal surface.[17] Jan Rossmeisl and coworkers proposed to use the binding energies of *CO and *H to describe the product preferences, as shown in Figure 1.7.[25] They found that the metals in group 2 have a weak *CO binding energy and can adsorb *H at the potential of CO_2 reduction and thus produce mainly CO. Group 1 also shows a weak *CO binding energy but negligible *H adsorption at CO_2 reduction potentials and thus produces mainly formate.[25] Jens K. Nørskov and coworkers attributed the difference between groups 1 and 2 to the atom in the adsorbed COOH bound to the catalyst's surface.[26] They found that the metals in group 1 bound *COOH through C, while group 2 bound it through O (denoted as *OCHO). Metals in group 4 have very strong *H binding energy and thus barely reduce CO_2.

Figure 1.7 also shows that copper's unique ability to reduce CO_2 to C_{2+} is due to its negative *CO binding energy and positive *H binding energy. Therefore, copper has attracted the most attention in terms of the catalysts for eCO_2RR. From optimizing their facets, defects, oxidation states, and grain boundaries to engineering their morphologies and roughness, copper-based materials have been

extensively investigated in terms of producing various products via eCO$_2$RR,[27] as discussed in the next section in detail.
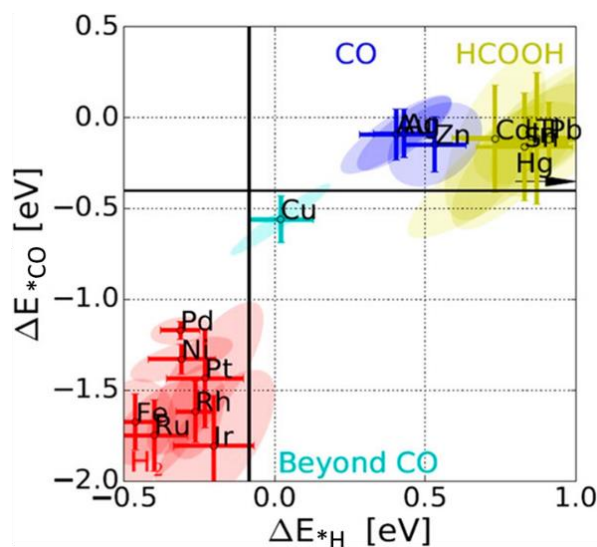
Figure 1.7 Classification of the single metallic catalysts for CO$_2$ reduction based on their binding energies for *CO and *H. Reproduced with permission from Bagger et al.,[25] copyright 2017, John Wiley and Sons.

1.2.3 Effects of the local reaction environments

In addition to catalyst materials, the local reaction environments also greatly affect the selectivity and activity of eCO$_2$RR. This local environments include the local pH value, applied potential, anions, cations, mass transfer, partial pressure of CO$_2$, and temperature.[17] Extensive study has been devoted to understanding the mechanisms behind the effects of the various local environmental parameters, which, in turn, has allowed the researchers to make use of the local reaction environments to tune product selectivity and activity. Several effects are involved in our study. Therefore, we will briefly discuss how each of these environmental parameters affects the eCO$_2$RR results and the possible explanations for these effects. We refer the reader to review papers for detailed and comprehensive discussion.[17, 27]

Effect of pH The pH effect is due to the variable local pH caused by the accumulation of OH$^-$ near the electrode during eCO$_2$RR.[27] The eCO$_2$RR produces OH$^-$ by consuming the protons from water because each electron transfer is coupled with a transfer of a proton. A high pH electrolyte enhances the selectivity of C$_{2+}$ products from eCO$_2$RR on copper catalysts (Figure 1.8a), while a low pH environment preferentially produces CH$_4$ and enhances HER.[28-31] Even though the mechanism behind the pH effect on eCO$_2$RR is still not explicitly clear, several explanations has been proposed.[17] The increased selectivity of C$_{2+}$ products under higher pH conditions could be partially attributed to the higher real overpotential for the rate-determining step to C$_{2+}$ products compared to that for the whole reaction because the rate-determining step shows independence from pH, while the whole reaction involving proton transfer depends on the pH.[32, 33] Meanwhile, the pH may also affect the reaction intermediates and change the selectivity of the final products.[30] For example, at low pH, the coverage of *H is higher, which decreases the coverage of *CO; and therefore, the dimerization of *CO to C$_{2+}$ products becomes difficult. In contrast, the hydrogenation of *CO to CH$_4$ becomes easier.[34, 35]
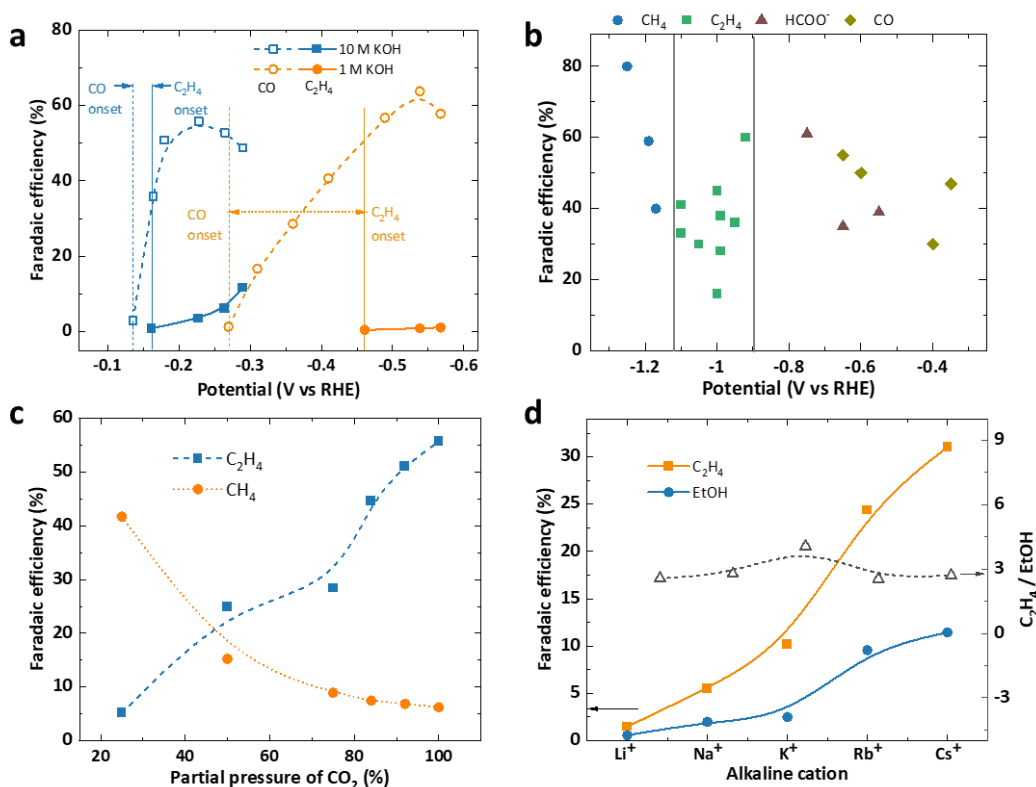
Figure 1.8 Effects of pH, applied potential, partial pressure of CO_2, and alkaline metal cations on the selectivity of C_2 products. (a) Comparison of the Faradaic efficiencies of CO and C_2H_4 from eCO_2RR in 1 M KOH and 10 M KOH on copper catalysts in a flow cell with a gas diffusion electrode.[30] (b) Correlations between the Faradaic efficiencies of C_1 and C_2 products from eCO_2RR and the applied potential on copper catalysts.[36] (c) Faradaic efficiencies of C_2H_4 and CH_4 from eCO_2RR as functions of partial pressure of CO_2 on gold-modified copper catalysts.[37] (d) Faradaic efficiencies of C_2H_4 and ethanol versus the types of the alkali metal cations for eCO_2RR on copper catalysts.[38]

Effect of applied potential   Even though the effect of the applied potential is always convoluted with the effect of the local pH,[17] the trend of the product distribution versus the potential of eCO_2RR on copper catalysts is still valid to a certain extent (Figure 1.8b).[36] This trend could be roughly explained by considering the activation energies, current densities, and coverage of *H and *CO. At low overpotential, copper catalyzes eCO_2RR to produce mainly CO and formate with a small current density because the coverage of *CO is too low, and the overpotential is unable to overcome the activation energy of C-C dimerization. At moderate overpotential, the current density is high enough to produce a high coverage of *CO on the copper surface, and the overpotential also can surmount the barrier energy for C-C coupling, resulting in C_2H_4 and ethanol as the dominate products. Finally, a high overpotential leads to a high production rate of H_2 and thus high coverage of *H, which repels *CO and decreases the coverage of *CO, making C-C coupling difficult and hydrogenation of *CO to CH_4 easier. Therefore, CH_4 becomes dominant at high overpotential.[16, 36, 39] Hence, there is an optimal potential range for the selective production of C_2H_4 and ethanol on copper catalysts.

Effect of anions and cations   Increasing the size of alkali metal cations in the electrolyte improves the selectivity and activity of C_{2+} products from eCO_2RR on copper catalysts and suppresses the selectivity for HER (Figure 1.8c).[38, 40-43] On the one hand, larger alkaline metal cations (e.g., Cs^+)

enhance the electric field much more than smaller cations (e.g., Li$^+$) do, thus promoting C-C coupling.[43, 44] On the other hand, the adsorption of CO and other intermediates may also be influenced differently by different cations.[44] Anions affect the selectivity of C$_{2+}$ products mainly through influencing the local pH via their pH buffering capabilities, such as Cl$^-$, ClO$_4^-$, SO$_4^-$, and dilute HCO$_3^-$, all of which have low buffering capabilities, result in higher local pH's during eCO$_2$RR, and make C$_{2+}$ products preferentially produced, as compared to concentrated HPO$_4^{2-}$ and HCO$_3^-$.[45] Halide ions may also alter the product distribution of eCO$_2$RR on copper catalysts by changing the surface structure, morphology, and oxidation state.[46] The specific adsorption of halide ions may contribute to changes in the product selectivity.[47]

Effect of partial pressure of CO$_2$ The partial pressure of CO$_2$ affects the solubility of CO$_2$, which affects the product distribution by changing the mass transfer of CO$_2$ and consequently the coverage of *CO and *H. Researchers have used the partial pressure of CO$_2$ to tune the selectivity of eCO$_2$RR on copper catalysts for C$_2$H$_4$ and CH$_4$ (Figure 1.8d).[37, 40, 48, 49]

Effect of temperature   The temperature affects the solubility of CO$_2$, reaction rate constant, pH of the electrolyte, and adsorption equilibria and thus likely alters the selectivity of the products from eCO$_2$RR. [17] It has been found that high temperatures favor HER over eCO$_2$RR[50] and that the selectivity of CH$_4$ increases as reaction temperature decreases,[51, 52] likely because at higher temperatures CO$_2$ has a lower solubility, and temperature impacts the intermediates of HER and eCO$_2$RR differently.

Most of the conclusions about the effects of the local environments on eCO$_2$RR are based on the study in the batch cell (also named H-cell), in which the mass transfer limitation is hard to be eliminated and strong basic solutions cannot survive. In this work, we demonstrate the effects of pH, mass transfer, and overpotential on the selectivity and activity of eCO$_2$RR on copper catalysts by comparing the results in an H-cell and a flow cell.

1.3   CO$_2$ reduction to C$_{2+}$ on copper-based catalysts

1.3.1   Reaction Pathways

The pathways of eCO$_2$RR to C$_{2+}$ products on copper catalysts in aqueous solution involve the transfer of more than 12 electron-proton pairs and numerous intermediates that are impacted by the copper facets, defects of the copper surface, overpotential, local pH, HER, and the solvent layer.[17, 27, 53, 54] All these factors together make it extremely difficult to explicitly reveal the pathways, even though extensive experimental and computational studies have been devoted in doing so.[17, 27] However, it is important to understand the pathways because this information can help the researchers to customize the catalyst materials for production of certain products. More than twelve research groups have proposed overview pathways for the most common products, which are classified into six groups based on their consistencies.[17]

Figure 1.9 presents the overview of the simplified reaction pathways from CO$_2$ to various products, in which only the key intermediates are shown.[27] It has been agreed that CO is the key intermediates towards C$_{2+}$ but the way C-C coupling takes place is still under debate.[17] Pathways to C$_2$H$_4$ and ethanol share some steps after C-C coupling, while the step where the bifurcation takes place is still not clear,

making it difficult to tune the selectivity between C_2H_4 and ethanol.[17, 27, 54] We refer the reader to the review papers[17, 27, 54] and original studies for detailed discussions.

As CO is the key intermediate for CO_2 to C_{2+} products, it is possible to design a tandem catalyst consisting of a CO-preferred material and copper. With such a design, the CO produced on the CO-preferred sites can spill over onto the copper surface and be further reduced to C_{2+} products. Thus, tandem catalysts have the potential to increase the selectivity for C_{2+} products compared to monometallic copper catalysts.[55] This thesis also contributes to demonstrate the tandem effect in nanoscale in Chapter 3.
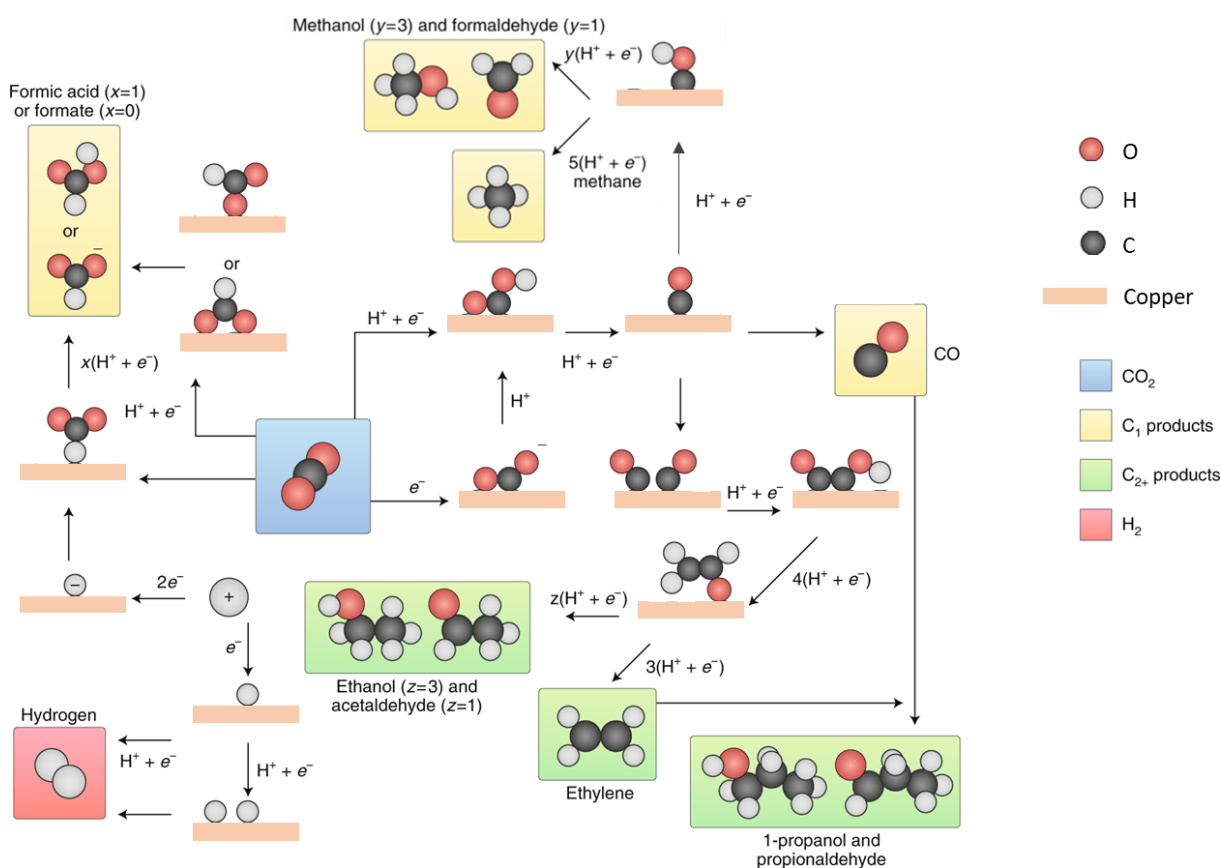
Figure 1.9 Overview of the reaction pathways for eCO_2RR to common products. The pathways were proposed by Marc T.M. Koper's group.[27] Reproduced with modification under the permission from Birdja et al.,[27] copyright 2019, Springer Nature.

1.3.2　Active sites on copper catalysts

Knowledge about the active sites that are selective for C_{2+} products can guide researchers in tailoring the materials to produce a target product. The active sites on copper catalysts for C_{2+} products of eCO_2RR are related to crystal facets, grain boundaries, and the subsurface oxygen in the catalyst materials (Figure 1.10a).[17, 27] The complex structure of polycrystalline copper makes it difficult to unambiguously identify the selectivity of each type of site. Therefore, model catalysts with controlled surface properties should be developed to understand the active sites.
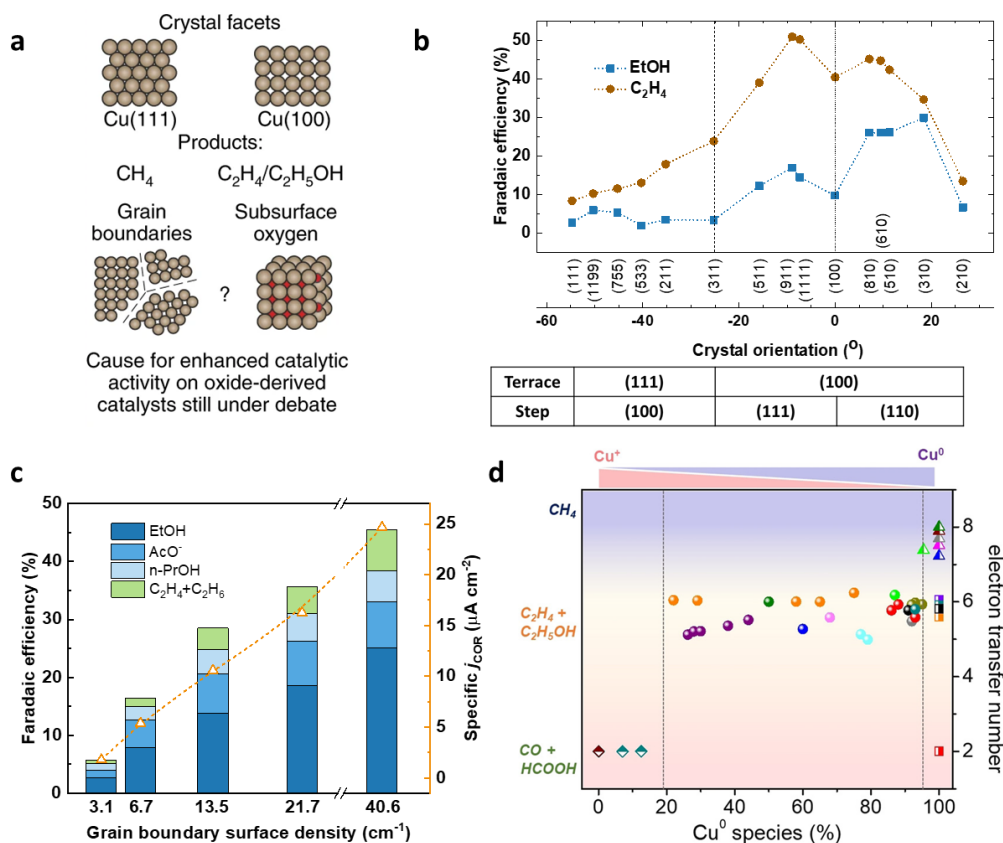
Figure 1.10 Effects of crystal facets, grain boundaries, and oxidation states of copper catalysts on electrochemical CO$_2$ reduction. (a) Schematics of the three different active sites on copper catalysts for eCO$_2$RR at nanoscale. (b) Faradaic efficiencies of C$_2$H$_4$ and ethanol (EtOH) as functions of the copper crystal orientation.[59] (c) Faradaic efficiencies and current densities of the products from CO reduction on copper electrodes as functions of the grain boundary density on the catalyst surface.[61] (d) Correlation of the copper oxidation state (content of Cu$^+$) with the dominant products of eCO$_2$RR, including CO/formate, C$_2$ (C$_2$H$_4$ and ethanol), and CH$_4$, on various state-of-the-art copper catalysts. Reproduced with permission from (a) Birdja et al.,[27] copyright 2019, Springer Nature and (d) Wang et al.,[66] copyright 2021, Wiley-VCH GmbH.

Previous studies have shown that the Cu(100) surface preferentially produces C$_2$H$_4$ and ethanol over CH$_4$, while Cu(111) and Cu(110) surfaces are more selective in terms of producing CH$_4$ over C$_{2+}$ molecules.[56-58] The uncoordinated sites derived from the presence of Cu(111) or Cu(110) steps on the Cu(100) terrace enhance the selectivity for C$_2$H$_4$ and ethanol compared to their presence on Cu(100) surface, as shown in Figure 1.10b.[56, 59, 60]

One of the effective methods for increasing the density of the uncoordinated numbers or defects in copper materials is to introduce grain boundaries. The copper catalysts derived from copper oxide contain rich grain boundaries and show higher activity and selectivity in catalyzing eCO$_2$RR to C$_{2+}$ products compared with single-crystal copper surfaces.[61-64] Kanan and coworkers have explicitly revealed the relation between the selectivity and activity of C$_{2+}$ products and the grain boundary density (Figure 1.10c), and they also directly demonstrated that the grain boundary is more active for eCO$_2$RR on a gold model catalyst via using in situ scanning electrochemical cell microscopy.[64] Another way to introduce the active sites of uncoordinated numbers to copper materials is to increase the specific area or surface roughness.[65]

It has also be claimed that the oxidation state of copper and subsurface oxygen play key roles in catalyzing eCO_2RR selectively to C_{2+} products (Figure 1.10d).[66, 67] Most of the copper catalysts with the top selectivity for C_{2+} products are derived from copper oxide, and it is claimed that their subsurface oxidized copper produces the main active sites.[66, 68-70] However, subsurface oxygen always coexists with high-density grain boundaries because both are introduced by the same precursor, copper oxide. On the other hand, the existence of subsurface oxygen is still a debated topic because it is difficult to detect the oxidation state of copper in a subsurface, and copper should be in a metallic state during eCO_2RR according to its Pourbaix diagram.[71-75]

On the basis of the above understanding of the active sites, in this thesis, we developed several copper oxide-derived catalysts with high-density grain boundaries and excellent selectivity towards C_{2+} products.

1.3.3   Dynamics of catalysts

The reconstruction of the metallic catalyst surface is a common phenomenon during the heterogeneous catalytic reaction.[76] Both chemical conditions (e.g., adsorbates and reactants) and physical conditions (e.g., temperature, pressure, and electrical potential) can cause the catalyst to alter its surface structure.[22] Almost all prior investigations have assumed that the detected active sites are stable or identical during eCO_2RR, which, however, is probably not true because most copper catalysts have been found to reconstruct during CO_2 reduction (Figure 1.11).[77-80] The local CO concentration plays a big role in this reconstruction during eCO_2RR.[81] The reconstruction increases the active sites, e.g., grain boundaries, for some catalysts and thus benefits the production of C_{2+} molecules.[62] However, some catalysts gravitate towards a state that decreases the selectivity of C_{2+} molecules, e.g., phase separation in a Cu/Ag alloy.[82] Therefore, the mechanism for the copper reconstruction should be elucidated and the methods to prevent this reconstruction should be developed. Most of the related reports demonstrate the reconstruction of a bulk surface or a top-down reconstruction from nanoparticles to its fragments. In this thesis, we reveal a bottom-up reconstruction process of copper that starts with single atoms, then proceeds to nanoclusters, then to nanoparticles. We also established a relationship between the catalyst structure and eCO_2RR performance by using this evolution.
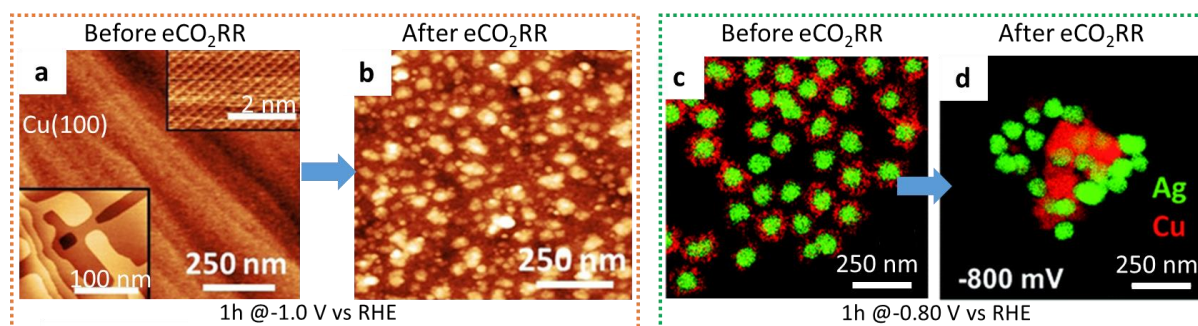
Figure 1.11 Comparison of the copper catalysts before and after electrochemical CO_2 reduction. (a, b) Comparison of the ex situ AFM images of a Cu(100) single-crystal surface before and after 1 hour of eCO_2RR at -1.0 V vs RHE in 0.1 M $KHCO_3$. The images were acquired in air. (c, d) Comparison of the ex situ EDX elemental maps of AgCu core-shell nanoparticles before and after 1 hour of eCO_2RR at -0.80 V vs RHE in 0.1 M $KHCO_3$.

1.3.4 Copper-based bimetallic catalysts

Many strategies can be used to engineer copper catalysts towards different products, such as controlling the exposed facets of the copper nanoparticles, enriching the grain boundary, controlling the oxidation state by doping another element, decorating the copper surface with other materials, and alloying the copper with another metal.[84] Among these materials, copper-based bimetallic catalysts, such as Cu-Au,[85] Cu-Ag,[86, 87] and Cu-Zn,[88] are especially interesting because they can improve the selectivity of C$_{2+}$ products, such as C$_2$H$_4$ and ethanol, compared to monometallic copper catalysts.

However, what accounts for this improvement is still unclear, and there are big inconsistencies in the product preferences and explanations in the reported work. Here, we take the Cu-Ag bimetallic catalyst as an example. Silver catalyzes eCO$_2$RR with nearly 100% Faradaic efficiency for CO, [89, 90] and copper has the capability to further reduce CO to produce C$_{2+}$ molecule.[17] Several reports found that the addition of silver in copper catalysts greatly improved the selectivity of C$_2$H$_4$ (Figure 1.12c),[91-95] while, in other works, Cu-Ag catalysts were reported to preferentially produce ethanol over C$_2$H$_4$ (Figure 1.12d).[86, 96-101] There are two explanations for the enhancement of the selectivity – that is, the tandem and interface effects. In the tandem effect, the CO produced from eCO$_2$RR on silver diffuses to the surface on copper and then is further reduced to C$_{2+}$ products (Figure 1.12a).[55, 87, 102]
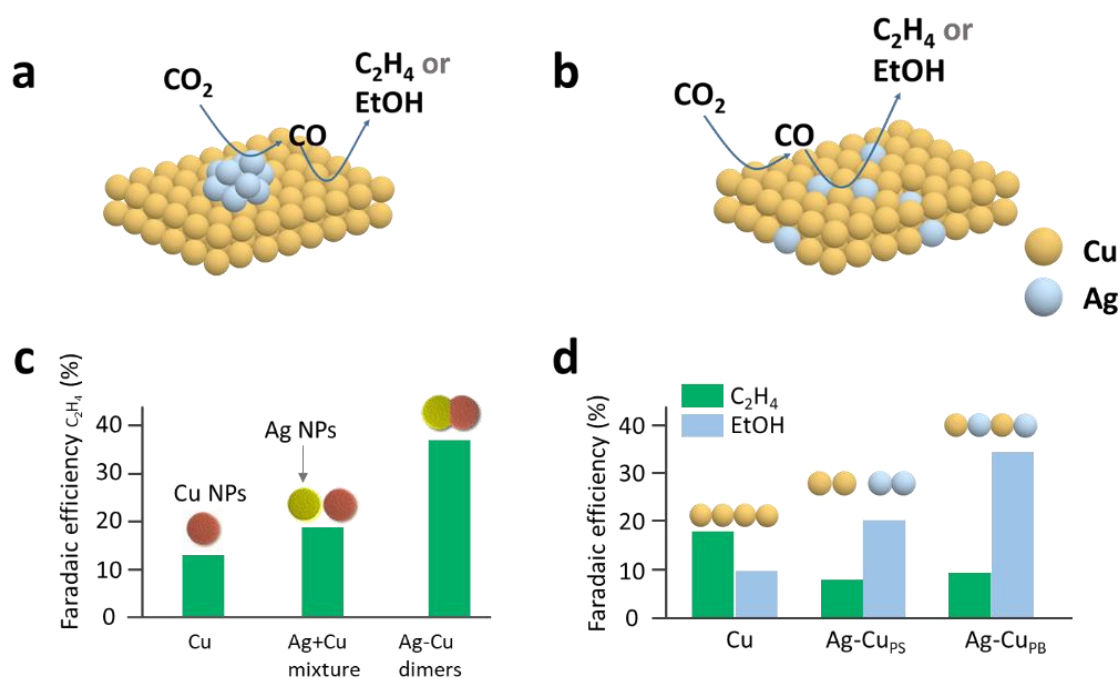
Figure 1.12 Schematic of the tandem and interface effects in the Cu-Ag bimetallic catalyst for electrochemical CO$_2$ reduction. Schematic of the tandem process (a) and the effect of coordination environment (b) for eCO$_2$RR on the Cu-Ag bimetallic catalyst. (c) Comparison of the selectivity of C$_2$H$_4$ produced from eCO$_2$RR on Cu nanoparticles (NPs), a mixture of Cu NPs and Ag NPs, and Ag-Cu dimers.[93] (d) Comparison of the selectivity of ethanol produced from eCO$_2$RR on Cu, Ag-Cu bimetallic with separated phase, and Ag-Cu bimetallic with blended phase.[99]

The interface effect assumes that the silver atoms dope into the copper's crystal lattice, which alters the coordination environment to favor C-C coupling for C_{2+} products (Figure 1.12b).[86] However, both tandem and interface effects have been ascribed to enhancement in the selectivity of both C_2H_4 and ethanol (Figure 1.12c, d). [86, 92, 93, 95] Therefore, it is essential to distinguish the tandem and interface effects and clarify why Cu-Ag bimetallic enhances the selectivity of C_2H_4 or ethanol. In this work, we design and synthesize a model catalyst, Ag@C@Cu core-shell nanoparticles, in which the formation of the interface of Cu and Ag is controlled. Using this model catalyst, we comparatively reveal the interface and tandem effects in the copper-based bimetallic catalyst for eCO_2RR.

1.4   Electrolysis reactors with a gas diffusion electrode

Most studies concerning eCO_2RR use an H-cell to evaluate the selectivity and activity of the catalyst. In an H-cell where the electrode is immersed in the electrolyte, CO_2 molecules must diffuse to the surface of the catalyst through the bulk electrolyte. Thus, eCO_2RR is easily limited by the mass transfer of CO_2 due to the low solubility (34 mM in 0.1 M $KHCO_3$ at 25°C) of the CO_2 in the electrolyte.[103] Consequently, it is hard to evaluate the real performance of an eCO_2RR catalyst in an H-cell, including activity, selectivity, and stability.

The configuration of a gas diffusion electrode (GDE) in a flow cell (Figure 1.13) allows CO_2 molecules to transfer to the catalyst surface in gas phase via the gas diffusion layer because the electrolyte remains at the other side of the gas diffusion layer. Thus, eCO_2RR in a flow reactor occurs with almost no mass transfer limitation and can easily generate a current density of up to 1 A cm^{-1}, which is impossible to realize in H-cell.[104, 105] Meanwhile, the GDE reactor allows the use of an alkaline electrolyte, which also benefits the production C_{2+} products. Therefore, more and more studies have started to evaluate eCO_2RR catalysts in a GDE reactor in recent years.
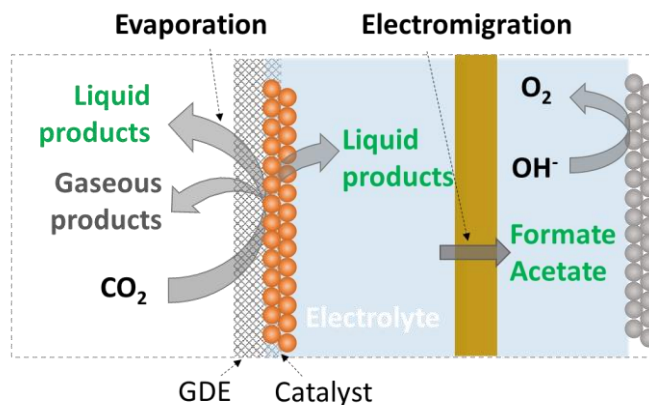
Figure 1.13 Schematic of the crossover of the liquid products through the gas diffusion electrode and anion exchange membrane in a flow cell.

The gas diffusion layer supporting the catalyst in a GDE determines the stability and even the selectivity of the eCO_2RR. Carbon paper, consisting of a carbon fiber layer coated by a microporous layer of carbon black, is the most commonly used gas diffusion layer; unfortunately it is easily flooded by the electrolyte.[106] The hydrophobicity of the gas diffusion layer, normally controlled by its PTFE content, is one key factor affecting the flooding and thus the stability of the GDE during eCO_2RR. GDEs based on carbon paper remain stable just for several hours under eCO_2RR with the most commonly

used 1 M KOH electrolyte.[39] To improve the stability of the GDE, Sargent and coworkers used a porous PTFE membrane as the gas diffusion layer, which had a stability of 150 hours at current densties between 75 and 100 mA cm^{-2} for eCO$_2$RR with a copper catalyst.[30] Therefore, it is important to develop a new gas diffusion layer for eCO$_2$RR.

As most of the liquid products from eCO$_2$RR in a GDE reactor are volatile and generated at the interface between CO$_2$ gas and the electrolyte, they may evaporate into the CO$_2$ flow. It is also possible for the liquid products to diffuse through the anion exchange membrane that is used in the flow cell to prevent the liquid products from reaching the anode and being oxidized there.[107] However, almost all the published reports assume that the liquid products completely dissolve in the electrolyte and thus only analyze the catholyte to quantify these products. Meanwhile, the total Faradaic efficiencies of eCO$_2$RR in the flow cells are reported to be less than 100% in several papers, which is possibly due to the incomplete collection of liquid products. Hence, the possible crossover of the liquid products through the GDE and the anions exchange membrane should be investigated.[108-111]

1.5   Objectives and outline of thesis

This thesis aims to solve several key problems for eCO$_2$RR on copper catalysts toward C$_{2+}$ products, especially ethanol, in terms of the active sites and size effects of copper catalysts in nanoscale, the effects of the local CO concentration and local pH in macroscale, and the crossover of liquid products in reactor scale. This thesis is thus motivated by the following four objectives:

1. To demonstrate the evolution of copper catalysts from a bottom-up perspective and to use this evolution to reveal the size effects and active sites of copper catalysts for catalyzing CO$_2$ reduction to C$_{2+}$ products; at the same time, to identify the factors that determine the reconstruction of the copper clusters during evolution.
2. To deconvolute the interface and tandem effects of Ag-Cu bimetallic catalysts for eCO$_2$RR towards ethanol by designing a Ag-Cu catalyst for which the formation of the interface is controllable.
3. To reveal the effects of the pH and mass transfer on the selectivity and activity of eCO$_2$RR by directly comparing eCO$_2$RRs using the same catalyst in an H-cell and a flow cell.
4. To design a set-up to investigate if liquid products from eCO$_2$RR on copper catalysts pass through the gas diffusion layer and anion exchange membrane in a flow cell; in the meanwhile, to identify the factors that determine the amount of crossover of liquid products.

In Chapter 2, we revealed the decomposition of the copper phthalocyanine by using in situ Raman and ex situ XPS analysis. we found that copper phthalocyanine was a precursor to form copper clusters and copper nanoparticles during eCO$_2$RR. High density of grain boundaries on the final copper nanoparticles were identified as the active site for producing C$_{2+}$ molecules. The intermediates of eCO$_2$RR were found to play a key role in the evolution of the copper nanoparticles.

In Chapter 3, by synthesizing a Ag@C@Cu catalyst that contains no interface between the silver core and copper shell, we showed that the local CO concentration around the surface of copper catalyst improved the selectivity of ethanol.

In Chapter 4, we developed a type of self-supported copper catalysts with GDE configuration. By using these GDEs in a flow cell, we demonstrated that enhanced mass transfer and high local pH improved the activity and selectivity of C_{2+} products.

Chapter 5 demonstrates the crossover of liquid products through the GDE and anion exchange membrane, an occurrence that has been generally neglected in the literature but significantly affects the measured results. The crossover rate is affected by the current density and flow rates of CO_2 and the catholyte.

These findings provide new strategies in synthesizing copper-based catalysts with rich and proper active sites for the production of C_{2+} products. This thesis also provides rigorous protocols to accurately quantify the liquid products for better evaluation of eCO_2RR performance in a flow cell.

1.6 References

[1]   D. Larcher, J.M. Tarascon, Towards greener and more sustainable batteries for electrical energy storage, Nature Chemistry, 7 (2015) 19-29.

[2]   M. Höök, X. Tang, Depletion of fossil fuels and anthropogenic climate change—A review, Energy Policy, 52 (2013) 797-809.

[3]   R. Lindsey, Climate Change: Atmospheric Carbon Dioxide, NOAA, https://www.climate.gov/news-features/understanding-climate/climate-change-atmospheric-carbon-dioxide, 2020.

[4]   I. Haldar, Global Warming: The Causes and Consequences, Readworthy.

[5]   O. Hoegh-Guldberg, P.J. Mumby, A.J. Hooten, R.S. Steneck, P. Greenfield, E. Gomez, C.D. Harvell, P.F. Sale, A.J. Edwards, K. Caldeira, N. Knowlton, C.M. Eakin, R. Iglesias-Prieto, N. Muthiga, R.H. Bradbury, A. Dubi, M.E. Hatziolos, Coral Reefs Under Rapid Climate Change and Ocean Acidification, Science, 318 (2007) 1737-1742.

[6]   J.C. Orr, V.J. Fabry, O. Aumont, L. Bopp, S.C. Doney, R.A. Feely, A. Gnanadesikan, N. Gruber, A. Ishida, F. Joos, R.M. Key, K. Lindsay, E. Maier-Reimer, R. Matear, P. Monfray, A. Mouchet, R.G. Najjar, G.-K. Plattner, K.B. Rodgers, C.L. Sabine, J.L. Sarmiento, R. Schlitzer, R.D. Slater, I.J. Totterdell, M.-F. Weirig, Y. Yamanaka, A. Yool, Anthropogenic ocean acidification over the twenty-first century and its impact on calcifying organisms, Nature, 437 (2005) 681-686.

[7]   D.J. Wuebbles, A.K. Jain, Concerns about climate change and the role of fossil fuel use, Fuel Processing Technology, 71 (2001) 99-119.

[8]   H. Ritchie, Energy mix, Vaclav Smil (2017). Energy Transitions: Global and National Perspectives. & BP Statistical Review of World Energy., Our World in Data, 2021.

[9]   S. Ould Amrouche, D. Rekioua, T. Rekioua, S. Bacha, Overview of energy storage in renewable energy systems, International Journal of Hydrogen Energy, 41 (2016) 20914-20927.

[10]   W.A. Smith, T. Burdyny, D.A. Vermaas, H. Geerlings, Pathways to Industrial-Scale Fuel Out of Thin Air from CO_2 Electrolysis, Joule, 3 (2019) 1822-1834.

[11]   Mauna Loa CO_2 annual mean data, NOAA, https://gml.noaa.gov/ccgg/trends/data.html, 2021.

[12]   Our World in Data CO_2 and Greenhouse Gas Emissions dataset, Our World in Data, https://github.com/owid/co2-data, 2021.

[13]   H.R.M. Roser, CO_2 and Greenhouse Gas Emissions, Our Would in Data, https://ourworldindata.org/co2-and-other-greenhouse-gas-emissions#citation, 2020.

[14]   Daily electricity generation in Germany in 2021, Fraunhofer Institute for Solar Energy Systems ISE, https://energy-charts.info/charts/energy/chart.htm?l=en&c=DE&interval=day, 2021.

[15]   P. De Luna, C. Hahn, D. Higgins, S.A. Jaffer, T.F. Jaramillo, E.H. Sargent, What would it take for renewably powered electrosynthesis to displace petrochemical processes?, Science, 364 (2019) eaav3506.

[16]   K.P. Kuhl, E.R. Cave, D.N. Abram, T.F. Jaramillo, New insights into the electrochemical reduction of carbon dioxide on metallic copper surfaces, Energy & Environmental Science, 5 (2012) 7050-7059.

[17]   S. Nitopi, E. Bertheussen, S.B. Scott, X. Liu, A.K. Engstfeld, S. Horch, B. Seger, I.E.L. Stephens, K. Chan, C. Hahn, J.K. Nørskov, T.F. Jaramillo, I. Chorkendorff, Progress and Perspectives of Electrochemical CO_2 Reduction on Copper in Aqueous Electrolyte, Chemical Reviews, 119 (2019) 7610-7672.

[18]   S. Verma, S. Lu, P.J.A. Kenis, Co-electrolysis of CO_2 and glycerol as a pathway to carbon chemicals with improved technoeconomics due to low electricity consumption, Nature Energy, 4 (2019) 466-474.

[19]   W. Ju, A. Bagger, G.-P. Hao, A.S. Varela, I. Sinev, V. Bon, B. Roldan Cuenya, S. Kaskel, J. Rossmeisl, P. Strasser, Understanding activity and selectivity of metal-nitrogen-doped carbon catalysts for electrochemical reduction of CO_2, Nature Communications, 8 (2017) 944.

[20]   D. Karapinar, N.T. Huan, N. Ranjbar Sahraie, J. Li, D. Wakerley, N. Touati, S. Zanna, D. Taverna, L.H. Galvão Tizei, A. Zitolo, F. Jaouen, V. Mougel, M. Fontecave, Electroreduction of CO_2 on

Single-Site Copper-Nitrogen-Doped Carbon Material: Selective Formation of Ethanol and Reversible Restructuration of the Metal Sites, Angewandte Chemie International Edition, 58 (2019) 15098-15103.

[21]   L. Sun, V. Reddu, A.C. Fisher, X. Wang, Electrocatalytic reduction of carbon dioxide: opportunities with heterogeneous molecular catalysts, Energy & Environmental Science, 13 (2020) 374-403.

[22]   Z. Weng, Y. Wu, M. Wang, J. Jiang, K. Yang, S. Huo, X.-F. Wang, Q. Ma, G.W. Brudvig, V.S. Batista, Y. Liang, Z. Feng, H. Wang, Active sites of copper-complex catalytic materials for electrochemical carbon dioxide reduction, Nature Communications, 9 (2018) 415.

[23]   H.B. Yang, S.-F. Hung, S. Liu, K. Yuan, S. Miao, L. Zhang, X. Huang, H.-Y. Wang, W. Cai, R. Chen, J. Gao, X. Yang, W. Chen, Y. Huang, H.M. Chen, C.M. Li, T. Zhang, B. Liu, Atomically dispersed Ni(i) as the active site for electrochemical CO_2 reduction, Nature Energy, 3 (2018) 140-147.

[24]   Y. Hori, CO_2 Reduction Using Electrochemical Approach a comprehensive review for metal catalysts, in: M. Sugiyama, K. Fujii, S. Nakamura (Eds.) Solar to Chemical Energy Conversion: Theory and Application, Springer International Publishing, Cham, 2016, pp. 191-211.

[25]   A. Bagger, W. Ju, A.S. Varela, P. Strasser, J. Rossmeisl, Electrochemical CO_2 Reduction: A Classification Problem, ChemPhysChem, 18 (2017) 3266-3273.

[26]   J.T. Feaster, C. Shi, E.R. Cave, T. Hatsukade, D.N. Abram, K.P. Kuhl, C. Hahn, J.K. Nørskov, T.F. Jaramillo, Understanding Selectivity for the Electrochemical Reduction of Carbon Dioxide to Formic Acid and Carbon Monoxide on Metal Electrodes, ACS Catalysis, 7 (2017) 4822-4827.

[27]   Y.Y. Birdja, E. Pérez-Gallent, M.C. Figueiredo, A.J. Göttle, F. Calle-Vallejo, M.T.M. Koper, Advances and challenges in understanding the electrocatalytic conversion of carbon dioxide to fuels, Nature Energy, 4 (2019) 732-745.

[28]   K.J.P. Schouten, E. Pérez Gallent, M.T.M. Koper, The influence of pH on the reduction of CO and CO_2 to hydrocarbons on copper electrodes, Journal of Electroanalytical Chemistry, 716 (2014) 53-57.

[29]   H.S. Jeon, J. Timoshenko, C. Rettenmaier, A. Herzog, A. Yoon, S.W. Chee, S. Oener, U. Hejral, F.T. Haase, B. Roldan Cuenya, Selectivity Control of Cu Nanocrystals in a Gas-Fed Flow Cell through CO_2 Pulsed Electroreduction, Journal of the American Chemical Society, 143 (2021) 7578-7587.

[30]   C.-T. Dinh, T. Burdyny, M.G. Kibria, A. Seifitokaldani, C.M. Gabardo, F.P. García de Arquer, A. Kiani, J.P. Edwards, P. De Luna, O.S. Bushuyev, C. Zou, R. Quintero-Bermudez, Y. Pang, D. Sinton, E.H. Sargent, CO_2 electroreduction to ethylene via hydroxide-mediated copper catalysis at an abrupt interface, Science, 360 (2018) 783.

[31]   R. Kas, R. Kortlever, H. Yılmaz, M.T.M. Koper, G. Mul, Manipulating the Hydrocarbon Selectivity of Copper Nanoparticles in CO_2 Electroreduction by Process Conditions, ChemElectroChem, 2 (2015) 354-358.

[32]   Y. Hori, R. Takahashi, Y. Yoshinami, A. Murata, Electrochemical Reduction of CO at a Copper Electrode, The Journal of Physical Chemistry B, 101 (1997) 7075-7081.

[33]   L. Wang, S.A. Nitopi, E. Bertheussen, M. Orazov, C.G. Morales-Guio, X. Liu, D.C. Higgins, K. Chan, J.K. Nørskov, C. Hahn, T.F. Jaramillo, Electrochemical Carbon Monoxide Reduction on Polycrystalline Copper: Effects of Potential, Pressure, and pH on Selectivity toward Multicarbon and Oxygenated Products, ACS Catalysis, 8 (2018) 7445-7454.

[34]   A.D. Handoko, C.W. Ong, Y. Huang, Z.G. Lee, L. Lin, G.B. Panetti, B.S. Yeo, Mechanistic Insights into the Selective Electroreduction of Carbon Dioxide to Ethylene on Cu2O-Derived Copper Catalysts, The Journal of Physical Chemistry C, 120 (2016) 20058-20067.

[35]   X. Liu, P. Schlexer, J. Xiao, Y. Ji, L. Wang, R.B. Sandberg, M. Tang, K.S. Brown, H. Peng, S. Ringe, C. Hahn, T.F. Jaramillo, J.K. Nørskov, K. Chan, pH effects on the electrochemical reduction of CO(2) towards C2 products on stepped copper, Nature Communications, 10 (2019) 32.

[36]   D. Ren, J. Fong, B.S. Yeo, The effects of currents and potentials on the selectivities of copper toward carbon dioxide electroreduction, Nature Communications, 9 (2018) 925.

[37]   X. Wang, P. Ou, J. Wicks, Y. Xie, Y. Wang, J. Li, J. Tam, D. Ren, J.Y. Howe, Z. Wang, A. Ozden, Y.Z. Finfrock, Y. Xu, Y. Li, A.S. Rasouli, K. Bertens, A.H. Ip, M. Graetzel, D. Sinton, E.H. Sargent, Gold-in-copper at low *CO coverage enables efficient electromethanation of CO_2, Nature Communications, 12 (2021) 3387.

[38]   M.R. Singh, Y. Kwon, Y. Lum, J.W. Ager, A.T. Bell, Hydrolysis of Electrolyte Cations Enhances the Electrochemical Reduction of CO_2 over Ag and Cu, Journal of the American Chemical Society, 138 (2016) 13006-13012.

[39]   J.-J. Lv, M. Jouny, W. Luc, W. Zhu, J.-J. Zhu, F. Jiao, A Highly Porous Copper Electrocatalyst for Carbon Dioxide Reduction, Advanced Materials, 30 (2018) 1803111.

[40]   Y. Lum, B. Yue, P. Lobaccaro, A.T. Bell, J.W. Ager, Optimizing C–C Coupling on Oxide-Derived Copper Catalysts for Electrochemical CO_2 Reduction, The Journal of Physical Chemistry C, 121 (2017) 14191-14203.

[41]   A. Murata, Y. Hori, Product Selectivity Affected by Cationic Species in Electrochemical Reduction of CO_2 and CO at a Cu Electrode, Bulletin of the Chemical Society of Japan, 64 (1991) 123-127.

[42]   E. Pérez-Gallent, G. Marcandalli, M.C. Figueiredo, F. Calle-Vallejo, M.T.M. Koper, Structure- and Potential-Dependent Cation Effects on CO Reduction at Copper Single-Crystal Electrodes, Journal of the American Chemical Society, 139 (2017) 16412-16419.

[43]   J. Resasco, L.D. Chen, E. Clark, C. Tsai, C. Hahn, T.F. Jaramillo, K. Chan, A.T. Bell, Promoter Effects of Alkali Metal Cations on the Electrochemical Reduction of Carbon Dioxide, Journal of the American Chemical Society, 139 (2017) 11277-11287.

[44]   A.S. Malkani, J. Li, N.J. Oliveira, M. He, X. Chang, B. Xu, Q. Lu, Understanding the electric and nonelectric field components of the cation effect on the electrochemical CO reduction reaction, Science Advances, 6 (2020) eabd2569.

[45]   Y. Hori, A. Murata, R. Takahashi, S. Suzuki, Enhanced formation of ethylene and alcohols at ambient temperature and pressure in electrochemical reduction of carbon dioxide at a copper electrode, Journal of the Chemical Society, Chemical Communications, (1988) 17-19.

[46]   D. Gao, F. Scholten, B. Roldan Cuenya, Improved CO_2 Electroreduction Performance on Plasma-Activated Cu Catalysts via Electrolyte Design: Halide Effect, ACS Catalysis, 7 (2017) 5112-5120.

[47]   A.S. Varela, W. Ju, T. Reier, P. Strasser, Tuning the Catalytic Activity and Selectivity of Cu for CO_2 Electroreduction in the Presence of Halides, ACS Catalysis, 6 (2016) 2136-2144.

[48]   Y.C. Tan, K.B. Lee, H. Song, J. Oh, Modulating Local CO_2 Concentration as a General Strategy for Enhancing C–C Coupling in CO_2 Electroreduction, Joule, 4 (2020) 1104-1120.

[49]   X. Wang, A. Xu, F. Li, S.-F. Hung, D.-H. Nam, C.M. Gabardo, Z. Wang, Y. Xu, A. Ozden, A.S. Rasouli, A.H. Ip, D. Sinton, E.H. Sargent, Efficient Methane Electrosynthesis Enabled by Tuning Local CO_2 Availability, Journal of the American Chemical Society, 142 (2020) 3525-3531.

[50]   S. Kaneco, N.-h. Hiei, Y. Xing, H. Katsumata, H. Ohnishi, T. Suzuki, K. Ohta, Electrochemical conversion of carbon dioxide to methane in aqueous NaHCO3 solution at less than 273 K, Electrochimica Acta, 48 (2002) 51-55.

[51]   H. Hashiba, S. Yotsuhashi, M. Deguchi, Y. Yamada, Systematic Analysis of Electrochemical CO_2 Reduction with Various Reaction Parameters using Combinatorial Reactors, ACS Combinatorial Science, 18 (2016) 203-208.

[52]   S.T. Ahn, I. Abu-Baker, G.T.R. Palmore, Electroreduction of CO_2 on polycrystalline copper: Effect of temperature on product selectivity, Catalysis Today, 288 (2017) 24-29.

[53]   Y. Li, Q. Sun, Recent Advances in Breaking Scaling Relations for Effective Electrochemical Conversion of CO_2, Advanced Energy Materials, 6 (2016) 1600463.

[54]   T.K. Todorova, M.W. Schreiber, M. Fontecave, Mechanistic Understanding of CO_2 Reduction Reaction (CO_2RR) Toward Multicarbon Products by Heterogeneous Copper-Based Catalysts, Acs Catalysis, 10 (2020) 1754-1768.

[55]   Y. Lum, J.W. Ager Iii, Sequential catalysis controls selectivity in electrochemical CO_2 reduction on Cu, Energy & Environmental Science, (2018).

[56]   Y. Hori, I. Takahashi, O. Koga, N. Hoshi, Selective Formation of C_2 Compounds from Electrochemical Reduction of CO_2 at a Series of Copper Single Crystal Electrodes, The Journal of Physical Chemistry B, 106 (2002) 15-17.

[57]   Y. Hori, H. Wakebe, T. Tsukamoto, O. Koga, Adsorption of CO accompanied with simultaneous charge transfer on copper single crystal electrodes related with electrochemical reduction of CO_2 to hydrocarbons, Surface Science, 335 (1995) 258-263.

[58]   Y. Huang, A.D. Handoko, P. Hirunsit, B.S. Yeo, Electrochemical Reduction of CO_2 Using Copper Single-Crystal Surfaces: Effects of CO* Coverage on the Selective Formation of Ethylene, ACS Catalysis, 7 (2017) 1749-1756.

[59]   Y. Hori, I. Takahashi, O. Koga, N. Hoshi, Electrochemical reduction of carbon dioxide at various series of copper single crystal electrodes, Journal of Molecular Catalysis A: Chemical, 199 (2003) 39-47.

[60]   I. Takahashi, O. Koga, N. Hoshi, Y. Hori, Electrochemical reduction of CO_2 at copper single crystal Cu(S)-[n(111)×(111)] and Cu(S)-[n(110)×(100)] electrodes, Journal of Electroanalytical Chemistry, 533 (2002) 135-143.

[61]   X. Feng, K. Jiang, S. Fan, M.W. Kanan, A Direct Grain-Boundary-Activity Correlation for CO Electroreduction on Cu Nanoparticles, ACS Central Science, 2 (2016) 169-174.

[62]   H. Jung, S.Y. Lee, C.W. Lee, M.K. Cho, D.H. Won, C. Kim, H.-S. Oh, B.K. Min, Y.J. Hwang, Electrochemical Fragmentation of Cu2O Nanoparticles Enhancing Selective C–C Coupling from CO_2 Reduction Reaction, Journal of the American Chemical Society, 141 (2019) 4624-4633.

[63]   Q. Lei, H. Zhu, K. Song, N. Wei, L. Liu, D. Zhang, J. Yin, X. Dong, K. Yao, N. Wang, X. Li, B. Davaasuren, J. Wang, Y. Han, Investigating the Origin of Enhanced C_{2+} Selectivity in Oxide-/Hydroxide-Derived Copper Electrodes during CO_2 Electroreduction, Journal of the American Chemical Society, 142 (2020) 4213-4222.

[64]   R.G. Mariano, K. McKelvey, H.S. White, M.W. Kanan, Selective increase in CO_2 electroreduction activity at grain-boundary surface terminations, Science, 358 (2017) 1187.

[65]   L. Wang, S. Nitopi, A.B. Wong, J.L. Snider, A.C. Nielander, C.G. Morales-Guio, M. Orazov, D.C. Higgins, C. Hahn, T.F. Jaramillo, Electrochemically converting carbon monoxide to liquid fuels by directing selectivity with electrode surface area, Nature Catalysis, 2 (2019) 702-708.

[66]   J. Wang, H.Y. Tan, Y. Zhu, H. Chu, H.M. Chen, Linking the Dynamic Chemical State of Catalysts with the Product Profile of Electrocatalytic CO_2 Reduction, Angewandte Chemie, (2021).

[67]   S.-C. Lin, C.-C. Chang, S.-Y. Chiu, H.-T. Pai, T.-Y. Liao, C.-S. Hsu, W.-H. Chiang, M.-K. Tsai, H.M. Chen, Operando time-resolved X-ray absorption spectroscopy reveals the chemical nature enabling highly selective CO_2 reduction, Nature Communications, 11 (2020) 3525.

[68]   W. Zhang, C. Huang, Q. Xiao, L. Yu, L. Shuai, P. An, J. Zhang, M. Qiu, Z. Ren, Y. Yu, Atypical Oxygen-Bearing Copper Boosts Ethylene Selectivity toward Electrocatalytic CO_2 Reduction, Journal of the American Chemical Society, 142 (2020) 11417-11427.

[69]   P.-P. Yang, X.-L. Zhang, F.-Y. Gao, Y.-R. Zheng, Z.-Z. Niu, X. Yu, R. Liu, Z.-Z. Wu, S. Qin, L.-P. Chi, Y. Duan, T. Ma, X.-S. Zheng, J.-F. Zhu, H.-J. Wang, M.-R. Gao, S.-H. Yu, Protecting Copper Oxidation State via Intermediate Confinement for Selective CO_2 Electroreduction to C_{2+} Fuels, Journal of the American Chemical Society, 142 (2020) 6400-6408.

[70]   X. Yuan, S. Chen, D. Cheng, L. Li, W. Zhu, D. Zhong, Z.-J. Zhao, J. Li, T. Wang, J. Gong, Controllable Cu0-Cu+ Sites for Electrocatalytic Reduction of Carbon Dioxide, Angewandte Chemie International Edition, n/a (2021).

[71]   B. Beverskog, I. Puigdomenech, Revised Pourbaix Diagrams for Copper at 25 to 300°C, Journal of The Electrochemical Society, 144 (1997) 3476-3483.

[72]   S.H. Lee, J.C. Lin, M. Farmand, A.T. Landers, J.T. Feaster, J.E. Avilés Acosta, J.W. Beeman, Y. Ye, J. Yano, A. Mehta, R.C. Davis, T.F. Jaramillo, C. Hahn, W.S. Drisdell, Oxidation State and Surface

Reconstruction of Cu under CO_2 Reduction Conditions from In Situ X-ray Characterization, Journal of the American Chemical Society, 143 (2021) 588-592.

[73] M. Löffler, K.J.J. Mayrhofer, I. Katsounaros, Oxide Reduction Precedes Carbon Dioxide Reduction on Oxide-Derived Copper Electrodes, The Journal of Physical Chemistry C, 125 (2021) 1833-1838.

[74] A.A. Permyakova, J. Herranz, M. El Kazzi, J.S. Diercks, M. Povia, L.R. Mangani, M. Horisberger, A. Pătru, T.J. Schmidt, On the Oxidation State of Cu2O upon Electrochemical CO_2 Reduction: An XPS Study, ChemPhysChem, 20 (2019) 3120-3127.

[75] S.B. Scott, T.V. Hogg, A.T. Landers, T. Maagaard, E. Bertheussen, J.C. Lin, R.C. Davis, J.W. Beeman, D. Higgins, W.S. Drisdell, C. Hahn, A. Mehta, B. Seger, T.F. Jaramillo, I. Chorkendorff, Absence of Oxidized Phases in Cu under CO Reduction Conditions, ACS Energy Letters, 4 (2019) 803-804.

[76] B. Eren, D. Zherebetskyy, L.L. Patera, C.H. Wu, H. Bluhm, C. Africh, L.-W. Wang, G.A. Somorjai, M. Salmeron, Activation of Cu(111) surface by decomposition into nanoclusters driven by CO adsorption, Science, 351 (2016) 475.

[77] J. Huang, N. Hörmann, E. Oveisi, A. Loiudice, G.L. De Gregorio, O. Andreussi, N. Marzari, R. Buonsanti, Potential-induced nanoclustering of metallic catalysts during electrochemical CO_2 reduction, Nature Communications, 9 (2018) 3117.

[78] D. Kim, C.S. Kley, Y. Li, P. Yang, Copper nanoparticle ensembles for selective electroreduction of CO_2 to C2–C3 products, Proceedings of the National Academy of Sciences, 114 (2017) 10560.

[79] Y.-G. Kim, J.H. Baricuatro, M.P. Soriaga, Surface Reconstruction of Polycrystalline Cu Electrodes in Aqueous KHCO3 Electrolyte at Potentials in the Early Stages of CO_2 Reduction, Electrocatalysis, 9 (2018) 526-530.

[80] J. Vavra, T.-H. Shen, D. Stoian, V. Tileli, R. Buonsanti, Real-time Monitoring Reveals Dissolution/Redeposition Mechanism in Copper Nanocatalysts during the Initial Stages of the CO_2 Reduction Reaction, Angewandte Chemie International Edition, 60 (2021) 1347-1354.

[81] P. Wilde, P.B. O'Mara, J.R.C. Junqueira, T. Tarnev, T.M. Benedetti, C. Andronescu, Y.-T. Chen, R.D. Tilley, W. Schuhmann, J.J. Gooding, Is Cu instability during the CO_2 reduction reaction governed by the applied potential or the local CO concentration?, Chemical Science, 12 (2021) 4028-4033.

[82] C. Yang, B.H. Ko, S. Hwang, Z. Liu, Y. Yao, W. Luc, M. Cui, A.S. Malkani, T. Li, X. Wang, J. Dai, B. Xu, G. Wang, D. Su, F. Jiao, L. Hu, Overcoming immiscibility toward bimetallic catalyst library, Science Advances, 6 (2020) eaaz6844.

[83] B. Roldán Cuenya, F. Scholten, K.-L.C. Nguyen, J.P. Bruce, M. Heyde, Identifying structure-selectivity correlations in the electrochemical reduction of CO_2: comparison of well-ordered atomically-clean and chemically-etched Cu single crystal surfaces, Angewandte Chemie International Edition, n/a (2021).

[84] S. Zhu, E.P. Delmo, T. Li, X. Qin, J. Tian, L. Zhang, M. Shao, Recent Advances in Catalyst Structure and Composition Engineering Strategies for Regulating CO_2 Electrochemical Reduction, Advanced Materials, n/a (2021) 2005484.

[85] C.G. Morales-Guio, E.R. Cave, S.A. Nitopi, J.T. Feaster, L. Wang, K.P. Kuhl, A. Jackson, N.C. Johnson, D.N. Abram, T. Hatsukade, C. Hahn, T.F. Jaramillo, Improved CO_2 reduction activity towards C_{2+} alcohols on a tandem gold on copper electrocatalyst, Nature Catalysis, 1 (2018) 764-771.

[86] Y.C. Li, Z. Wang, T. Yuan, D.-H. Nam, M. Luo, J. Wicks, B. Chen, J. Li, F. Li, F.P.G. de Arquer, Y. Wang, C.-T. Dinh, O. Voznyy, D. Sinton, E.H. Sargent, Binding Site Diversity Promotes CO_2 Electroreduction to Ethanol, Journal of the American Chemical Society, 141 (2019) 8584-8591.

[87] C. Chen, Y. Li, S. Yu, S. Louisia, J. Jin, M. Li, M.B. Ross, P. Yang, Cu-Ag Tandem Catalysts for High-Rate CO_2 Electrolysis toward Multicarbons, Joule, 4 (2020) 1688-1699.

[88]   D. Ren, J. Gao, L. Pan, Z. Wang, J. Luo, S.M. Zakeeruddin, A. Hagfeldt, M. Grätzel, Atomic Layer Deposition of ZnO on CuO Enables Selective and Efficient Electroreduction of Carbon Dioxide to Liquid Fuels, Angewandte Chemie International Edition, 58 (2019) 15036-15040.

[89]   S.A. Mahyoub, F.A. Qaraah, C.Z. Chen, F.H. Zhang, S.L. Yan, Z.M. Cheng, An overview on the recent developments of Ag-based electrodes in the electrochemical reduction of CO_2 to CO, Sustainable Energy & Fuels, 4 (2020) 50-67.

[90]   D.L. Sun, X.M. Xu, Y.L. Qin, S. Jiang, Z.P. Shao, Rational Design of Ag-Based Catalysts for the Electrochemical CO_2 Reduction to CO: A Review, Chemsuschem, 13 (2020) 39-58.

[91]   J. Gao, H. Zhang, X. Guo, J. Luo, S.M. Zakeeruddin, D. Ren, M. Grätzel, Selective C–C Coupling in Carbon Dioxide Electroreduction via Efficient Spillover of Intermediates As Supported by Operando Raman Spectroscopy, Journal of the American Chemical Society, 141 (2019) 18704-18714.

[92]   L. Hou, J. Han, C. Wang, Y. Zhang, Y. Wang, Z. Bai, Y. Gu, Y. Gao, X. Yan, Ag nanoparticle embedded Cu nanoporous hybrid arrays for the selective electrocatalytic reduction of CO_2 towards ethylene, Inorganic Chemistry Frontiers, 7 (2020) 2097-2106.

[93]   J. Huang, M. Mensi, E. Oveisi, V. Mantella, R. Buonsanti, Structural Sensitivities in Bimetallic Catalysts for Electrochemical CO_2 Reduction Revealed by Ag–Cu Nanodimers, Journal of the American Chemical Society, 141 (2019) 2490-2499.

[94]   A.N. Kuhn, H. Zhao, U.O. Nwabara, X. Lu, M. Liu, Y.-T. Pan, W. Zhu, P.J.A. Kenis, H. Yang, Engineering Silver-Enriched Copper Core-Shell Electrocatalysts to Enhance the Production of Ethylene and C_{2+} Chemicals from Carbon Dioxide at Low Cell Potentials, Advanced Functional Materials, n/a (2021) 2101668.

[95]   J. Wang, Z. Li, C. Dong, Y. Feng, J. Yang, H. Liu, X. Du, Silver/Copper Interface for Relay Electroreduction of Carbon Dioxide to Ethylene, ACS Applied Materials & Interfaces, 11 (2019) 2763-2767.

[96]   A. Dutta, I.Z. Montiel, R. Erni, K. Kiran, M. Rahaman, J. Drnec, P. Broekmann, Activation of bimetallic AgCu foam electrocatalysts for ethanol formation from CO_2 by selective Cu oxidation/reduction, Nano Energy, 68 (2020) 104331.

[97]   T.T.H. Hoang, S. Verma, S. Ma, T.T. Fister, J. Timoshenko, A.I. Frenkel, P.J.A. Kenis, A.A. Gewirth, Nanoporous Copper–Silver Alloys by Additive-Controlled Electrodeposition for the Selective Electroreduction of CO_2 to Ethylene and Ethanol, Journal of the American Chemical Society, 140 (2018) 5791-5797.

[98]   P. Iyengar, M.J. Kolb, J.R. Pankhurst, F. Calle-Vallejo, R. Buonsanti, Elucidating the Facet-Dependent Selectivity for CO_2 Electroreduction to Ethanol of Cu–Ag Tandem Catalysts, ACS Catalysis, 11 (2021) 4456-4463.

[99]   S. Lee, G. Park, J. Lee, Importance of Ag–Cu Biphasic Boundaries for Selective Electrochemical Reduction of CO_2 to Ethanol, ACS Catalysis, 7 (2017) 8594-8604.

[100]   X. Lv, L. Shang, S. Zhou, S. Li, Y. Wang, Z. Wang, T.-K. Sham, C. Peng, G. Zheng, Electron-Deficient Cu Sites on Cu3Ag1 Catalyst Promoting CO_2 Electroreduction to Alcohols, Advanced Energy Materials, 10 (2020) 2001987.

[101]   L.R.L. Ting, O. Piqué, S.Y. Lim, M. Tanhaei, F. Calle-Vallejo, B.S. Yeo, Enhancing CO_2 Electroreduction to Ethanol on Copper–Silver Composites by Opening an Alternative Catalytic Pathway, ACS Catalysis, 10 (2020) 4059-4069.

[102]   Gurudayal, D. Perone, S. Malani, Y. Lum, S. Haussener, J.W. Ager, Sequential Cascade Electrocatalytic Conversion of Carbon Dioxide to C–C Coupled Products, ACS Applied Energy Materials, 2 (2019) 4551-4559.

[103]   N. Gupta, M. Gattrell, B. MacDougall, Calculation for the cathode surface concentrations in the electrochemical reduction of CO_2 in $KHCO_3$ solutions, Journal of Applied Electrochemistry, 36 (2006) 161-172.

[104]   F.P.G. de Arquer, C.T. Dinh, A. Ozden, J. Wicks, C. McCallum, A.R. Kirmani, D.H. Nam, C. Gabardo, A. Seifitokaldani, X. Wang, Y.G.C. Li, F.W. Li, J. Edwards, L.J. Richter, S.J. Thorpe, D.

Sinton, E.H. Sargent, CO_2 electrolysis to multicarbon products at activities greater than 1 A cm(-2), Science, 367 (2020) 661-+.

[105] T. Burdyny, W.A. Smith, CO_2 reduction on gas-diffusion electrodes and why catalytic performance must be assessed at commercially-relevant conditions, Energy & Environmental Science, 12 (2019) 1442-1453.

[106] E.R. Cofell, U.O. Nwabara, S.S. Bhargava, D.E. Henckel, P.J.A. Kenis, Investigation of Electrolyte-Dependent Carbonate Formation on Gas Diffusion Electrodes for CO_2 Electrolysis, ACS Applied Materials & Interfaces, 13 (2021) 15132-15142.

[107] G.O. Larrazábal, P. Strøm-Hansen, J.P. Heli, K. Zeiter, K.T. Therkildsen, I. Chorkendorff, B. Seger, Analysis of Mass Flows and Membrane Cross-over in CO_2 Reduction at High Current Densities in an MEA-Type Electrolyzer, ACS Applied Materials & Interfaces, 11 (2019) 41281-41288.

[108] G. Dunfeng, W. Pengfei, L. Hefei, L. Long, W. Guoxiong, B. Xinhe, Designing Electrolyzers for Electrocatalytic CO 2 Reduction, Acta Physico-Chimica Sinica, 37 (2021) 2009021-2009020.

[109] B. Endrődi, G. Bencsik, F. Darvas, R. Jones, K. Rajeshwar, C. Janáky, Continuous-flow electroreduction of carbon dioxide, Progress in Energy and Combustion Science, 62 (2017) 133-154.

[110] G.O. Larrazábal, M. Ma, B. Seger, A Comprehensive Approach to Investigate CO_2 Reduction Electrocatalysts at High Current Densities, Accounts of Materials Research, 2 (2021) 220-229.

[111] R.A. Tufa, D. Chanda, M. Ma, D. Aili, T.B. Demissie, J. Vaes, Q. Li, S. Liu, D. Pant, Towards highly efficient electrochemical CO_2 reduction: Cell designs, membranes and electrocatalysts, Applied Energy, 277 (2020) 115557.

Chapter 2 Size Effect of Copper Nanoparticles on the Selectivity of C_{2+} Products

Jie Zhang[a, b], Thi Ha My Pham[a, b], Mo Li[a, b], Youngdon Ko[a, b], Loris Lombardo[a, b], Wen Luo[a, b]*, Andreas Züttel[a, b]

Abstract

Copper catalysts reconstruct during electrochemical CO_2 reduction (eCO_2RR), making it difficult to identify the active sites for C_{2+} product. We here demonstrate the reconstruction of copper catalyst from a bottom-up perspective during CO_2 reduction – that is, solitary copper atoms gather into clusters that further agglomerate into nanoparticles, by using copper phthalocyanine as the precursor. The bottom-up evolution of copper nanoclusters allowed us to reveal the size effect of copper nanoparticles for eCO_2RR by showing that the increase of the particle size was accompanied by the increase of the selectivity of C_{2+} products. Large-sized particles were more active because they contained higher density of grain boundary that is the active sites for producing C_{2+} products. Furthermore, we achieved a selectivity up to 70% for C_{2+} products with partial current density of 560 mA cm^{-2} by using the copper nanoparticles derived from copper phthalocyanine in a flow cell.

[a] *Laboratory of Materials for Renewable Energy (LMER), Institute of Chemical Sciences and Engineering (ISIC), Basic Science Faculty (SB), École Polytechnique Fedérale de Lausanne (EPFL) Valais/Wallis, Energypolis, Rue de l'Industrie 17, CH-1951 Sion, Switzerland.*
[b] *Empa Materials Science & Technology, CH-8600 Dübendorf, Switzerland*

Author Contributions: Jie Zhang, Wen Luo, and Andreas Züttel conceived the experiments and co-wrote the manuscript. Jie Zhang designed and performed the experiment. Thi Ha My Pham did the HRTEM and EDX analysis. Mo Li did XPS analysis. Youngdon Ko did TEM analysis. Loris Lombardo did part of the NMR analysis.

2.1   Introduction

Electrochemical CO_2 reduction reaction (eCO_2RR) has attracted extensive attention because of its capability to store the intermittent renewable energy by producing liquid fuels (e.g., alcohols) and commodity chemical feedstocks (e.g., C_2H_4).[1, 2] However, the production of the high-valued C_{2+} products (e.g., C_2H_4, ethanol, and n-propanol) from eCO_2RR is still suffering from the low selectivity and high overpotential, which is mainly determined by the catalysts.[3-5] Cu is the only monometallic catalyst that can catalyse eCO_2RR to produce C_{2+} products. In order to engineer Cu materials towards the direction to improve its selectivity of C_{2+} products, the active sites on Cu surface have to be identified.[6]

Several properties of Cu surface impact the selectivity of C_{2+} products, such as crystal facets, size and shape of nanoparticles, and subsurface oxygen.[7-9] For example, grain boundary in Cu catalysts show correlation with the activity and selectivity for C_{2+} products,[10] and the selectivity of C_{2+} products shows a dependence on the size of Cu colloid nanoparticles.[11] However, most of the as-prepared Cu catalysts not only contain various surface properties but also are unstable and thus reconstruct during eCO_2RR[12-16], making the catalytic active sites for C_{2+} product difficult to identify. Here we take colloid nanoparticles as an example. The Cu colloid nanoparticles as the catalysts for eCO_2RR inevitably have the surface covered by a layer of surfactant that impacts the catalytic process and the reconstruction of the nanoparticles.[13, 17] In addition, nanoparticles in different sizes or shapes contain different distributions of the coordination numbers in the surface atoms.[11] Consequently, effect of the surfactants, surface atomic coordination, and the reconstruction intertwine together and thus make it difficult to explain the size effect of the Cu nanoparticles synthesized by colloid approach. Therefore, a new type of model catalysts without these intertwined properties need to be developed to investigate the structure-reactivity relation of Cu catalysts for eCO_2RR.

Copper complexes have shown their potential as the catalysts for eCO_2RR by achieving high selectivity for CH_4 or C_2H_4.[18-22] However, the Cu complex, normally with a Cu atom anchored by four nitrogen atoms, is unstable under the CO_2 reduction.[19, 22, 23] Copper phthalocyanine (CuPc) molecules, as a typical example of Cu complex can release its Cu atoms to produce Cu clusters consisting of several atoms during CO_2 reduction.[19, 22, 23] We suspect that these Cu clusters have a potential to agglomerate into nanoparticles gradually because of the reconstruction of Cu under eCO_2RR. This inspires us to exploit CuPc molecules as the Cu atom sources to observe the evolution of Cu nanoparticles during CO_2 reduction from a bottom-up perspective – that is, from solitary Cu atoms to clusters to nanoparticles. The bottom-up derived Cu nanoparticles are also ideal model catalysts to reveal the structure-reactivity relation because they are in situ formed during eCO_2RR and contain no surface properties introduced by the synthesis.

Therefore, in this work we used CuPc as the precursor to in situ produce the Cu nanoparticles under CO_2 reduction conditions to observe the reconstruction of Cu catalysts from a bottom-up perspective. The decomposition of CuPc was further monitored with the in situ Raman and ex situ XPS analysis, in which we observed the new formed amino group and the decrease of the amount of nitrogen element in the catalysts. The intermediates from CO_2 reduction accounted for the agglomeration of the Cu nanoparticles, as the small-sized nanoparticles kept no change under hydrogen evolution conditions.

We found that the size of Cu nanoparticles from 8 nm to 20 nm was proportionally correlated with the selectivity of C_{2+} products. The bigger nanoparticles showed a higher selectivity for C_{2+} products because of their higher density of the grain boundaries derived from the agglomeration of the Cu clusters. Finally, we demonstrated that the Cu nanoparticles derived from CuPc produced C_{2+} products with a selectivity of 70 % and partial current density of 560 mA cm^{-2} in a flow cell, which indicated the bottom-up approach by using copper complex is a promising method to synthesize Cu nanoparticles with rich grain boundaries.

2.2 Results and discussion

2.2.1 Formation of Cu nanoparticles

CuPc crystal particles (around 30 nm) were mixed with carbon black to act as the catalysts (denoted as CuPcCB) because CuPc is an organic semiconductor[24] that needs carbon black to enhance the conductivity. To confirm the Cu nanoparticles could be derived from CuPc, the CuPcCB catalysts before and after CO_2 reduction were analyzed with elemental and crystal structure related analysis. The CuPc in the as-prepared CuPcCB catalyst belonged to β phase based on the X-ray diffraction pattern (Figure S2.3) and the lattice length obtained from the high resolution transmission electron microscopy (HRTEM) images (Figure 2.1a and Figure S2.4).[25] Bright dots appeared in the backscattered electron (BSE) images (Figure 2.1b) of CuPcCB after CO_2 reduction, which consisted of copper and oxygen and thus were copper oxide nanoparticles according to the energy-dispersive X-ray spectroscopy (EDX) elemental map (Figure 2.1c and Figure S2.5). The X-ray photoelectron spectrum (XPS) of CuPcCB after
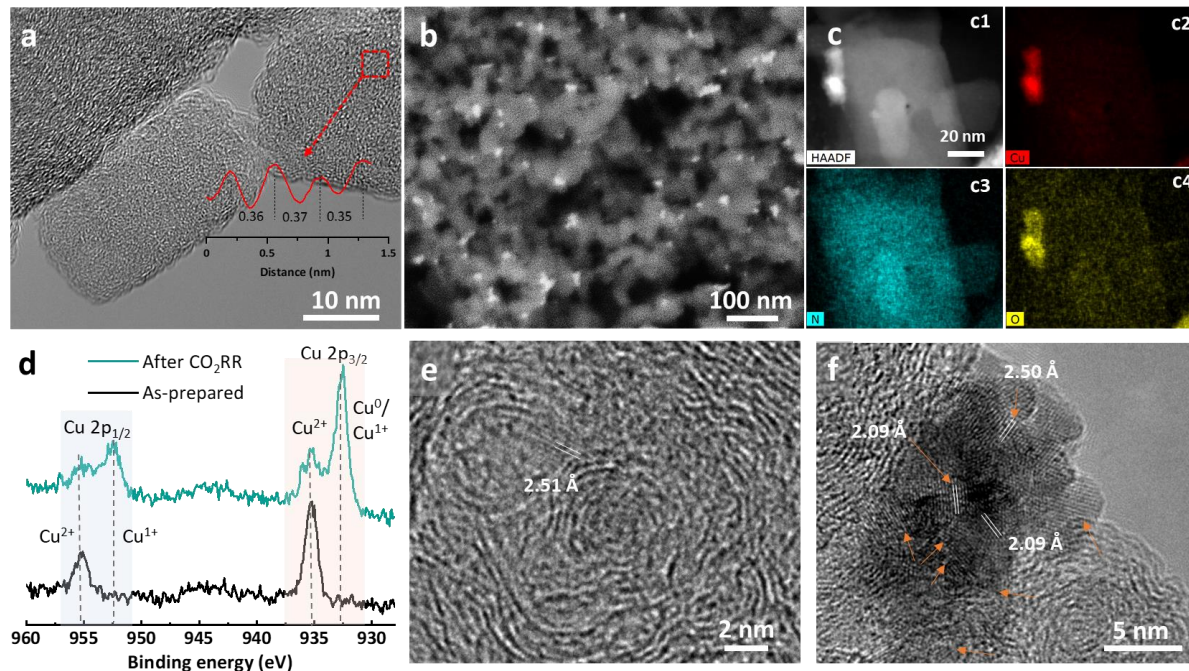
Figure 2.1 (a) TEM image of the as-prepared CuPcCB catalyst, in which the inset is the profile plot of square region. BSE image (b), EDX elemental mapping (c), and XPS spectrum (d) of CuPcCB catalyst after CO_2 reduction at -1.03 V vs RHE for 800 s in 0.1 M KHCO$_3$. The XPS spectrum of the as-prepared CuPcCB catalyst is also presented in (f) for comparison. TEM images of a single Cu_2O cluster (b) and a Cu_2O nanoparticles$_+$ (c) derived from CuPc during CO_2 reduction in 0.1 M KHCO$_3$.

CO_2 reaction showed a new peak at around 932.5 eV (Figure 2.1d) that belonged to Cu^0 and/or Cu^{1+}, compared with that of the as-prepared CuPcCB.[26] HRTEM images (Figure 2.1e-f, and Figure S2.6) revealed that some new lattices attached on the carbon black had plane distances of 0.209 nm and 0.250 nm, corresponding to the Cu (111) and Cu_2O (111), respectively.

All the above results demonstrate that during CO_2 reduction CuPc molecules can release their Cu atoms that further gather together to become Cu-related clusters and nanoparticles. According to the Pourbaix diagram [27] of Cu, the copper-related nanoparticles derived from CuPc should be metallic Cu. This was further confirmed by the analysis of chronoamperometry and cyclic voltammetry of CuPcCB in the CO_2 reduction conditions (Figure S2.7). Because the chronoamperogram at the initial stage of CO_2 reduction showed a peak due to electrochemical nucleation[28] and the cyclic voltammograms showed two oxidation peaks at around 0.75 V vs RHE that are derived from the oxidation of metallic Cu.[29, 30] The Cu_2O was probably formed from the oxidizing of Cu in air during the sample transfer after eCO_2RR. Therefore, the copper-related nanoparticles derived from CuPc were metallic Cu under CO_2 reduction conditions. In addition, as pure CuPc without the formation of metallic Cu species showed no activity for CO_2 reduction (Figure S2.8), thus it was the metallic Cu nanoparticles derived from CuPc, rather than CuPc itself, that accounted for the activity of CO_2 reduction, consistent with the reports.[19, 22, 31]

2.2.2 Catalytic behavior in H-cell

Figure 2.2 shows the Faradaic efficiencies and current densities versus potential of the CO_2 reduction catalysed by CuPcCB in a H-cell with 0.1 M $KHCO_3$ as the electrolyte. Formate and CO were the main products for eCO_2RR at low overpotential (< -0.90 V vs RHE). With the potential increasing to around -1.1 V vs RHE, C_2H_4 and ethanol became the main products. When the overpotential was too high (> -1.25 V vs RHE), CH_4 and hydrogen dominated the products. These trends of the product selectivity versus potential are quite similar to that on Cu catalysts,[32] further confirming that the active species in CuPcCB for eCO_2RR are metallic Cu. In addition, the pH of the electrolyte greatly affected the selectivity of CH_4 on CuPcCB by increasing the Faradaic efficiency of CH_4 from around 10 % in 0.1 M $KHCO_3$ to 30 % in 0.5 M $KHCO_3$ (Figure S2.9). This is consistent to Hailiang Wang et al.'s report[19], in which they achieved 60% of CH_4 faradaic efficiency in 0.5 M $KHCO_3$ with carbon nanotubes as the supporter of CuPc.
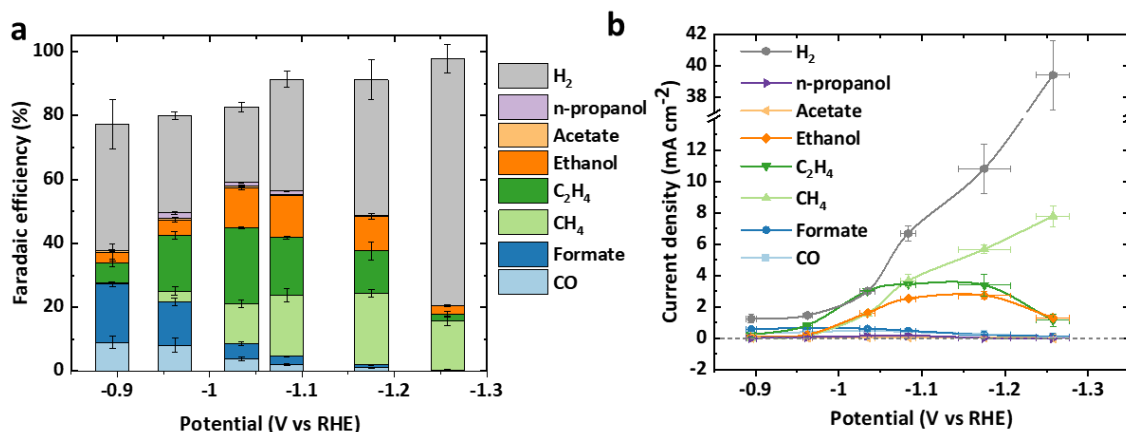
Figure 2.2 (a) Faradaic efficiencies and (b) the corresponding partial current densities versus potential of the products from eCO_2RR on CuPcCB in H-cell with 0.1 M $KHCO_3$ as the electrolyte.

2.2.3   The evolution from CuPc to Cu nanoparticles

Demetalation of CuPc during eCO$_2$RR

To reveal the demetalation and possible decomposition of the CuPc molecules during CO$_2$ reduction, we used in situ Raman spectroscopy and ex situ XPS to monitor the CuPc molecules. The Raman spectra of CuPc molecules on a Cu plate faded away during CO$_2$ reduction (Figure 2.3 (a)) because of the decomposition. We also observed the new formed amino groups, –NH$_2$ and –NH– in the N1s XPS due to the bond breaks in CuPc molecules by comparing N1s XPS peaks of the CuPcCB after 11 hour of CO$_2$ reduction with that (Figure S2.11) of raw CuPc, H$_2$Pc (29 H , 31 H phthalocyanine) and the data from literatures.[33-37] In addition, the amount of the nitrogen element in the electrode decreased with the reaction time (Figure 2.3c) according to XPS analysis, and this decrease was faster than that of Cu, as the atomic ratio of nitrogen to Cu also declined with reaction time (Figure 2.3c). Hence it was mainly the decomposition of the CuPc molecules that caused the loss of nitrogen, rather than detachment of the CuPc particles, as the loss of nitrogen and Cu were not correlated. Therefore, CuPc molecules decompose while releasing their Cu atoms to form Cu clusters during CO$_2$ reduction.
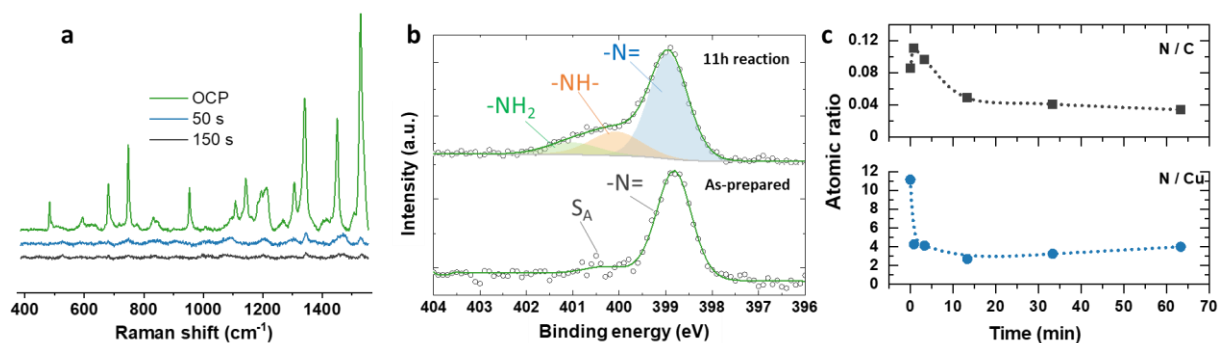
Figure 2.3 (a) In situ Raman spectrum of the CuPc molecules attached on Cu plate at various reaction time and -0.60 V vs RHE in 0.1 M KHCO$_3$. (b) The comparison of the N1s XPS spectra of the as-prepared CuPcCB and that after continuously 11h of CO$_2$ reduction. (c) The atomic ratio determined by XPS of nitrogen to carbon and nitrogen to Cu in the CuPcCB as a function of reaction time. The CO$_2$ reduction for (b) and (c) was conducted in 0.1 M KHCO$_3$ at -1.03 V vs RHE.

Evolution of the Cu nanoparticles

We revealed the evolution of the Cu nanoparticles derived from the decomposition of CuPc under CO$_2$ reduction conditions and correlated it with the C$_{2+}$ product selectivity. Figure 2.4a-e show the BSE images of the CuPcCB after various durations of CO$_2$ reduction at -1.03 V vs RHE in 0.1 KHCO$_3$. Similar to that in Figure 2.1b, the white dots were corresponding to the Cu$_2$O nanoparticles derived from the Cu nanoparticles formed during CO$_2$ reduction. Cu$_2$O nanoparticles existed in all the BSE images with the reaction time from 0.8 min to 63 min. The average sizes (Figure 2.4f and Figure S2.14) of Cu$_2$O nanoparticles showed an increasing trend from 8 nm at 0.8 min to 20 nm at 63 min and their densities showed a decreasing trend with time, indicating the agglomeration of the small nanoparticles into bigger ones. Meanwhile, the amount of the Cu(I) determined by XPS peak area decreased with the reaction time, which further confirmed the agglomeration of the small nanoparticles, as the

agglomeration resulted in the decrease of the Cu signal detected by XPS because of the limited detection depth of XPS (Figure S2.15a).

Voltammetry stripping was used to further uncover the nucleation and agglomeration process of the Cu nanoparticles during CO_2 reduction. The peak area of the Cu oxidation in the voltammograms after CO_2 reduction increased with the reaction time (Figure S2.17). This indicates that new Cu nanoclusters continuously nucleate from CuPc while old formed particles are agglomerating. This also explained that the size distribution of the Cu nanoparticles from CuPcCB after continuously 11 hours of CO_2 reduction (Figure S2.14) fell in a huge range from 2 nm to 62 nm.
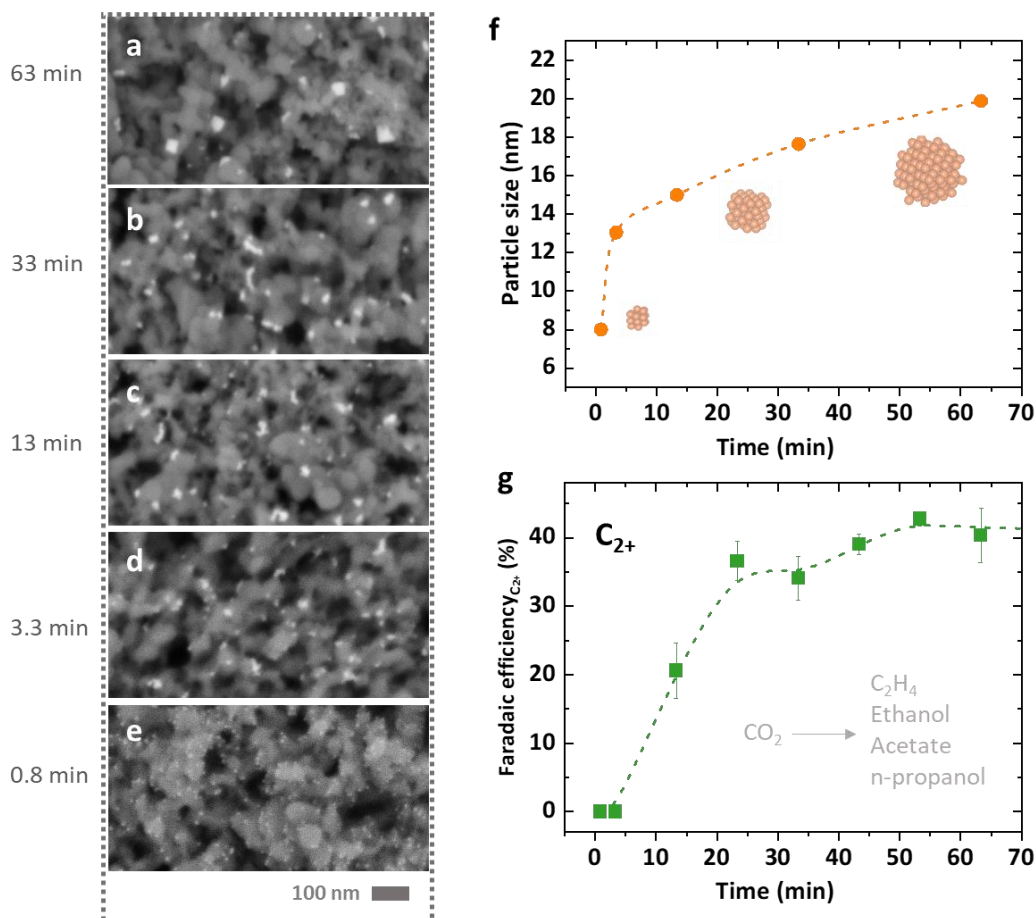
Figure 2.4 BSE images (a - e) of the CuPcCB catalyst after CO_2 reduction at -1.03 V vs REH in 0.1 M $KHCO_3$ for various durations. (g) the average particle size of Cu_2O, and (f) Faradaic efficiency of C_{2+} products as a function of the reaction time of CO_2 reduction.

With the increase of the particle size, we observed the increase of the Faradaic efficiency of C_{2+} products, including C_2H_4, ethanol, acetate, and n-propanol. Actually in the first 200 s of reaction, no C_{2+} products could be detected at -1.03 V vs RHE in 0.1 M $KHCO_3$. This phenomenon correlated the selectivity of C_{2+} products with the particle size (Figure S2.15b). To further confirm this correlation, we prevented the Cu particles from agglomerating by applying only 100 s of CO_2 reduction followed by cyclic voltammetry (CV) to dissolve the formed nanoclusters (see details in SI). Under this conditions with the size of Cu nanoparticles controlled less than 10 nm, no production of C_2H_4 was observed, and the charge derived from the copper oxidation in the CVs was always smaller than that in the preceding

measurement (Figure S2.18b). In addition, after eight times of repeating, no Cu particles could be observed in the BSE images of the electrode (Figure S2.18d). These results confirmed that the formation of C$_{2+}$ products needs a relative bigger particles (around 15 nm) and the demetalation of CuPc crystal is not reversible, not like the clusters from CuPc crystal on carbon nanotubes reported by Karapinar[23] and Weng[19] et al.

The Cu nanoparticles derived from CuPc consisted of several grains and were thus in rich of grain boundaries, as shown in the HRTEM images (Figure 2.1e-f and Figure S2.20). Meanwhile, the bigger-sized nanoparticles contained higher density of grain boundary than small-sized nanoparticles. The density of grain boundary have been demonstrated to show proportional correlation with the selectivity of C$_{2+}$ products.[10, 38] Therefore, the fact that the selectivity of C$_{2+}$ products was proportional with the size of Cu nanoparticles from 8 nm to 20 nm proved that grain boundaries were the active sites in the Cu nanoparticles derived from CuPc.

Important factors

Identical location BSE images was used to demonstrate the factors that induced the agglomeration of the Cu nanoclusters during CO$_2$ reduction. Copper nanoparticles with small size (less than 10 nm, Figure 2.5a) was also observed in the CuPcCB by applying 2000 s of HER in 0.1 M KHCO$_3$ deaerated by N$_2$, indicating the formation of the nanoclusters was induced by the reduction potential. The small sized Cu nanoparticles formed in HER conditions further agglomerated after applied another 2000 s of CO$_2$ in 0.1 M KHCO$_3$, while kept no change under another 2000 s of HER. We also found no bigger Cu nanoparticles formed after various durations of the HER (Figure S2.21).

This reconstruction of Cu nanoparticles were also found in other reports, takes placing not only in small-sized particles (< 10 nm)[13, 17, 39] but also in bigger particles and bulk surface.[12, 14, 40] Our results indicate that the Cu nanoparticles are more dynamic during CO$_2$ reduction than under HER, and thus
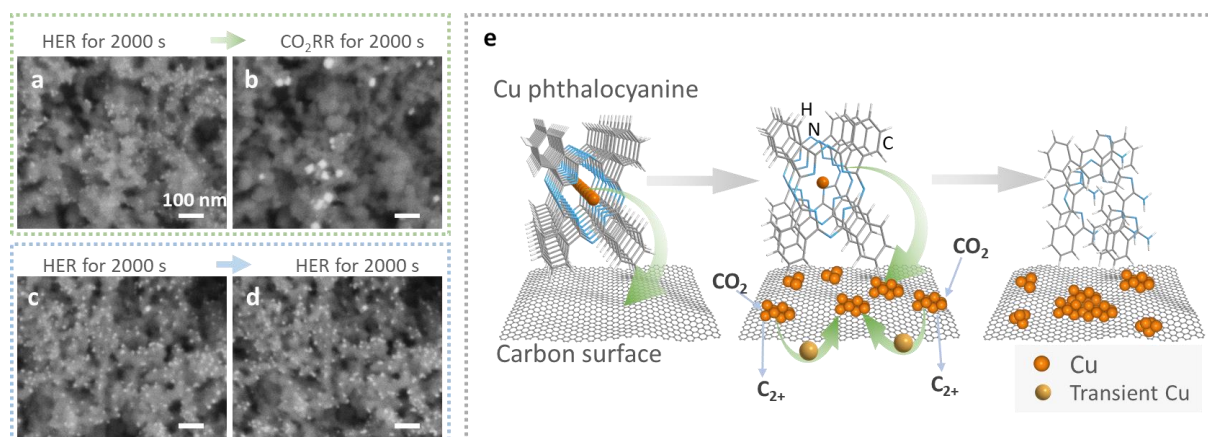
Figure 2.5 (a) and (c) BSE images of the CuPcCB after 2000 s of reaction (mainly HER) at -0.8 V vs RHE in 0.1 M KHCO$_3$ deaerated by N$_2$. (b) Identical location SEM image, corresponding to (a), of the same CuPcCB electrode under another 2000 s of reaction (mainly eCO$_2$RR) at -1.0 V vs RHE in 0.1 M KHCO$_3$ saturated by CO$_2$ after taking image (a). (d) Identical location SEM image, corresponding to (c), of the same CuPcCB electrode under another 2000 s of reaction (mainly HER) at -1.0 V vs RHE in 0.1 M KHCO$_3$ deaerated by N$_2$ after taking image (c). (e) Schematics of the evolution of the CuPcCB during CO$_2$ reduction.

are more likely to agglomerate. Previous report found that it is the adsorbed CO rather than the reduction potential[14] that induced the reconstruction of Cu nanoparticles, consistent with our results that no agglomeration takes place under HER condition. Higher overpotential resulted in the formation of bigger particles in a shorter reaction time (Figure S2.22), while pH showed no effect on the agglomeration of the nanoparticles (Figure S2.23).

To sum up (Figure 2.5e), we found that under CO_2 reduction conditions CuPc molecules, induced by reduction potential, first release their Cu atoms that gather together and form clusters on the carbon surface. The CO and other intermediates from CO_2 reduction further induced the clusters to move and agglomerate into bigger nanoparticles. The agglomeration results in a higher density of grain boundary in bigger nanoparticle and thus higher C_{2+} selectivity. At the same time new clusters are continuously generated and the H_2Pc derived from CuPc demetalation fragments.

2.2.4 CO_2 reduction under practical conditions

Knowing that the evolution of CuPc strongly enhanced the C_{2+} selectivity, we further evaluated the CuPcCB for CO_2 reduction in a gas diffusion electrode (GDE) in a flow cell in order to verify its performance under a commercial-scale current densities (> 200 mA cm^{-2}). As shown in Figure 2.6a, the Faradaic efficiency of C_{2+} products (including C_2H_4, ethanol, acetate, and n-propanol) reached 70% during -0.6 V to -0.72 V vs RHE with the partial current density of C_{2+} products reaching 550 mA cm^{-2} at -0.73 V vs RHE in 5 M KOH, which was comparable to the best Cu catalysts ever reported.[41, 42] With the decreasing of the applied potential from -0.43 V to -0.73 V vs HRE, the selectivity of C_1 products (including CO, CH$_4$, and formate) decreased rapidly, C_{2+} products showed an increasing selectivity, and the total current density increased from 50 mA cm^{-2} to 800 mA cm^{-2}. C_2H_4 and ethanol showed a partial current density of 280 mA cm^{-2} and 206 mA cm^{-2} (Figure 2.6b), respectively. Similar Cu nanoparticles were also observed in the BSE images of the GDE after CO_2 reduction in the flow cell (Figure S2.24), which was also confirmed by the XPS spectra (Figure S2.25). The enhanced C_{2+} selectivity in flow cell compared to that H-cell was because of the high pH and mass transfer,[41] according to the comparison of the eCO_2RR performance in various electrolyte with different pH values (Figure S2.27).
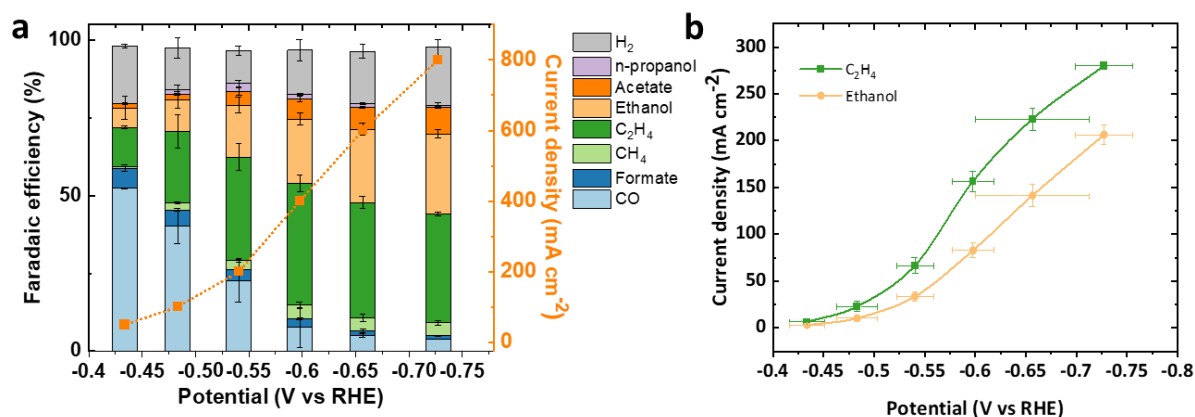
Figure 2.6 (a) Faradaic efficiency distribution versus potential of the products from eCO_2RR on CuPcCB in a flow cell with 5 M KOH as the electrolytes. (b) The partial current densities of the main products versus potential corresponding to (a). (c) Comparison of the selectivity ratio of C_{2+} to C_1 products in three electrolytes with different pH as a function of potential in a flow cell.

2.3   Conclusions

We identified the Cu nanoparticles derived from the copper phthalocyanine (CuPc) crystals as the active sites for electrochemical CO$_2$ reduction when using the mixture of CuPc and carbon black (CuPcCB) as the catalysts. From the bottom-up perspective, we revealed the evolution of Cu nanoclusters into nanoparticles by using CuPc molecules as the precursor. Copper atoms released from CuPc under reduction potential first gather together to form Cu clusters that further agglomerate to form the nanoparticles (5 to 60 nm) with rich grain boundaries. The grain boundary in bigger particles is the active sites for converting CO$_2$ to C$_{2+}$ products, which explains the size effect of Cu nanoparticles on C$_{2+}$ selectivity. Meanwhile, the phthalocyanine molecules derived from CuPc decomposed, according to the analysis of in situ Raman and XPS. Finally, we achieved a Faradaic efficiency of 70 % for C$_{2+}$ products with a total current density of 800 mA cm^{-2} at -0.72 V vs RHE in a flow cell, by using the Cu nanoparticles derived from CuPcCB. The mechanism of the demetalation of CuPc could inspire researchers to reveal the stability and active sites of other metal complex catalysts and the evolution of the Cu nanoparticles also have the potential to be used to design and develop catalysts for other applications.

2.4   Acknowledgements

2.5   References

[1]   P. De Luna, C. Hahn, D. Higgins, S.A. Jaffer, T.F. Jaramillo, E.H. Sargent, What would it take for renewably powered electrosynthesis to displace petrochemical processes?, Science, 364 (2019) eaav3506.

[2]   M.B. Ross, P. De Luna, Y. Li, C.-T. Dinh, D. Kim, P. Yang, E.H. Sargent, Designing materials for electrochemical carbon dioxide recycling, Nature Catalysis, 2 (2019) 648-658.

[3]   M. Jouny, W. Luc, F. Jiao, General Techno-Economic Analysis of CO$_2$ Electrolysis Systems, Industrial & Engineering Chemistry Research, 57 (2018) 2165-2177.

[4]   M.G. Kibria, J.P. Edwards, C.M. Gabardo, C.-T. Dinh, A. Seifitokaldani, D. Sinton, E.H. Sargent, Electrochemical CO$_2$ Reduction into Chemical Feedstocks: From Mechanistic Electrocatalysis Models to System Design, Advanced Materials, 31 (2019) 1807166.

[5]   O.G. Sánchez, Y.Y. Birdja, M. Bulut, J. Vaes, T. Breugelmans, D. Pant, Recent advances in industrial CO$_2$ electroreduction, Current Opinion in Green and Sustainable Chemistry, 16 (2019) 47-56.

[6]   Y. Wang, J. Liu, G. Zheng, Designing Copper-Based Catalysts for Efficient Carbon Dioxide Electroreduction, Advanced Materials, n/a (2021) 2005798.

[7]   S. Nitopi, E. Bertheussen, S.B. Scott, X. Liu, A.K. Engstfeld, S. Horch, B. Seger, I.E.L. Stephens, K. Chan, C. Hahn, J.K. Nørskov, T.F. Jaramillo, I. Chorkendorff, Progress and Perspectives of Electrochemical CO$_2$ Reduction on Copper in Aqueous Electrolyte, Chemical Reviews, 119 (2019) 7610-7672.

[8]   Y. Zheng, A. Vasileff, X. Zhou, Y. Jiao, M. Jaroniec, S.-Z. Qiao, Understanding the Roadmap for Electrochemical Reduction of CO$_2$ to Multi-Carbon Oxygenates and Hydrocarbons on Copper-Based Catalysts, Journal of the American Chemical Society, 141 (2019) 7646-7659.

[9]   D. Karapinar, C.E. Creissen, J.G. Rivera de la Cruz, M.W. Schreiber, M. Fontecave, Electrochemical CO_2 Reduction to Ethanol with Copper-Based Catalysts, ACS Energy Letters, 6 (2021) 694-706.

[10]   X. Feng, K. Jiang, S. Fan, M.W. Kanan, A Direct Grain-Boundary-Activity Correlation for CO Electroreduction on Cu Nanoparticles, ACS Central Science, 2 (2016) 169-174.

[11]   R. Reske, H. Mistry, F. Behafarid, B. Roldan Cuenya, P. Strasser, Particle Size Effects in the Catalytic Electroreduction of CO_2 on Cu Nanoparticles, Journal of the American Chemical Society, 136 (2014) 6978-6986.

[12]   J. Huang, N. Hörmann, E. Oveisi, A. Loiudice, G.L. De Gregorio, O. Andreussi, N. Marzari, R. Buonsanti, Potential-induced nanoclustering of metallic catalysts during electrochemical CO_2 reduction, Nature Communications, 9 (2018) 3117.

[13]   D. Kim, C.S. Kley, Y. Li, P. Yang, Copper nanoparticle ensembles for selective electroreduction of CO_2 to C_2–C_3 products, Proceedings of the National Academy of Sciences, 114 (2017) 10560.

[14]   P. Wilde, P.B. O'Mara, J.R.C. Junqueira, T. Tarnev, T.M. Benedetti, C. Andronescu, Y.-T. Chen, R.D. Tilley, W. Schuhmann, J.J. Gooding, Is Cu instability during the CO_2 reduction reaction governed by the applied potential or the local CO concentration?, Chemical Science, 12 (2021) 4028-4033.

[15]   W. Luo, Q. Zhang, J. Zhang, E. Moioli, K. Zhao, A. Züttel, Electrochemical reconstruction of ZnO for selective reduction of CO_2 to CO, Applied Catalysis B: Environmental, 273 (2020) 119060.

[16]   J. Zhang, W. Luo, A. Züttel, Self-supported copper-based gas diffusion electrodes for CO_2 electrochemical reduction, Journal of Materials Chemistry A, 7 (2019) 26285-26292.

[17]   Y. Oh, J. Park, Y. Kim, M. Shim, T.-S. Kim, J.Y. Park, H.R. Byon, Coverage of capping ligands determining the selectivity of multi-carbon products and morphological evolution of Cu nanocatalysts in electrochemical reduction of CO_2, Journal of Materials Chemistry A, (2021).

[18]   S. Kusama, T. Saito, H. Hashiba, A. Sakai, S. Yotsuhashi, Crystalline Copper(II) Phthalocyanine Catalysts for Electrochemical Reduction of Carbon Dioxide in Aqueous Media, ACS Catalysis, 7 (2017) 8382-8385.

[19]   Z. Weng, Y. Wu, M. Wang, J. Jiang, K. Yang, S. Huo, X.-F. Wang, Q. Ma, G.W. Brudvig, V.S. Batista, Y. Liang, Z. Feng, H. Wang, Active sites of copper-complex catalytic materials for electrochemical carbon dioxide reduction, Nature Communications, 9 (2018) 415.

[20]   N.M. Latiff, X. Fu, D.K. Mohamed, A. Veksha, M. Handayani, G. Lisak, Carbon based copper(II) phthalocyanine catalysts for electrochemical CO_2 reduction: Effect of carbon support on electrocatalytic activity, Carbon, 168 (2020) 245-253.

[21]   Z. Weng, J. Jiang, Y. Wu, Z. Wu, X. Guo, K.L. Materna, W. Liu, V.S. Batista, G.W. Brudvig, H. Wang, Electrochemical CO_2 Reduction to Hydrocarbons on a Heterogeneous Molecular Cu Catalyst in Aqueous Solution, Journal of the American Chemical Society, 138 (2016) 8076-8079.

[22]   Y. Xu, F. Li, A. Xu, J.P. Edwards, S.-F. Hung, C.M. Gabardo, C.P. O'Brien, S. Liu, X. Wang, Y. Li, J. Wicks, R.K. Miao, Y. Liu, J. Li, J.E. Huang, J. Abed, Y. Wang, E.H. Sargent, D. Sinton, Low coordination number copper catalysts for electrochemical CO_2 methanation in a membrane electrode assembly, Nature Communications, 12 (2021) 2932.

[23]   D. Karapinar, A. Zitolo, T.N. Huan, S. Zanna, D. Taverna, L.H. Galvão Tizei, D. Giaume, P. Marcus, V. Mougel, M. Fontecave, Carbon-Nanotube-Supported Copper Polyphthalocyanine for Efficient and Selective Electrocatalytic CO_2 Reduction to CO, ChemSusChem, 13 (2020) 173-179.

[24]   J.M. Assour, S.E. Harrison, Electrical conductivity of metal-free and copper phthalocyanine crystals, Journal of Physics and Chemistry of Solids, 26 (1965) 670-672.

[25]   C.J. Brown, Crystal structure of β-copper phthalocyanine, Journal of the Chemical Society A: Inorganic, Physical, Theoretical, (1968) 2488-2493.

[26]   B. Adolphi, O. Berger, W.-J. Fischer, Copper Pthalocyanine by XPS, Surface Science Spectra, 8 (2001) 87-96.

[27]   B. Beverskog, I. Puigdomenech, Revised Pourbaix Diagrams for Copper at 25 to 300°C, Journal of The Electrochemical Society, 144 (1997) 3476-3483.

[28]   J. Zhang, A. Liu, X. Ren, J. Zhang, P. Yang, M. An, Electrodeposit copper from alkaline cyanide-free baths containing 5,5′-dimethylhydantoin and citrate as complexing agents, RSC Advances, 4 (2014) 38012-38026.

[29]   D. Hochfilzer, J.E. Sørensen, E.L. Clark, S.B. Scott, I. Chorkendorff, J. Kibsgaard, The Importance of Potential Control for Accurate Studies of Electrochemical CO Reduction, ACS Energy Letters, (2021) 1879-1885.

[30]   G.H. Simon, C.S. Kley, B. Roldan Cuenya, Potential-Dependent Morphology of Copper Catalysts During CO$_2$ Electroreduction Revealed by In Situ Atomic Force Microscopy, Angewandte Chemie International Edition, 60 (2021) 2561-2568.

[31]   B. Mei, C. Liu, J. Li, S. Gu, X. Du, S. Lu, F. Song, W. Xu, Z. Jiang, Operando HERFD-XANES and surface sensitive Δμ analyses identify the structural evolution of copper(II) phthalocyanine for electroreduction of CO$_2$, Journal of Energy Chemistry, 64 (2022) 1-7.

[32]   Y. Hori, A. Murata, R. Takahashi, Formation of hydrocarbons in the electrochemical reduction of carbon dioxide at a copper electrode in aqueous solution, Journal of the Chemical Society, Faraday Transactions 1: Physical Chemistry in Condensed Phases, 85 (1989) 2309-2326.

[33]   K. Liu, J. Li, H. Qi, M. Hambsch, J. Rawle, A.R. Vázquez, A.S. Nia, A. Pashkin, H. Schneider, M. Polozij, A Two‐Dimensional Polyimide‐Graphene Heterostructure with Ultra‐fast Interlayer Charge Transfer, Angewandte Chemie, (2021).

[34]   M. Furukawa, T. Yamada, S. Katano, M. Kawai, H. Ogasawara, A. Nilsson, Geometrical characterization of adenine and guanine on Cu(110) by NEXAFS, XPS, and DFT calculation, Surface Science, 601 (2007) 5433-5440.

[35]   F. Klappenberger, A. Weber-Bargioni, W. Auwärter, M. Marschall, A. Schiffrin, J.V. Barth, Temperature dependence of conformation, chemical state, and metal-directed assembly of tetrapyridyl-porphyrin on Cu(111), The Journal of Chemical Physics, 129 (2008) 214702.

[36]   Y.-P. Lin, O. Ourdjini, L. Giovanelli, S. Clair, T. Faury, Y. Ksari, J.-M. Themlin, L. Porte, M. Abel, Self-Assembled Melamine Monolayer on Cu(111), The Journal of Physical Chemistry C, 117 (2013) 9895-9902.

[37]   R.A. Zangmeister, T.A. Morris, M.J. Tarlov, Characterization of Polydopamine Thin Films Deposited at Short Times by Autoxidation of Dopamine, Langmuir, 29 (2013) 8619-8628.

[38]   Q. Lei, H. Zhu, K. Song, N. Wei, L. Liu, D. Zhang, J. Yin, X. Dong, K. Yao, N. Wang, X. Li, B. Davaasuren, J. Wang, Y. Han, Investigating the Origin of Enhanced C$_{2+}$ Selectivity in Oxide-/Hydroxide-Derived Copper Electrodes during CO$_2$ Electroreduction, Journal of the American Chemical Society, 142 (2020) 4213-4222.

[39]   J. Vavra, T.-H. Shen, D. Stoian, V. Tileli, R. Buonsanti, Real-time Monitoring Reveals Dissolution/Redeposition Mechanism in Copper Nanocatalysts during the Initial Stages of the CO$_2$ Reduction Reaction, Angewandte Chemie International Edition, 60 (2021) 1347-1354.

[40]   H. Jung, S.Y. Lee, C.W. Lee, M.K. Cho, D.H. Won, C. Kim, H.-S. Oh, B.K. Min, Y.J. Hwang, Electrochemical Fragmentation of Cu2O Nanoparticles Enhancing Selective C–C Coupling from CO$_2$ Reduction Reaction, Journal of the American Chemical Society, 141 (2019) 4624-4633.

[41]   C.-T. Dinh, T. Burdyny, M.G. Kibria, A. Seifitokaldani, C.M. Gabardo, F.P. García de Arquer, A. Kiani, J.P. Edwards, P. De Luna, O.S. Bushuyev, C. Zou, R. Quintero-Bermudez, Y. Pang, D. Sinton, E.H. Sargent, CO$_2$ electroreduction to ethylene via hydroxide-mediated copper catalysis at an abrupt interface, Science, 360 (2018) 783.

[42]   J.-J. Lv, M. Jouny, W. Luc, W. Zhu, J.-J. Zhu, F. Jiao, A Highly Porous Copper Electrocatalyst for Carbon Dioxide Reduction, Advanced Materials, 30 (2018) 1803111.

2.6 Supporting information

Experimental methods

Chemicals

Copper phthalocyanine (CuPc), deuterium oxide (D_2O), 29 H, 31 H phthalocyanine (H_2Pc), potassium hydroxide (KOH), nafion solution (5wt%), perchloric acid ($HClO_4$), and trifluoroacetic acid (TFA) were ordered from Sigma-Aldrich and used as received. Carbon black (Vulcan XC72R) were ordered from FuelCellStore. Tetrahydrofuran (THF) and isopropanol (IPA) were ordered from Fisher Scientific International, Inc. Potassium bicarbonate ($KHCO_3$) came from the Carl Roth GmbH + Co . KG. Potassium dihydrogen phosphate (KH_2PO_4) was ordered from Merck KGaA. CO_2 gas (99.999%) was supplied by Carbagas. Ag|AgCl reference electrode (with a jacket) were ordered from Metrohm Autolab. MiliQ water ($18M\Omega$) were used to prepare the electrolyte and rinse the electrode.

Synthesis of the catalyst

The catalysts are prepared by physically mixing copper phthalocyanine crystals with carbon black. The CuPc crystal particles (100 mg) was firstly dispersed in the THF (100 ml) by sonicating for 5 min. Then the carbon black (100 mg) was added into the above dispersion, and 30 minutes of sonication was conducted to disperse the carbon black. The dispersion of CuPc and carbon black in THF was centrifuged at 7830 rpm for 20 minutes. The solid residue (denoted as CuPcCB) was dried under vacuum at room temperature to obtain the final product, which was used as the catalyst for eCO_2RR.

Electrochemical evaluation of the catalysts for eCO_2RR

Constant current mode controlled by a potentiostat (Autolab) was used to electrochemically reduce CO_2 and the potential was converted to refer to reversible hydrogen electrode (RHE) by using equation: E (versus RHE) = E (versus Ag|AgCl (3 M KCl)) + 0.21 V + 0.059 × pH. Ohmic drop was compensated by using the ohmic resistance determined by current-interrupt method. Three different electrodes were evaluated for eCO_2RR at the same current density in order to create the error bar.

eCO_2RR in the H-cell

The H-cell for evaluating the CuPcCB for electrochemical CO_2 reduction consisted of two chambers separated by a nafion membrane, as shown in Figure S2.1. The cell was made of polytetrafluoroethylene (PTFE) and had a volume of 15ml for each chamber. The catholyte chamber was filled with 6ml of 0.1 M $KHCO_3$ and thus had 9 ml of headspace. The reference electrode was Ag|AgCl (3 M KCl). The counter electrode was a platinum gauze, placed in the anolyte chamber that was filled with 9ml of 0.1 M $KHCO_3$.
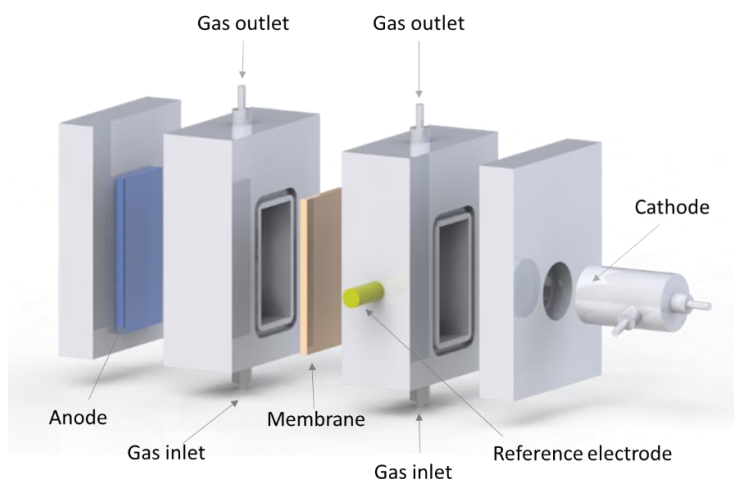
Figure S2.1 Schematics of the H-cell for CO_2 reduction, in which the cathode has the glassy carbon disk imbedded in the PTFE rod.

The working electrode was a glassy carbon disk (θ = 10 mm) embedded in a PTFE rod, which was inserted into the catholyte chamber. The glassy carbon disk was coated by a layer of the CuPcCB (0.16 mg cm^{-2}) by drop casting the ink, which is prepared by sonicating mixture of CuPcCB (4 mg), nafion (5wt%, 20ul), and isopropanol (1 ml). In terms of the control experiments with pure CuPc as the catalyst, the ink of CuPc (4 mg / ml) and nafion (5wt%) in isopropanol was drop-casted on the glassy carbon electrode.

The catholyte was bubbled with CO_2 (20 ml min^{-1}) for 30 min before reaction to saturate the electrolyte with CO_2 and 20 ml min^{-1} of CO_2 flow was continuously bubbling the electrolyte during reaction. The outlet of the H-cell was connected to the injection loop of a gas chromatography (GC, SRI 8610C) to analyze the concentration of the gas products on-line. The catholyte after reaction was collected and further analyzed by ^{1}H nuclear magnetic resonance (NMR) to determine the Faradaic efficiency of liquid products.

Gas diffusion electrode in the flow cell

The gas diffusion electrode (GDE) was prepared by drop-casting the ink of the catalyst (CuPcCB (4 mg), nafion (5wt%, 20ul), and isopropanol (1 ml)) on the microporous layer of the carbon paper (YLS-30T, SUZHOU SINERO TECHNOLOGY CO., LTD). Four drops of the ink with 30 ul per drop was sequentially drop-casted on the carbon paper (1.2 cm^{-2}), which led the loading the CuPcCB to be 0.4 mg cm^{-2}. Then the GDE was dried at 30 ^{o}C for 10 min.

The same flow cell system as that in our previous report was used to evaluate the eCO$_2$RR in 1 M KOH and 5 M KOH (*Journal of Catalysis 385 (2020) 140–145*). Briefly, a CO_2 flow of 100 ml min^{-1} was delivered to the back side of the GDE and the off-gas was collected to the injection loop of the GC. The catholyte was pumped into the flow cell with a flow rate of 0.3 ml min^{-1} and collected with another tank. The anolyte was circulated. A water bath of 5 ml between the flow cell and GC was used to absorb the vapor of the liquid products. Ag|AgCl (3 M KCl) electrode and platinum plate were reference electrode and counter electrode, respectively. After reaction, the catholyte, anolyte, and the water bath were mixed into a volumetric flask and then analyzed by ^{1}H NMR.

Calculation of Faradaic efficiency

The Faradaic efficiency was calculated with the same protocol as that in our previous report (*Journal of Catalysis 385 (2020) 140–145*), in which the operation protocols and calibration of GC and NMR could also found.

Electrochemical methods for revealing the evolution of the copper nanoparticles derived from CuPc

The same potentiostat (Autolab) were used for all the electrochemical measurements in this section. Different protocols to carry out the chronoamperometry measurements were used for H-cell and flow cell because of the different electrolytes used in these to electrolysis cells. Different protocols were also used for cyclic voltammetry analysis and cyclic voltammetry stripping to control the growth of the copper nanoparticles, in order to reduce the errors in the analysis measurements.

Chronoamperometry in H-cell

Chronoamperometry at various potentials was carried out on CuPcCB-coated glassy carbon electrode for various durations in 0.1 M $KHCO_3$ saturated by CO_2 or deaerated by N_2. The electrodes were rinsed with water and then observed by SEM. For the effect of pH on the copper nanoparticles formed during HER, 0.1 M KH_2PO_4 solution deaerated by N_2 were used with the pH adjusted by adding 1 M NaOH or 1 M $KHClO_4$.

Chronoamperometry for flow cell

No copper nanoparticles in the high-contrast SEM images could be observed on the CuPcCB-coated on gas diffusion electrode (GDE) after CO_2 reduction in 1 M or 5 M KOH in the flow cell, because the copper nanoparticles completely dissolved into KOH solution during transferring the electrode to rinsing water.

To prevent the copper nanoparticles from dissolving during the transfer, once the reaction stopped, the 1 M KOH or 5 M KOH electrolyte were replaced by 0.1 M $KHCO_3$ by flushing the cathodic chamber under -1.2 V vs Ag|AgCl, a potential that could not make Cu nanoparticles grow. For example, a GDE with CuPcCB first catalyzed CO_2 reduction at 400 mA cm^{-2} for 400s in 1 M KOH in the flow cell, and then the potential was immediately switched to -1.2 V vs Ag|AgCl. The inlet of the catholyte were switched to a 0.1 M $KHCO_3$ reservoir. The flow rate of the catholyte was tuned to the maximal value to minimize the time to flushing the cathodic chamber. The pH of the electrolyte at the outlet were monitored with pH paper until the pH value reach 7. And finally the GDE was taken out of the flow cell and rinsed with water.

Analysis of cyclic voltammetry

To avoid the oscillation of the current caused by the bubbles at high overpotentials, the analysis of the cyclic voltammetry was conducted in another H-cell made from glass, also with two chambers separated by a nafion membrane. The transparent glassy wall of this electrolysis cell also allowed us to observed and remove the CO_2 bubbles sticking on the electrode before the cyclic voltammetry because the catalyst layer on the electrode before reaction was relatively hydrophobic and the CO_2 bubbling process, to saturate the electrolyte, probably made some bubbles stick on the catalyst layer.

0.16 mg cm^{-2} of CuPcCB catalyst were drop-casted on a glassy carbon electrode with a diameter of 5 mm, which was used as the working electrode. The electrolyte was saturated with CO_2 before the measurement. The scanning rate was 50 mV s^{-1}. The cycles of voltammograms were obtained, in which the second cycle were used to plot the curves in the figures.

Chronoamperometry followed by a cyclic voltammetry for the growths of copper nanoparticles were also conducted in this setup. First, a certain duration of chronoamperometry at -1.03 V vs RHE in 0.1 M KHCO$_3$ were carried out and then immediately the potentiostat automatically switched to the cyclic voltammetry. The potential scanned from -1.03 V to 1.00 V vs RHE with a scanning rate of 50 mV s^{-1}. All the electrodes were used only once.

Cyclic voltammetry stripping to control the growth of the copper nanoparticles

These measurements of cyclic voltammetry stripping were carried out on the glassy carbon electrode same as that for evaluating the performance of CO_2 in H-cell.

The procedure for the chronoamperometry coupled with cyclic voltammetry is same to that in the above section (Analysis of cyclic voltammetry), except that after scanning to 1.0 V vs RHE in the first scan of voltammetry, the potential cycled in the range of 0.3 V to 1.0 V vs RHE for another 2.5 times to completely dissolve the formed copper nanoparticles.

The chronoamperometry coupled with cyclic voltammetry was repeated seventh times and finally a 100s of chronoamperometry were carried out and then the catalyst was observed by SEM.

Identical location SEM

In order to find the same location in the next SEM observation, the electrodes were marked by scratching gently with a tip of a needle and during the SEM observation, marks were also made at various magnifications.

Electrochemical measurements under HER conditions

All the other parameters were same as that for CO_2 reduction, except that the electrolytes were deaerated by N_2. To investigate the effect of pH, the electrolyte was 0.1 M KH$_2$PO$_4$ solution deaerated by N_2, with the pH adjusted by adding 1 M NaOH or 1 M KHClO$_4$.

In situ Raman

The electrolysis cell and systems for in situ Raman measurement was same as that in our previous report (Applied Catalysis B: Environmental 273 (2020) 1190602). The electrode was a copper plate which was first electropolished for 60s in H$_3$PO$_4$ at 2.5 V vs a copper counter electrode. Then the copper plate was dipped into a solution of CuPc in TFA and rinsed twice with TFA.

XRD analysis

The spectra of the X-ray diffraction were obtained from a Bruke XRD D8 ADVANCE using CuKα (λ = 1.54 Å) radiation at 40.0 KV and 40.0 mA with a scanning step 0.029 (2θ). Samples were place on a holder of silicon single crystal. The Si holder contributed a tiny background spectrum that was subtracted from the spectra of the samples.

XPS analysis

X-ray photoelectron spectroscopy (XPS) analysis was performed in Kratos Axis Supra XPS system (analysis chamber base pressure 1×10^{-9} mbar) equipped with a monochromated Al Ka (1486.61 eV) X-ray source at a nominal power of 225 W. The fixed analyzer transmission (FAT) mode was used for XPS spectra acquisition with pass energies of 160 eV for the survey and 20 eV for the narrow scans. No charge compensation was applied as the samples were well conductive, except for H_2Pc. All spectra were calibrated with the binding energy of Cu 2p3/2 core level of CuPc at 935.0 eV. Quantification of components containing Cu, C, and N was performed by deconvolution of Cu 2p3/2, C 1s, and N 1s peaks after a Shirley-type background subtraction using CasaXPS software. All symmetric peaks were modeled with Gaussian–Lorentzian line shape (GL30). The peak position and full width at half maximum (FWHM) of each component were constrained for different samples. The atomic ratios were calculated by using the area of the peaks and the atomic scattering factors.

TEM

High resolution transmission electron microscopy (TEM) images and Scanning TEM (STEM) EDX elemental mapping were obtained by using FEI Tecnai Osiris 200 KV. Conventional TEM images were obtained using FEI Tecnai G2 Spirit Twin 120 KV.

The high resolution TEM images were obtained from the sample deposited on a holey carbon membrane supported by copper grids. The STEM EDX elemental mapping were obtained from the sample deposited on a carbon membrane supported by nickel grids.

The catalysts after CO_2 reaction were scratched from the glassy carbon electrode, then dispersed in ethanol, and then dropped on the grids. For the catalyst before reaction, the inks were directly dropped on the grids.

SEM

The scanning electron microscope (SEM, FEI Teneo) used to observe the morphology and copper nanoparticles in the catalysts were equipped with four lenses, denoted as T1, T2, T3, and ETD. By adjusting the working distance, the electron trajectories could be tuned to reach certain detector, as shown in Figure S2.2. In the condition shown in Figure S2.2, T1 detector almost receive only the backscattered electrons and thus generates an image with contrast derived from the element distribution in the materials. We denoted this type of image as backscattered electron (BSE) images. Topography information could be obtained from the images generated by T2 and T3.
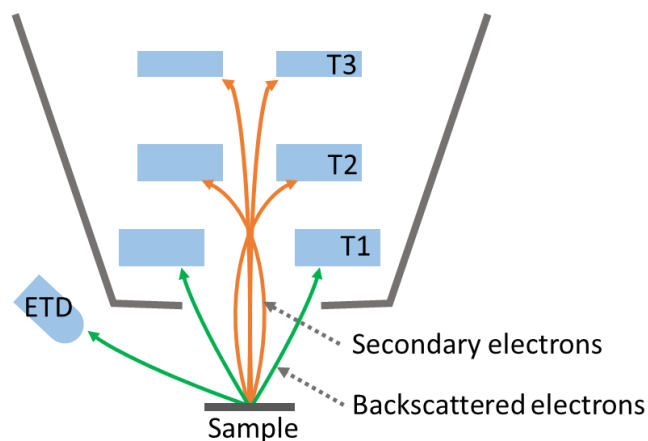
Figure S2.2 Schematics of the distribution of the signals relative to the positions of the detectors in the SEM (FEI Teneo). T1, T2, T3, and ETD are the labels of the detectors.

Calculation of the particle size

The particle size was determined from the nanoparticles in the SEM and TEM images. The perimeters of the nanoparticles were first measured by using the software ImageJ (Fiji). Then the nanoparticles were considered as spherical particles with the diameters calculated from the perimeters. The size of the Cu_2O nanoparticles generated at -1.03 V vs RHE for 50 s in 0.1 M $KHCO_3$ came from the average size of 85 particles from only TEM images. More than 150 particles from both TEM and SEM images were measured to obtained the average size of the nanoparticle generated in other conditions.
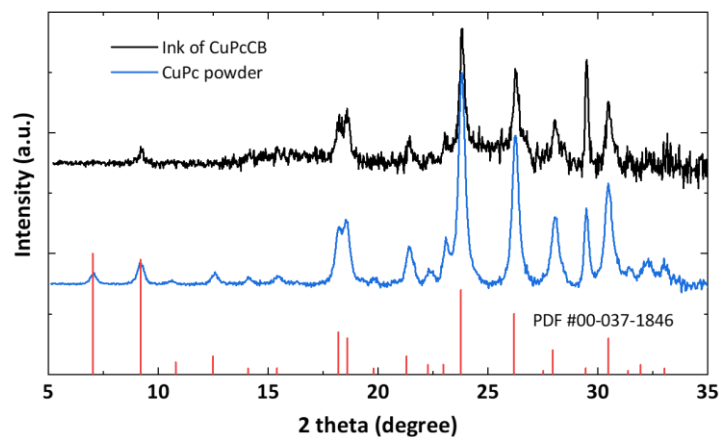
Figure S2.3 XRD spectrum of the as-received copper phthalocyanine (CuPc) and the deposits from the ink of the mixture of copper phthalocyanine and carbon black (CB), which was used as the catalsyts for eCO_2RR and is denoted as CuPcCB. Both as-received CuPc and the as-prepared CuPcCB catalyst have the XRD patterns that match the spectrum from the PDF #00-037-1846, corresponding to β form copper phthalocyanine. This indicates that the process of mixing CuPc and CB in the tetrahydrofuran (THF) did not change the crystal structure of CuPc, which has a negligible solubility, around 87.6 µmol L^{-1} at 20 °C, in THF.[1]
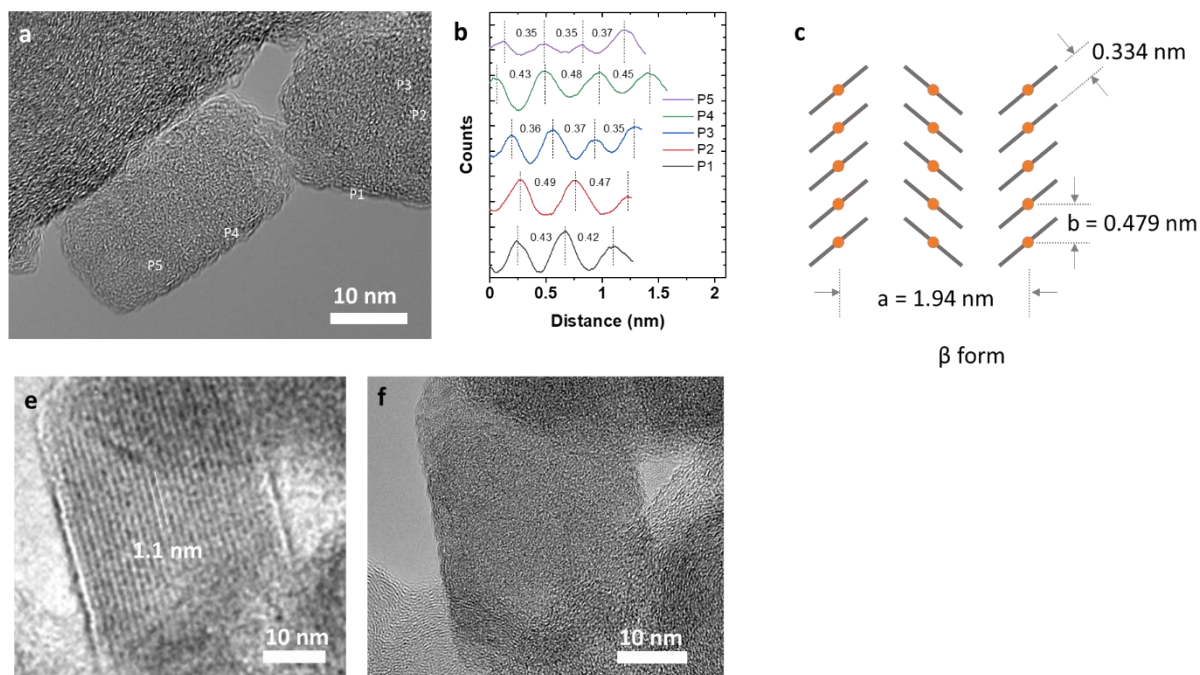
Figure S2.4 TEM image (a) and the corresponding profile (b) of the as-prepared CuPcCB catalyst. (c) The Schematic illustration of CuPc molecules stacked in the form of β phase. (e) TEM image of a CuPc crystal at low magnification and its corresponding image (f) at high magnification. The comparison of (e) and (f) shows that the structure of CuPc crystal is quite sensitive to the electron beam. The long range lattice pattern could be observed at low magnification while it disappears when we zoomed in to the high magnification.
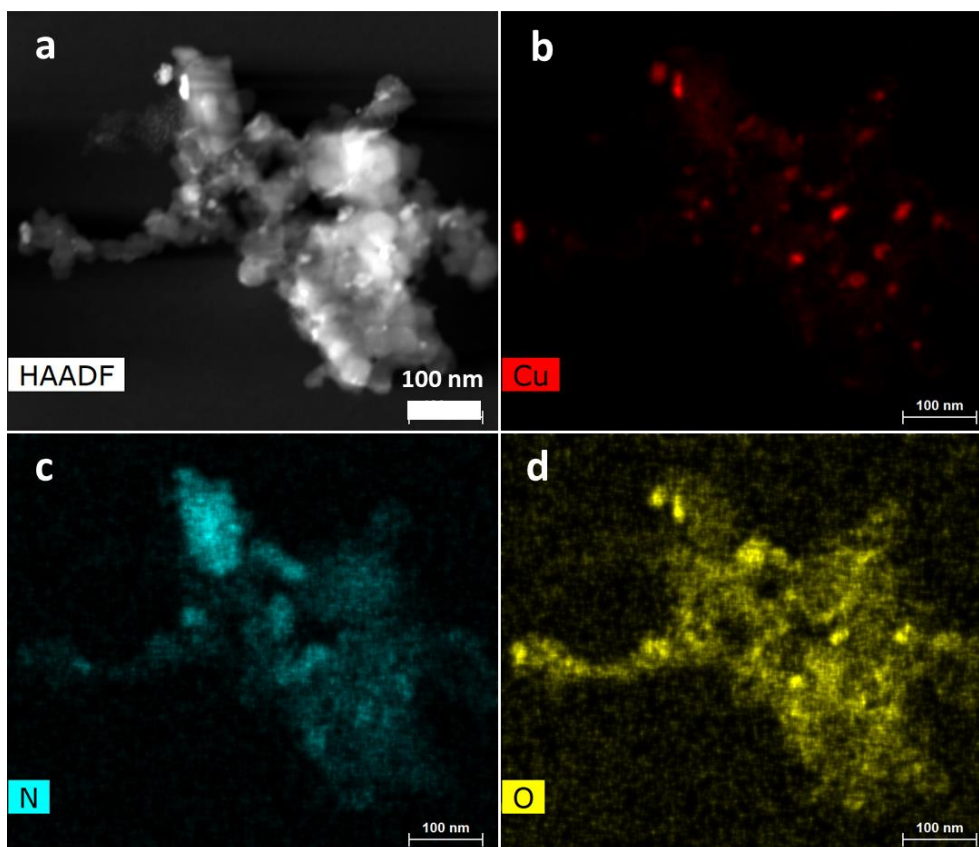
Figure S2.5 Elemental mapping of CuPcCB after CO_2 reduction at -1.03 V vs RHE for 800 s in 0.1 M $KHCO_3$.
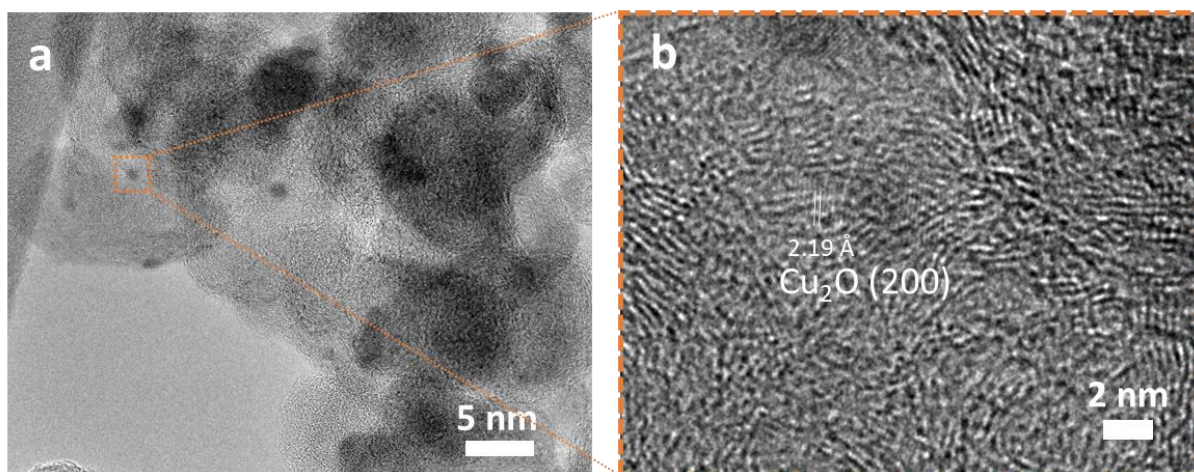
Figure S2.6 TEM images of the clusters formed from CuPcCB during eCO_2RR at -1.03 V vs RHE for 2010 s in 0.1 M $KHCO_3$.
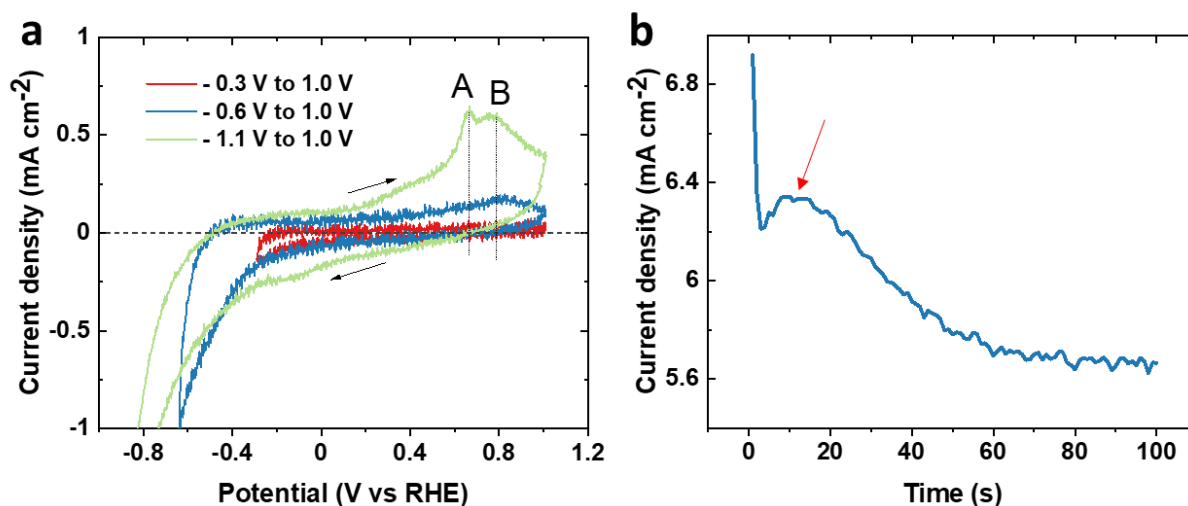
Figure S2.7 (a) Cyclic voltammograms with various potential ranges of the CuPcCB on glassy carbon electrode in 0.1 M $KHCO_2$ saturated by CO_2. The scanning rate is 50 mV s^{-1}. (b) Evolution of the current density with time at the initial stage of eCO_2RR at -1.03 V vs RHE in 0.1 M $KHCO_3$. Peak A and B in Figure S2.7(a) are corresponding to Cu(0) to Cu(I) and Cu(I) to Cu(II), respectively, which indicates the formation of metallic copper. The peak at around 10 s in Figure S2.7(b) is the behavior of the electrocrystallization at the early stage.
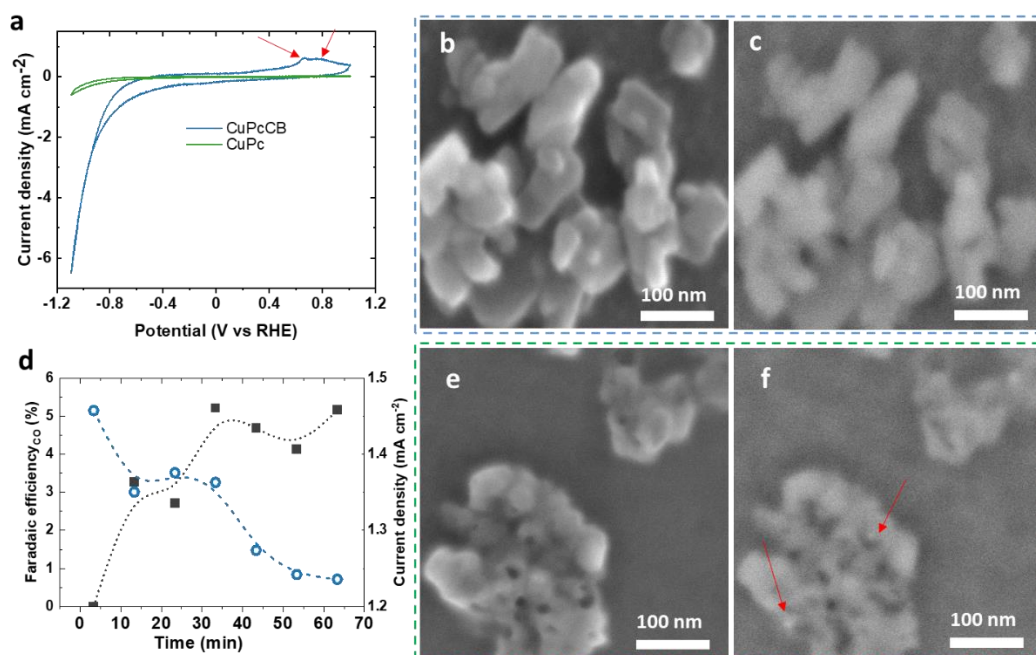
Figure S2.8 (a) Comparison of the cyclic voltammograms of the CuPcCB and CuPc on glassy carbon electrode at 50 mV s^{-1} in 0.1 M $KHCO_3$ saturated by CO_2. (b) SEM and (c) BSE images of the pure CuPc on glassy carbon before CO_2 reduction. (d) Faradaic efficiency of CO and current density versus time of CuPc at -1.03 V vs RHE in 0.1 M $KHCO_3$. (e) SEM and (f) BSE images of the pure CuPc on glassy carbon after CO_2 reduction, corresponding to (d). Carbon black is essential for CuPc to demetallized, confirmed by using pure CuPc deposited on the glassy carbon for the CO_2 reduction. Pure CuPc shows a much smaller electrochemical activity (1.4 mA cm^{-2} at -1.03 V vs RHE in Figure S2.8d) than that (7.0 mA cm^{-2} in Figure S2.17a) of CuPcCB catalyst in the CO_2 reduction conditions. Only CO could be detected as the product of CO_2 reduction on pure CuPc with a Faradaic efficiency decreasing from

42

5% to 0.6% during 1 hour. Moreover, no oxidation peak of Cu(0) could be observed in the cyclic voltammogram of pure CuPc when the potential scanned from -1.1 V to 1.0 V vs RHE. Even though the morphology of the CuPc crystal changed, almost no copper nanoparticles could be observed on the electrode of pure CuPc after CO_2 reduction. We also found from the HRTEM images that most of the Cu_2O nanoparticles attach on the carbon black, not on CuPc crystal. Therefore, CuPc molecules need carbon black or other conductive supports to be activated to release its atoms.
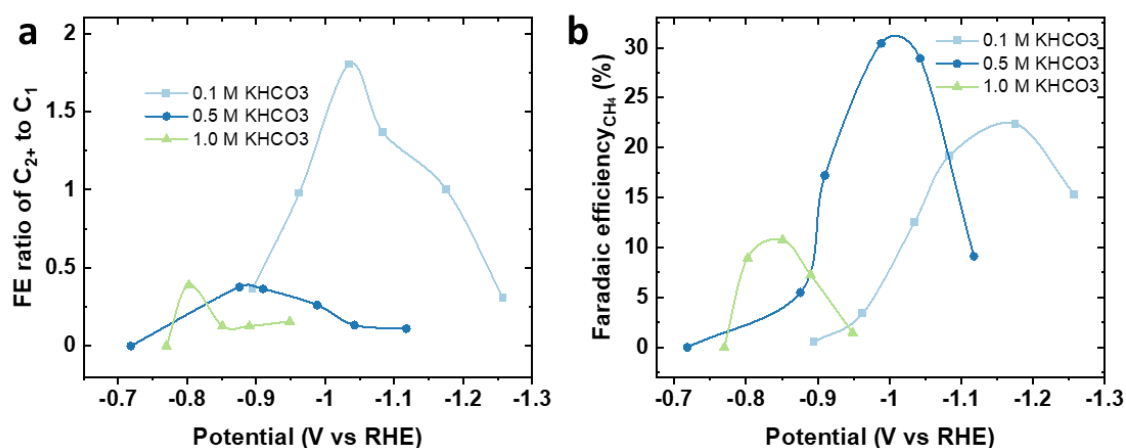
Figure S2.9 The ratio of C_{2+} to C_1 products and (b) Faradaic efficiency of CH_4 versus potentials of CO_2 reduction on CuPcCB in $KHCO_3$ electrolytes with various concentrations in H-cell.
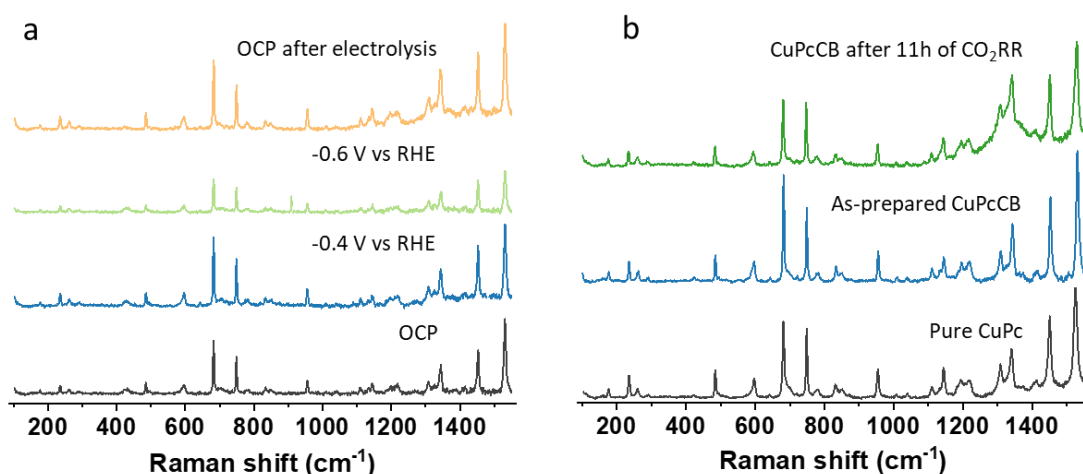
Figure S2.10 (a) In situ Raman spectra at various applied potentials in 0.1 $KHCO_3$ for more than 300 s. (b) Comparison of the Raman spectra of the pure CuPc, as-prepared CuPcCB, and the CuPcCB after 11 h of eCO_2RR at -1.03 V vs RHE in 0.1 M $KHCO_3$. No change in the Raman spectra could be observed on the CuPcCB catalysts deposited on glassy carbon electrode during CO_2 reduction, and even after 11 hour of CO_2 reduction. We hypothesize that only the CuPc crystal particles contacting carbon black could be demetallized due to the bad conductivity of the CuPc crystal. As the ratio of CuPc to CB in the CuPcCB catalyst is quite high (1:1 in wt%), there is always some CuPc crystal not enough contacting the carbon black and not demetallized. At the same time, the fragments from the decomposition of CuPc may go off the electrode and no enough left on the electrode to be detected by Raman spectroscopy.
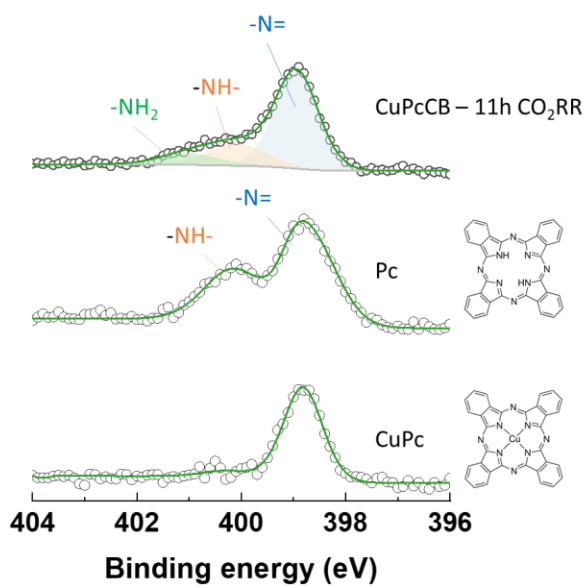
Figure S2.11 Comparison of the XPS spectra of N of CuPc, H_2Pc (29 H , 31 H phthalocyanine), and CuPcCB catalyst after 11 h of CO_2 reduction at -1.03 V vs RHE in 0.1 M $KHCO_3$.
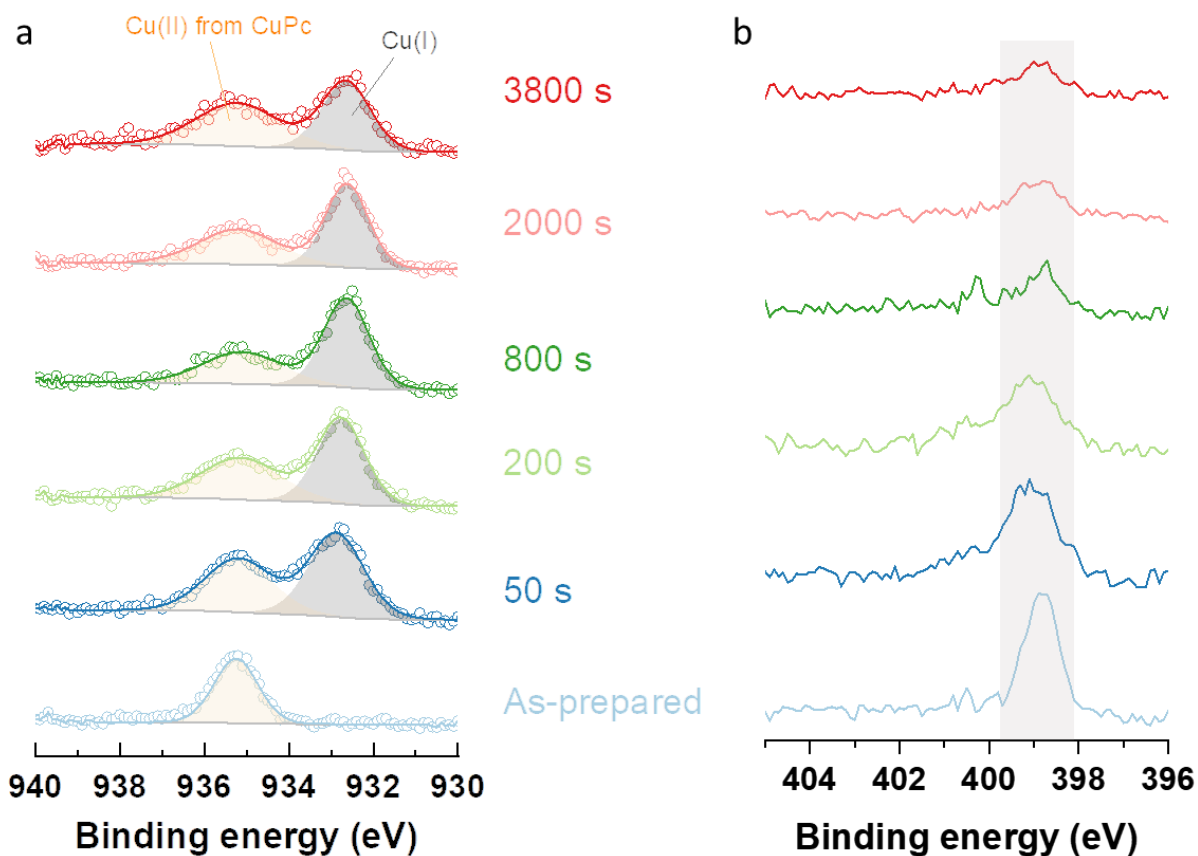
Figure S2.12 XPS spectra of (a) Cu $2P_{2/3}$ and (b) N1s of the CuPcCB after various durations of the CO_2 reduction at -1.03 V vs RHE in 0.1 M $KHCO_3$.
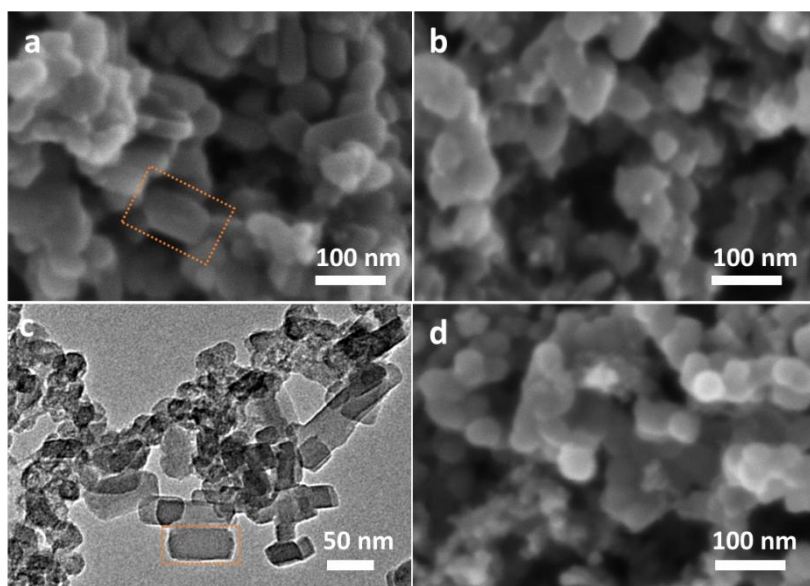
Figure S2.13 BSE images of the as prepared CuPcCB (a), CuPcCB after 50 s of CO_2 reduction at -1.03 V vs RHE in 0.1 M $KHCO_3$ (b), and carbon black (d). (c) TEM images of the as prepared CuPcCB. The amount of the rectangular shape decreased in the CuPcCB after reaction compared to the as-prepared CuPcCB.
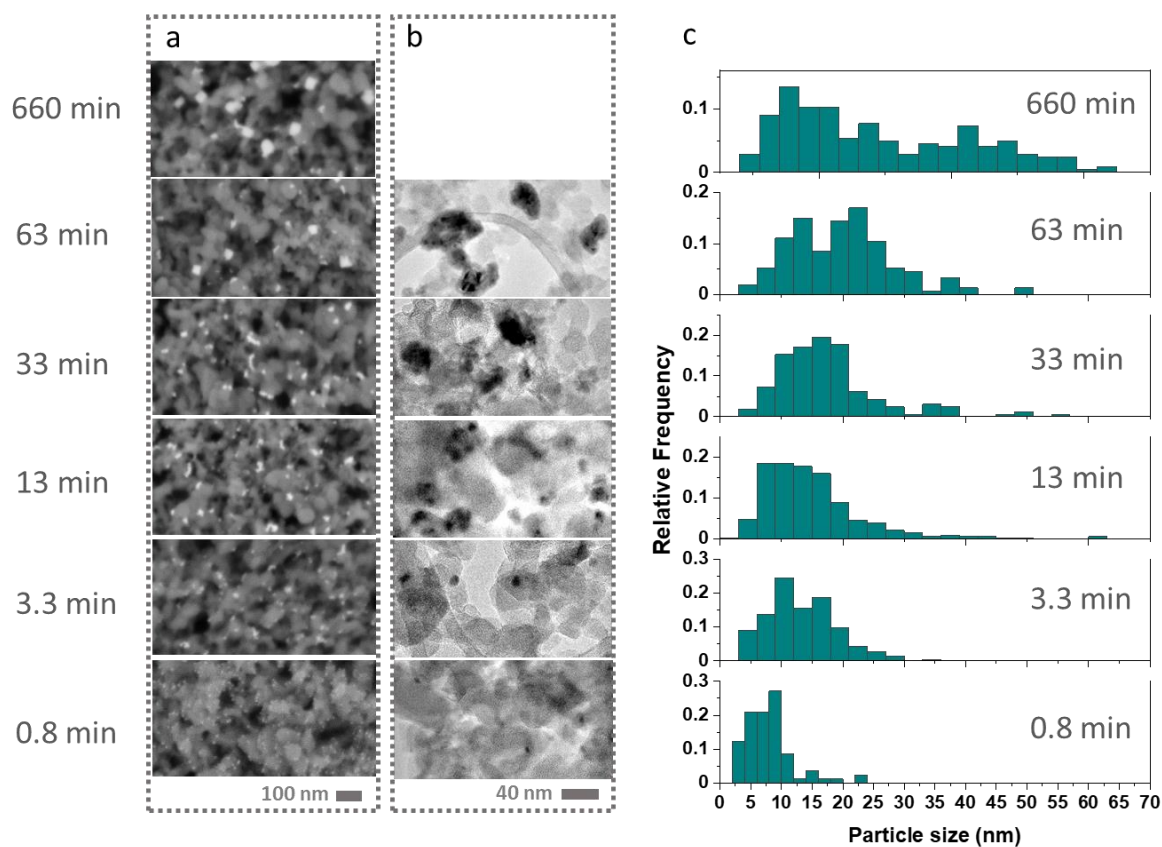
Figure S2.14 BSE images (a), the corresponding TEM images (b), and the corresponding particle size distributions (c) of the Cu nanoparticles derived from CuPc at various reaction durations of CO_2 reduction at -1.03 V vs RHE in 0.1 M $KHCO_3$.
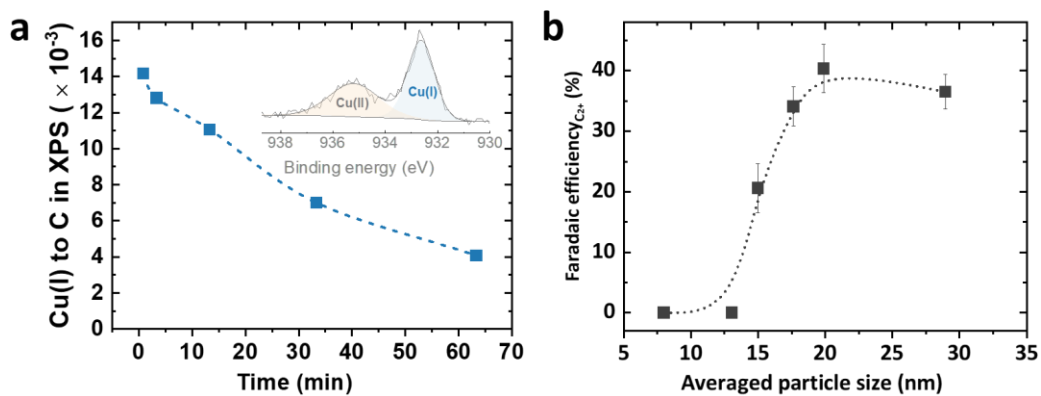
Figure S2.15 (a) Atomic ratio of Cu(I) to carbon in the CuPcCB determined by XPS. (b) Faradaic efficiency of C_{2+} products as a function of particles size, corresponding Figure 2.4.
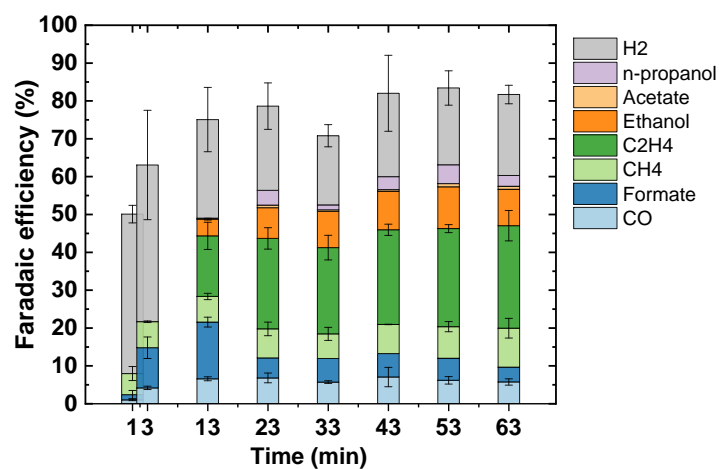
Figure S2.16 Evolution of the product distribution of eCO_2RR on CuPcCB at -1.03 V vs RHE in 0.1 M $KHCO_3$.
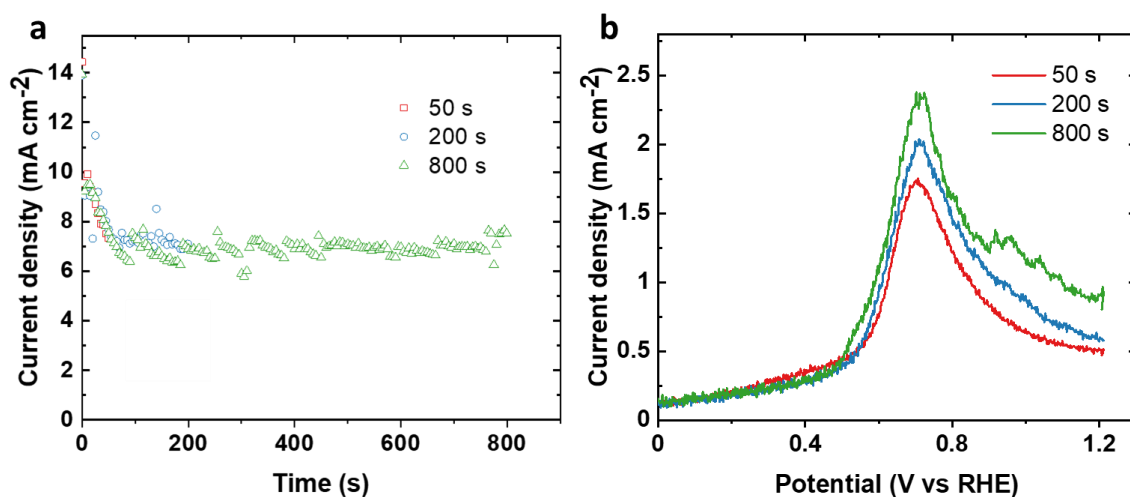
Figure S2.17 (a) Current density versus time of the CuPcCB on glassy carbon electrode at -1.03 V vs RHE with various durations in 0.1 M $KHCO_3$ saturated by CO_2. (b) The cyclic voltammograms with a scanning rate of 50 mV s^{-1} after various durations of reaction at -1.03 V vs RHE corresponding to (a).
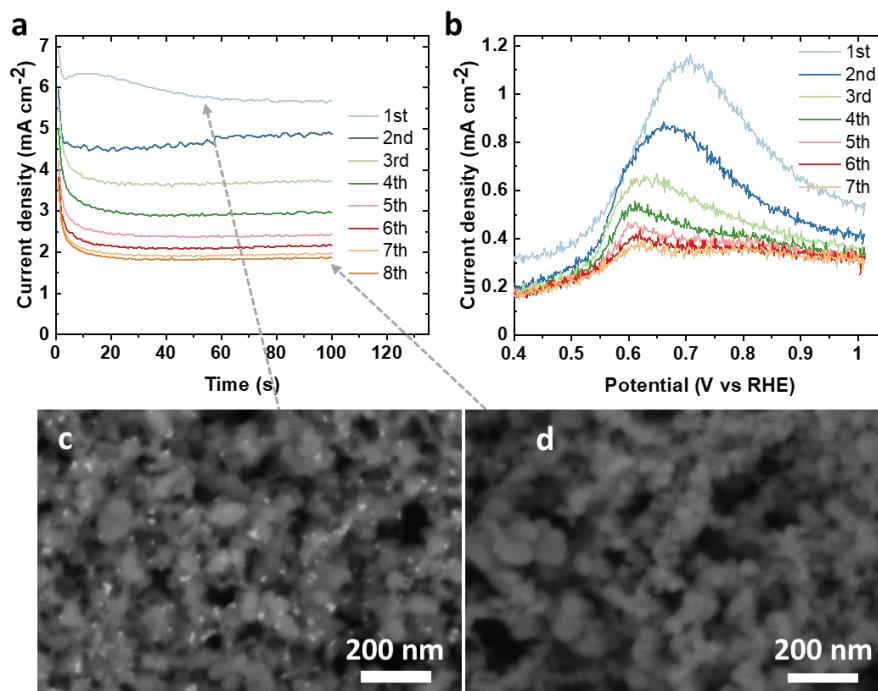
Figure S2.18 (a) Current density versus time of the CuPcCB on glassy carbon electrode at -1.03 V vs RHE in 0.1 M KHCO$_3$ saturated by CO$_2$, which was repeated eight times with a cyclic voltammetry between each. (b) Cyclic voltammograms with a scanning rate of 50 mV s^{-1} after each chronoamperometry for the first seven in (a). BSE images of the CuPcCB after the first chronoamperometry (a) and after the eighth one (d), corresponding to (a).
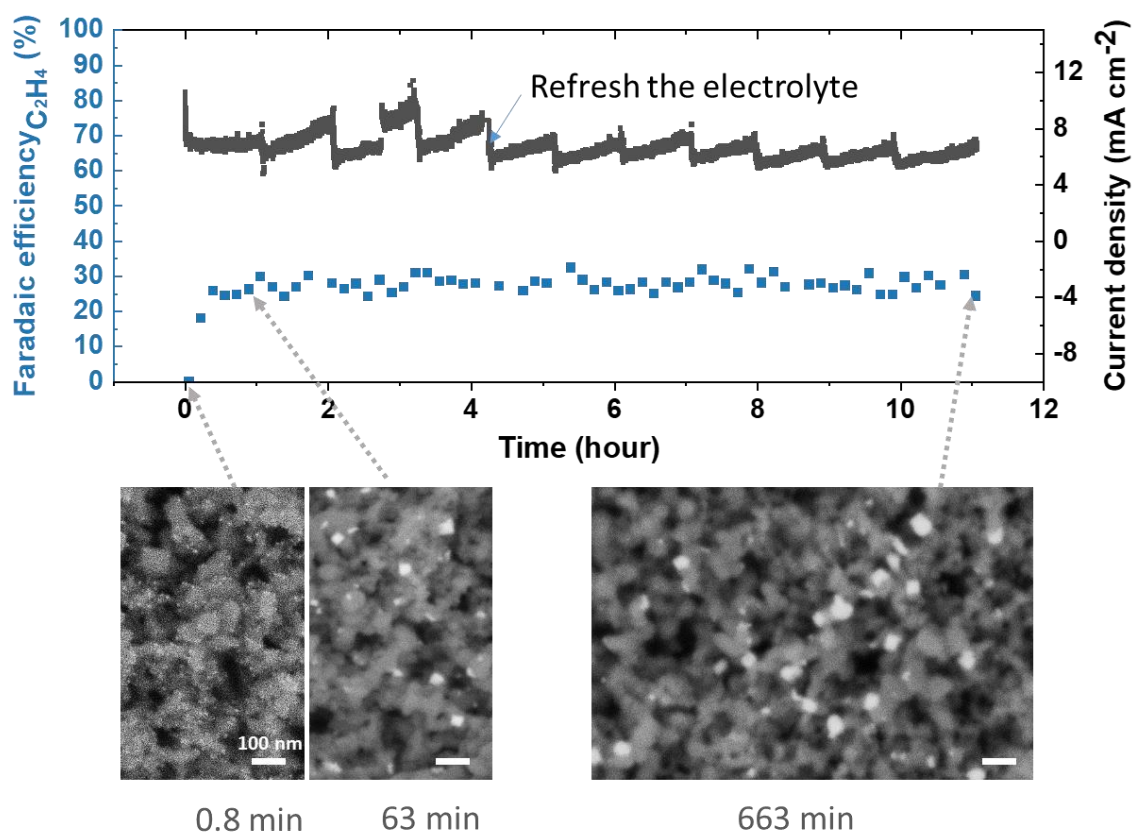
Figure S2.19 Faradaic efficiency of C$_2$H$_4$ versus reaction time on CuPcCB on glassy carbon electrode at -1.03 V vs RHE in 0.1 M KHCO$_3$ saturated by CO$_2$ and the BSE images of the electrode at various reaction time point.
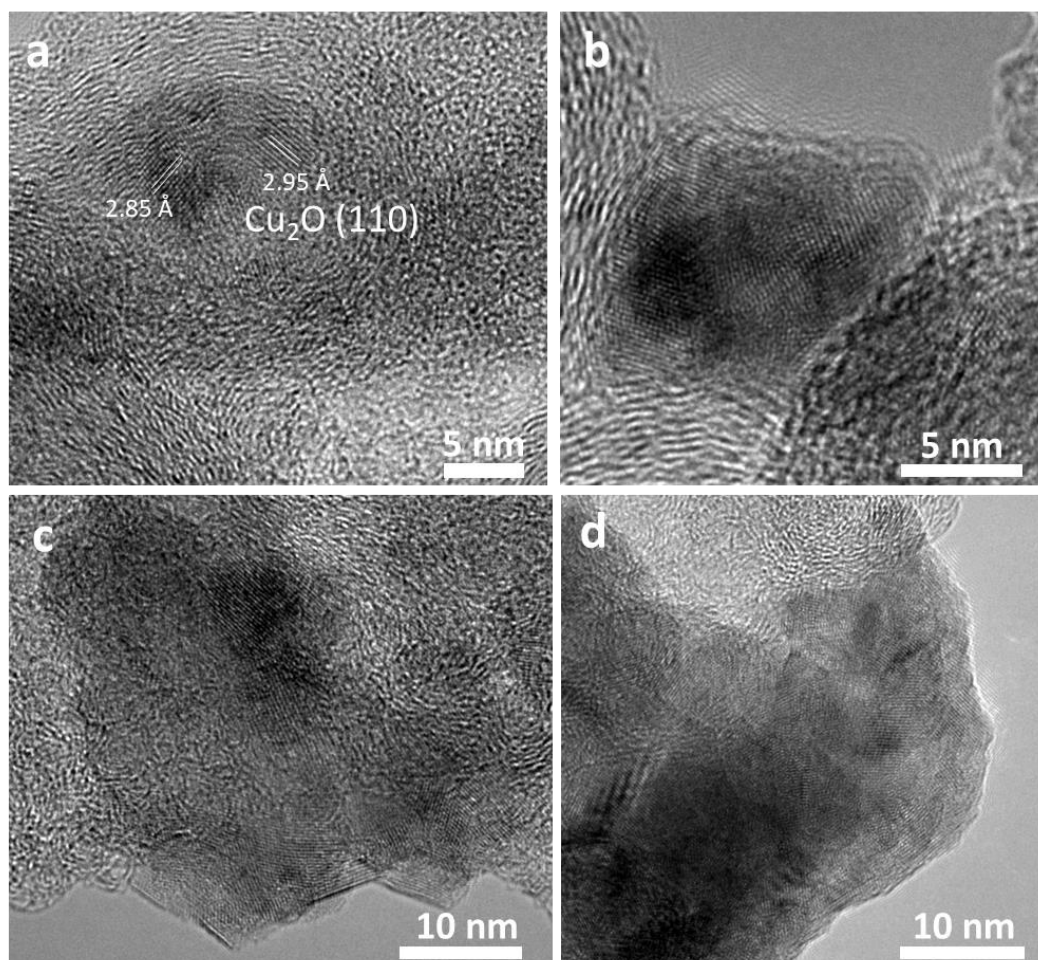
Figure S2.20 HRTEM images of the nanoparticles formed from CuPcCB during eCO$_2$RR at -1.05 V vs RHE for 50s (a), 800s (b), 2000s (c), and 3800s (d) in 0.1 M KHCO$_3$.
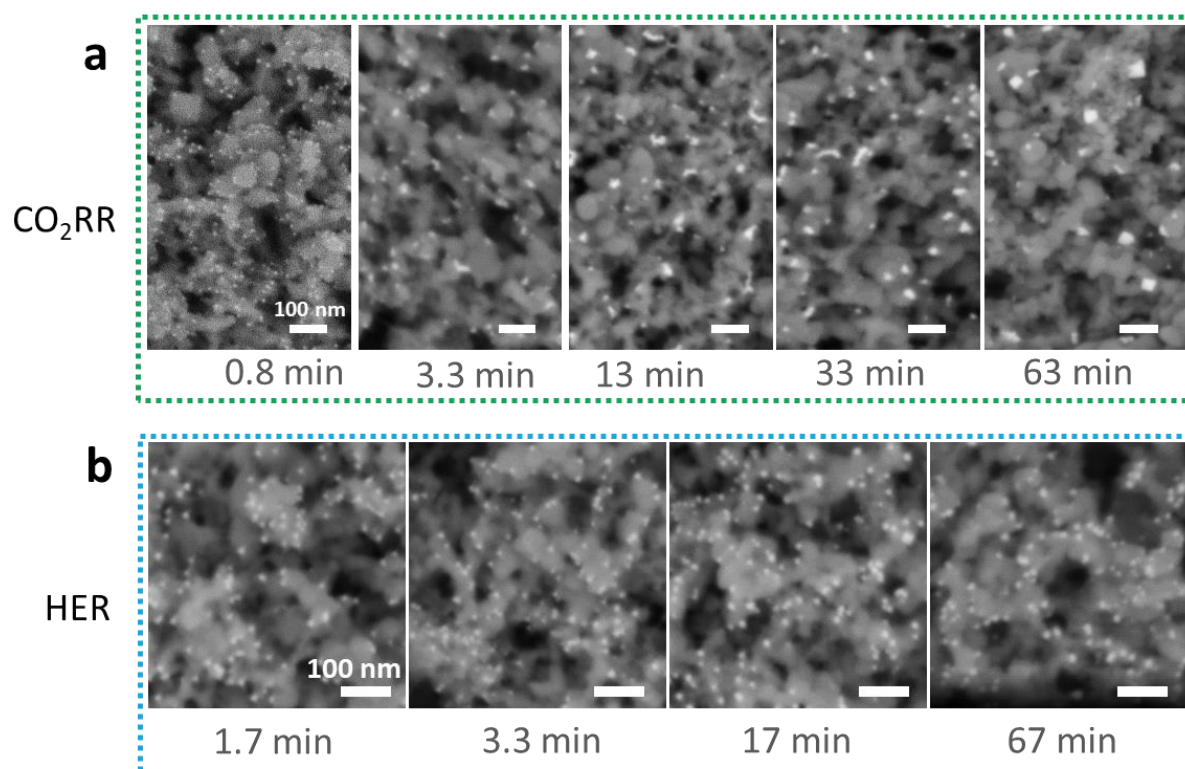
Figure S2.21 (a) BSE images of CuPcCB after various durations of reaction at -1.03 V vs RHE in 0.1 M KHCO$_3$ saturated by CO$_2$. (b) BSE images of CuPcCB after various durations of reaction at -0.90 V vs RHE in 0.1 M K$_2$HPO$_4$ deaerated by N$_2$ with a pH of 7. To exclude the effect of the pH, we used 0.1 M K$_2$HPO$_4$ deaerated by N$_2$ with a pH of 7 for HER, which has the same pH as the 0.1 M KHCO$_3$ saturated by CO$_2$.
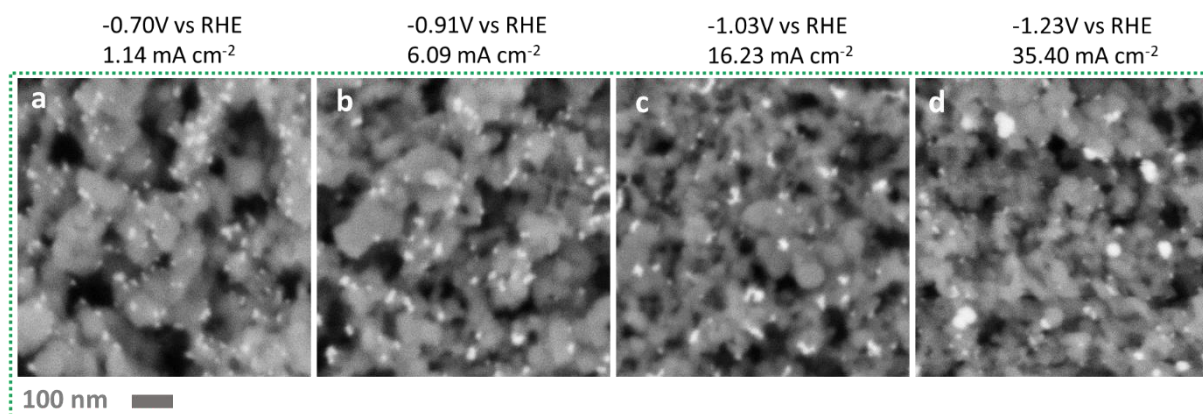
Figure S2.22 BSE images (a - d) of CuPcCB after 800 s of CO$_2$ reduction at various potential in 0.1 M KHCO$_3$.

pH 5 pH 7 pH 9 pH 11

-0.91 V vs RHE -0.89 V vs RHE -0.89 V vs RHE -0.86 V RHE
59.87 mA cm^{-2} 16 mA cm^{-2} 18 mA cm^{-2} 9.50 mA cm^{-2}
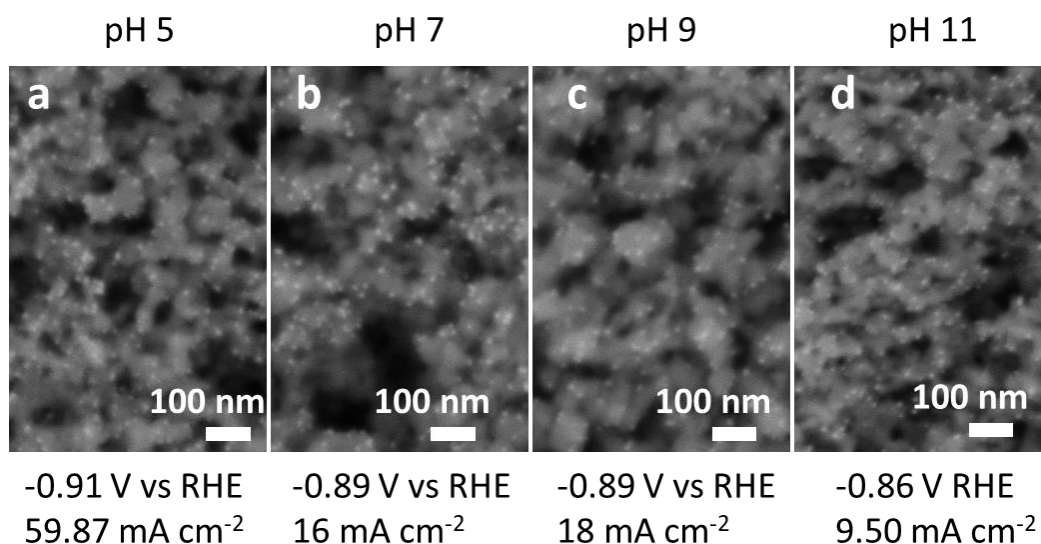
Figure S2.23 (a - d) BSE images of the CuPcCB after 1000 s of reaction (mainly HER) at around -0.90 V vs RHE in 0.1 M KH$_2$PO$_4$ with various pH values and deaerated by N$_2$.
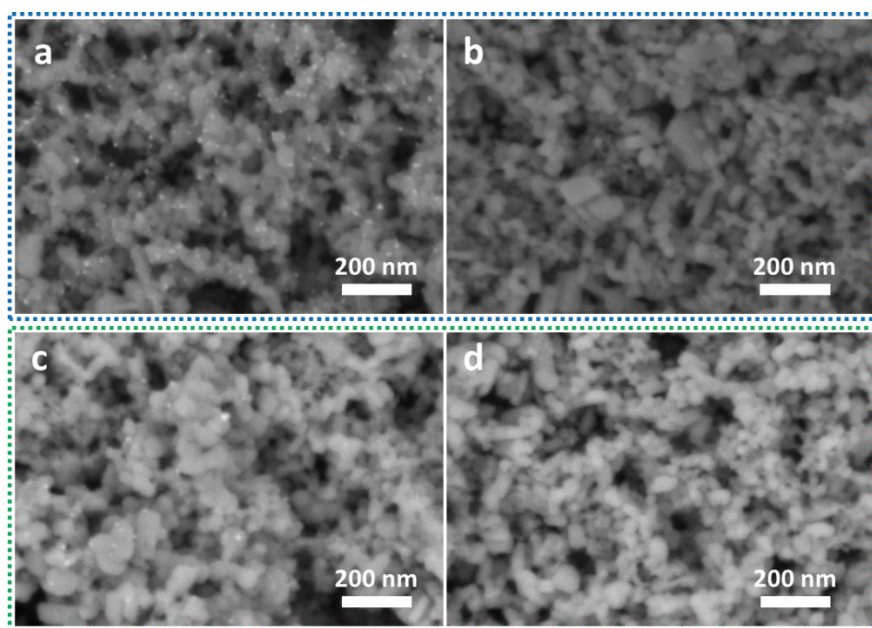
Figure S2.24 BSE images of the CuPcCB on the gas diffusion electrode after various treatments.

(a) 400s of CO$_2$ reduction in 1 M KOH at 400 mA cm^{-2}, followed by immediately applying a potential of -1.2 V vs Ag|AgCl (3M KCl) and at the same pumping 0.1 M KHCO$_3$ to catholyte chamber until the pH of the solution at the outlet of catholyte chamber reachs reaches the value of 7.

(b) -1.2 V vs Ag|AgCl (3M KCl) in 1 M KOH for 200s, then switch to 0.1 M KHCO$_3$ until pH reach 7,

(c) 400 mA cm^{-2} in 5 M KOH for 400s, then -1.2 V vs Ag|AgCl (3M KCl), then switch to 0.1 M KHCO$_3$ until pH reach 7

(d) -1.2 V vs Ag|AgCl (3M KCl) in 5 M KOH for 200s, then Switch to 0.1 M KHCO$_3$ until pH reach 7

Because the copper nanoparticles almost completely dissolved in the KOH solution while oxidized by oxygen from the air before the KOH solution on the GDE was rinsed off. Therefore, we developed a procedure to prevent the copper nanoparticles from being dissolved in the KOH by switching the catholyte to 0.1 M KHCO$_3$ at a controlled negative potential.
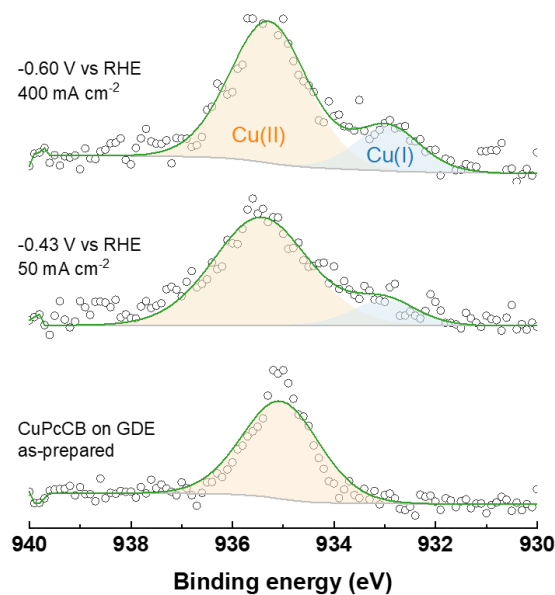
Figure S2.25 Cu $2P_{2/3}$ XPS spectra of the CuPcCB on gas diffusion electrodes after CO_2 reduction at various potentials in 5 M KOH for 800s.
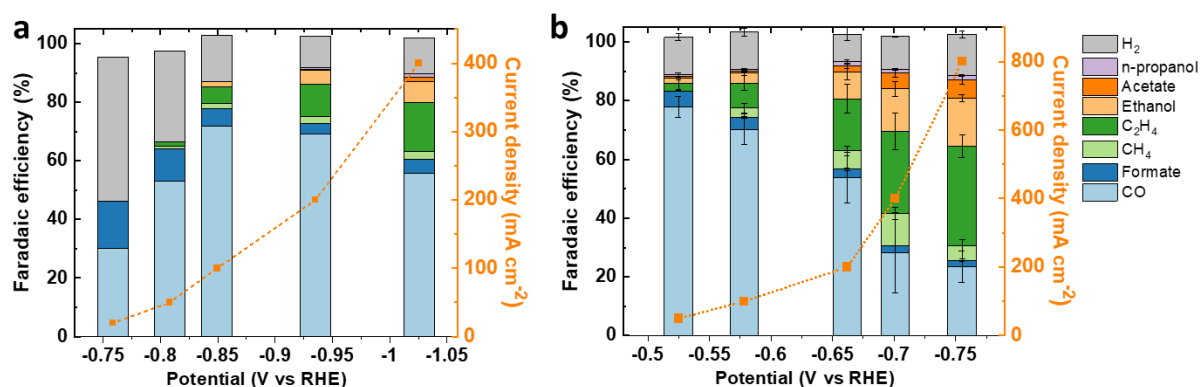
Figure S2.26 Faradaic efficiencies and total current densities versus potential of the products from eCO_2RR on CuPcCB in a flow cell with 1 M $KHCO_3$ (a) and 1 M KOH (b) as the electrolytes.
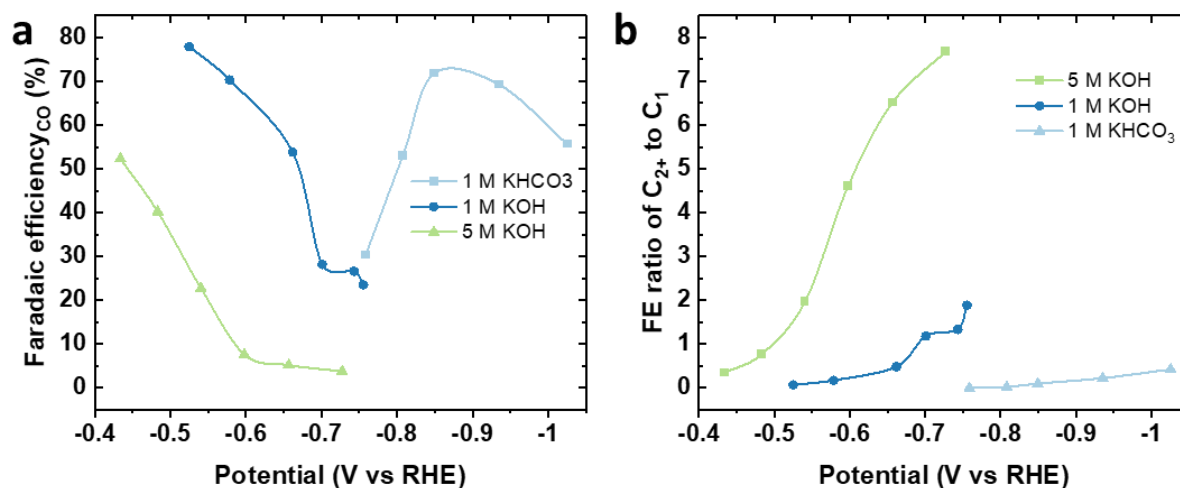
Figure S2.27 (a) Faradaic efficiency of CO versus potentials of CO_2 reduction and (b) the corresponding ratio of C_{2+} to C_1 products on CuPcCB in various electrolytes with different local pH in flow cell.

The huge difference in the product selectivity of the CO_2 reduction in 0.1 M $KHCO_3$ in a bath-type cell (H-cell) and that in a flow cell with GDE could be attributed to the difference in the local reaction environments, as the CO_2 reduction in the flow cell had much higher mass transport capability due to the GDE and higher local pH due to the 5 M KOH electrolyte than that in the H-cell. To de-convoled the effect of the mass transport and local pH, the product distribution of the CO_2 reduction in several electrolytes with various pH in both flow cell and in H-cell. We compared the selectivity ratios of the C_{2+} to C_1 versus potential of the CO_2 reduction in flow cell filled with 1 M $KHCO_3$, 1 M KOH, and 5 M KOH, the pH values of which had an increasing order. Still a huge difference existed in the selectivity of C_{2+} and C_1 in these three electrolytes, probably because of the difference in pH as they were all obtained with the GDE in the same flow cell and should had the same mass transport of CO_2. CO_2 reduction in 5 M KOH with the highest pH produced the highest ratio (up to 8 at -0.73 V vs RHE) of C_{2+} to C_1, and that in 1 M $KHCO_3$ with the lowest pH produced the lowest ratio (< 0.5) of C_{2+} to C_1. Similar trend also existed in the selectivity of C_{2+} and C_1 obtained in H-cell with 0.1 M $KHCO_3$, 0.5M $KHCO_3$, and 1M $KHCO_3$ as the electrolytes, which had different local pH due the different buffering capability.

Referecnes

[1]   F. Ghani, J. Kristen, H. Riegler, *Journal of Chemical & Engineering Data* **2012**, *57*, 439-449.

Chapter 3 Tandem Effect of Silver-Copper Bimetallic Catalysts Enhances Ethanol Selectivity

Jie Zhang[a, b], Thi Ha My Pham[a, b], Youngdon Ko[a, b], Shuliang Yang [c], Cedric David Koolen [a, b], Wen Luo[d]*, Andreas Züttel[a, b]

Abstract

Copper-based bimetallic catalysts (e.g., Ag-Cu) can improve the selectivity of C_2H_4 and ethanol from electrochemical CO_2 reduction, compared to monometallic Cu catalysts. These improvements have been attributed to both the tandem and interface effects between the two metals in the bimetallic catalysts. However, it is still unclear how each effect influences the selectivity of C_2H_4 and ethanol because in most cases the two effect are present simultaneously. To deconvolute these two effects, we designed and synthesized a Ag@C@Cu core-shell catalyst, in which the thin carbon layer prevented Ag and Cu from forming interface and in the meanwhile allowed the reduction CO_2 to CO on Ag surface. Therefore, we can isolate the tandem effect from the interface effect for CO_2 reduction by using this catalyst. We found that the increased local CO concentration derived from the CO_2 reduction on Ag core decreased the C_2H_4 selectivity while increased the ethanol selectivity on the Cu shell, which illustrated that the increased CO concentration due to the tandem effect favoured ethanol production over C_2H_4.

[a] *Laboratory of Materials for Renewable Energy (LMER), Institute of Chemical Sciences and Engineering (ISIC), Basic Science Faculty (SB), École Polytechnique Fedérale de Lausanne (EPFL) Valais/Wallis, Energypolis, Rue de l'Industrie 17, CH-1951 Sion, Switzerland.*
[b] *Empa Materials Science & Technology, CH-8600 Dübendorf, Switzerland*
[c] *College of Energy, Xiamen University, Xiang'an South Road, Xiamen 361102, China*
[d] *School of Environmental and Chemical Engineering, Shanghai University, 99 Shangda Road, Shanghai 200444, China*

3.1   Introduction

Electrochemical CO_2 reduction is one of the most promising technologies that can produce commodity chemical feedstocks by using renewable electricity as the energy sources.[1] However, the selectivity and energy efficiency of producing C_2H_4 or ethanol are still too low to make this technology industrially viable.[2] Electrocatalyst is one of the main factors that determine the selectivity and energy efficiency of CO_2 reduction.[3-5] Copper (Cu) is the only metallic catalyst that catalyses eCO_2RR to C_{2+} with attractive selectivity. Thus, various approaches have been used to engineer Cu materials to improve the selectivity and activity for producing C_{2+} molecules.[3] C_2H_4 and ethanol from CO_2 reduction on Cu catalysts are always generated simultaneously at the same overpotential range because in their formation pathways several intermediates are shared.[6] However, the selectivity of C_2H_4 on Cu monometallic catalysts is always much higher than that of ethanol.[7-9] Although this selectivity difference can be reversed by modifying the Cu surface with another metal, such as gold, zinc, or silver (Ag), but the mechanism is still under debate.[10-12]

Compared with monometallic Cu, silver-copper (Ag-Cu) bimetallic catalysts with certain structures and elemental ratios showed improved selectivity for C_2 products from CO_2 reduction, either C_2H_4 or ethanol.[11, 13-15] Two mechanisms have been proposed to explain this improvement of the C_2 products: tandem and interface effects.[13, 16] The tandem effect means that Ag and Cu work sequentially as the different active sites – that is, the CO_2 molecules are first reduced to CO on the Ag surface, and then the CO molecules diffuse to the surface of Cu and are further reduced to C_2H_4 or ethanol.[16] Interface effect, on the other hand, refers to that Ag atoms are doped into copper lattice, at least in the surface layers, electronic and geometric structures of Cu surface and thus affecting the adsorption of certain intermediates toward C_2H_4 and ethanol.[13]

Most developed Ag-Cu bimetallic catalysts contain both the interface and the separated phases of Ag and Cu, resulting in the co-exist of the tandem effect and interface effect.[11, 13, 15, 17] This makes it difficult to distinguish how each effect influences the selectivity of C_2H_4 and ethanol, separately. Therefore, it is important to deconvolute the tandem and interface effect in bimetallic catalysts to rationally develop more efficient catalysts for CO_2 reduction to either C_2H_4 or ethanol.

Herein, we designed and synthesized Ag@C@Cu core-shell nanoparticles with the Ag core and Cu shell separated by a layer of carbon. The carbon layer prevented the formation of the Ag-Cu interface, but still allowed the reduction of CO_2 molecules to CO on the Ag core. On Ag@C@Cu nanoparticles, a higher ratio of ethanol to C_2H_4 was observed compared to that on the corresponding Cu nanoparticles, revealing that the ethanol production from CO_2 reduction can be enhanced by the tandem effect.

3.2   Results and discussion

3.2.1   Co-existence of tandem and interface effects

To demonstrate the co-existence of tandem and interface effects in Ag-Cu bimetallic catalysts, we prepared a Ag@Cu core-shell (Figure 3.1a) and a physical mixture of Ag and Cu nanoparticles (Ag-Cu mixture, Figure 3.1b) as the catalysts for CO_2 reduction. Figure 3.1c compares the product distribution and ratio of ethanol to C_2H_4 on the Ag-Cu mixture, Ag@Cu core-shell, and monometallic Cu at -0.64 V vs RHE and 400 mA cm^{-2} in a flow cell with 1 M KOH as the electrolyte. Both Ag-Cu mixture and Ag@Cu

catalysts showed higher ratio of ethanol to C_2H_4 than Cu itself did (Figure 3.1d), indicating that the Ag-Cu bimetallic catalysts could improve the selectivity of ethanol relative to C_2H_4 in our reaction conditions. However, both ethanol and C_2H_4 on Ag-Cu mixture had their absolute Faradaic efficiencies (FEs) decreased compared with that on Cu (Figure 3.1c) because of the increase of the CO FE from 7% to 32%. This demonstrated that the CO molecules produced on Cu was difficult to be captured and further reduced by the copper surface in Ag-Cu mixture catalyst. In contrast, this CO escape problem was mitigated on the Ag@Cu catalysts, as the CO FE only increased from 7% to 15%. Like that in previous reports[11, 13, 15, 17], the higher ethanol/C_2H_4 ratio on Ag@Cu than that on Ag-Cu mixture can be ascribed to both the tandem and interface effects because the compact core-shell structure in Ag@Cu (i) contains more Ag-Cu interfaces and (ii) also benefits more the tandem effect than the Ag-Cu mixture, as CO molecules produced on Ag core have to pass through Cu shell.
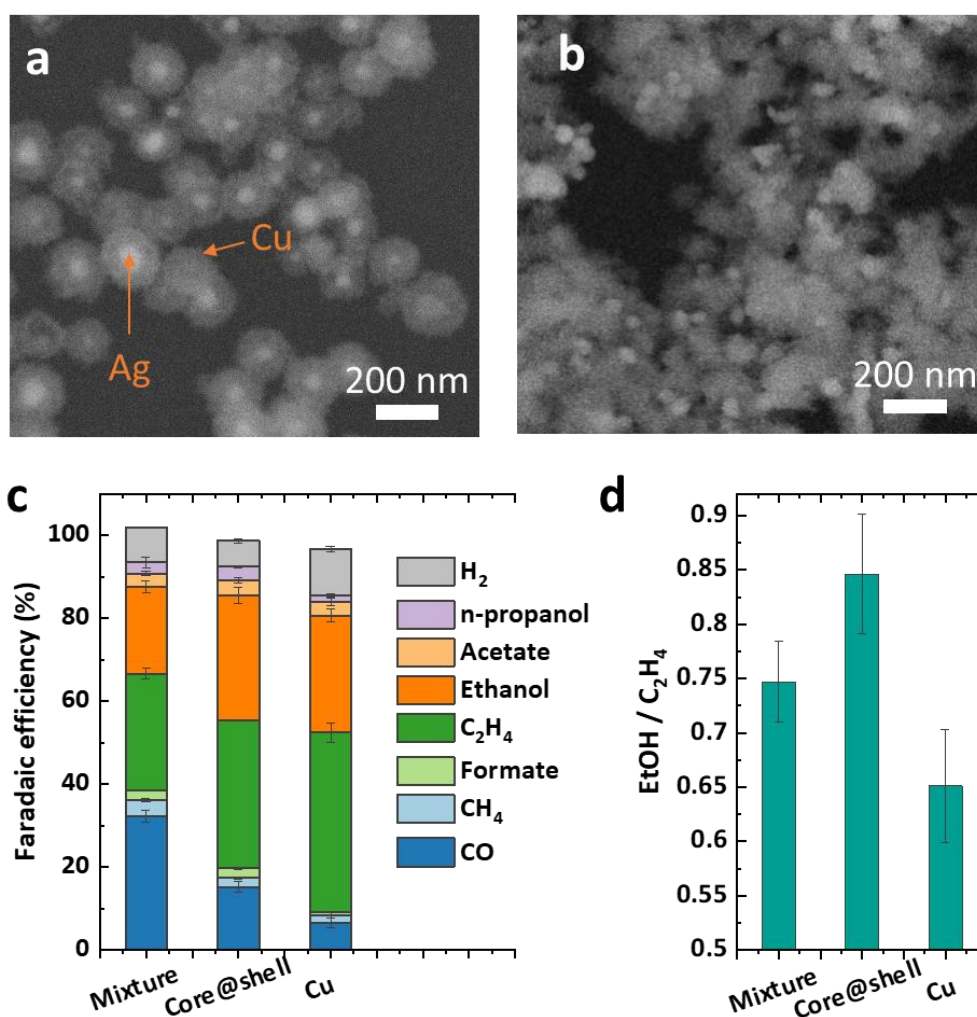
Figure 3.1 (a) Backscattered electron images of Ag@CuO core-sell nanoparticles. (b) Backscattered electron images of the random mixture of Ag nanoparticles and CuO. (c) Comparison of the product distribution of CO_2 reduction on Ag-Cu mixture, Ag@Cu core-shell, and monometallic Cu evaluated at -0.64 V vs RHE and 400 mA cm^{-2} in a flow cell with 1 M KOH. (d) Comparison of the selectivity ratio of ethanol (EtOH) to C_2H_4 on Ag-Cu mixture, Ag@Cu core-shell, and monometallic Cu, corresponding to (c). The particles in (a, b) are obtained by oxidizing Ag@Cu_2O core-shell nanoparticles (Figure S3.1). The Cu catalysts were also in situ derived from CuO precursors (Figure 3.6) synthesized with the same method as that in Ag-CuO.

The simultaneous presence of these two effects hinders us from understanding the role of each effect on the reaction mechanism and thus obstructs our rationally designing of more efficient catalysts. Therefore, in the next step we tried to deconvolute these two effects in the Ag@Cu core-shell structure by growing a carbon layer between Ag core and Cu shell to form a catalyst with the Ag@C@Cu core-shell structure.

3.2.2 Synthesis of Ag@C@CuO

Firstly, Ag@C@CuO core-shell nanoparticles (the precursor of Ag@C@Cu) were synthesized with the procedure shown in Figure 3.2 (see the details in the supporting information). The Ag nanoparticles, obtained by reducing $AgNO_3$ with glucose, were first coated by a layer of polydopamine (PDA, around 4 nm thick) that is then coated by a layer of silica (around 8 nm thick) to form $Ag@PDA@SiO_2$ nanoparticles. The $Ag@PDA@SiO_2$ particles were annealed at 700 ^{o}C under nitrogen environment to carbonize the PDA layer. The formed $Ag@C@SiO_2$ was treated by a solution of NaOH and diethylamine to dissolve the SiO_2 layer and to obtain Ag@C with a carbon layer of around 4 nm in thickness. The function of SiO_2 layer is to prevent nanoparticles from agglomerating during the carbonization of PDA (see Figure S3.2). The Ag@C was then coated by a layer of PVP to increase the hydrophilicity so that Cu_2O nucleated on the Ag@C particles in the $Cu(NO_3)_2$ solution with ascorbic acid as the reducing agent (Figure S3.3). The Cu_2O layer was finally oxidized by the oxygen molecules in the mixture of ammonia and ethanol to obtain the Ag@C@CuO nanoparticles. The transmission electron microscopy (TEM) images in Figure 3.2 and Figure S3.4 and S3.5 clearly show the formation of each layer, including PDA, SiO_2, carbon, Cu_2O, and CuO, and confirm the successful coating of the Ag nanoparticles with the carbon layer.
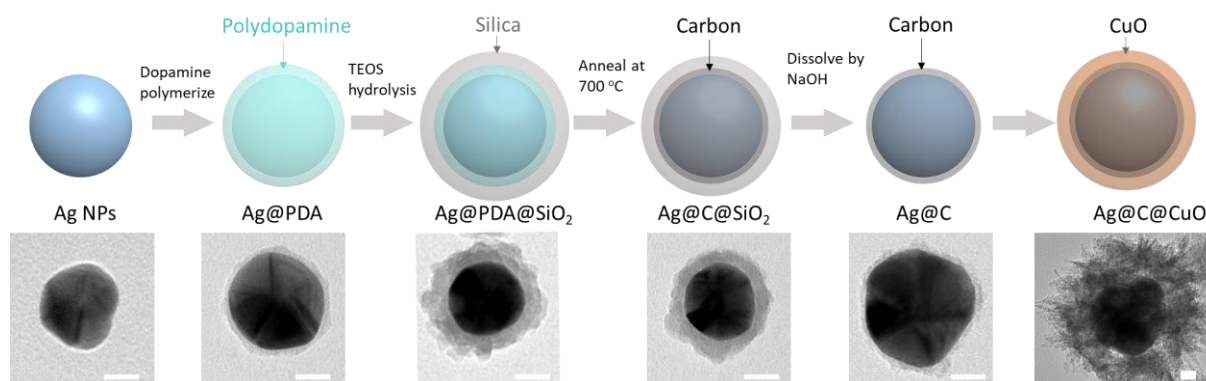
Figure 3.2 Schematics for synthesis procedure of Ag@C@Cu nanoparticles and the corresponding TEM images of the single particle in each step. Scale bar represents 20 nm.

The carbon layer on the Ag@C nanoparticles was amorphous with a thickness of around 4 nm revealed by the high resolution TEM (HRTEM) image in Figure 3.3a. Meanwhile, the carbon layer wrapped the Ag surface compactly, which inhibited the Cu layer from directly growing on the Ag surface. Indeed, CuO shell did not contact the surface of Ag core in the Ag@C@Cu nanoparticles, as shown in the TEM image in Figure 3.3b, where a clear gap between the Ag core and the Cu shell was observed. At the same time, energy-dispersive X-ray spectroscopy (EDX) elemental map shows the overlap of Ag and carbon element (Figure S3.6 and S3.7) and the clear separation of Ag core and CuO shell (Figure 3.3d). The CuO shell layer consisted of the needle shape of CuO particles and thus was

porous (Figure 3.3b), which allowed CO_2 molecules accessible to the Ag core during CO_2 reduction. The CuO shell also contained high density of grain boundary shown in the HRTEM images (Figure 3.3c), ensuring its high selectivity of C_{2+} products as grain boundary has been proved to be the active sites for C-C coupling.[18, 19]
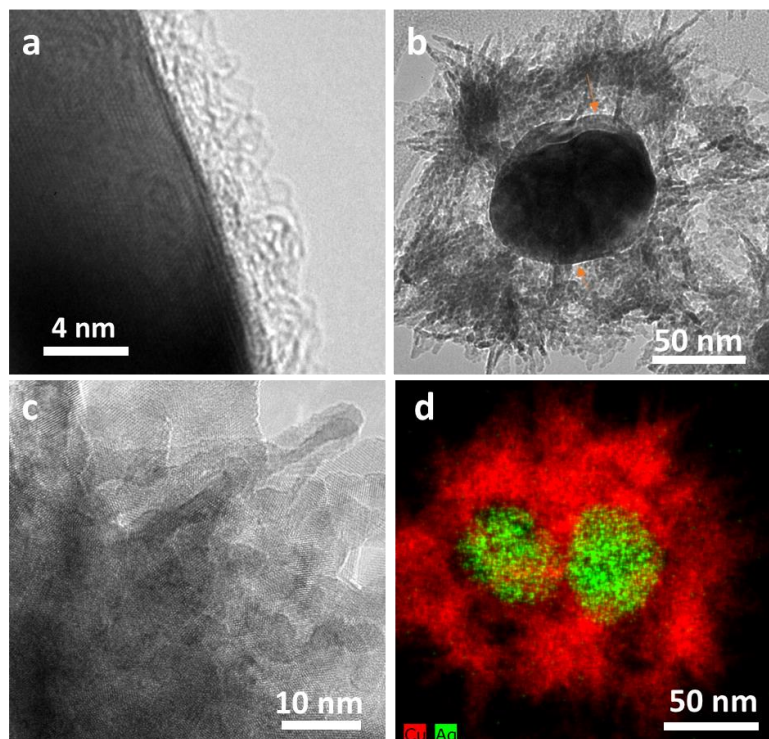
Figure 3.3 (a) HRTEM image of carbon layer on Cu nanoparticles. (b) TEM image of the Ag@C@CuO core-shell nanoparticles. (c) HRTEM images of the CuO in Ag@C@CuO core-shell nanoparticles. (d) EDX elemental map of Ag and Cu in the Ag@C@CuO core-shell nanoparticles.

3.2.3   Tandem effect on C_{2+} products

The performance of the catalysts in terms of the selectivity, activity, and overpotential was evaluated in gas diffusion electrode in a flow cell with 1 M KOH as the electrolyte. The carbon sphere particles (Figure S3.9), synthesized from the carbonization of PDA, showed almost no activity for CO_2 reduction (Figure 3.4a), which excluded the contribution from the carbon layer in Ag@C@Cu to CO_2 reduction. Ag@C nanoparticles showed a similar selectivity of CO to pure Ag nanoparticles in the potential range from -0.5 V to -0.75 V vs RHE (Figure 3.4a), while the partial current density of CO on Ag@C particles was smaller than that on Ag nanoparticles at high overpotential range (-0.6 V to -0.75 V vs RHE) (Figure 3.4b) because the coverage of carbon layer blocked part of the active sites. While Ag@C nanoparticles still showed a quite high activity for catalyzing CO_2 reduction to CO that was enough to impact the local CO concentration in the Cu shell.

Under CO_2 reduction conditions, the CuO was reduced to Cu and thus Ag@C@CuO became Ag@C@Cu. CO, C_2H_4, and ethanol are the three main products from CO_2 reduction on both Cu and Ag@C@Cu catalysts (Figure 3.5 and S10). In comparison with Cu, Ag@C@Cu (50 wt% Ag - 50 wt% Cu) showed bigger CO FEs but a smaller C_2H_4 and ethanol FEs in a potential range of -0.52 V to -0.64 V vs RHE. This indicated that the Ag core was indeed active for reducing CO_2 to CO. The CO molecules from
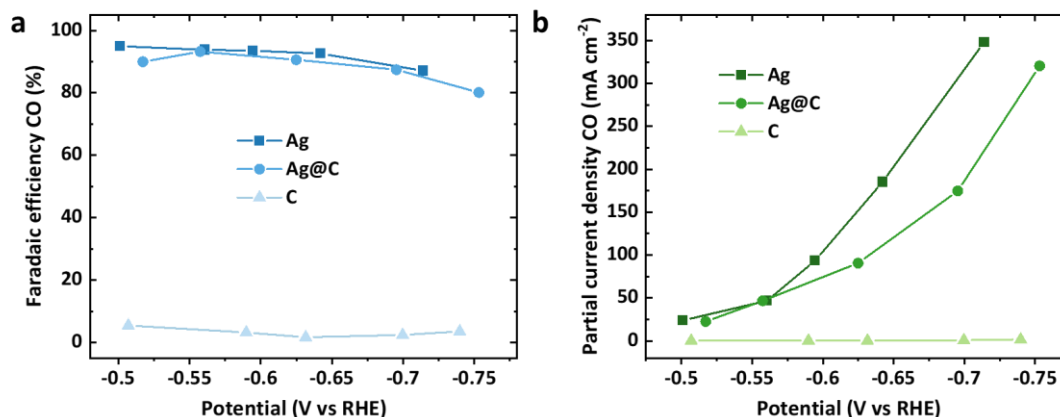
Figure 3.4 (a) Comparison of Faradaic efficiency (a) and partial current density (b) of CO at various potentials on Ag, Ag@C, and carbon nanoparticles.

Ag surface, however, were not completely captured and further reduced by the Cu shell in this condition. This, thus, caused the increase of CO FE, e.g., 18% to 49 % at -0.57 V vs RHE and the decrease of both C_2H_4 and ethanol correspondingly. The degrees of decrease of ethanol and C_2H_4 FE were similar at low overpotential (-0.52 V vs RHE) but were different significantly at higher overpotential (-0.64 V vs RHE), which made the ratio of ethanol FE to C_2H_4 FE on Ag@C@Cu bigger than that on Cu (Figure 3.5b). We estimated the CO production rate by assuming all C_{2+} products and CH_4 were derived from *CO intermediate and found that Ag@C@Cu produced CO with a higher rate than Cu (Figure S3.11), which confirmed the higher local concentration of CO on Ag@C@Cu than Cu. The higher local concentration increased the coverage of adsorbed *CO on the Cu surface, which further favored the bifurcation intermediates *CHCOH to be hydrogenated toward ethanol, rather than C_2H_4, as predicted by DFT calculation results from Sargent et al.[20, 21] Because no Ag-Cu interface existed in this Ag@C@Cu catalyst, this change in the ratio of ethanol FE to C_2H_4 FE must be ascribed only to the increased local CO concentration from the CO_2 reduction on Ag core – that is, the tandem effect. These results demonstrate that the tandem effect favors the production of ethanol more than C_2H_4 and thus has a potential to be used to improve the selectivity of ethanol.
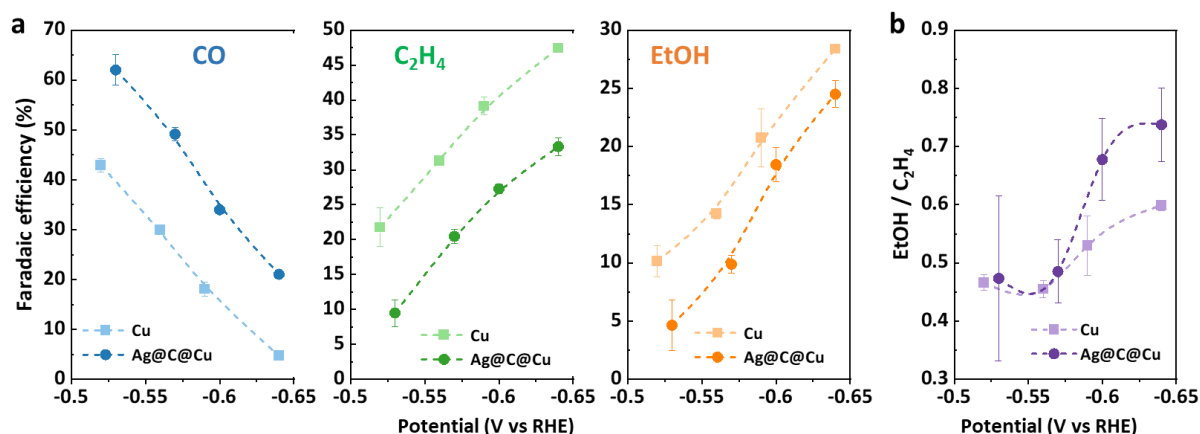
Figure 3.5 Comparison of Faradaic efficiencies of CO (a), C_2H_4 (b), and ethanol (c) from CO_2 reduction on C@Cu and Ag@C@Cu at various potentials in a flow cell with 1 M KOH. (d) Comparison of the ratios of ethanol FE to C_2H_4 FE on C@Cu and Ag@C@Cu.

58

We then investigated the effect of the Cu shell thickness on the selectivity of C_2H_4 and ethanol. The same Ag nanoparticles were used for all shell thickness, so the thickness of the Cu shell was controlled by the mass ratio of Ag to Cu. As shown in Figure 3.6a – e and Figure S3.12, with the mass ratios of Ag to Cu (Ag/Cu) increased from 0 to 1.0, the thickness of Cu shell decreased gradually. The FEs of CO, C_2H_4, and ethanol on Ag@C@Cu as a function of the Ag/Cu mass ratio are shown in Figure 3.6f. The CO FE increases with the increase of the Ag/Cu mass ratio, i.e., the decrease of the thickness of Cu shell, because thicker Cu shell not only captured the CO from Ag surface better than thinner Cu shell, but also made the relative amount of Ag decreased and thus decreased the CO production rate. While C_2H_4 FE decreased continually with the increase of Ag/Cu ratio, ethanol FE first increased from 28.2% to 31.5% and then decreased with the increase of the Ag/Cu mass ratio(Figure 3.6g). This results again demonstrate that the tandem effect favours the production of ethanol to C_2H_4.
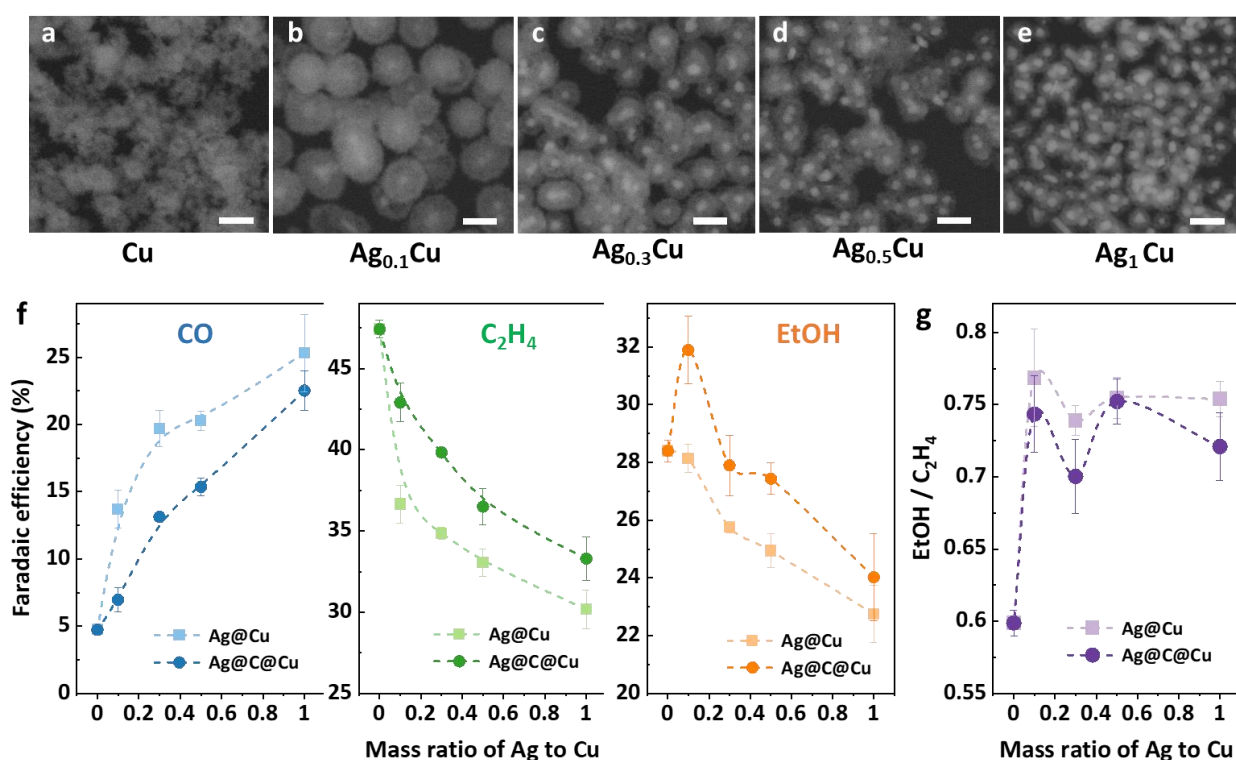
Figure 3.6 Backscattered electron images of the CuO (a) and Ag@CuO (b - e) with various thickness of CuO shell. The scale represents 200 nm. The mass ratios of Ag to Cu in the core-shell nanoparticles in (b – e) are 0.1, 0.3, 0.5, and 1.0, respectively. (f) Comparison of Faradaic efficiencies of CO (a), C_2H_4 (b), and ethanol (c) from CO_2 reduction on Ag@Cu and Ag@C@Cu with various mass ratio of Ag to Cu at -0.64 V vs RHE and 400 mA cm^{-2} in a flow cell with 1 M KOH. (g) Comparison of the ratios of ethanol FE to C_2H_4 FE on Ag@Cu and Ag@C@Cu.

To illustrate if the interface effect existed in the Ag@Cu nanoparticles for CO_2 reduction, we compared the FEs of CO, C_2H_4, and ethanol on Ag@Cu and Ag@C@Cu at various mass ratios of Ag to Cu (Figure 3.6f). Clearly, Ag@Cu always showed higher CO FEs and lower FEs of C_2H_4 and ethanol than Ag@C@Cu did. This difference was because Ag in Ag@Cu was more active in producing CO than the Ag in Ag@C@Cu as exhibited in Figure 3.4. This high activity for producing CO also resulted in higher ratio of ethanol FE to C_2H_4 FE on Ag@Cu than that on Ag@C@Cu (Figure 3.6g), further confirming that high local CO concentration favoured the production of ethanol more than C_2H_4. As the difference of

the product distribution on Ag@Cu and Ag@C@Cu was mainly derived from the different CO production rates on the Ag cores of Ag@Cu and Ag@C@Cu, Ag@Cu showed neglected interface effect for CO_2 reduction. This was because no Ag-Cu interface existed in the catalyst precursor Ag@CuO, and the Ag and Cu themselves were hard to form interface while in situ reducing CuO shell to Cu under CO_2 reduction, as eutectic Ag-Cu alloy even tends to gradually separate their two phases under CO_2 reduction.[22]

3.3 Conclusions

We have synthesized Ag@C@Cu core-shell nanoparticles that contains a carbon layer between Ag core and Cu shell to prevent the formation of the interface between Ag and Cu for electrochemical CO_2 reduction. CO_2 molecules can still pass through the middle carbon layer to access to and be reduced by the Ag core, so that only tandem effect for CO_2 reduction can exist in this Ag@C@Cu core-shell nanoparticles. We found that tandem effect on the Ag-Cu core-shell increases the selectivity of ethanol relative to C_2H_4 by increasing the CO coverage on the Cu surface. The ethanol selectivity on Ag@C@Cu can be optimized through tuning the thickness of the Cu shell. Our results reveal that the tandem effect in Ag-Cu bimetallic prefers to enhance the ethanol production rather than C_2H_4 production.

3.4 Acknowledgements

3.5 References

[1]   M.G. Kibria, J.P. Edwards, C.M. Gabardo, C.-T. Dinh, A. Seifitokaldani, D. Sinton, E.H. Sargent, Electrochemical CO_2 Reduction into Chemical Feedstocks: From Mechanistic Electrocatalysis Models to System Design, Advanced Materials, 31 (2019) 1807166.

[2]   D. Karapinar, C.E. Creissen, J.G. Rivera de la Cruz, M.W. Schreiber, M. Fontecave, Electrochemical CO_2 Reduction to Ethanol with Copper-Based Catalysts, ACS Energy Letters, 6 (2021) 694-706.

[3]   S. Nitopi, E. Bertheussen, S.B. Scott, X. Liu, A.K. Engstfeld, S. Horch, B. Seger, I.E.L. Stephens, K. Chan, C. Hahn, J.K. Nørskov, T.F. Jaramillo, I. Chorkendorff, Progress and Perspectives of Electrochemical CO_2 Reduction on Copper in Aqueous Electrolyte, Chemical Reviews, 119 (2019) 7610-7672.

[4]   W. Luo, W. Xie, R. Mutschler, E. Oveisi, G.L. De Gregorio, R. Buonsanti, A. Züttel, Selective and Stable Electroreduction of CO_2 to CO at the Copper/Indium Interface, ACS Catalysis, 8 (2018) 6571-6581.

[5]   W. Luo, J. Zhang, M. Li, A. Züttel, Boosting CO Production in Electrocatalytic CO_2 Reduction on Highly Porous Zn Catalysts, ACS Catalysis, 9 (2019) 3783-3791.

[6]   T.K. Todorova, M.W. Schreiber, M. Fontecave, Mechanistic Understanding of CO_2 Reduction Reaction (CO_2RR) Toward Multicarbon Products by Heterogeneous Copper-Based Catalysts, Acs Catalysis, 10 (2020) 1754-1768.

[7]   K.P. Kuhl, E.R. Cave, D.N. Abram, T.F. Jaramillo, New insights into the electrochemical reduction of carbon dioxide on metallic copper surfaces, Energy & Environmental Science, 5 (2012) 7050-7059.

[8]   J. Zhang, W. Luo, A. Züttel, Self-supported copper-based gas diffusion electrodes for CO_2 electrochemical reduction, Journal of Materials Chemistry A, 7 (2019) 26285-26292.

[9]   J. Zhang, W. Luo, A. Züttel, Crossover of liquid products from electrochemical CO_2 reduction through gas diffusion electrode and anion exchange membrane, Journal of Catalysis, 385 (2020) 140-145.

[10]   C.G. Morales-Guio, E.R. Cave, S.A. Nitopi, J.T. Feaster, L. Wang, K.P. Kuhl, A. Jackson, N.C. Johnson, D.N. Abram, T. Hatsukade, C. Hahn, T.F. Jaramillo, Improved CO_2 reduction activity towards C_{2+} alcohols on a tandem gold on copper electrocatalyst, Nature Catalysis, 1 (2018) 764-771.

[11]   J. Huang, M. Mensi, E. Oveisi, V. Mantella, R. Buonsanti, Structural Sensitivities in Bimetallic Catalysts for Electrochemical CO_2 Reduction Revealed by Ag–Cu Nanodimers, Journal of the American Chemical Society, 141 (2019) 2490-2499.

[12]   D. Ren, J. Gao, L. Pan, Z. Wang, J. Luo, S.M. Zakeeruddin, A. Hagfeldt, M. Grätzel, Atomic Layer Deposition of ZnO on CuO Enables Selective and Efficient Electroreduction of Carbon Dioxide to Liquid Fuels, Angewandte Chemie International Edition, 58 (2019) 15036-15040.

[13]   Y.C. Li, Z. Wang, T. Yuan, D.-H. Nam, M. Luo, J. Wicks, B. Chen, J. Li, F. Li, F.P.G. de Arquer, Y. Wang, C.-T. Dinh, O. Voznyy, D. Sinton, E.H. Sargent, Binding Site Diversity Promotes CO_2 Electroreduction to Ethanol, Journal of the American Chemical Society, 141 (2019) 8584-8591.

[14]   S. Lee, G. Park, J. Lee, Importance of Ag–Cu Biphasic Boundaries for Selective Electrochemical Reduction of CO_2 to Ethanol, ACS Catalysis, 7 (2017) 8594-8604.

[15]   J. Wang, Z. Li, C. Dong, Y. Feng, J. Yang, H. Liu, X. Du, Silver/Copper Interface for Relay Electroreduction of Carbon Dioxide to Ethylene, ACS Applied Materials & Interfaces, 11 (2019) 2763-2767.

[16]   J. Gao, H. Zhang, X. Guo, J. Luo, S.M. Zakeeruddin, D. Ren, M. Grätzel, Selective C–C Coupling in Carbon Dioxide Electroreduction via Efficient Spillover of Intermediates As Supported by Operando Raman Spectroscopy, Journal of the American Chemical Society, 141 (2019) 18704-18714.

[17]   A.N. Kuhn, H. Zhao, U.O. Nwabara, X. Lu, M. Liu, Y.-T. Pan, W. Zhu, P.J.A. Kenis, H. Yang, Engineering Silver-Enriched Copper Core-Shell Electrocatalysts to Enhance the Production of Ethylene and C_{2+} Chemicals from Carbon Dioxide at Low Cell Potentials, Advanced Functional Materials, n/a (2021) 2101668.

[18]   X. Feng, K. Jiang, S. Fan, M.W. Kanan, A Direct Grain-Boundary-Activity Correlation for CO Electroreduction on Cu Nanoparticles, ACS Central Science, 2 (2016) 169-174.

[19]   Q. Lei, H. Zhu, K. Song, N. Wei, L. Liu, D. Zhang, J. Yin, X. Dong, K. Yao, N. Wang, X. Li, B. Davaasuren, J. Wang, Y. Han, Investigating the Origin of Enhanced C_{2+} Selectivity in Oxide-/Hydroxide-Derived Copper Electrodes during CO_2 Electroreduction, Journal of the American Chemical Society, 142 (2020) 4213-4222.

[20]   F. Li, Y.C. Li, Z. Wang, J. Li, D.-H. Nam, Y. Lum, M. Luo, X. Wang, A. Ozden, S.-F. Hung, B. Chen, Y. Wang, J. Wicks, Y. Xu, Y. Li, C.M. Gabardo, C.-T. Dinh, Y. Wang, T.-T. Zhuang, D. Sinton, E.H. Sargent, Cooperative CO_2-to-ethanol conversion via enriched intermediates at molecule–metal catalyst interfaces, Nature Catalysis, 3 (2020) 75-82.

[21]   J. Li, Z. Wang, C. McCallum, Y. Xu, F. Li, Y. Wang, C.M. Gabardo, C.-T. Dinh, T.-T. Zhuang, L. Wang, J.Y. Howe, Y. Ren, E.H. Sargent, D. Sinton, Constraining CO coverage on copper promotes high-efficiency ethylene electroproduction, Nature Catalysis, 2 (2019) 1124-1131.

[22]   C. Yang, H. Ko Byung, S. Hwang, Z. Liu, Y. Yao, W. Luc, M. Cui, S. Malkani Arnav, T. Li, X. Wang, J. Dai, B. Xu, G. Wang, D. Su, F. Jiao, L. Hu, Overcoming immiscibility toward bimetallic catalyst library, Science Advances, 6 eaaz6844.

3.6   Supporting information

Experimental methods

Chemicals

Silver nitrate (AgNO$_3$, > 99.0%), L-glucose, polyvinylpyrrolidone (PVP, 5 5000), tetraethoxysilane (TEOS), nitric acid (HNO$_3$), hydrazine (N$_2$H$_4$, 35wt% aqueous solution), and deuterium (D$_2$O) were ordered from Sigma-Aldrich. NaOH was ordered from Reactolab S.A. and KOH from Carl Roth GmbH & Co KG. MiliQ water (18MΩ) were used to prepare electrolyte and rinse the electrode.

Synthesis of Ag nanoparticles

Silver nanoparticles were synthesized by reducing silver ions with glucose in aqueous solution with the PVP as the surfactant. [1] Firstly, the aqueous solution (180 ml) containing glucose (9 g) and PVP (4.5g, MW = 55000) was heated to 90 ^{o}C in a round-bottom flask with a silicon oil bath and kept at 90 ^{o}C for 45 min under stirring and refluxing in air. Then the aqueous solution of AgNO$_3$ (2.272 M, 10.5 ml) was quickly injected into the above solution. The solution stayed at 90 ^{o}C for 60 min and then cooled with an ice bath. The reaction took place under the ambient light exposure. The produced dispersion was precipitated by centrifugation and then washed twice by water. The centrifugation (20 min, 25 160 g) was used to collect the nanoparticles. Finally, the Ag nanoparticles were dispersed in water and stored in fridge (5 ^{o}C) under dark for further use.

Synthesis of Ag@C core-shell

Ag@C was synthesized by carbonizing a polymer wrapping on the Ag nanoparticles. To prevent the particle sintered together during carbonization, a silica layer was grown on the polymer shell before carbonization.

Ag nanoparticles were firstly coated by a layer of polydopamine through polymerizing the free-dopamine on the Ag nanoparticles.[2] The free-dopamine was provided by Shuliang Yang who synthesized it with the method described in his previous work.[2] Ag (average size of 50nm, 11.1 mg) nanoparticles was precipitated by adding 20 ml of acetone into 9 ml of Ag nanoparticle dispersion and then centrifuging at 7830 rpm for 10 min. The Ag nanoparticles were re-dispersed in ethanol (60 ml). 24 mg of free-dopamine was added into the dispersion, which was then sonicated for 20 s to quickly dissolve the dopamine. The dispersion was stirred for 12 h with the cover of the container having a hole open to air. The product, Ag@DPA, was precipitated by centrifugation, washed twice with ethanol, and finally dispersed in 60 ml of ethanol.

Ag@PDA was further coated by SiO$_2$ through the hydrolysis of tetraethoxysilane (TEOS). 2.27 ml of water and 0.9 ml of ammonia (28wt%) aqueous solution were added into the dispersion (60 ml) of Ag@PDA in ethanol. Then 120 ul of TEOS were added into the dispersion under stirring. The dispersion was then stirred for 12 h at room temperature. The product denoted as Ag@PDA@SiO$_2$ was centrifuged, washed twice with ethanol, and finally dried under vacuum at 90 ^{o}C.

The Ag@PDA@SiO$_2$ was annealed at 700 ^{o}C for 1h under nitrogen in a tube furnace, which was heated to 700 ^{o}C from room temperature by 5 ^{o}C min^{-1}. Then the temperature cooled down naturally

to room temperature. After the PDA layer in Ag@PDA@SiO$_2$ was carbonized, the Ag@C@SiO$_2$ was obtained.

To remove the SiO$_2$ layer, the Ag@C@SiO$_2$ was dispersed (0.67 mg nanoparticles per milliliter) in an aqueous solution consisting of NaOH (5 mM) and dimethylamine (50 mM). The dispersion was then refluxed at 70 °C for 1 hour under the protection of nitrogen. The dispersion was washed twice with ethanol and collected by centrifugation at 7830 rpm and the final product, Ag@C, was dispersed in ethanol.

Synthesis of Ag@C@CuO and Ag@CuO

Ag@C was coated with PVP in order to improve its hydrophilic. 3 ml of Ag@C (1.72mg in EtOH) was dispersed in 28.76 ml of PVP solution (10wt%) in ethanol. The dispersion was sonicated for 10 min and then stirred for 10 hours at room temperature. The PVP-coated AgC was precipitated by centrifugation at 7830 rpm for 30 min and washed twice with ethanol and finally dispersed in 3 ml of water and denoted as Ag@C@PVP.

Ag@C@PVP and Ag nanoparticles were coated by a layer of Cu$_2$O with a controllable thickness by precipitation of Cu(OH)$_2$, which was then reduced by ascorbic acid. First, 5 mg, 2.5 mg, 1.7 mg, or 0.5 mg of Ag nanoparticles or Ag@C nanoparticles (equivalent Ag amount) were dispersed in 30 ml of PVP (0.2wt%) aqueous solution. Then 39 ul of Cu(NO$_3$)$_2$ (2 M) and 115.5 ul of NH$_4$NO$_3$ (2.5 M) were added into the dispersion. After stirring for 5 min, 1.32 ml of NaOH solution (0.2 M) were dropped into the dispersion with a rate of 1.2 ml min^{-2} controlled with a peristaltic pump. After stirring for 2 min, 2.31 ml of ascorbic acid solution (0.1 M) were dropped into the dispersion with a rate of 0.4 ml min^{-2}. After stirring for 1 min, the nanoparticles in the dispersion was precipitated by centrifugation, washed twice with ethanol, and finally dispersed in 3.87 ml of ethanol.

The Cu$_2$O layer on Ag@C @Cu$_2$O and Ag@Cu$_2$O was oxidized by the oxygen in air with the help of NH$_3$ H$_2$O in order to make the copper oxide layer porous and at the same time increase the density of the grain boundaries in it, which was able to enhance the selectivity C$_{2+}$ products. 25 ul of NH$_3$ H$_2$O aqueous solution (28wt%) was dropped into the 250 ul of Ag@Cu$_2$O or Ag@C@PVP@Cu$_2$O dispersion under stirring. The dispersion was stirred for another 10 min with the cap of the container having a hole open to air. The nanoparticles in the dispersion was precipitated by centrifugation, washed twice with ethanol, and finally dispersed in ethanol for further use. The final products were denoted as Ag@CuO and Ag@C@CuO, respectively.

Electrochemical CO$_2$ Reduction

The gas diffusion electrodes were prepared by first dropping-casting the ink of the catalysts on the carbon paper (YLS-30T, 1.2 cm^2). To make the geometric activity of CuO and Ag-Cu bimetallic nanoparticles similar, the loading of the CuO was 100 ug cm^{-2} and the loading of Ag@C@CuO and Ag@CuO was 50 ug cm^{-2}. Then 15 ul of nafion solution (0.035 wt%) in isopropanol was drop-casted on the catalyst layer.

The electrochemical measurements were conducted in a flow cell with the same setup as that described in our previous work.[3] The operation protocol and quantification of products were also described in our previous work.[3]

Characterization of the materials

The scanning electron microscope (SEM, FEI Teneo) used to observe the morphology and elemental contrast in the nanoparticles. High resolution transmission electron microscopy (TEM) images and Scanning TEM (STEM) EDX elemental mapping were obtained by using FEI Tecnai Osiris 200 KV. The concentration of Ag and Cu in the catalyst ink was determined by the analysis of inductively coupled plasma optical emission spectrometry (ICP-OES, Agilent 5110).

References

[1]   S. Banerjee, K. Loza, W. Meyer-Zaika, O. Prymak, M. Epple, Structural Evolution of Silver Nanoparticles during Wet-Chemical Synthesis, Chemistry of Materials, 26 (2014) 951-957.
[2]   S. Yang, L. Peng, D.T. Sun, M. Asgari, E. Oveisi, O. Trukhina, S. Bulut, A. Jamali, W.L. Queen, A new post-synthetic polymerization strategy makes metal–organic frameworks more stable, Chemical Science, 10 (2019) 4542-4549.
[3]   J. Zhang, W. Luo, A. Züttel, Crossover of liquid products from electrochemical CO_2 reduction through gas diffusion electrode and anion exchange membrane, Journal of Catalysis, 385 (2020) 140-145.
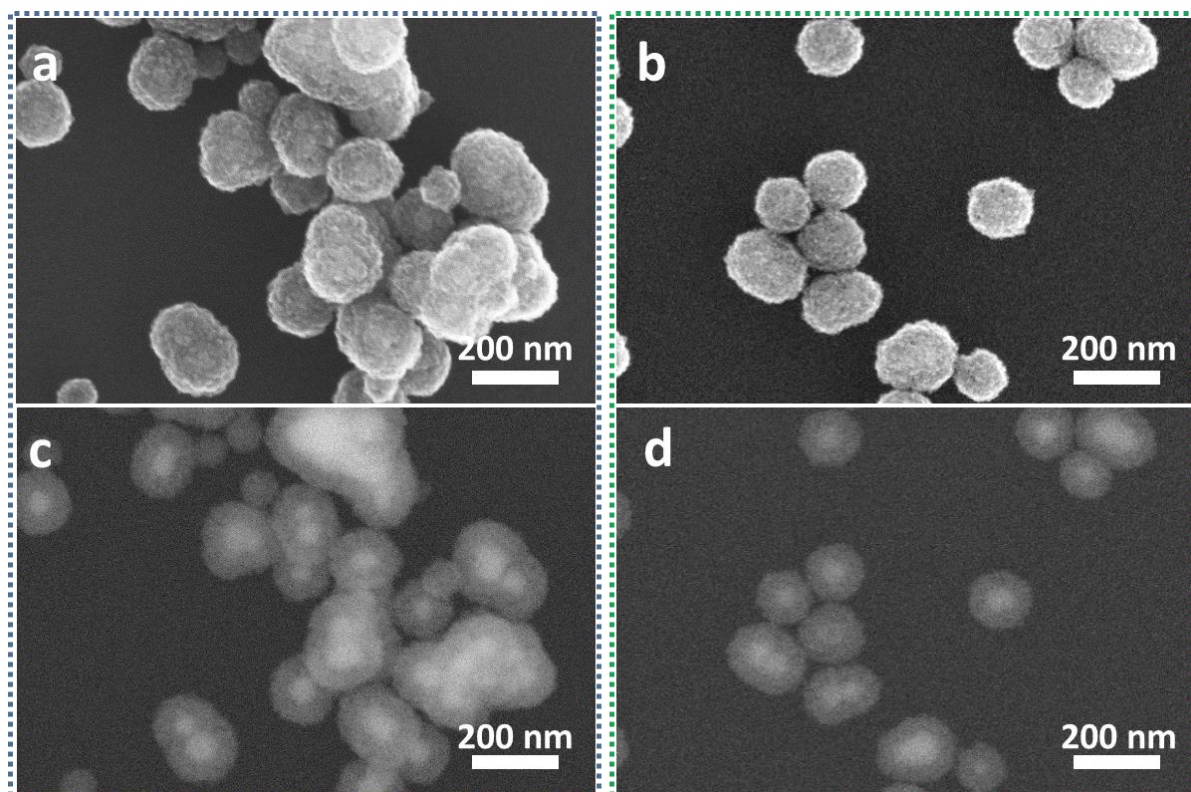
Figure S3.1 SEM and BSE images of Ag@Cu$_2$O core-shell nanoparticles as precursors for random mixture of Ag-Cu (a, c) and core-shell Ag-Cu (b, d). (c, d) were obtained mainly from the backscattered electrons and thus showed the elemental contrast. Ascorbic acid was used as the reducer to synthesize (a, c) and (b, d) with (NH$_4$)$_2$SO$_4$ and (NH$_4$)$_2$NO$_3$, respectively.
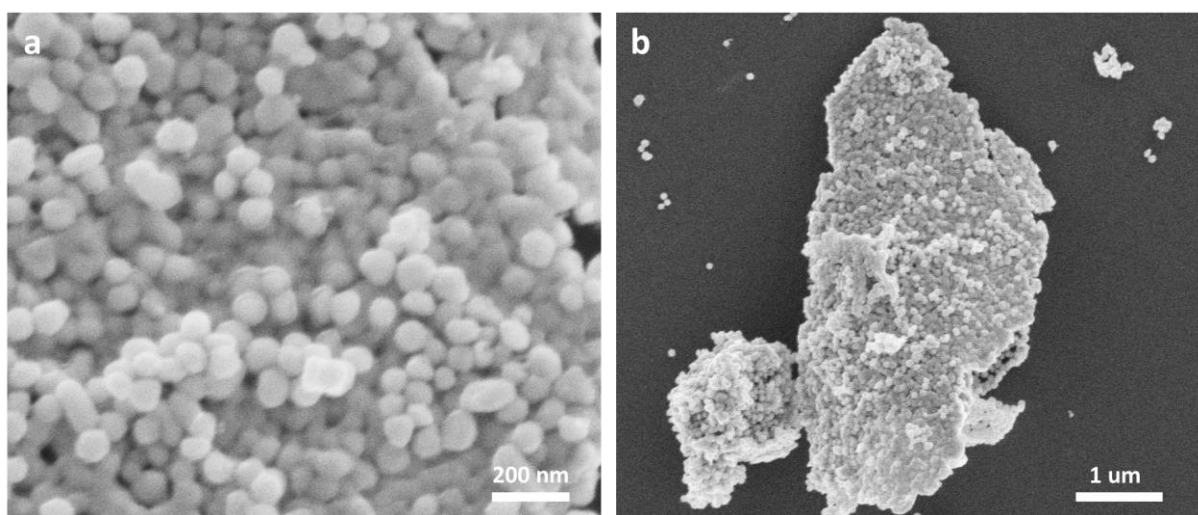
Figure S3.2 SEM images of the Ag@C core-shell nanoparticles synthesized without the protection of SiO$_2$ layer
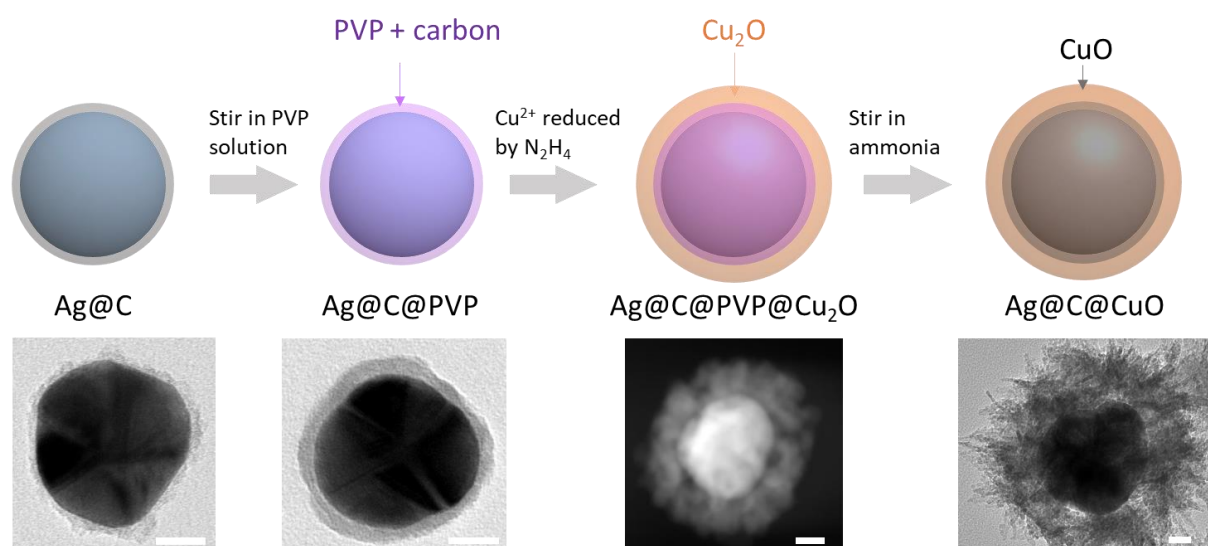
Figure S3.3 Schematics for synthesis procedure of Ag@C@Cu core-shell nanoparticles and the corresponding TEM images of the single particle in each step. Scale bar represents 20 nm.
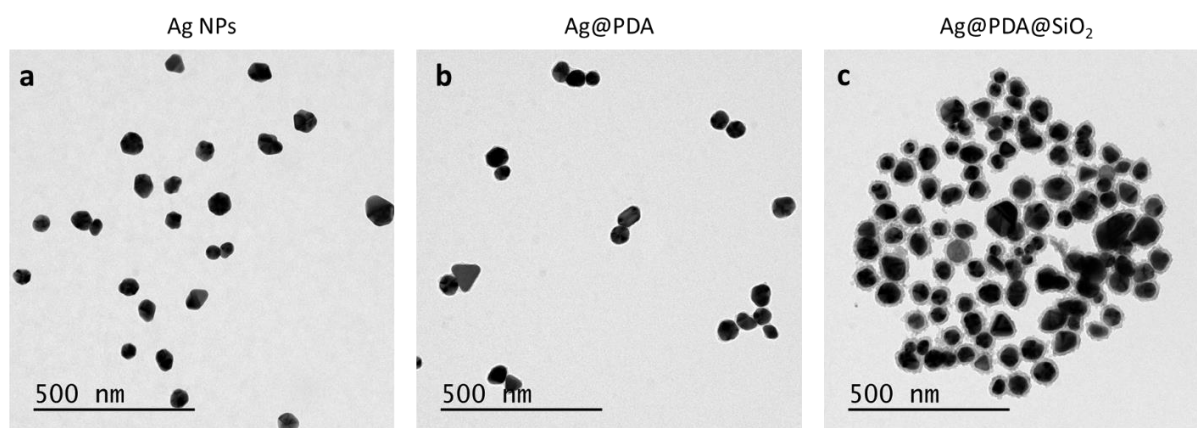
Figure S3.4 TEM images of the as-prepared Ag nanoparticles (NPs) (a), Ag@PDA core-shell nanoparticles (b), and Ag@PDA@SiO$_2$ core-shell nanoparticles (c).
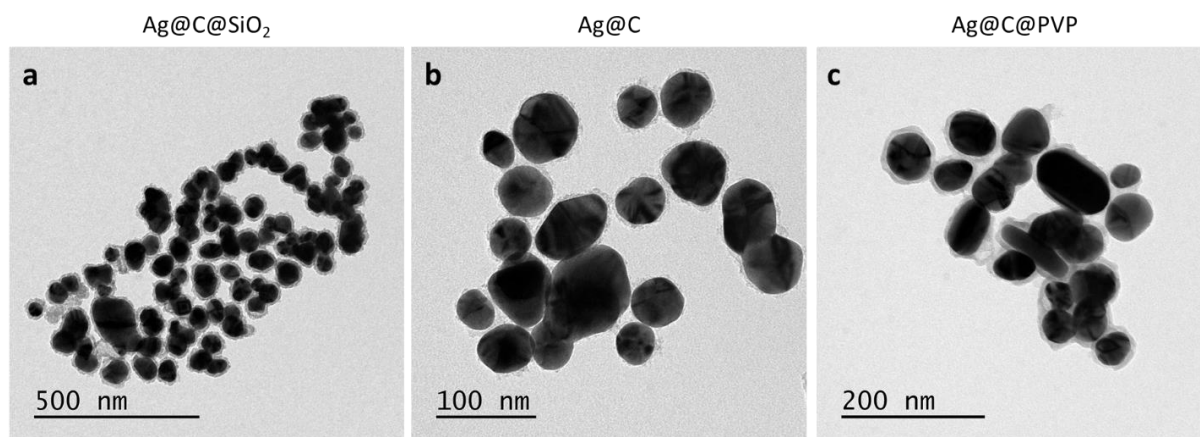
Figure S3.5 TEM images of the Ag@C@SiO$_2$ (a), Ag@C (d), and Ag@C@PVP (c) core-shell nanoparticles.
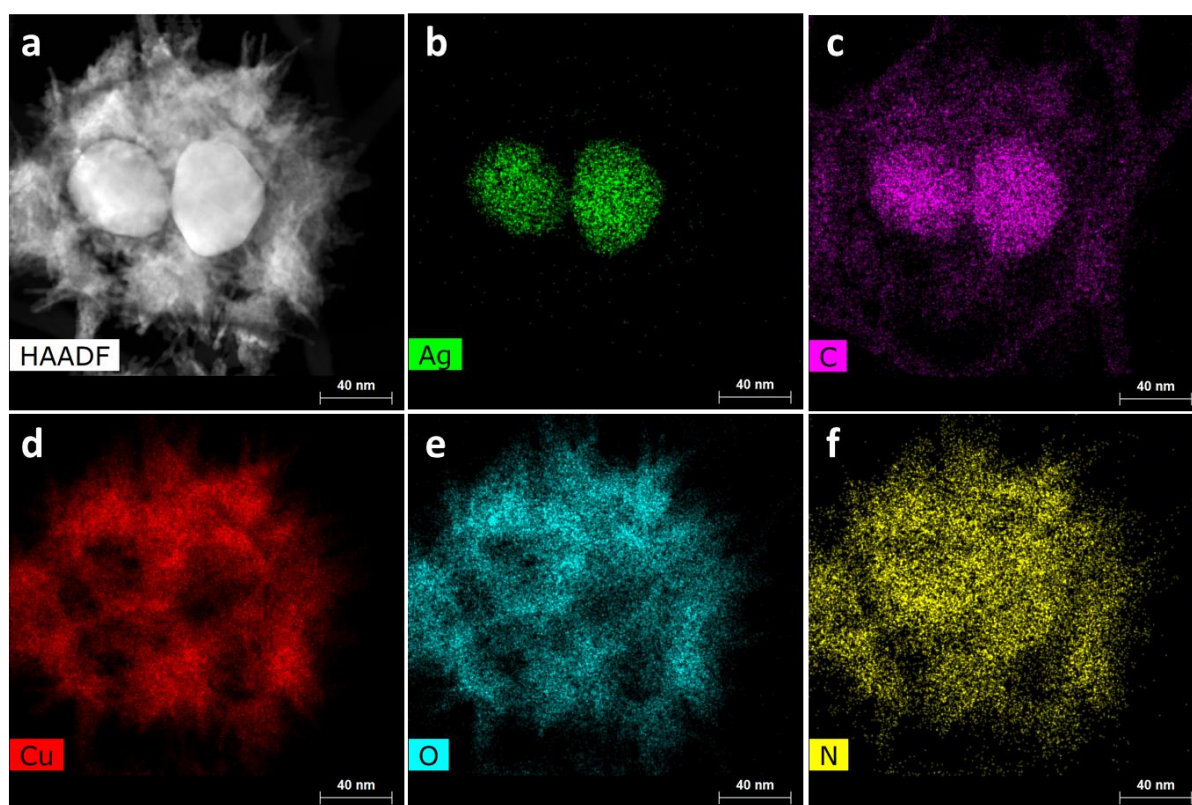
Figure S3.6 STEM images (a) of Ag@C@CuO core-shell nanoparticles and the corresponding EDX elemental map of Ag (b), C (c), Cu (d), O (e), N (f).
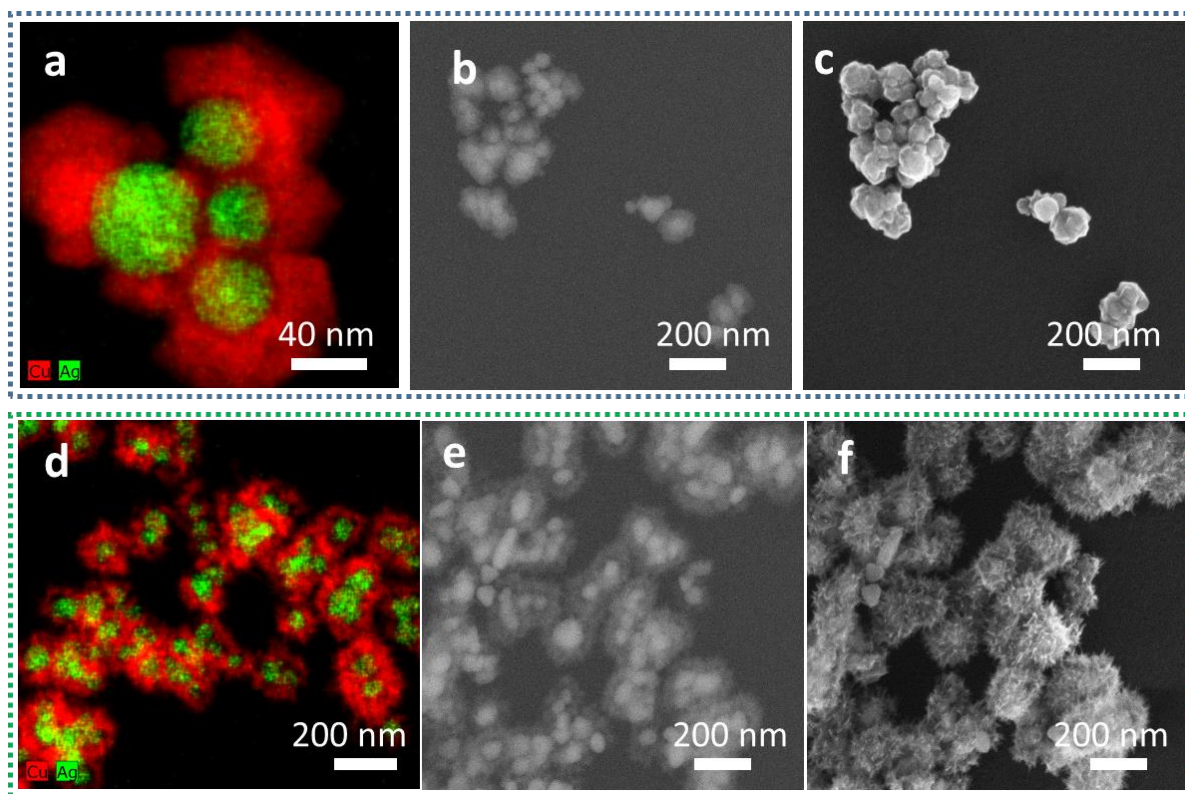
Figure S3.7 EDX elemental maps and SEM images of the Ag@C@PVP@Cu$_2$O (a, b, c) and Ag@C@CuO (d, e, f). (a, c) obtained from the backscattered electrons, and (c, d) from the secondary electrons.
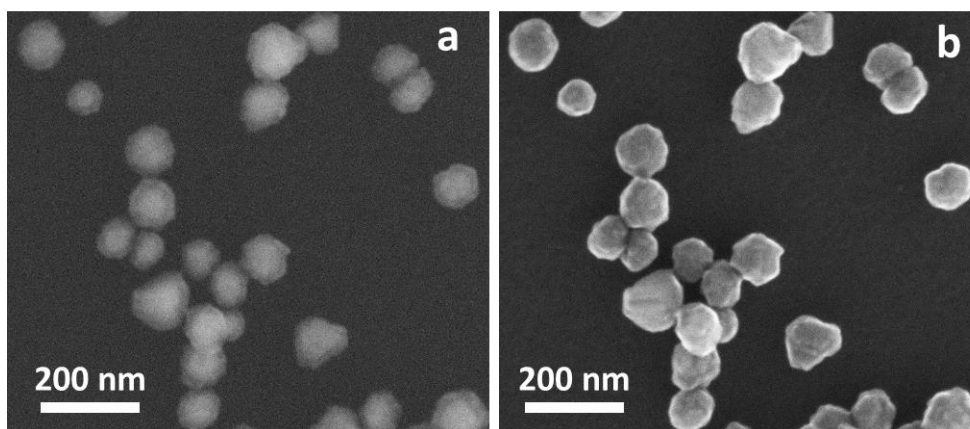
Figure S3.8 SEM images of the Ag@Cu$_2$O.). (a) obtained from the backscattered electrons, and (b) from the secondary electrons.
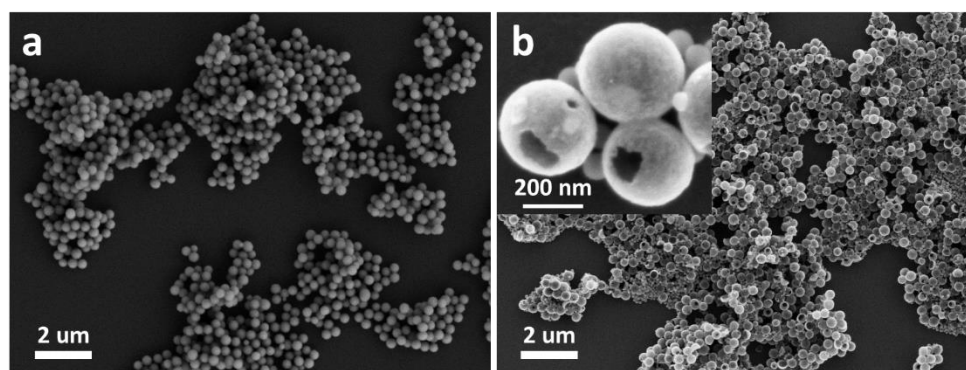
Figure S3.9 SEM images of SiO_2@PDA core-shell nanoparticles (a) and carbon sphere particles (b).
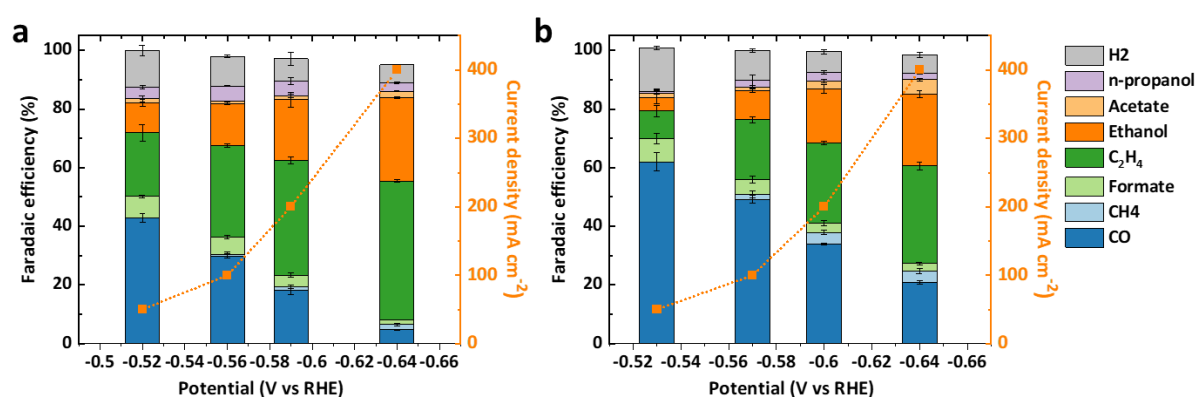
Figure S3.10 Faradaic efficiencies of the products from CO_2 reduction on CuO (a) and Ag@C@CuO (b) and the corresponding total current densities as a function of the potential. The electrolyte is 1 M KOH in a flow cell.
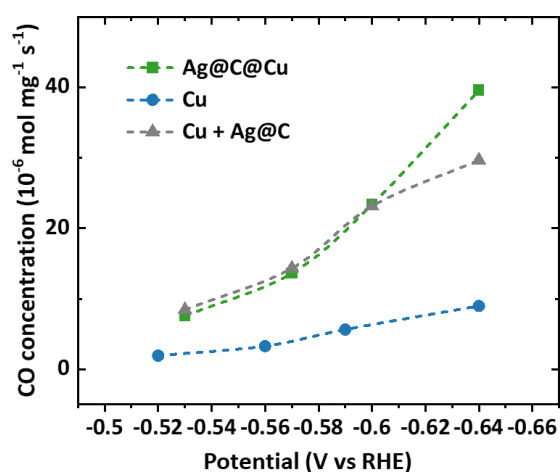
Figure S3.11 Calculated CO production rate by assuming all C_{2+} products and CH_4 derived from *CO intermediate. The gray line is from the sum of the CO production rate on Cu and on Ag@C (Figure 3.4b in the main text) at the same potential.
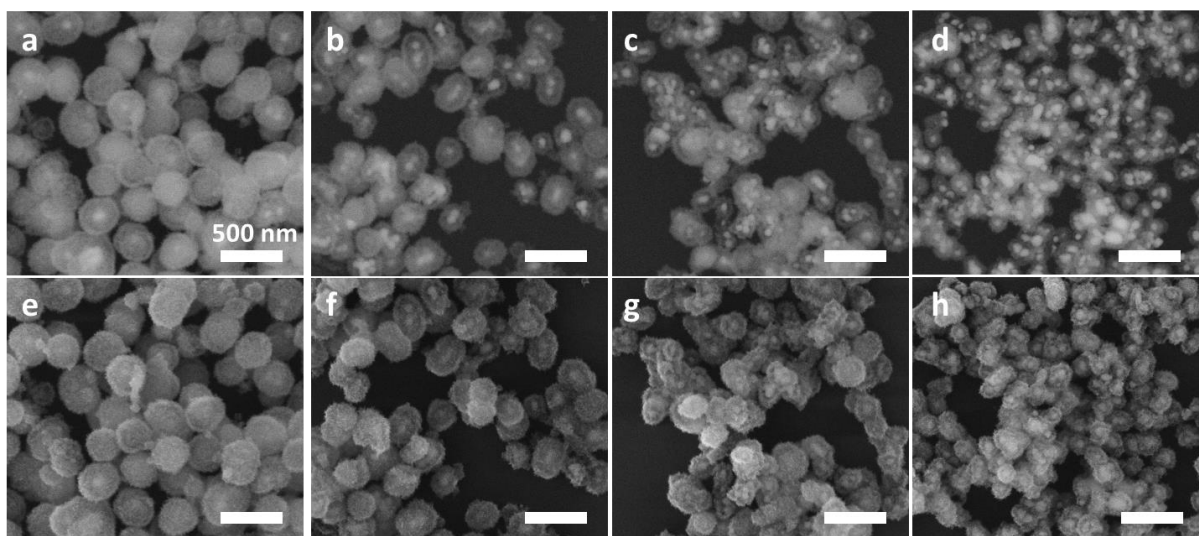
Figure S3.12 Backscattered electrons (a - d) and the corresponding SEM (e - h) images of Ag@C@CuO with various thickness of CuO shell. The scale represents 500 nm. The mass ratios of Ag to Cu in the core-shell nanoparticles in (a - b) are 0.1, 0.3, 0.5, and 1.0 respectively.

Chapter 4 Self-Supported Copper-Based Gas Diffusion Electrodes

Jie Zhang[a,b], Wen Luo[a,b] *, and Andreas Züttel[a,b]

Abstract

Nanostructured copper materials are catalytically active for the electrochemical reduction of CO_2 (eCO_2RR) to produce hydrocarbons. However, most of these catalysts were investigated in conventional batch reactors at low current densities (< 50 mA cm^{-2}) due to the limit of mass transport. Herein, a nondestructive strategy is proposed to transform nanostructured Cu catalysts into self-supported gas diffusion electrodes (GDEs), which enables us to evaluate the CO_2 reduction performance in flow cell at high current densities (up to 300 mA cm^{-2}). Two typical self-supported GDEs were prepared through simply coating a hydrophobic microporous layer onto the Cu_xO nanowires grown on Cu gauzes. Both GDEs show high selectivity (> 40%) for converting CO_2 to multi-carbon products, e.g. C_2H_4 and ethanol, at the commercial relevant current densities (> 100 mA cm^{-2}) and low overpotential (η < 0.65 V). The GDEs are stable for more than 6 hours at the current densities higher than 100 mA cm^{-2}. Moreover, the nondestructive method allows us to directly compare the product distributions of the nanostructured Cu catalysts in batch reactor and flow reactor and to demonstrate the influence of the reaction environment and mass transport on eCO_2RR. While eCO_2RR in the H-cell shows high selectivity towards CO and formate, the reaction in the flow cell delivers a greater amount of multi-carbon products due to the fast CO_2 diffusion and high pH. Combined, the electrode design strategies and the experimental findings presented in this work are valuable for the development of other self-supported electrodes for practical applications.

[a] *Laboratory of Materials for Renewable Energy (LMER), Institute of Chemical Sciences and Engineering (ISIC), Basic Science Faculty (SB), École Polytechnique Fedérale de Lausanne (EPFL) Valais/Wallis, Energypolis, Rue de l'Industrie 17, CH-1951 Sion, Switzerland.*
[b] *Empa Materials Science & Technology, CH-8600 Dübendorf, Switzerland*

Author Contributions: Jie Zhang, Wen Luo, and Andreas Züttel conceived the experiments and co-wrote the manuscript. Jie Zhang designed and performed the experiment.

4.1   Introduction

Electrochemical reduction of carbon dioxide (eCO$_2$RR), using renewably generated electricity, is a promising strategy to produce valuable chemicals and liquid fuels.[1, 2] Under aqueous conditions, this process can generate a wide range of products, including carbon monoxide (CO), formic acid (HCOOH), methane (CH$_4$), ethylene (C$_2$H$_4$), ethanol (C$_2$H$_5$OH) and so on.[1, 3-6] However, due to the high stability of CO$_2$, large overpotentials are required for CO$_2$ reduction to outcompete H$_2$O reduction. Thus, to realize an energetic efficient eCO$_2$RR process, it is essential to develop advanced electrocatalysts.

To date, Cu is the only monometallic catalyst that can reduce CO$_2$ into multi-carbon (C$_{2+}$) products with a significant selectivity.[4, 7] Although both polycrystalline and single crystal Cu have been applied for studying the structure-property relationships and CO$_2$ reduction pathways, their surface area hinders them from larger-scale eCO$_2$RR applications.[4, 7, 8] In recent years, much effort has been devoted to developing new nanostructured Cu catalysts, aiming to increase the density of active sites and the intrinsic activity and ultimately to improve the eCO$_2$RR performance.[7, 9, 10] Among those nanostructured catalysts, oxide-derived Cu materials have shown great potential due to their facile synthesis method, tuneable properties and promising catalytic performance.[5, 11-14] For instance, Kanan and co-workers showed that oxidized Cu foil with a thick oxide layer could be reduced to nano-crystallized Cu that exhibits a high density of grain boundaries and high selectivity toward CO and formate.[5] Raciti et al. prepared highly dense Cu oxide (Cu$_x$O) nanowires through a thermal annealing method and found that the catalyst reduces CO$_2$ to CO at low overpotentials with a Faradaic efficiency (FE) of ~ 60%.[11] Additionally, Cu foil oxidized by O$_2$ plasma showed excellent selectivity for CO$_2$ reduction to C$_2$H$_4$ (~ 60% FE).[14] However, all of these performances were evaluated at low-current densities (< 50 mA cm^{-2}) in batch reactor systems, which are hardly scaled up for commercialization.

Apart from the catalyst, the reaction environment and the reactor design also play an important role in determining the activity and selectivity of the reaction.[2, 7, 15] To date, most reported catalysts (e.g., oxide-derived Cu catalysts) have been evaluated in classical H-cell configurations (Scheme 4.1b) using a neutral-pH electrolyte (i.e., 0.1 M KHCO$_3$), where current densities were limited to a few dozen mA cm^{-2}.[5, 11, 14] To evaluate the catalytic performance under industrially relevant conditions, measurement should be carried out in a reaction system capable of achieving high current densities (> 100 mA cm^{-2}), for example, a flow-cell reactor (Scheme 4.1c).[16-18] In such a reactor, the catalyst has to be incorporated into a gas diffusion electrode (GDE) configuration to provide a gas-electrolyte-catalyst interface for the reaction taking place. However, this is not straightforward for oxide-derived Cu catalysts synthesized from bulk Cu oxidation, as they are gas impermeable and the oxidation layer is difficult to be transferred onto the gas diffusion layer (e.g., carbon paper) to prepare a GDE.[5, 12]

In this work, we developed a new strategy to directly transform oxide-derived Cu catalysts into self-supported GDEs, which allowed us to examine their catalytic properties for eCO$_2$RR at a current density of up to 300 mA cm^{-2}. Two types of oxidized Cu with nanowires were first grown on Cu gauzes that were then coated with a microporous layer to form self-supported GDEs. These GDEs exhibited high selectivity (> 40% FE) for C$_{2+}$ products at a potential of around −0.6 V compared to a reversible hydrogen electrode (RHE) and maintained their activity and selectivity for more than 6 hours at > 100 mA cm^{-2}. Furthermore, we found significant differences in the activity and selectivity of the catalyst

when tested in an H-cell vs. a flow cell, highlighting the importance of evaluating eCO_2RR catalysts under commercially-relevant conditions.

4.2 Materials and methods

Chemicals

Sodium hydroxide (NaOH, 98%), ammonium persulfate ((NH_4)S_2O_8, 98%), and Polytetrafluoroethylene (PTFE) dispersion (60wt%) were purchased from Sigma-Aldrich. Potassium bicarbonate ($KHCO_3$, 99.5%) and potassium hydroxide (KOH, 50wt% of solution) were purchased from Carl Roth. Cu gauze (200 mesh, 99.99%) was purchased from Jiangxi Copper Corporation limited. Carbon black (Vulcan XC 72R) was purchased from Fuel Cell Store. All of the chemicals were used without purification. Carbon dioxide (99.998%) was purchased from Carbagas. Deionized water (18.2 MΩ) was produced by a Milipore system.

Preparation of the Cu_xO nanowires

The Cu oxide nanowires were prepared on Cu gauze using two methods: wet chemical oxidation[13, 19] and thermally annealing.[11] The Cu gauze was firstly cleaned by sonication in acetone and water. For the wet chemical oxidation, the clean Cu gauze (10 mm x 30 mm) was immersed in a solution (12 mL) of 2.5 M NaOH and 0.125 M (NH_4)S_2O_8 for 10 min. After being rinsed with H_2O and dried with N_2 flow, the oxidized Cu gauze was then immersed in the 10 wt% of PTFE dispersion for 10 s and dried. The amount of the PTFE attached on the electrode is 2.78 (± 0.26) wt% or 3.59 (± 3.10) mg cm^{-2}. The obtained material is designated as WCO-Cu. To synthesize thermally annealed Cu nanowires (TA-Cu), the cleaned Cu gauze was annealed in a muffle furnace at 500 ℃ for 6 hours in air.

Preparation of the GDEs

The coating ink consists of 5 mg mL^{-1} carbon black particles (50 nm) and 5 mg mL^{-1} PTFE particles (50 nm) in a mixture solvent of isopropanol and water with a volume ratio of 3:1. This ink was air-brushed onto one side of the oxidized Cu gauze to form the gas diffusion layer. The loading of the mixture was 8.65 ± 0.50 mg cm^{-2}, measured using a high-precision microbalance. The electrodes were then annealed in the muffle furnace at 350 ℃ for 1 hour to obtain the final self-supported GDEs.

Electrochemical measurements

Two electrochemical cells were used in this work. The flow cell reactor, shown in Scheme 4.1C, consists of three chambers: a CO_2 chamber, catholyte chamber, and anolyte chamber. An anion exchange membrane was inserted between the catholyte and anolyte to prevent the liquid products from diffusing to the anode and being oxidized there. The catholyte chamber was a 3-mm-thick PTFE spacer with a precisely machined window of 5 mm wide and 10 mm long. The anolyte chamber was a 5-mm-thick PTFE spacer with the same size of window as the catholyte chamber. The geometric area of the working electrode in the flow cell is 0.5 cm^{-2}, which is determined by the size of opening in the catholyte chamber. An Ag/AgCl (3 M KCl) reference electrode was connected at the upstream of the catholyte flow. The counter electrode was a platinum plate. The GDEs were evaluated in the flow cell using constant current mode controlled by a galvanostat (Autolab PGSTAT302N). The FEs and potential at each current density were repeatedly measured on three electrodes from three different batches. Before each measurement, the electrode was firstly reduced at 50 mA cm^{-2} until the potential

decreased to a constant value. During the stability test, salt accumulation on the GDE presented a technical challenge associated with CO_2 electrolysis in the flow cell, especially when a strong base (e.g., KOH) is used as the catholyte; thus, the electrode was washed every 1 hours with clean water.[17, 20]

The H-cell (Scheme 4.1b) was made from PTFE and consisted of two compartments separated by a Nafion membrane. Each chamber had dimensions of 15 by 20 by 30 mm. The catholyte chamber was filled with 6 mL of 0.1 M $KHCO_3$ and had 5 mL headspace. The reference electrode was an Ag/AgCl (3 M KCl) electrode and the counter electrode was a platinum gauze. The CO_2 was bubbled into the electrolyte through a glass frit to dissolve CO_2 faster into the electrolyte. The geometric area of the working electrode in the H-cell is 1.0 cm^{-2}. Before each measurement, CO_2 was bubbled into the electrolyte for 20 min to saturate the electrolyte. Then, the electrodes were pre-reduced at 10 mA cm^{-2} until the potential decreased to a constant value. For H-cell measurements, the WCO-Cu was also heated at 350 ℃ for 1 h to convert $Cu(OH)_2$ to Cu_xO for comparison with the WCO-Cu based GDE.

For both H-cell and flow cell measurements, the potential was post compensated by ohmic resistance that was determined by the current interrupt method. The value of the potential versus Ag/AgCl was converted to the scale of the reversible hydrogen electrode (RHE) using the equation: E (versus RHE) = E (versus Ag/AgCl (3 M KCl)) + 0.21 V + 0.059 X pH.

Quantification of products

Gas products were analysed using a gas chromatograph (GC, SRI Instrument 8610C) with the sample loop connected to the outlet of the electrolyser (H-cell or flow cell). The gas products on each electrode were repeatedly sampled and analysed for at least three times. The liquid products were quantified by analysing the electrolyte after the experiment using HPLC (Sigma Supelcogel 8H column, Thermo Scientific Ultimate 3000 UHPLC Systems). The Faradaic efficiency was calculated for gas and liquid products, respectively, by the equations: FE $=\frac{nFC_i vP}{jRT}$ and the equation: FE $=\frac{nFC_i V}{Q}$, where n is the transferred electron number to produce one molecule of the target product i, F is the Faradaic efficiency, C_i is the concentration of the target product i determined by GC or HPLC, v is the flow rate of CO_2 bubbled into the electrolyte, P and T are the pressure (101325 Pa) and temperature (22 ℃) of the gas sampled by the GC sample loop, respectively, j is the total current when sampling, R is the gas constant, V is the volume of the electrolyte, and Q is the total charge transfer to produce the target product.

Material characterization

Scanning electron microscope (SEM) images were taken using an FEI Teneo SEM. X-ray diffraction (XRD) patterns were obtained using a Bruker D8 Advance X-ray diffractometer with Cu Kα (λ = 1.54 Å) radiation.

4.3   Results and discussion

4.3.1   Synthesis and characterization

Scheme 4.1a presents the design and synthesis of self-supported Cu-based GDEs. Briefly, nanowire-structured Cu_xO and $Cu(OH)_2$ were directly grown on Cu gauze substrates, using thermal annealing

and wet chemical oxidation methods, respectively. Cu gauze was selected based on the following considerations: (1) it can serve as a precursor for Cu-based nanowires and (2) the uniform pores of the gauze allows the diffusion of CO_2 and gas products during eCO_2RR compared to a nonporous Cu foil. In the next step, an ink of carbon black and PTFE mixture (1:1 weight ratio) was airbrushed onto one side of the oxidized Cu gauze to form a microporous layer. In this layer, carbon black serves to increase the conductivity of the electrode, and PTFE increases the hydrophobicity of the GDE to prevent the electrolyte from flooding the pores of the electrode. During the following heating step, PTFE was softened to enhance the coating and $Cu(OH)_2$ was transferred to Cu_xO in the case of the WCO-Cu sample. The as-prepared Cu-based GDEs were then evaluated in the flow cell reactor (Scheme 4.1c) for eCO_2RR, and prior to the reduction of CO_2, the Cu_xO nanowires were reduced electrochemically to Cu as the active centres of eCO_2RR. Since the fabrication method of the GDE is independent of the morphology of the electrode, other types of nanostructured Cu that could be grown on Cu gauze, e.g. porous Cu,[21] dendritic Cu etc.,[22, 23] can also be prepared as self-supported GDEs.
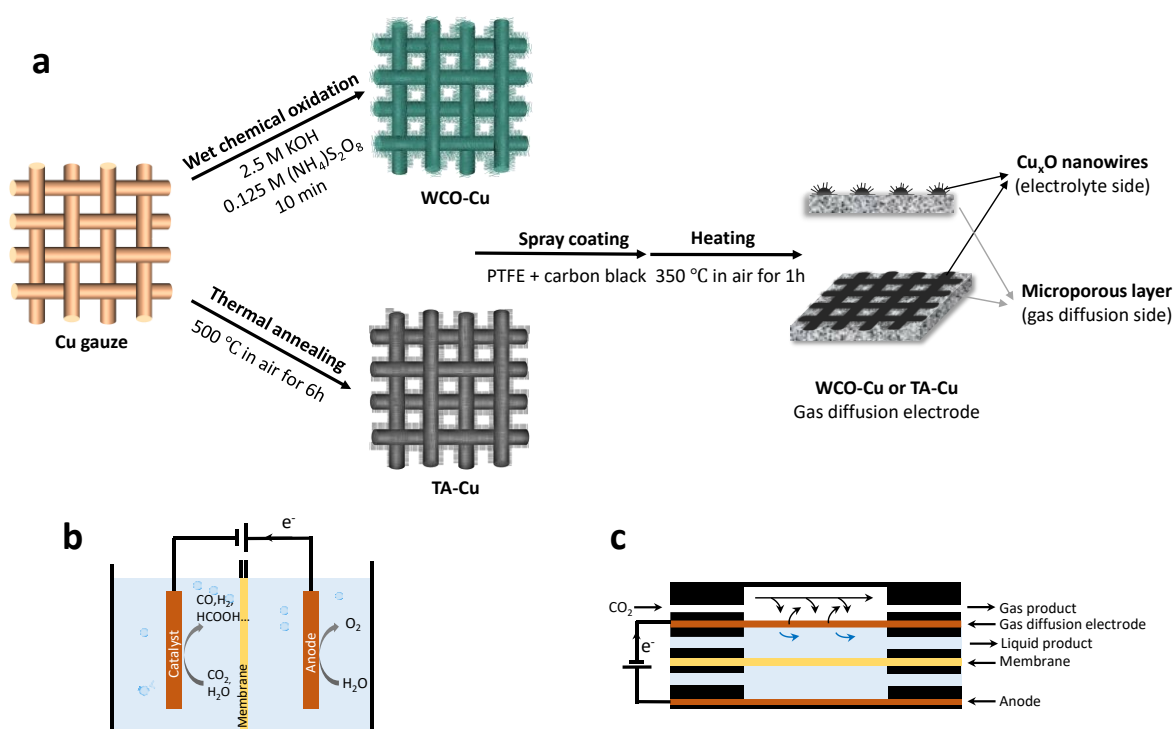
Scheme 4.1 (a) Preparation of self-supported Cu-based GDEs, (b) H-cell reactor and (c) flow-cell reactor.

Figure 4.1 shows the morphological evolution of the two types of GDEs. After oxidation, the surfaces of the Cu gauzes were homogeneously covered by Cu_xO (Figure 4.1a, b) or $Cu(OH)_2$ (Figure 4.1d, e) nanowires. After coating with the mixture of carbon black and PTFE, the framework of the Cu gauze was absent (Figure 4.1f, h). Instead, a flat microporous layer was present with cracks generated during the heating step. Notably, the electrolyte could not penetrate theses cracks because of the thickness (hundreds of micrometres) and the strong hydrophobicity of the microporous layer. A thin layer of carbon black and PTFE was also deposited onto the other side of the GDEs in the initial stage of airbrushing (Figure 4.1e, g and Figure S4.1), which partially covered the nanowires but still allowed the electrolyte access to the nanowires.
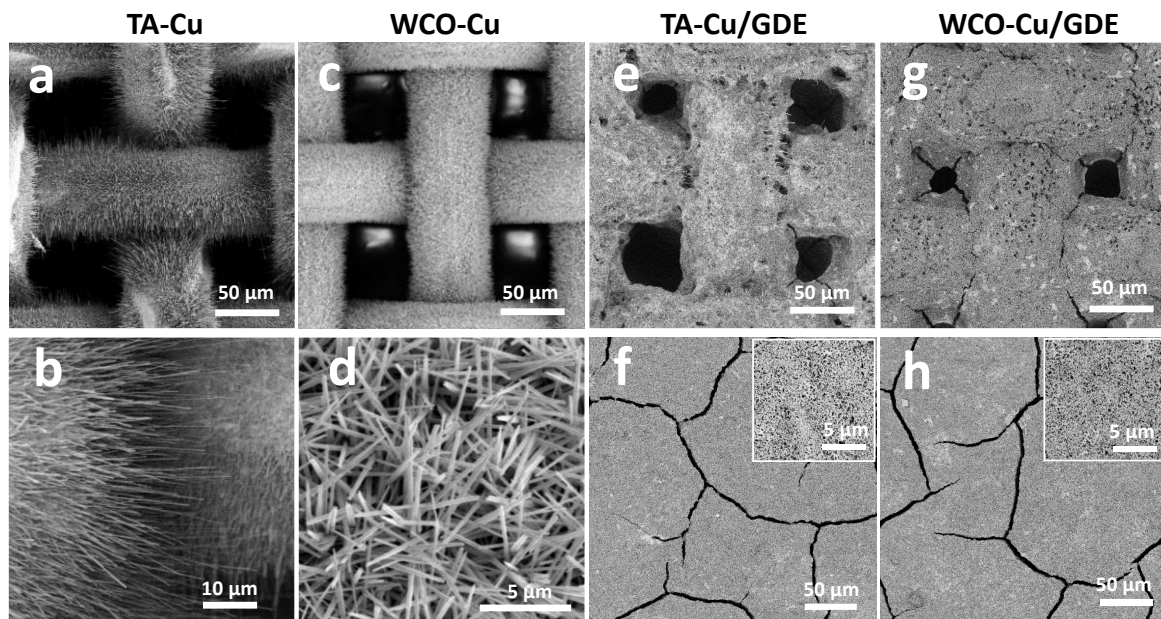
Figure 4.1 SEM images of the as-prepared electrodes. (a, b) TA-Cu at different magnifications, (c, d) WCO-Cu at different magnifications, (e, f) TA-Cu based GDE and (g, h) WCO-Cu based GDE. For the images of GDEs, (e) and (g) are the sides facing electrolyte and (f) and (h) are the sides facing CO_2 flow.

Figure 4.2 shows the XRD patterns of TA-Cu and WCO-Cu based GDEs before and after reduction under eCO$_2$RR conditions. The XRD patterns of as-prepared TA-Cu and WCO-Cu GDEs show diffraction peaks from Cu, CuO, and Cu$_2$O phases. The Cu phase was detected from the Cu gauze substrate, and the CuO and Cu$_2$O phases from the Cu$_x$O nanowires. In addition, TA-Cu exhibits higher-intensity CuO and Cu$_2$O peaks but lower intensity Cu peaks compared to those for the WCO-Cu GDE. This indicates that the thermal annealing method applied here formed a thicker oxidation layer over the Cu gauze than the wet chemical oxidation method. This difference may lead to different facet orientations and different densities of grain boundaries during the pre-reduction process and consequently impact the
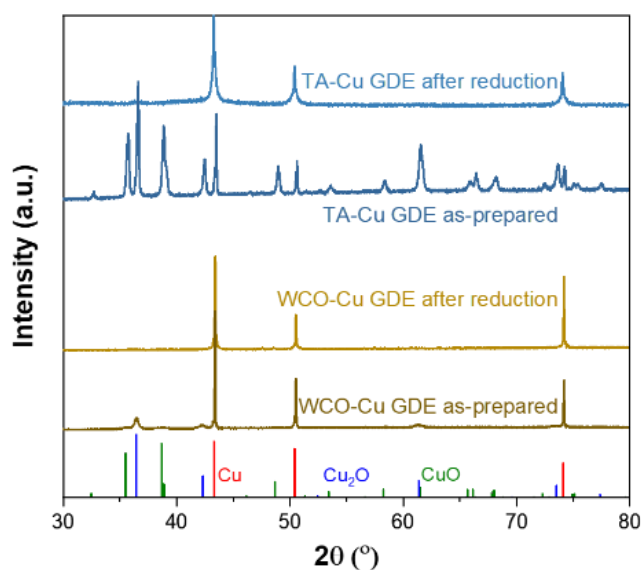
Figure 4.2 XRD patterns of the TA-Cu and WCO-Cu based GDEs before and after being electrochemically reduced.

product distribution of eCO_2RR. For example, Kanan et al. found that the Cu catalysts derived from a thick layer of Cu_xO contained more grain boundaries, which enhances the activity and stability of a Cu catalyst for eCO_2RR.[5, 24] After electrochemical reduction under eCO_2RR condition, all diffraction peaks from Cu_xO species disappeared, confirming that the nanowires at the electrolyte side could contact with the electrolyte and be reduced. The reduction of Cu oxides to metallic Cu is consistent with the results obtained from samples reduced in the H-cell (Figure S4.2) as well as the previously reported results,[11, 13, 19] indicating that Cu should be the active center for eCO_2RR.

4.3.2 Electrochemical performance of the GDEs

The eCO_2RR performance of the TA-Cu and WCO-Cu based GDEs was evaluated in the flow cell using 1.0 M KOH electrolyte. Gas-phase and liquid-phase products were detected and quantified by GC and HPLC, respectively. Owning to the highly porous structure of the self-supported GDEs as well as their sufficient hydrophobicity, CO_2 can be abundantly delivered to the catalyst surface and be readily reduced at the gas-catalyst-electrolyte interface. Figure 4.3(a, b) shows the total current densities and FEs of the main products, plotted against the applied potential, for the two GDEs. The total current density of both electrodes increased almost exponentially from less than 50 mA cm^{-2} to 300 mA cm^{-2} when the applied potential decreased from around -0.3 V to -0.6 V vs RHE, demonstrating that the self-supported Cu GDEs are highly active under the eCO_2RR conditions.

Both GDEs delivered the same reduction products, consisting of H_2, CO, formate, C_2H_4, ethanol, and n-propanol, similar to previous reports for Cu-based catalysts.[1, 20, 25] Moreover, with the decrease in potential from -0.3 V to -0.5 V, the H_2 selectivity decreased dramatically for both electrodes, implying that a higher overpotential is preferred for eCO_2RR. At around -0.5V vs RHE, ~55% and ~65% FEs for eCO_2RR were achieved for TA-Cu and WCO-Cu, respectively. However, the H_2 selectivity did not decrease with further decrease in the applied potential, possibly because the high-rate gas evolution on the electrode surface limits the transport of CO_2 onto the electrode.[20] Nevertheless, as shown in Figure 4.3c, the partial current density for eCO_2RR can still reach as high as 150 mA cm^{-2} and 200 mA cm^{-2} for TA-Cu and WCO-Cu, respectively. Apart from the similar evolution trends of the product selectivity versus the potential for the two GDEs, we also observed differences in selectivity towards 2-electron-transfer reduction products, particularly for CO and H_2. As shown in Figure 4.3a and b, the TA-Cu electrode exhibited an H_2 FE approx. 2 times higher but a CO FE 2 times lower than those for WCO-Cu.

The better activity for hydrogen evolution reaction (HER) of TA-Cu is confirmed by voltammograms (Figure S4.3) of the TA-Cu and WCO-Cu electrodes in argon saturated 1.0 M KOH in the flow-cell reactor. The lower CO selectivity, higher H_2 and C_{2+} selectivity of TA-Cu (Figure 4.3a, b) might be attributed to the difference in the material properties (Figure S4.3). As discussed in the XRD results as well as in previous reports, thermal annealing generates thicker oxide layer than wet chemical oxidation, which could lead to more under-coordinated sites, grain boundaries and stepped facets in the reduced TA-Cu.[5, 24, 26] These sites have been suggested to adsorb *CO intermediate stronger than the close-packed surfaces (e.g. Cu(111)) and benefit the C-C coupling, leading to higher FEs for C_{2+} products (as illustrated in Figure S4.4). On the other hand, stronger adsorption of *CO also indicates a slower desorption rate of CO which results in a lower CO FE. Moreover, theoretical simulations have
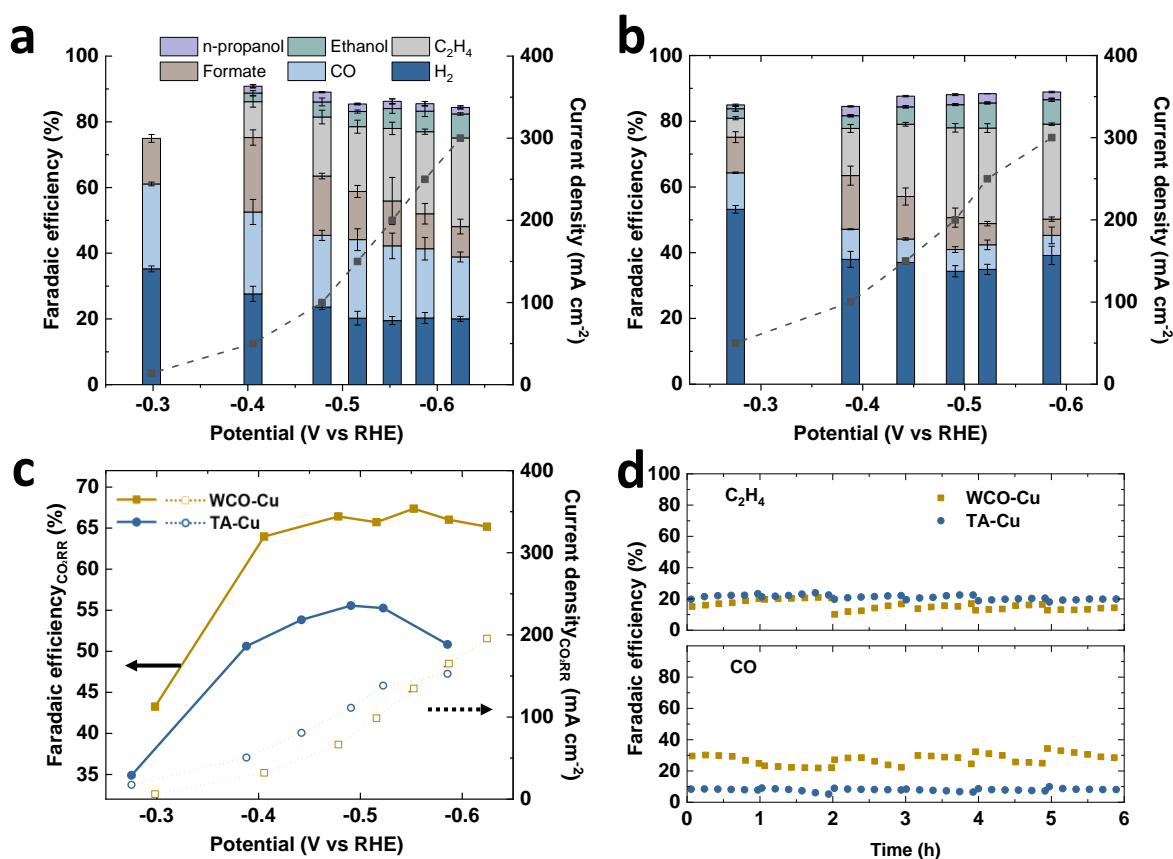
Figure 4.3 FEs of the main products and total current density of the WCO-Cu GDE (a) and TA-Cu GDE (b). (c) eCO$_2$RR FEs and current density of the WCO-Cu GDE and TA-Cu GDE. (d) The stability of the CO and C$_2$H$_4$ selectivity of the two GDEs at constant current densities of 100 mA cm^{-2} and 150 mA cm^{-2} were applied for WCO-Cu and TA-Cu, respectively.

shown that the *CO adsorption energy scales linearly with the *H adsorption energy.[27, 28] This could explain the higher H$_2$ selectivity of TA-Cu compared to that of WCO-Cu.

Cu-based catalysts often suffer from rapid deactivation during eCO$_2$RR due to the contamination and/or carbon deposition.[29] When those catalysts are prepared as GDEs, typically supported on carbon papers, flooding of electrolyte may play a more critical role in the stability of the electrode.[1, 20] To evaluate the stability of our self-supported GDEs, we carried out a continuous CO$_2$ electrolysis at constant current mode for TA-Cu and WCO-Cu. The results indicate stable products selectivity for over 6 h (Figure 4.3d and Figure S4.5) and no significant voltage change is observed (Figure S4.6). The crystal structure and nanowire morphology of both electrodes are also well preserved (Figure S4.7 and S4.1). However, carbonate accumulation at the gas diffusion side of the GDEs was observed (Figure S4.8).[17] Therefore, future application using this type of flow cell requires the elimination of carbonate formation for an extended long-term performance (e.g. up to days).

4.3.3 Comparison of eCO$_2$RR in flow cell and H-cell

Through the direct transformation of nanostructured Cu catalysts into self-supported GDEs, the intrinsic properties of the catalyst, e.g., composition, crystal structure and morphology, could be maintained. The nanostructured catalysts and their self-supported GDE configurations can therefore

be used as model systems to understand the influence of reaction environment on catalytic performance. In order to make a direct comparison with the WCO-Cu based GDE, the as-prepared WCO-Cu was pre-heated at 350 °C in air for 1.0 h to convert $Cu(OH)_2$ to Cu_xO. Then, both TA-Cu and WCO-Cu were tested in the H-cell using CO_2 saturated 0.1 M $KHCO_3$. Figure 4.4 compares the FEs and partial current densities of C_1 products (CO and formate) and C_2 products (C_2H_4 and ethanol) for TA-Cu and WCO-Cu in the flow-cell reactor and the H-cell reactor. eCO_2RR in the H-cell vs. the flow cell leads to a significant difference in product distribution for both the TA-Cu and WCO-Cu catalysts. Much higher C_1 product selectivity can be achieved in the H-cell reactor than in the flow-cell reactor (Figure 4.4a). In particular, at around -0.55 V, both TA-Cu and WCO-Cu exhibited a C_1 FE of ~80% in the H-cell. On the other hand, the C_2 products generated in the H-cell reactor were only detected at more negative potentials (< -0.6 V vs RHE) with relatively low selectivity (< 16% FE for C_2H_4 and < 5% FE for ethanol). These observations agree well with the previous results obtained in the H-cell where the oxide-derived Cu nanowires are highly selective toward CO and formate.[5,11,12] However, such conclusions cannot hold for the eCO_2RR occurring in the flow cell, since high C_2H_4 (~ 30%) and ethanol (~8%) FEs can be obtained at a potential as low as -0.6 V vs RHE for both two GDEs (Figure 4.4c, e).
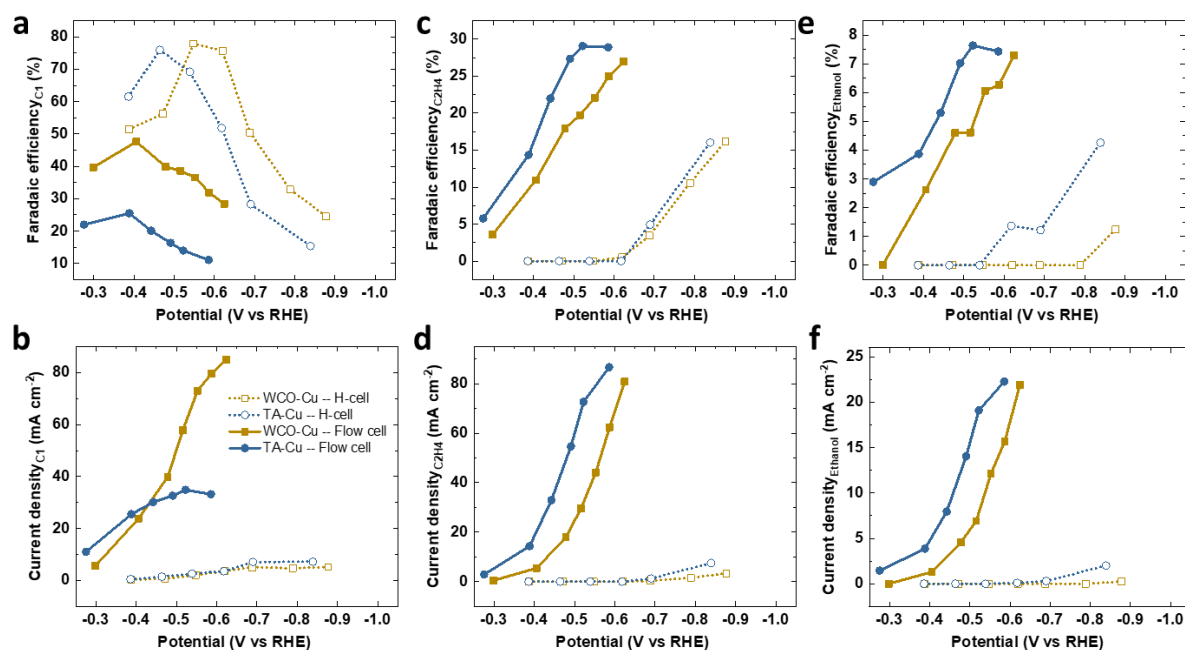
Figure 4.4 Faradaic efficiency (a, c, e) and partial current density (b, d, f) as a function of potential for C_1 products, C_2H_4, and ethanol, respectively, generated on the TA-Cu and WCO-Cu catalysts in a flow cell and H-cell.

While the intrinsic properties of the catalysts are independent of the reaction system, the different reaction environments accounts for the selectivity difference. Neutral pH electrolyte (i.e., 0.1 M $KHCO_3$) is mostly used in the H-cell reactor because CO_2 readily reacts with alkaline electrolyte, and acidic electrolyte favours HER.[30] However, GDE in the flow cell separates CO_2 gas from electrolyte, and thus alkaline electrolyte (i.e., 1.0 M KOH) is often used for a flow cell to decrease the ohmic resistance and suppress the activity of hydrogen evolution reaction. Since hydroxide can lower the binding energy of CO on the Cu surface and decrease the activation barrier for the CO dimerization

step, a flow-cell reactor using KOH electrolyte is then expected to lower the overpotential and increase the reaction rate for CO_2 to C_2 products.[1] In addition, a GDE in a flow cell does not suffer from slow CO_2 mass transport as the electrode in an H-cell does, and thus the rapid conversion of CO_2 to CO could build up higher *CO coverage on the catalyst surface, which improves the reaction rate for CO to C_2 products.[1] In order to further de-couple the influence of the reaction cell and electrolyte, we performed control experiments over WCO-Cu and TA-Cu based GDEs using 1.0 M $KHCO_3$ as electrolyte in flow cell. We found that at a given potential, the FEs of the C_2 products using 1 M $KHCO_3$ are higher than those obtained in H-cell with 0.1 M $KHCO_3$ but lower than those obtained in flow cell with 1 M KOH (Figure S4.11and S4.12). This indicates that the faster mass transfer contributes to the increase of the C_2 products selectivity and higher pH can further enhance the C_2 FEs.

Apart from the higher selectivity for C_2 products achieved in the flow-cell reactor, both TA-Cu and WCO-Cu showed one order of magnitude higher partial current density for not only C_2 products but also C_1 products. The boosted current density is mainly because of the fast mass transfer achieved in the flow-cell reactor, since the CO_2 diffusion layer in the GDE is around three orders of magnitude thinner than that in the H-cell (~50 nm versus ~50 um).[2] Moreover, we did not observe any obvious decrease in eCO_2RR selectivity up to 250 mA cm^{-2} in the flow-cell reactor, indicating an effective transporting of CO_2 in the self-supported GDE. However, in the case of the H-cell, H_2 becomes the dominant product at a current density higher than 20 mA cm^{-2} due to the depletion of CO_2 near the electrode.

Although the same catalysts tested in the two types of reactors exhibited large differences in current density and product distribution, some similarities still exist. Typically, TA-Cu showed higher C_2 product selectivity but lower C_1 product selectivity compared with the WCO-Cu catalyst in both reactors. As discussed above, this can be attributed to the high density of under-coordinated sites and grain binderies generated from the thick oxide layer of Cu_xO on the TA-Cu precursor. Moreover, the current density of TA-Cu is higher than that for WCO-Cu within the test potential range, independent of the reactor. As the two catalysts show similar normalized activity by electrochemical surface area (ECSA) (Figure S4.15), the higher current density of TA-Cu is mainly attributed to its higher surface area compared to WCO-Cu. This is consistent with recent findings that most of the nanostructured Cu catalysts show similar intrinsic activity.[7] These results imply that the results obtained in an H-cell reactor could be partially adapted to the flow-cell systems. Nevertheless, it is still necessary to emphasize that the catalytic performance needs to be evaluated in flow reactors under commercially relevant conditions to provide more representative conclusions and guidelines for the designing of advanced catalysts and reactors. Such assessment is particularly important for Cu-based catalysts, since up to 16 products can be reduced from CO_2 on the Cu surface.[3] The distinct reaction environment induced by the electrolyte, current density, and mass transport could therefore steer the reaction towards completely different pathways.

4.4   Conclusions

In summary, we presented a new strategy to directly transform nanostructured Cu catalysts into self-supported GDEs to investigate the eCO_2RR performance at high current densities. By simply coating Cu_xO–nanowires-covered Cu gauze with a hydrophobic microporous layer, we obtained two types of

self-supported GDEs and comparatively investigated their catalytic performance in a flow cell. The experimental results showed that after being transformed to GDEs, the two types of Cu nanowires still preserved their intrinsic catalytic properties, compared with that in H-cell. That is, Cu nanowires, formed by thermally annealing (TA-Cu), favours the production of C_2 products while the Cu nanowires, derived from wet chemical oxidation (WCO-Cu), produces more C_1 products. More importantly, the reaction environment strongly influences the catalytic activity and selectivity. In the H-cell, both of TA-Cu and WCO-Cu are selectively converted CO_2 to C_1 products, while in the flow cell environment, both selectively produced C_2 products due to the alkaline electrolyte and faster mass transfer. In particular, both catalysts showed > 40% FEs for C_2 products at current densities greater than 200 mA cm^{-2} with an overpotential less than 0.6 V. These results shed light on the importance of assessing the catalytic behaviour of nanostructured Cu catalysts under industrially relevant conditions and open new avenues for the rational design of self-supported GDEs based on nanostructured materials.

4.5   Acknowledgements

4.6   References

[1]   C.-T. Dinh, T. Burdyny, M.G. Kibria, A. Seifitokaldani, C.M. Gabardo, F.P. García de Arquer, A. Kiani, J.P. Edwards, P. De Luna, O.S. Bushuyev, C. Zou, R. Quintero-Bermudez, Y. Pang, D. Sinton, E.H. Sargent, CO_2 electroreduction to ethylene via hydroxide-mediated copper catalysis at an abrupt interface, Science, 360 (2018) 783-787.

[2]   T. Burdyny, W.A. Smith, CO_2 reduction on gas-diffusion electrodes and why catalytic performance must be assessed at commercially-relevant conditions, Energy & Environmental Science, 12 (2019) 1442-1453.

[3]   K.P. Kuhl, E.R. Cave, D.N. Abram, T.F. Jaramillo, New insights into the electrochemical reduction of carbon dioxide on metallic copper surfaces, Energy & Environmental Science, 5 (2012) 7050-7059.

[4]   Y. Hori, Electrochemical CO_2 Reduction on Metal Electrodes, in: C.G. Vayenas, R.E. White, M.E. Gamboa-Aldeco (Eds.) Modern Aspects of Electrochemistry, Springer New York, New York, NY, 2008, pp. 89-189.

[5]   C.W. Li, M.W. Kanan, CO_2 Reduction at Low Overpotential on Cu Electrodes Resulting from the Reduction of Thick Cu2O Films, Journal of the American Chemical Society, 134 (2012) 7231-7234.

[6]   W. Luo, W. Xie, M. Li, J. Zhang, A. Züttel, 3D hierarchical porous indium catalyst for highly efficient electroreduction of CO_2, J Mater Chem A, 7 (2019) 4505-4515.

[7]   S. Nitopi, E. Bertheussen, S.B. Scott, X. Liu, A.K. Engstfeld, S. Horch, B. Seger, I.E.L. Stephens, K. Chan, C. Hahn, J.K. Nørskov, T.F. Jaramillo, I. Chorkendorff, Progress and Perspectives of Electrochemical CO_2 Reduction on Copper in Aqueous Electrolyte, Chemical Reviews, 119 (2019) 7610-7672.

[8]   Y. Huang, A.D. Handoko, P. Hirunsit, B.S. Yeo, Electrochemical Reduction of CO_2 Using Copper Single-Crystal Surfaces: Effects of CO* Coverage on the Selective Formation of Ethylene, ACS Catalysis, 7 (2017) 1749-1756.

[9]   Z.-L. Wang, C. Li, Y. Yamauchi, Nanostructured nonprecious metal catalysts for electrochemical reduction of carbon dioxide, Nano Today, 11 (2016) 373-391.

[10]   Q. Lu, F. Jiao, Electrochemical CO_2 reduction: Electrocatalyst, reaction mechanism, and process engineering, Nano Energy, 29 (2016) 439-456.

[11]   D. Raciti, K.J. Livi, C. Wang, Highly Dense Cu Nanowires for Low-Overpotential CO_2 Reduction, Nano Letters, 15 (2015) 6829-6835.

[12]   M. Ma, K. Djanashvili, W.A. Smith, Selective electrochemical reduction of CO_2 to CO on CuO-derived Cu nanowires, Physical Chemistry Chemical Physics, 17 (2015) 20861-20867.

[13]   M. Ma, K. Djanashvili, A. Smith Wilson, Controllable Hydrocarbon Formation from the Electrochemical Reduction of CO_2 over Cu Nanowire Arrays, Angewandte Chemie International Edition, 55 (2016) 6680-6684.

[14]   H. Mistry, A.S. Varela, C.S. Bonifacio, I. Zegkinoglou, I. Sinev, Y.-W. Choi, K. Kisslinger, E.A. Stach, J.C. Yang, P. Strasser, B.R. Cuenya, Highly selective plasma-activated copper catalysts for carbon dioxide reduction to ethylene, Nature Communications, 7 (2016) 12123.

[15]   S. Verma, X. Lu, S. Ma, R.I. Masel, P.J.A. Kenis, The effect of electrolyte composition on the electroreduction of CO_2 to CO on Ag based gas diffusion electrodes, Physical Chemistry Chemical Physics, 18 (2016) 7075-7084.

[16]   W. Luo, J. Zhang, M. Li, A. Züttel, Boosting CO Production in Electrocatalytic CO_2 Reduction on Highly Porous Zn Catalysts, ACS Catalysis, 9 (2019) 3783-3791.

[17]   S. Verma, Y. Hamasaki, C. Kim, W. Huang, S. Lu, H.-R.M. Jhong, A.A. Gewirth, T. Fujigaya, N. Nakashima, P.J.A. Kenis, Insights into the Low Overpotential Electroreduction of CO_2 to CO on a Supported Gold Catalyst in an Alkaline Flow Electrolyzer, ACS Energy Letters, 3 (2018) 193-198.

[18]   D.A. Salvatore, D.M. Weekes, J. He, K.E. Dettelbach, Y.C. Li, T.E. Mallouk, C.P. Berlinguette, Electrolysis of Gaseous CO_2 to CO in a Flow Cell with a Bipolar Membrane, ACS Energy Letters, 3 (2018) 149-154.

[19]   W. Luo, W. Xie, R. Mutschler, E. Oveisi, G.L. De Gregorio, R. Buonsanti, A. Züttel, Selective and Stable Electroreduction of CO_2 to CO at the Copper/Indium Interface, ACS Catalysis, 8 (2018) 6571-6581.

[20]   J.-J. Lv, M. Jouny, W. Luc, W. Zhu, J.-J. Zhu, F. Jiao, A Highly Porous Copper Electrocatalyst for Carbon Dioxide Reduction, Advanced Materials, 0 (2018) 1803111.

[21]   A. Dutta, M. Rahaman, N.C. Luedi, M. Mohos, P. Broekmann, Morphology Matters: Tuning the Product Distribution of CO_2 Electroreduction on Oxide-Derived Cu Foam Catalysts, Acs Catal, 6 (2016) 3804-3814.

[22]   H.S. Jeon, S. Kunze, F. Scholten, B. Roldan Cuenya, Prism-Shaped Cu Nanocatalysts for Electrochemical CO_2 Reduction to Ethylene, Acs Catal, 8 (2018) 531-535.

[23]   C. Reller, R. Krause, E. Volkova, B. Schmid, S. Neubauer, A. Rucki, M. Schuster, G. Schmid, Selective Electroreduction of CO_2 toward Ethylene on Nano Dendritic Copper Catalysts at High Current Density, Advanced Energy Materials, 7 (2017) 1602114.

[24]   A. Verdaguer-Casadevall, C.W. Li, T.P. Johansson, S.B. Scott, J.T. McKeown, M. Kumar, I.E.L. Stephens, M.W. Kanan, I. Chorkendorff, Probing the Active Surface Sites for CO Reduction on Oxide-Derived Copper Electrocatalysts, Journal of the American Chemical Society, 137 (2015) 9808-9811.

[25]   M.G. Kibria, C.-T. Dinh, A. Seifitokaldani, P. De Luna, T. Burdyny, R. Quintero-Bermudez, M.B. Ross, O.S. Bushuyev, F.P. García de Arquer, P. Yang, D. Sinton, E.H. Sargent, A Surface Reconstruction Route to High Productivity and Selectivity in CO_2 Electroreduction toward C_{2+} Hydrocarbons, Advanced Materials, 0 (2018) 1804867.

[26]   C.W. Li, J. Ciston, M.W. Kanan, Electroreduction of carbon monoxide to liquid fuel on oxide-derived nanocrystalline copper, Nature, 508 (2014) 504-+.

[27]   C. Shi, H.A. Hansen, A.C. Lausche, J.K. Nørskov, Trends in electrochemical CO_2 reduction activity for open and close-packed metal surfaces, Physical Chemistry Chemical Physics, 16 (2014) 4720-4727.

[28]   E.R. Cave, C. Shi, K.P. Kuhl, T. Hatsukade, D.N. Abram, C. Hahn, K. Chan, T.F. Jaramillo, Trends in the Catalytic Activity of Hydrogen Evolution during CO_2 Electroreduction on Transition Metals, Acs Catal, 8 (2018) 3035-3040.

[29]   Y. Hori, H. Konishi, T. Futamura, A. Murata, O. Koga, H. Sakurai, K. Oguma, "Deactivation of copper electrode" in electrochemical reduction of CO 2, Electrochimica Acta, 50 (2005) 5354-5369.

[30]   Y. Chen, M.W. Kanan, Tin Oxide Dependence of the CO_2 Reduction Efficiency on Tin Electrodes and Enhanced Activity for Tin/Tin Oxide Thin-Film Catalysts, Journal of the American Chemical Society, 134 (2012) 1986-1989.

4.7 Supporting information
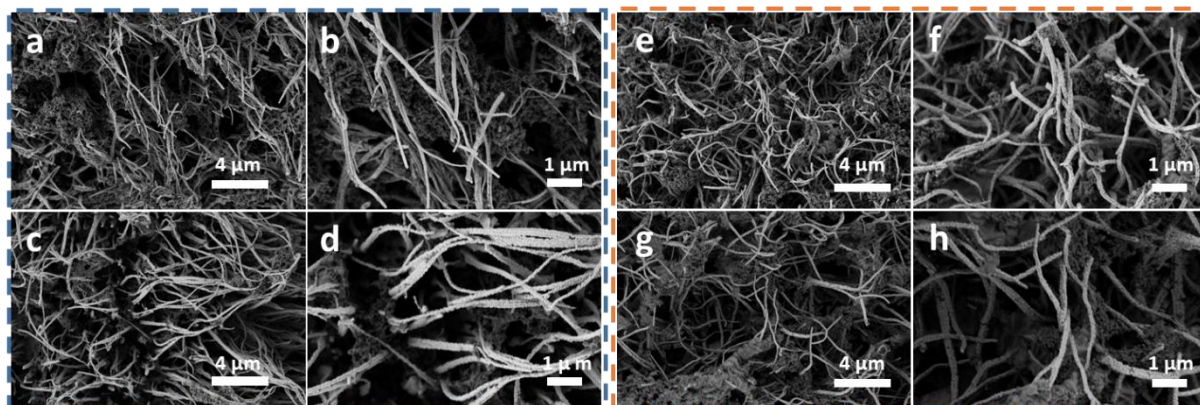
Figure S4.1 SEM images of the TA-Cu and WCO-Cu based GDE just-reduced and after 6 h of eCO$_2$RR in flow cell with 1 M KOH at 100 mA cm^{-2}. (a, b) TA-Cu based GDE just electrochemically reduced and before eCO$_2$RR, (c, d) TA-Cu based GDE after 6 h of reaction. (e, f) WCO-Cu based GDE just electrochemically reduced and before eCO$_2$RR, (g, h) WCO-Cu based GDE after 6 h of reaction.
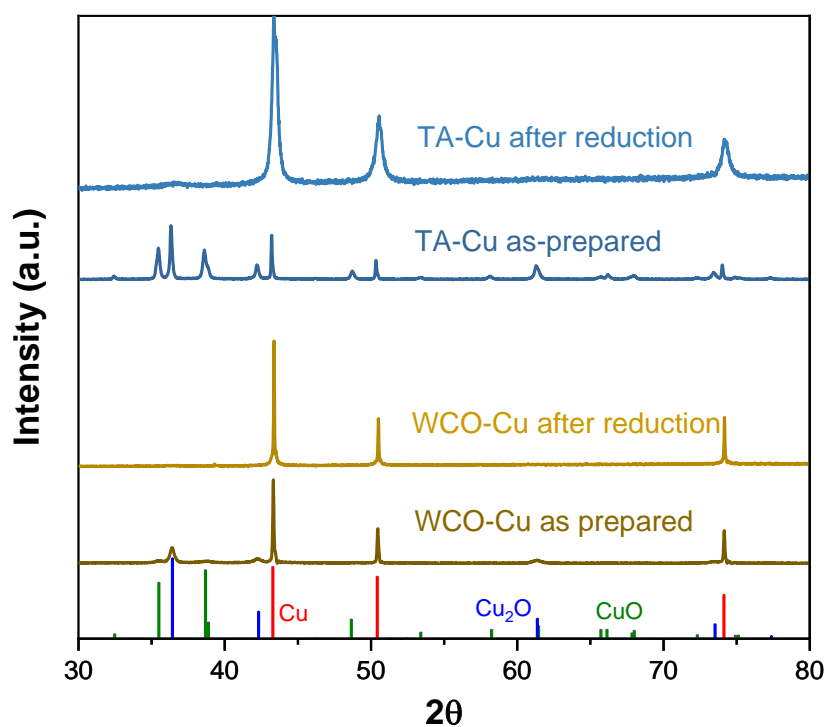
Figure S4.2 XRD patterns of TA-Cu and WCO-Cu before and after being electrochemically reduced in H-cell.
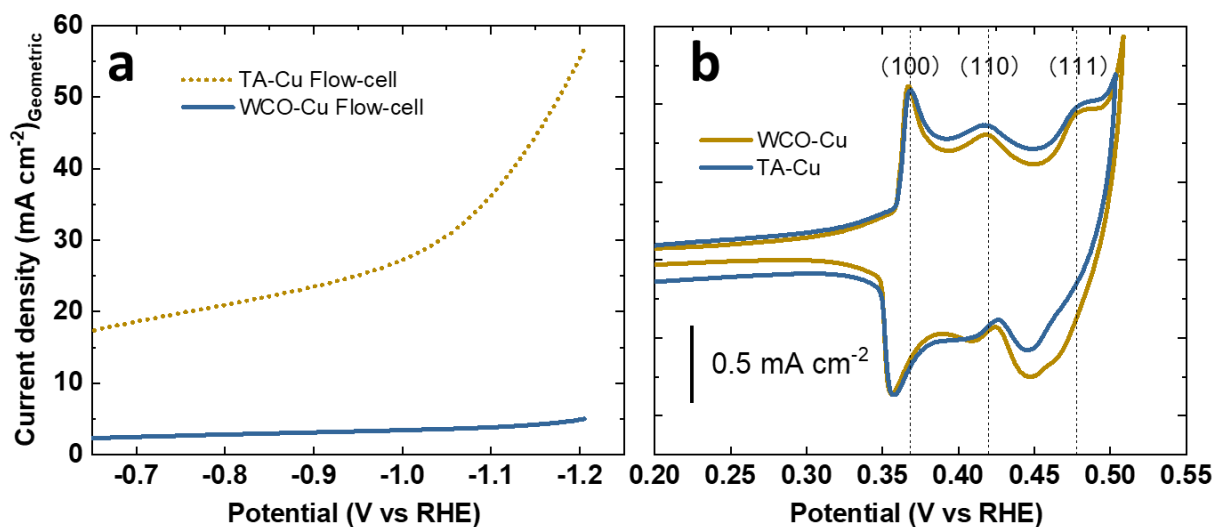
Figure S4.3 (a) Voltammograms of the WCO-Cu and TA-Cu based GDEs in flow cell with Ar saturated 1.0 M KOH at a scan rate of 50 mV/s. (b) Voltammograms of OH_{ads} peaks on the WCO-Cu and TA-Cu collected in H-cell with Ar saturated 1.0 M KOH at a scan rate of 10 mV/s.
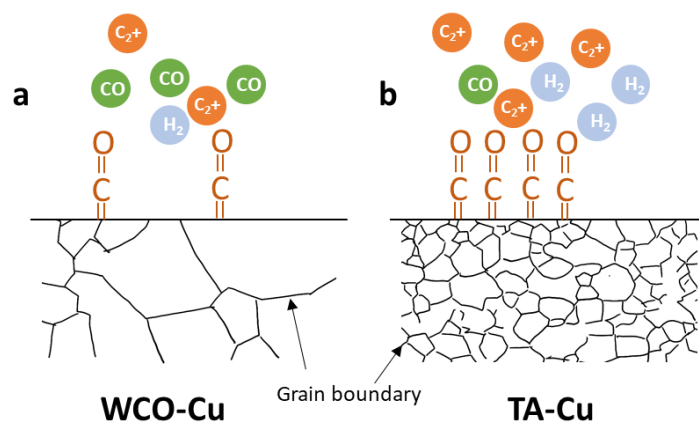
Figure S4.4 Schematics of the effect of the density of grain boundary on the adsorption of *CO intermediate and the formation of the CO and H_2 molecules. (a) WCO-Cu with smaller density of grain boundary, (b) TA-Cu with denser grain boundary.
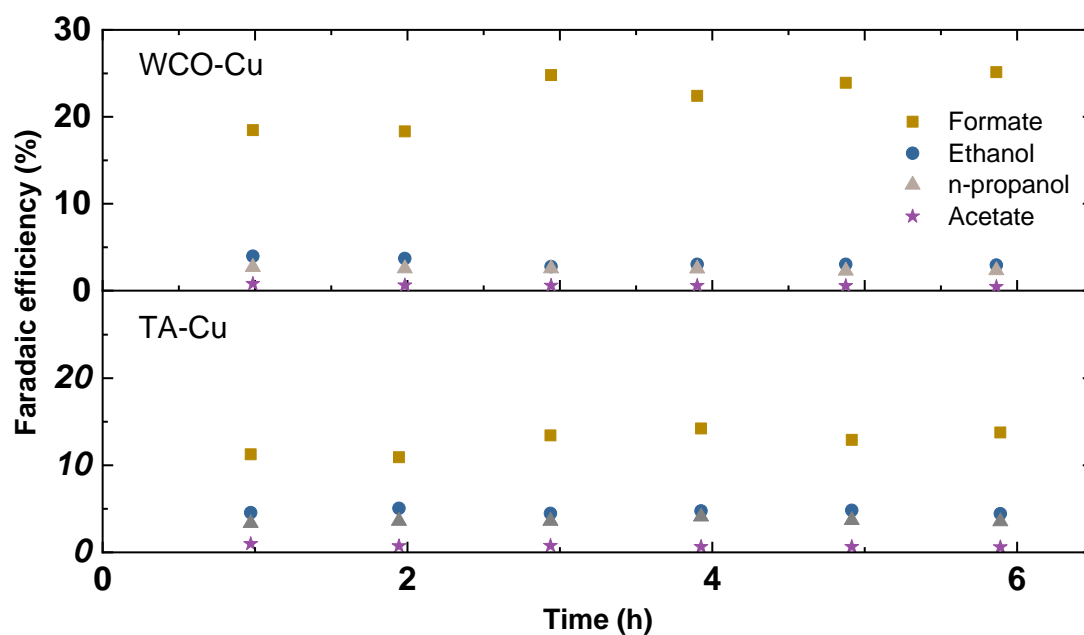
Figure S4.5 Faradaic efficiency of the liquid products as the function of time from the eCO$_2$RR on the TA-Cu and WCO-Cu based GDEs in 1.0 M KOH.
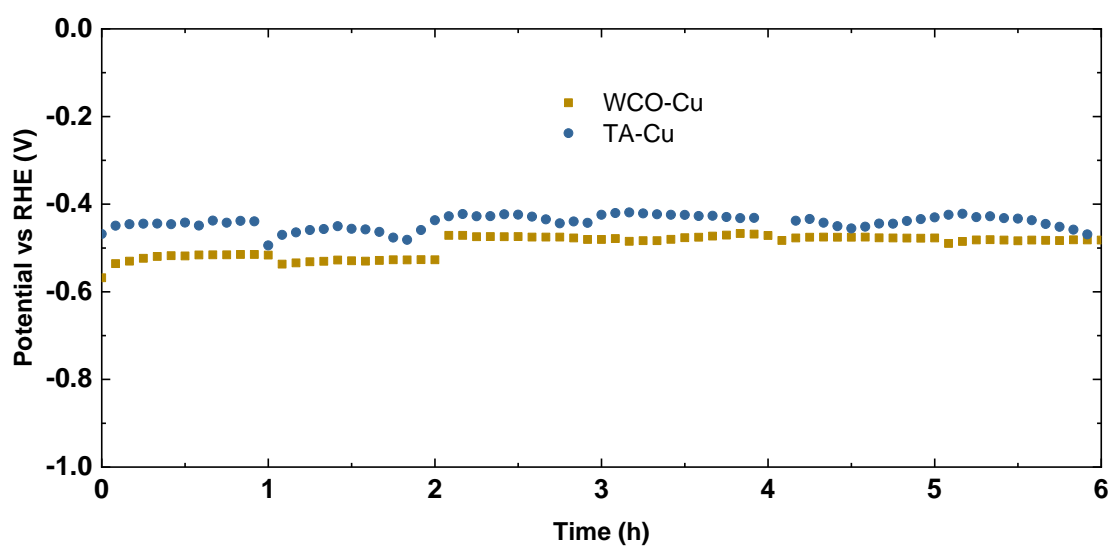
Figure S4.6 Potential versus time of the TA-Cu and WCO-Cu based GDEs in 1.0 M KOH. WCO-Cu electrode was measured at 100 mA cm^{-2} and TA-Cu electrode at 150 mA cm^{-2}.
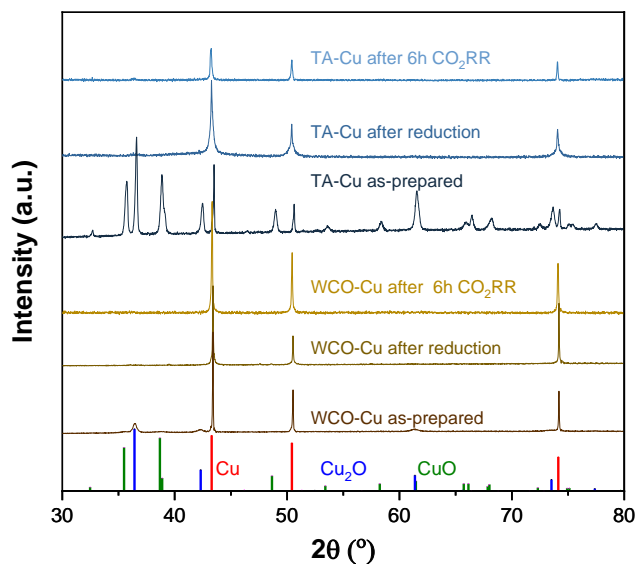
Figure S4.7 XRD patterns of the as prepared TA-Cu and WCO-Cu based GDEs and those after 20 min and 6 h of eCO$_2$RR in Flow-cell with 1 M KOH at 100 mA cm^{-2}.
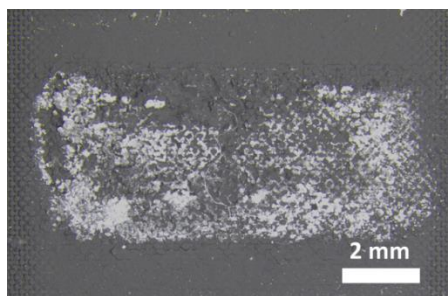
Figure S4.8 The accumulated salt on the gas diffusion side of TA-Cu based GDE after continuously working for 1 h at 150 mA cm^{-2} in flow cell using 1 M KOH as the electrolyte.
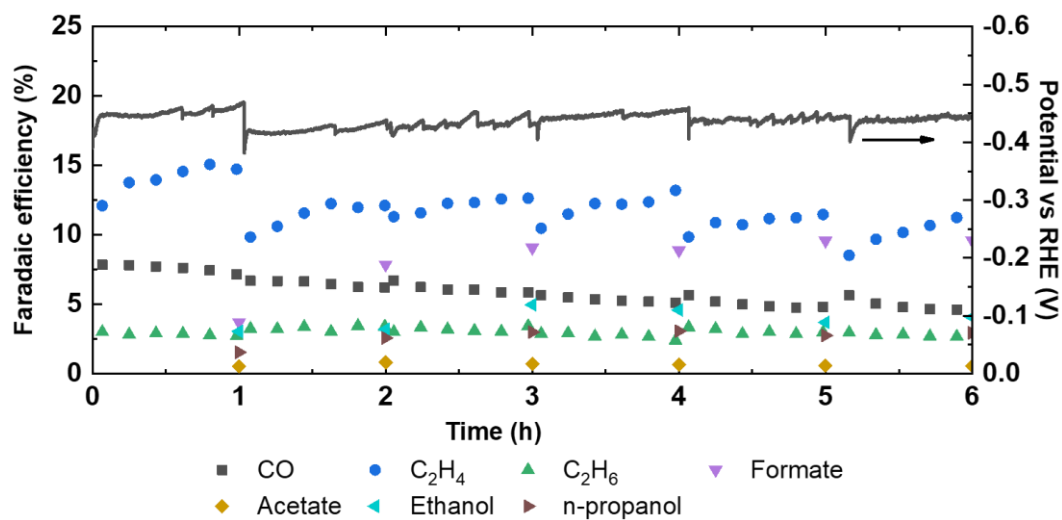
Figure S4.9 FEs and potential as a function of time of a TA-Cu GDE working for 6 h at 100 mA cm^{-2} in flow cell with 1 M KOH as the electrolyte. The electrode was rinsed by water every hour.
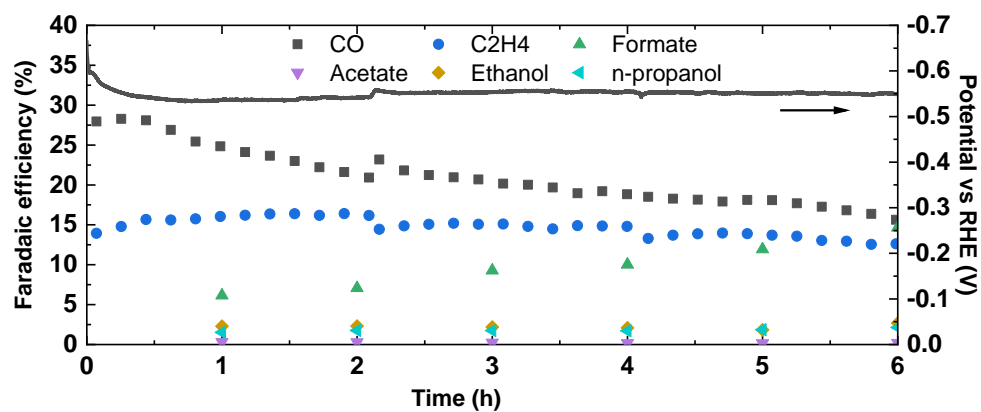
Figure S4.10 FEs and potential as a function of time of a WCO-Cu GDE continuously working for 6 h at 100 mA cm^{-2} in flow cell with 1 M KOH as the electrolyte.
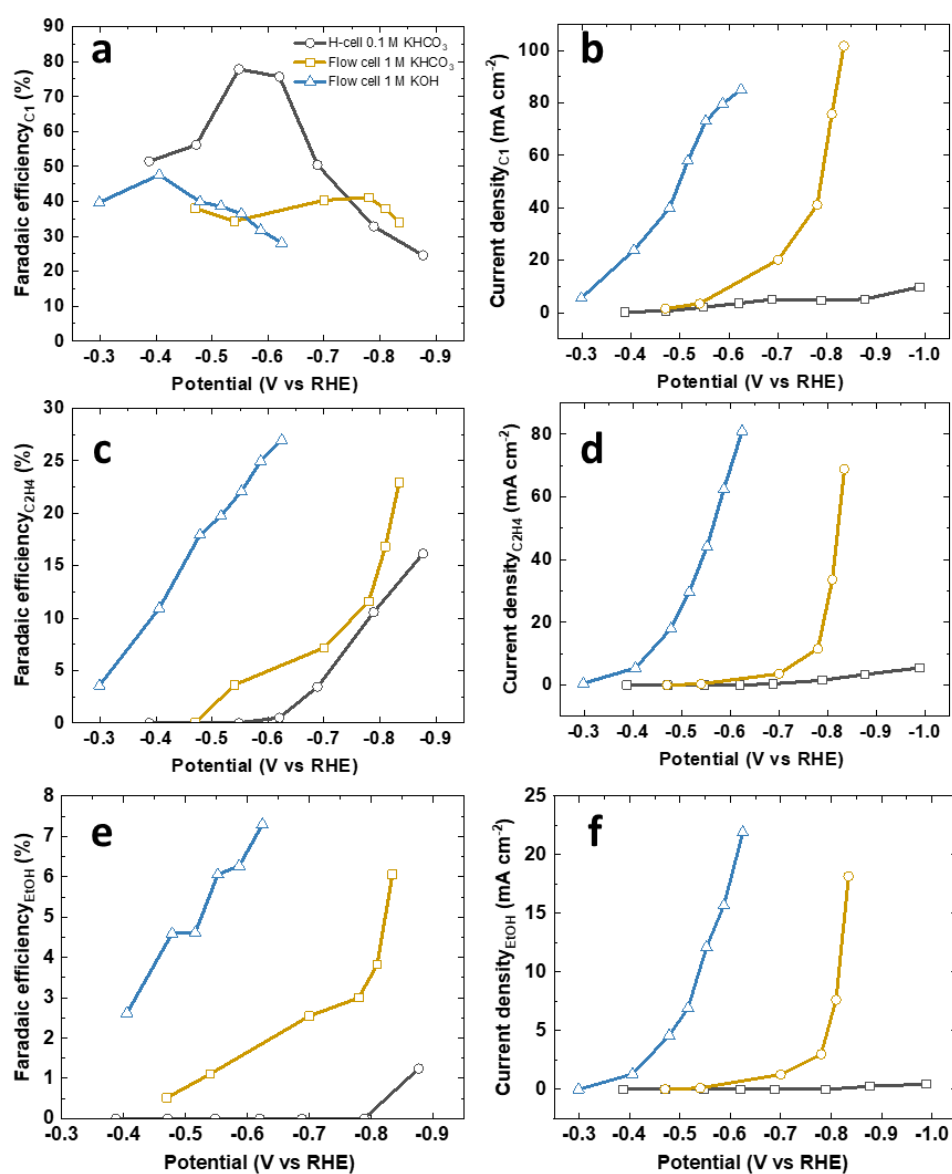
Figure S4.11 Faradaic efficiencies (a, c, e) and partial current densities (b, d, f) as a function of potential for C$_1$ products, C$_2$H$_4$, and ethanol, respectively, generated on the WCO-Cu catalysts in a flow cell with 1 M KOH or 1 M KHCO$_3$ and H-cell with 0.1 M KHCO$_3$.
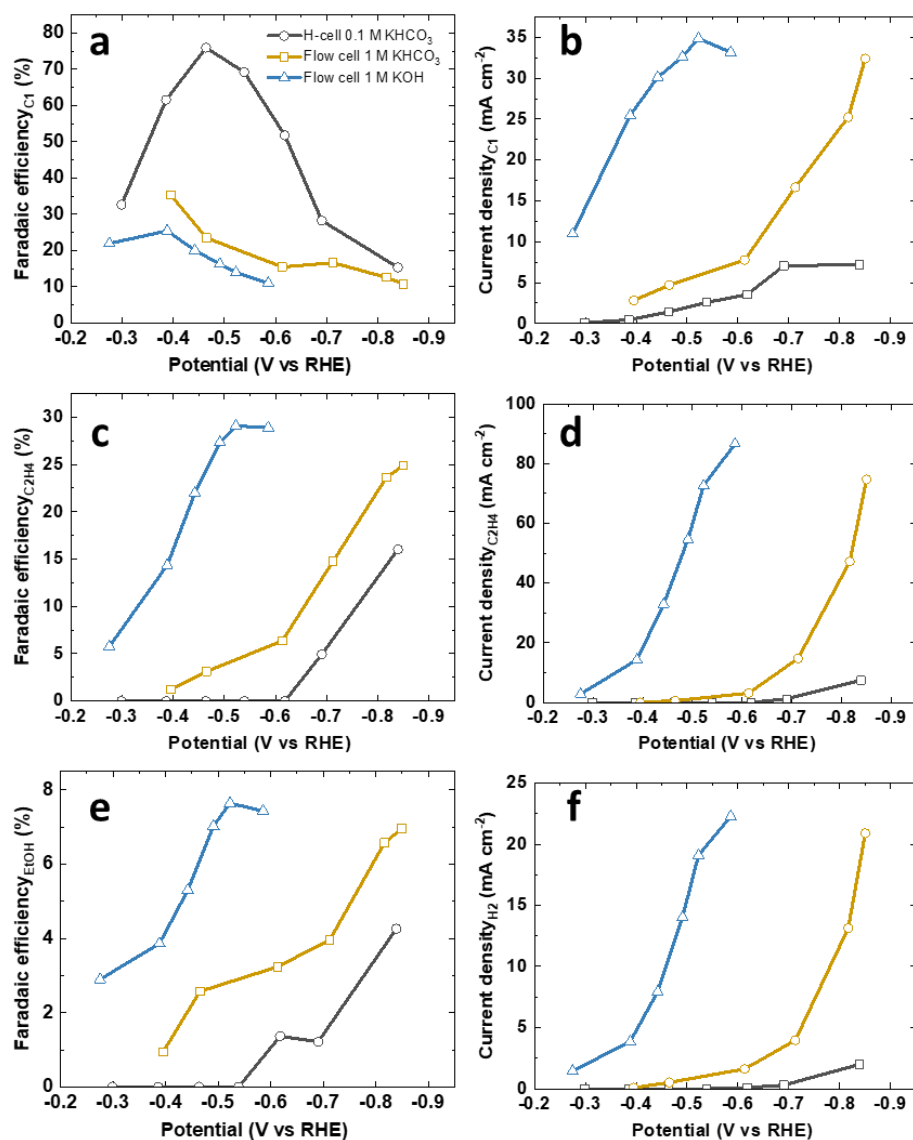
Figure S4.12 Faradaic efficiencies (a, c, e) and partial current densities (b, d, f) as a function of potential for C_1 products, C_2H_4, and ethanol, respectively, generated on the TA-Cu catalysts in a flow cell with 1 M KOH or 1 M $KHCO_3$ and H-cell with 0.1 M $KHCO_3$.
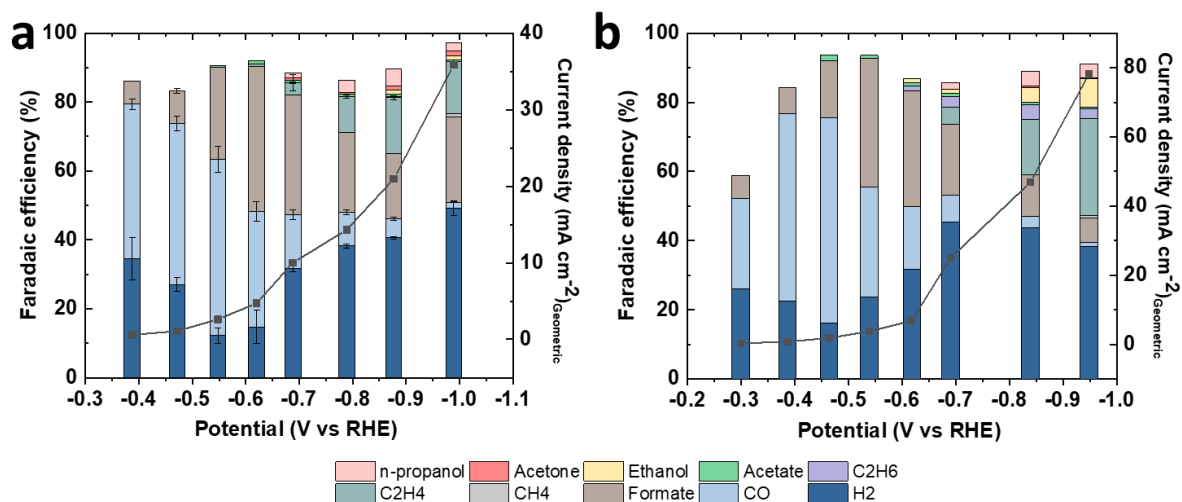
Figure S4.13 Faradaic efficiencies and total current densities as a function of potential of all the detected products from eCO$_2$RR on (a) WCO-Cu and (b) TA-Cu in H-cell reactor using 0.1 M KHCO$_3$.
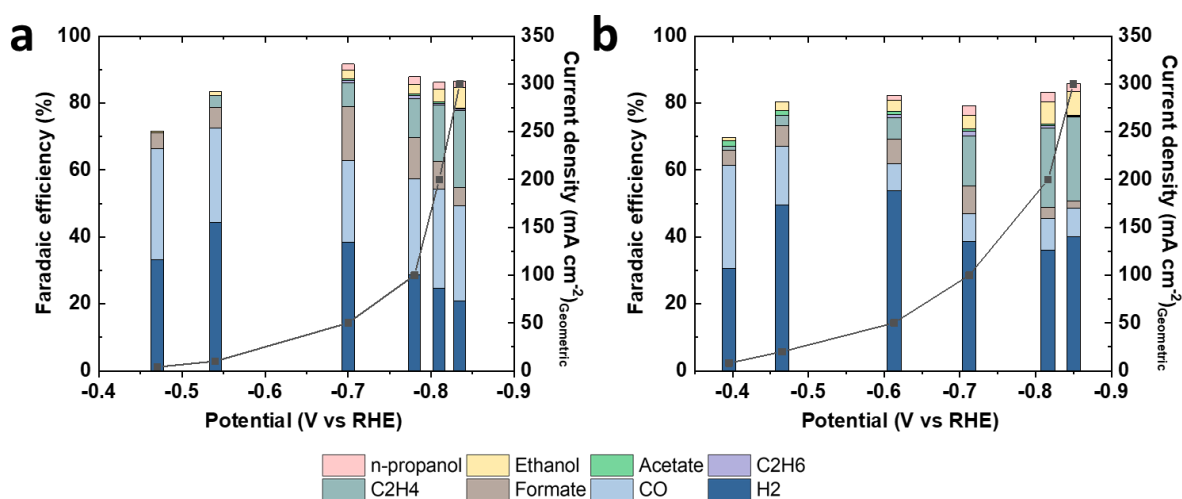
Figure S4.14 Faradaic efficiencies and total current densities as the function of potential of all the detected products from eCO$_2$RR on (a) WCO-Cu GDEs and (b) TA-Cu GDEs in flow with 1 M KHCO$_3$.
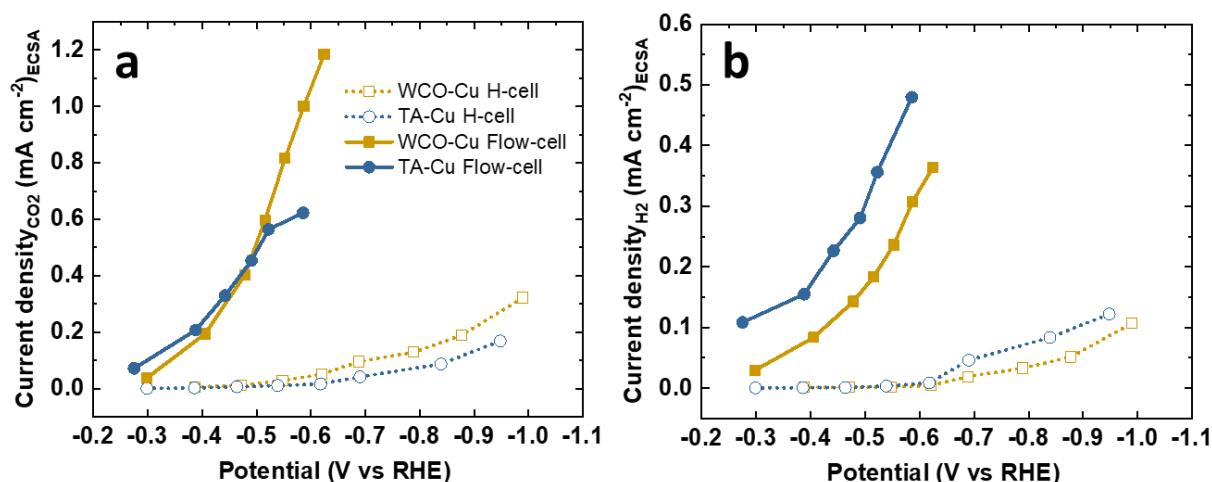
Figure S4.15 Comparison of eCO₂RR (a) and HER (b) intrinsic activity between WCO-Cu and TA-Cu in both flow cell and H-cell. The current density was normalized by the electrochemical active surface area derived from the roughness factor from Figure S4.16. The Flow cell has 1 M KOH as the electrolyte and the H-cell has 0.1 M KHCO₃ as the electrolyte.
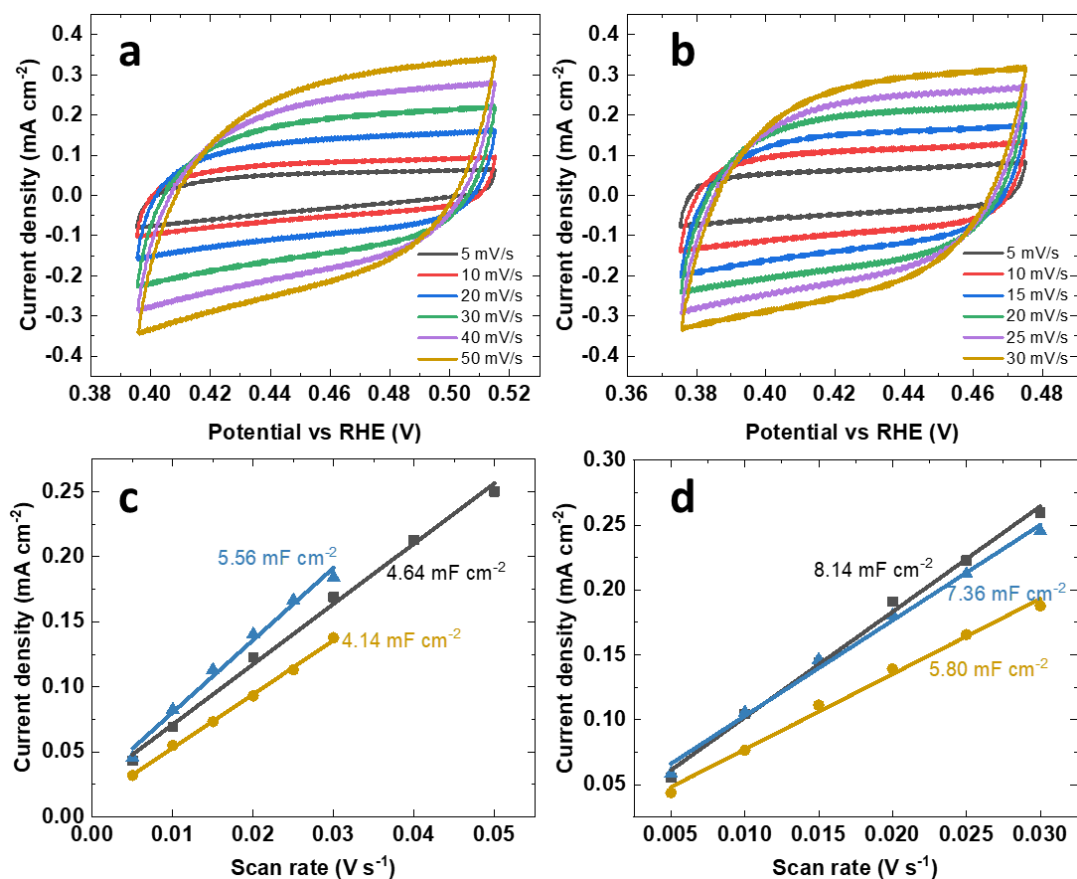
Figure S4.16 Determination of the double layer capacitance of the WCO-Cu and TA-Cu. Cyclic voltammograms of (a) WCO-Cu and (b) TA-Cu at various scan rates in a potential window where only double layer charging and discharging are involved. The plots of corresponding current density against CV scan rate on (C) WCO-Cu and (d) TA-Cu. For each catalyst, the CVs measurements were repeated on three independent samples.

Table S4.1 Capacitance values and surface roughness factors derived from the CVs corresponding to Figure S4.16. The surface roughness factor of polycrystalline Cu is from Ref 1 [1] and defined as 1.

Electrode	Capacitance	Surface roughness factor
Polycrystalline Cu [1]	29 µF cm^{-2}	1
WCO-Cu	4.78 $\pm$ 0.59 mF cm^{-2}	165
TA-Cu	7.10 $\pm$ 0.97 mF cm^{-2}	245

Table S4.2 Faradaic efficiencies and current densities as a function of potential of WCO-Cu and TA-Cu in three conditions: H-cell with 0.1 M KHCO₃, flow cell with 1 M KHCO₃, and flow cell with 1 M KOH, corresponding to Figure S4.10and S4.11, and Figure 4.3, respectively. The average values of at least three measurements were reported.

Potential	Faradaic efficiency (%)									Current density
V vs RHE	H₂	CO	C₂H₄	C₂H₆	Formate	Acetate	Ethanol	Acetone	n-propanol	mA cm⁻²
WCO-Cu in H-cell with 0.1 M KHCO3										
-0.39	34.60	44.73			6.73					0.59
-0.47	27.02	46.74	0.00	0.00	9.45	0.00	0.00	0.00	0.00	1.08
-0.55	12.21	51.14	0.00	0.00	26.73	0.55	0.00	0.00	0.00	2.62
-0.62	14.77	33.45	0.49	0.00	42.23	1.01	0.00	0.00	0.00	4.72
-0.69	31.61	15.75	3.43	0.10	34.71	0.75	0.00	0.63	1.53	10.00
-0.79	38.22	9.71	10.56	0.00	23.11	0.76	0.00	0.39	3.63	14.32
-0.88	40.57	5.48	16.16	0.27	19.08	0.67	1.24	1.22	4.82	20.94
-0.99	49.26	1.66	15.24	0.00	24.64	0.31	1.25	1.49	2.19	35.88
TA-Cu in H-cell with 0.1 M KHCO3										
-0.30	26.15	25.99	0.00	0.00	6.68	0.00	0.00	0.00	0.00	0.31
-0.39	22.62	54.13	0.00	0.00	7.39	0.00	0.00	0.00	0.00	0.74
-0.46	16.07	59.40	0.00	0.00	16.54	1.69	0.00	0.00	0.00	1.85
-0.54	23.60	31.95	0.00	0.00	37.23	0.82	0.00	0.00	0.00	3.75
-0.62	31.61	18.18	0.00	1.25	33.60	0.88	1.37	0.00	0.00	6.88
-0.69	45.35	7.89	4.94	3.10	20.39	0.90	1.22	0.00	1.92	25.00
-0.84	43.73	3.30	16.02	4.08	12.08	0.75	4.26	0.57	4.25	46.88
-0.95	38.37	1.06	27.97	2.91	7.07	0.38	8.22	0.36	3.99	78.13
WCO-Cu in flow cell with 1 M KHCO3										
-0.47	33.14	33.15			4.88		0.52			4.00
-0.54	44.28	28.29	3.63		6.05		1.11			10.00
-0.70	38.48	24.25	7.18	0.67	16.09	0.54	2.55		1.87	50.00
-0.78	28.61	28.64	11.60	0.87	12.46	0.43	3.00		2.22	100.00
-0.81	24.66	29.61	16.82	0.58	8.26	0.35	3.82		2.10	200.00
-0.83	20.81	28.48	22.95	0.53	5.45	0.24	6.06		1.94	300.00
TA-Cu in flow cell with 1 M KHCO3										
-0.40	30.50	30.83	1.21		4.51	1.60	0.94			8.00
-0.47	49.63	17.41	3.12		6.09	1.53	2.57			20.00
-0.61	53.81	8.00	6.37	0.79	7.50	1.01	3.23		1.60	50.00
-0.71	38.64	8.25	14.78	1.52	8.41	0.67	3.96		2.88	100.00
-0.82	36.15	9.47	23.64	0.88	3.15	0.47	6.57		2.92	200.00
-0.85	40.00	8.58	24.92	0.29	2.22	0.33	6.96		2.39	300.00
WCO-Cu in flow cell with 1 M KOH										
-0.30	35.25	25.85	3.56		13.86					14.00
-0.41	27.63	24.93	10.93	0.51	22.66	0.26	2.62		2.07	50.00
-0.48	23.63	21.80	17.95	0.65	18.07	0.36	4.60		2.99	100.00
-0.52	20.23	23.91	19.73	0.30	14.65	0.22	4.61		2.28	150.00
-0.55	19.50	22.73	22.08	0.30	13.68	0.22	6.06		2.19	200.00
-0.59	20.28	21.09	24.98	0.39	10.64	0.25	6.27		2.26	250.00
-0.62	20.03	18.85	26.98	0.31	9.24	0.24	7.30		1.99	300.00
TA-Cu in flow cell with 1 M KOH										
-0.28	53.19	11.14	5.76	1.47	10.83	1.65	2.89		1.15	50.00
-0.39	37.99	9.16	14.36	2.79	16.32	1.29	3.86		2.84	100.00
-0.44	37.03	7.15	21.98	2.22	12.93	0.99	5.30		3.26	150.00
-0.49	34.36	6.60	27.34	1.13	9.71	0.69	7.02		3.06	200.00
-0.52	34.91	7.50	29.07	1.11	6.45	0.67	7.64		2.82	250.00
-0.59	39.17	6.11	28.90	0.62	4.95	0.47	7.43		2.37	300.00

References

1.   C. W. Li and M. W. Kanan, *Journal of the American Chemical Society*, 2012, **134**, 7231-7234.

This page is intentionally left blank

Chapter 5 Crossover of Liquid Products through Gas Diffusion Electrode and Anion Exchange Membrane

Jie Zhang[a, b], Wen Luo [a, b*], Andreas Züttel[a, b]

Abstract

We reveal that a significant amount (>30%) of the liquid products from electrochemical CO_2 reduction (eCO_2RR) in a flow reactor can cross the gas diffusion electrode (GDE) and anion exchange membrane (AEM). Crossover of volatile products through the GDE occurs mainly by evaporation, and the migration rate increases linearly with current density and CO_2 flow rate. Non-volatile products prefer to cross the AEM through electromigration, and the migration rate is affected by the current density and the flow rate of the catholyte. These results highlight the importance of considering product crossover during eCO_2RR to adequately assess the catalytic performance.

[a] *Laboratory of Materials for Renewable Energy (LMER), Institute of Chemical Sciences and Engineering (ISIC), Basic Science Faculty (SB), École Polytechnique Fedérale de Lausanne (EPFL) Valais/Wallis, Energypolis, Rue de l'Industrie 17, CH-1951 Sion, Switzerland.*

[b] *Empa Materials Science & Technology, CH-8600 Dübendorf, Switzerland*

Author Contributions: Jie Zhang, Wen Luo, and Andreas Züttel conceived the experiments and co-wrote the manuscript. Jie Zhang designed and performed the experiment.

5.1 Introduction

The rapid development of human civilization over recent decades relies on energy and commodities produced from fossil fuels.[1, 2] However, the consumption of fossil fuels not only leads to a depletion of finite reserves but also drastically increases carbon dioxide (CO_2) emissions into the atmosphere, which is largely responsible for anthropogenic climate changes.[3, 4] The electrochemical reduction of CO_2 (eCO$_2$RR) into fuels, feedstocks, and commodity chemicals has great potential to transform the petrochemical sector toward sustainability and to mitigate greenhouse gas emissions.[5, 6] While much effort has been devoted to the development of advanced catalysts for eCO$_2$RR, most previous publications have applied a two-compartment batch reactor (H-cell) to evaluate the catalytic performance.[7] Due to the fact that CO_2 is supplied by "purging into electrolyte," the low CO_2 solubility in aqueous electrolytes (33 mM at ambient conditions) limits the current density in an H-cell to the order of 10 mA cm^{-2}. To meet the requirements of commercial operation (e.g., >200 mA cm^{-2}), an increasing number of studies[7-10] (Figure S5.1) including our works,[11, 12] have begun using flow reactors in which a gas diffusion electrode (GDE) is used and the CO_2 gas and electrolyte are supplied continuously from different reactor chambers, thus overcoming the mass transport limitation.

Although performing eCO$_2$RR in flow reactors can drastically improve the reaction rate, this technique still suffers from some critical issues, such as the flooding of the GDE,[13] salt accumulation,[8] CO_2 crossover,[14, 15] and the crossover of liquid products.[16] Among these issues, the crossover of liquid products through the GDE and ion exchange membrane (IEM) is relatively unexplored. More specifically, liquid products (e.g., formate, ethanol, n-propanol, etc.) from eCO$_2$RR are generated on the cathode and are supposed to fully dissolve in the catholyte, therefore IEMs are rquired in CO_2 electrolysis reactors to prevent liquid products from diffusing to and being oxidized by the anode (Scheme 5.1a). [17]
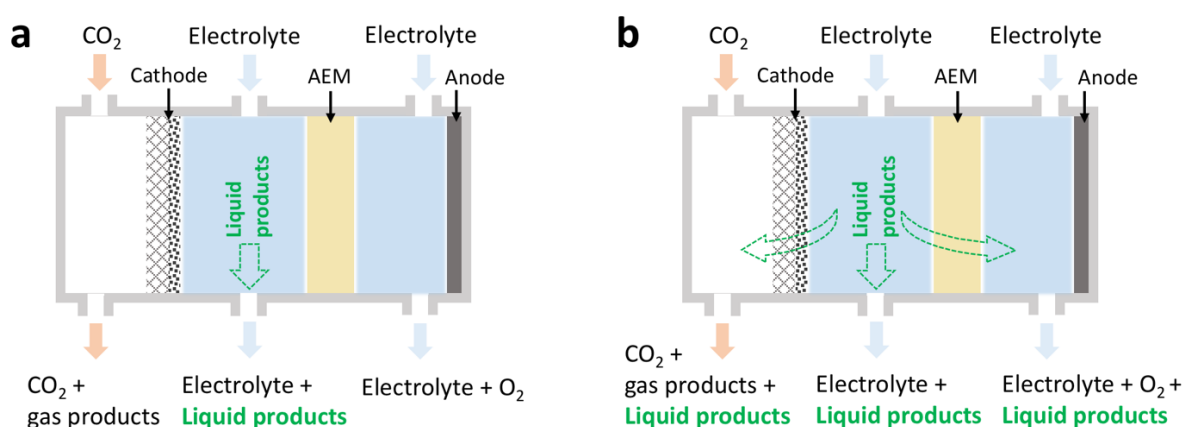
Scheme 5.1 (a) Schematic of the product distribution in the flow reactor according to the conventional assumption that liquid products are fully dissolved in the catholyte. (b) Schematic of the flow reactor showing the evaporation of volatile liquid products into the CO_2 off-gas and the diffusion of liquid products through the AEM.

However, IEMs are not fully impermeable to these molecules (Scheme 5.1b).[16, 18, 19] When using flow reactors operating under high current densities (e.g., >200 mA cm^{-2}), the crossover of liquid products through the IEM can be more pronounced due to the much higher product concentration.

Moreover, the oxygenated products (e.g., acetone, ethanol, and n-propanol, etc.) from eCO$_2$RR may evaporate through the GDE (Scheme 5.1b) into CO$_2$ off-gas because of their high volatility. However, to the best of our knowledge, such evaporation has not been considered in previous studies. Thus, it is necessary to quantitatively evaluate the crossover of the liquid products in flow reactors during eCO$_2$RR so as to avoid product loss and the misevaluation of catalytic performance.

Through a systematic investigation using a full-product-collection protocol, we identified herein that up to 30% of liquid products can cross the GDE and up to 10% can cross anion exchange membrane (AEM). In addition, the influences of the flow rate of CO$_2$ and catholyte and the type of AEM on the crossover of liquid products have also been addressed. As the accurate quantification of reaction products is a prerequisite for understanding the catalytic performance and the collection and separation of products are important steps in industrial production, our findings are of great importance for both fundamental studies and industrial applications.

5.2   Experimental part

The electrochemical measurement system is shown in Scheme 5.2, consisting of a mass flow controller, a typical three-chamber flow cell electrolyzer,[8, 17] two electrolyte storage tanks, two peristaltic pumps, a tube of water for washing the CO$_2$ off-gas, an on-line gas chromatography (GC) system, and an off-line nuclear magnetic resonance (NMR) system. The flow reactor consists of a CO$_2$ chamber made from stainless steel, a catholyte chamber and an anolyte chamber made from polytetrafluoroethylene (PTFE), and an AEM between the catholyte and anolyte chambers. The catholyte and anolyte chambers are 3 mm and 5 mm thick, respectively, with a window of 5 mm by 10 mm, which determines the area (0.5 cm^{-2}) of the working electrode. An Ag/AgCl (3 M KCl) reference electrode was connected at the upstream of the catholyte flow. The counter electrode was a nickel gauze. The gas diffusion electrodes were prepared by sputter-coating or drop-casting of catalysts on carbon paper (Sigracet 39BC).
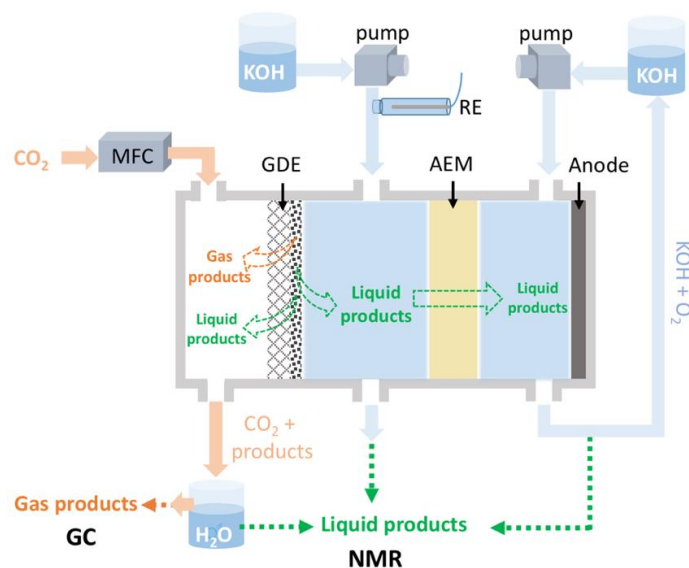
Scheme 5.2 Flow diagram of the flow cell setup for eCO$_2$RR. GDE: gas diffusion electrode, AEM: anion exchange membrane, MFC: mass flow controller, RE: reference electrode, NMR: nuclear magnetic resonance, GC: gas chromatography.

To identify the crossover of the liquid products from eCO$_2$RR, we collected possible migrated products in all three chambers of the flow cell (Scheme 5.2). Both the catholyte and the anolyte were collected and analyzed using NMR. CO$_2$ off-gas was washed with a water bath and analyzed using online GC, and the washing liquid was also analyzed using NMR. As confirmed by an additional water bath in series with the first water bath, neglected liquid products passed through the first water bath (Figure S5.2). Further experimental details are described in the Supporting Information.

5.3   Results and discussion

We prepared a typical Cu-based GDE by sputter-coating the carbon paper with a Cu layer (75 nm thick) and evaluated its eCO$_2$RR performance in a flow reactor using 1.0 M KOH electrolyte. Scanning electron microscope images of the GDE are presented in Figure S5.3. The Cu catalyst was selected because it can reduce CO$_2$ into a broad range of liquid products with sufficient Faradaic efficiency (FE).[20, 21] The design and operation conditions of the flow reactor (Experimental part) are consistent with those commonly reported conditions[10, 17, 21, 22] in the field and, thus, can comprehensively reflect the crossover issues of the flow reactor. The catalytic performance was evaluated under constant current density mode and the product distributions as a function of current density are shown in Figure 5.1. Figure 5.1a and Table S5.1 show that various gaseous (e.g., H$_2$, CO, CH$_4$, and C$_2$H$_4$) and liquid (e.g., formate, acetate, ethanol, n-propanol, and methanol) products were detected from CO$_2$ off-gas and catholyte, respectively, in agreement with previous results obtained from Cu-based catalysts.[8] However, the sum of FEs is significantly lower than 100%, ranging between 88% to 96% depending on the applied current density. As discussed earlier, liquid products can cross the GDE and AEM to the other two compartments of the flow reactor, leading to lower cumulative FEs when only the liquid products in the catholyte were analyzed (Scheme 5.1a). To verify this, we collected the anolyte and the water used to wash the CO$_2$ off-gas (Scheme 5.1b) and analyzed them with NMR. The ^{1}H NMR spectra of these two solutions also show obvious peaks of various liquid products (Figure S5.4), demonstrating that liquid products indeed migrated across the GDE and AEM. By adding up all of these detected products, the total FE reached 100 ±2% (Figure 5.1b), confirming that the liquid products in the CO$_2$ off-gas and anolyte were the "missing" products. This result also indicates that liquid products were barely oxidized on the anode, probably due to the short reaction time (~20 min) and the slow oxidation rate.

Furthermore, two control measurements were conducted: (1) changing the electrolyte to 1.0 M KHCO$_3$ and (2) changing the catalyst to commercial CuO nanoparticles. Similar to the above results, liquid products of the control experiments were also detected in the anolyte and CO$_2$ off-gas (Figure S5.5 and S5.6), indicating that the migration phenomena is independent of the catalyst preparation method and the electrolyte. We also measured the crossover of the liquid products when the catholyte was recirculated. As expected, due to the accumulation of liquid products in the catholyte, the recirculation enhanced the crossover through both GDE and AEM compared to that when the catholyte was supplied in a single pass (Figure S5.7).

Through analyzing the distribution of the liquid products in the three chambers of the flow cell (Figure 5.1c and Figure S5.8), we found that, surprisingly, acetone, acetaldehyde, and propionaldehyde were only detected in the CO$_2$-off gas but not in the catholyte or anolyte. This should

be attributed to their very low production rates (<0.02 μmol cm^{-2} min^{-1}) and high volatility. In addition, most of the migrated n-propanol and ethanol were present in the CO_2 off-gas rather than in the anolyte, implying that these volatile products prefer to cross the GDE through evaporation. Trace amounts of ethanol can also be found in the anolyte, likely due to the diffusion and electroosmotic drag of the ethanol, which has a higher concentration compared to other neutral oxygenates.[23] Formate and acetate, on the other hand, are nonvolatile and negatively charged, and thus prefer to cross the AEM into the anolyte through electromigration.[23]
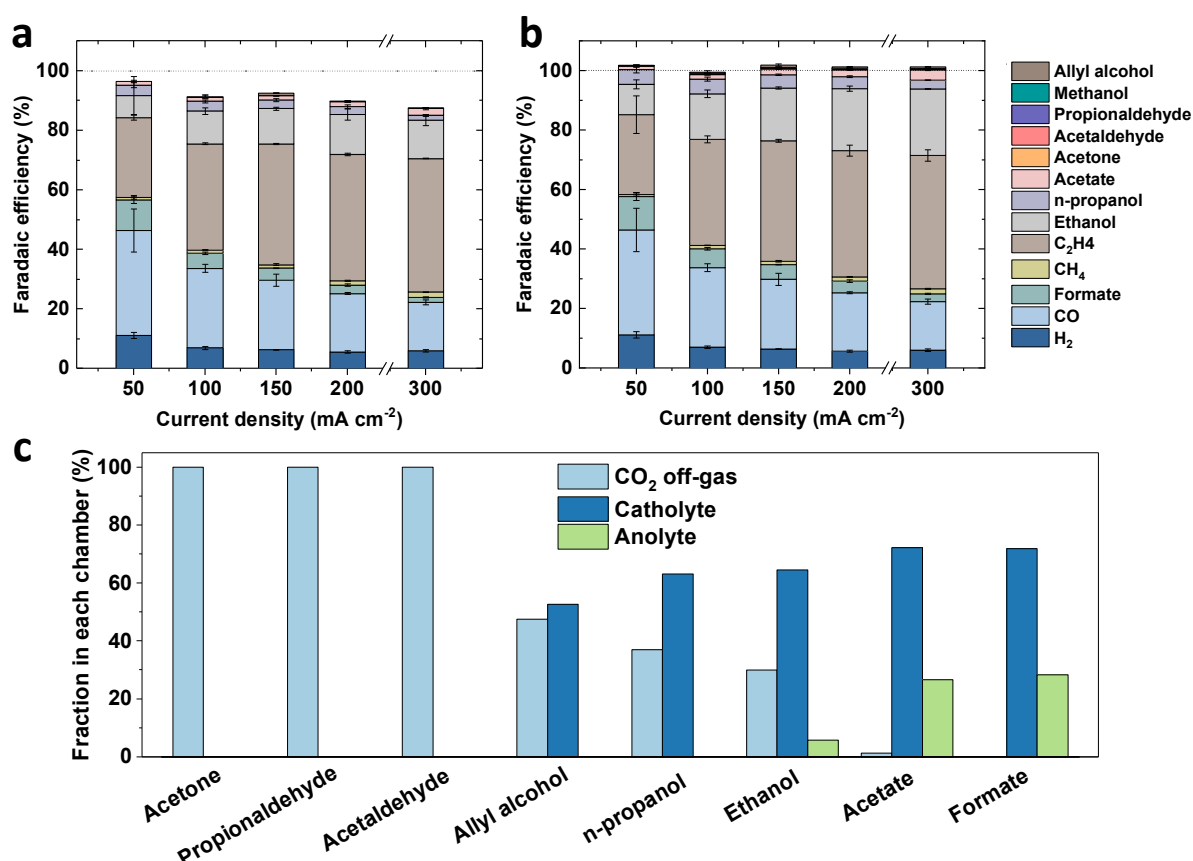
Figure 5.1 Faradaic efficiency, (a) excluding and (b) including the liquid products from the CO_2 off-gas and anolyte, of Cu catalysts as a function of current density. (c) Molar fraction of each liquid product in the three compartments of the flow cell for eCO_2RR at 200 mA cm^{-2}. Electrolyte: 1.0 M KOH, CO_2 flow rate: 50 ml min^{-1}, and AEM: from Lin Zhuang's lab. Error bars represent the standard deviation of three independent measurements with three different electrodes.

Figure 5.1 also shows that the amount of migrated liquid products increased with increasing applied current density. The current density impacts the migration of liquid products from three aspects. Firstly, an increase of current density leads to a higher concentration of liquid products at a constant catholyte flow rate, which then increases the crossover rate because the crossover rate is proportional to the product concentration (Figure S5.9). Secondly, current density and the corresponding potential affect the rate of electromigration and electroosmotic drag. Lastly, a higher current density also results in a higher production rate of gaseous products, and thus the gas bubbles may accelerate the evaporation of liquid products. Specifically, the evaporated alcohols rapidly increased from 26.8% to 36.3% for ethanol and from 29.3% to 46.7% for n-propanol when the current density rose from 50 mA

cm^{-2} to 300 mA cm^{-2} (Figure 5.2a). Interestingly, a high ratio of n-propanol evaporated through the GDE compared to ethanol, even though ethanol is more volatile than n-propanol. We suggest this counterintuitive phenomenon arises from that the production rate of n-propanol (0.28 µmol cm^{-2} min^{-1}) is much lower than that of ethanol (2.16 µmol cm^{-2} min^{-1}). Together with the fact that acetone, acetaldehyde, and propionaldehyde are only found in CO_2 off-gas, these results imply that volatile products with low production rates prefer to diffuse through the GDE into the CO_2 gas. This may be due to that a small number of volatile molecules formed at the gas-catalyst-liquid interface can readily diffuse into the gas phase while products with higher generation rates mostly dissolve in the electrolyte.

We then performed eCO$_2$RR over the sputtered Cu catalyst at different CO_2 flow rates to study the influence of CO_2 flow on the evaporation of volatile products. As shown in Figure 5.2b and Figure S5.10, the evaporated liquid products show an increasing trend with the increase of CO_2 flow rate from 25 ml min^{-1} to 100 ml min^{-1}. This is because the convection introduced by the CO_2 flow enhances the transfer of molecules away from the catalyst surface, and the higher CO_2 flow rate reduces the diffusion layer and thus increases the diffusion rate. The local mass transfer coefficient of the vapors of volatile products at the gas-chamber side can be estimated by using Lévêque-type equation (see supporting information for modelling details). The calculated results (Figure S5.14) show that the mass transfer coefficients of the vapors of the volatile products increase with increasing CO_2 flow rate, which is in good agreement with our experimental observations. Moreover, the importance of evaluating the crossover effect under eCO$_2$RR conditions can be further supported by our control experiments, where the product-crossover rates under steady state (without applying a potential) are much lower than those under eCO$_2$RR conditions (Figure S5.9).
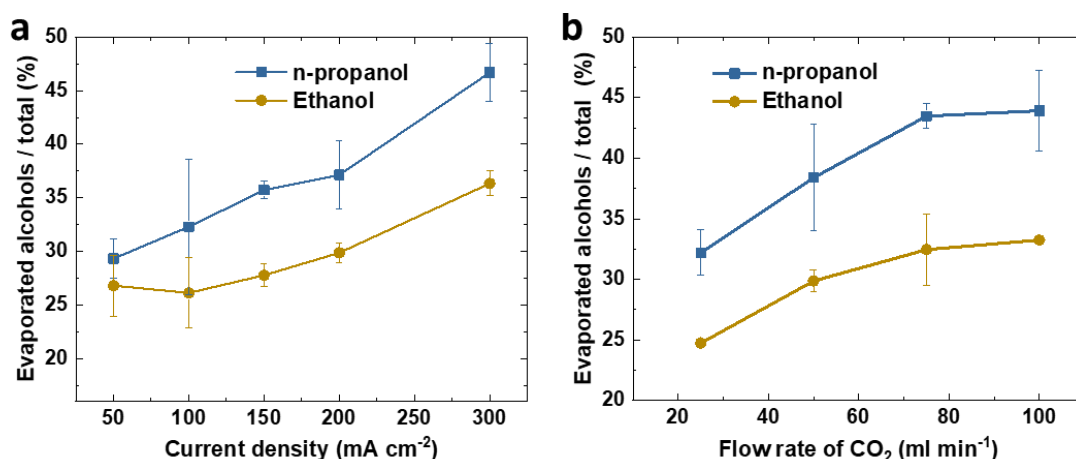
Figure 5.2 The ratio of the ethanol and n-propanol in the CO_2 off-gas to the total produced ethanol and n-propanol, respectively, (a) as a function of applied current density at 50 ml min^{-1} of CO_2 flow and (b) as a function of the CO_2 flow rate at 200 mA cm^{-2}. Electrolyte: 1.0 M KOH, and AEM: from Lin Zhuang's lab. Error bars represent the standard deviation of three independent measurements with three different electrodes.

To further investigate the crossover of liquid products across the AEM, we evaluated a formate selective catalyst, a Sn-based GDE, in the flow reactor with 1.0 M KOH as the electrolyte. As shown in Figure 5.3a and Table S5.3, this catalyst showed over 90% FE for formate in the current density range from 50 mA cm^{-2} to 300 mA cm^{-2}, consistent with previous reports.[24, 25] Including for CO and H$_2$, the

overall FEs can reach 100% (Table S5.3). Similar to the Cu catalyst, with the increase of current density, the increased formate concentration in the catholyte led to a higher ratio of formate in the anolyte (Figure 5.3a and Figure S5.11). Since a higher catholyte flow rate can decrease the concentration of formate in the catholyte at a given formate production rate and the migration rate of formate through AEM is proportional to the concentration (Figure S5.9), we did observe that an increase in the catholyte flow rate resulted in a decreased ratio of formate in the anolyte (Figure 5.3b). Specifically, when the flow rate of the catholyte reached 2.0 ml min^{-1} at a formate concentration of ~14.06 mM, the migrated formate can be neglected (0.41% of produced formate was in anolyte). It is worth noting, however, that it is not economically feasible to increase the electrolyte flow rate to reduce the product concentration in large-scale applications because of the increased separation costs. In addition, we also tested four different types of AEMs and found that all were formate permeable. 17% to 30% of produced formate were detected in the anolyte at a catholyte flow rate of 0.3 ml min^{-1} and a current density of 200 mA cm^{-2} (Figure 5.3c). Cation-exchange membranes, such as Nafion, were not considered since they are not suitable for high pH electrolysis and are known to allow product crossover.[14, 16] Overall, these results highlight that crossover can be a general issue in eCO$_2$RR using flow reactor system, requiring further consideration in future studies and applications.
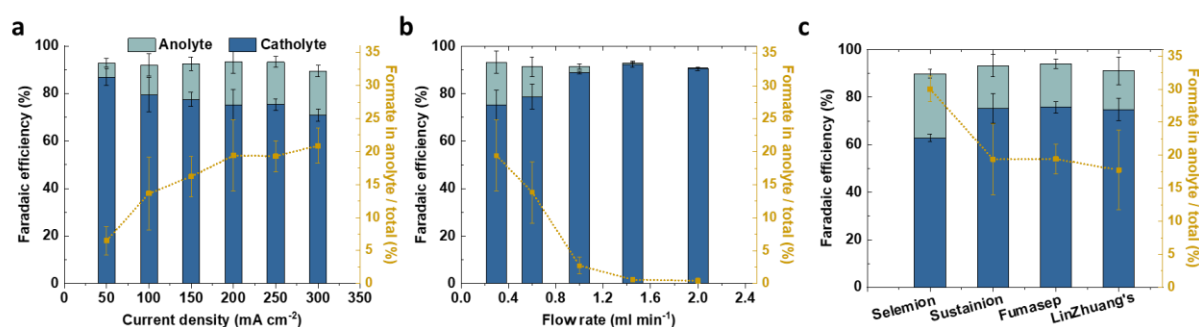
Figure 5.3 Influence of (a) the current density (catholyte flow rate: 0.3 ml min^{-1}), (b) the flow rate (current density: 200 mA cm^{-2}), and (c) the type of membrane (catholyte flow rate: 0.3 ml min^{-1}, current density: 200 mA cm^{-2}) on the Faradaic efficiency and crossover of formate of Sn-based GDEs. Electrolyte: 1.0 M KOH, CO$_2$ flow rate: 50 ml min^{-1}, and AEM for (a) and (b): Sustainion. Error bars represent the standard deviation of three independent measurements with three different electrodes.

Based on the results above, some implications and perspectives can be discussed. In practical applications, low catholyte and CO$_2$ flow rates are preferred to achieve high liquid product concentrations in catholyte and high single pass conversions of CO$_2$, respectively. According to our results, low catholyte flow rate (or recirculated catholyte) would exacerbate the crossover issue, so if crossover cannot be avoided some trade-offs may need to be considered. On the other hand, lowing the CO$_2$ flow rate is expected to mitigate the evaporation issue due to the reduced concentration gradient of volatile products. However, Larrazábal et al. recently reported that CO$_2$ can cross the GDE into the electrolyzer, resulting in low utilization of CO$_2$ and overestimation of gas product selectivity, both of which are worsen with decreasing CO$_2$ flow.[14] Although the influence of CO$_2$ crossover on our FE calculations can be neglected due to the small GDE size (0.5 cm^2) used in this work (Figure S5.12), these results suggest that the crossover issues cannot be simply solved by optimizing the CO$_2$ flow rate, and emphasize that a full mass balance analysis is required to accurately evaluate the eCO$_2$RR

performance. In addition, we note that product crossover may also take place in other reactions, such as the electrochemical reduction of CO and N_2 in flow reactors, since these reactions also produce molecules that can cross the GDE and AEM. Moreover, as GDE and/or AEM are also used in membrane electrode assemblies and solid electrolyte electrolyzers, we encourage the consideration of product crossover as a valuable metric to complement the evaluation of electrolyzers operating at high current densities.

5.4 Conclusions

In summary, we identified the migration of liquid products from eCO_2RR across the gas diffusion electrode and anion exchange membrane in a flow reactor and systematically investigated the factors that influence the migration. Our results show that volatile products, such as n-propanol, ethanol, allyl alcohol, methanol, acetone, acetaldehyde, and propionaldehyde, prefer evaporation through the GDE into the CO_2 off-gas, while nonvolatile products, such as formate and acetate, prefer to cross the AEM into the anolyte through electromigration. The evaporation rate of volatile products is affected by the applied current density and CO_2 flow rate, and up to 40% of the produced alcohols can cross the GDE under our experimental conditions. Moreover, we find that the applied current density, the flow rate of the catholyte and the type of AEM affect the crossover rate of liquid products through the AEM. Therefore, failure to account for the crossover of liquid products may lead to a substantial underestimation of the liquid product selectivity. Overall, we expect our work can help achieve more accurate product quantification and better assessment of catalytic performance and encourage future research into the design of advanced CO_2 electrolysis systems.

5.5 Acknowledgements

5.6 References

[1]   S. Verma, S. Lu, P.J.A. Kenis, Co-electrolysis of CO_2 and glycerol as a pathway to carbon chemicals with improved technoeconomics due to low electricity consumption, Nature Energy, 4 (2019) 466-474.

[2]   G.T. Miller, S. Spoolman, Living in the Environment, Cengage Learning2017.

[3]   O. Hoegh-Guldberg, P.J. Mumby, A.J. Hooten, R.S. Steneck, P. Greenfield, E. Gomez, C.D. Harvell, P.F. Sale, A.J. Edwards, K. Caldeira, N. Knowlton, C.M. Eakin, R. Iglesias-Prieto, N. Muthiga, R.H. Bradbury, A. Dubi, M.E. Hatziolos, Coral Reefs Under Rapid Climate Change and Ocean Acidification, Science, 318 (2007) 1737-1742.

[4]   J.C. Orr, V.J. Fabry, O. Aumont, L. Bopp, S.C. Doney, R.A. Feely, A. Gnanadesikan, N. Gruber, A. Ishida, F. Joos, R.M. Key, K. Lindsay, E. Maier-Reimer, R. Matear, P. Monfray, A. Mouchet, R.G. Najjar, G.-K. Plattner, K.B. Rodgers, C.L. Sabine, J.L. Sarmiento, R. Schlitzer, R.D. Slater, I.J. Totterdell, M.-F. Weirig, Y. Yamanaka, A. Yool, Anthropogenic ocean acidification over the twenty-first century and its impact on calcifying organisms, Nature, 437 (2005) 681-686.

[5]   P. De Luna, C. Hahn, D. Higgins, S.A. Jaffer, T.F. Jaramillo, E.H. Sargent, What would it take for renewably powered electrosynthesis to displace petrochemical processes?, Science, 364 (2019) eaav3506.

[6]   S. Nitopi, E. Bertheussen, S.B. Scott, X. Liu, A.K. Engstfeld, S. Horch, B. Seger, I.E.L. Stephens, K. Chan, C. Hahn, J.K. Nørskov, T.F. Jaramillo, I. Chorkendorff, Progress and Perspectives of Electrochemical CO_2 Reduction on Copper in Aqueous Electrolyte, Chemical Reviews, 119 (2019) 7610-7672.

[7]   D.M. Weekes, D.A. Salvatore, A. Reyes, A. Huang, C.P. Berlinguette, Electrolytic CO_2 Reduction in a Flow Cell, Accounts of Chemical Research, 51 (2018) 910-918.

[8]   J.-J. Lv, M. Jouny, W. Luc, W. Zhu, J.-J. Zhu, F. Jiao, A Highly Porous Copper Electrocatalyst for Carbon Dioxide Reduction, Advanced Materials, 0 (2018) 1803111.

[9]   T. Burdyny, W.A. Smith, CO_2 reduction on gas-diffusion electrodes and why catalytic performance must be assessed at commercially-relevant conditions, Energy & Environmental Science, 12 (2019) 1442-1453.

[10]   K. Liu, W.A. Smith, T. Burdyny, Introductory Guide to Assembling and Operating Gas Diffusion Electrodes for Electrochemical CO_2 Reduction, ACS Energy Letters, 4 (2019) 639-643.

[11]   W. Luo, J. Zhang, M. Li, A. Züttel, Boosting CO Production in Electrocatalytic CO_2 Reduction on Highly Porous Zn Catalysts, ACS Catalysis, 9 (2019) 3783-3791.

[12]   J. Zhang, W. Luo, A. Züttel, Self-supported copper-based gas diffusion electrodes for CO_2 electrochemical reduction, Journal of Materials Chemistry A, 7 (2019) 26285-26292.

[13]   S. Verma, Y. Hamasaki, C. Kim, W. Huang, S. Lu, H.-R.M. Jhong, A.A. Gewirth, T. Fujigaya, N. Nakashima, P.J.A. Kenis, Insights into the Low Overpotential Electroreduction of CO_2 to CO on a Supported Gold Catalyst in an Alkaline Flow Electrolyzer, ACS Energy Letters, 3 (2018) 193-198.

[14]   G.O. Larrazábal, P. Strøm-Hansen, J.P. Heli, K. Zeiter, K.T. Therkildsen, I. Chorkendorff, B. Seger, Analysis of Mass Flows and Membrane Cross-over in CO_2 Reduction at High Current Densities in an MEA-Type Electrolyzer, ACS Applied Materials & Interfaces, 11 (2019) 41281-41288.

[15]   M. Lin, L. Han, M.R. Singh, C. Xiang, An Experimental- and Simulation-Based Evaluation of the CO_2 Utilization Efficiency of Aqueous-Based Electrochemical CO_2 Reduction Reactors with Ion-Selective Membranes, ACS Applied Energy Materials, 2 (2019) 5843-5850.

[16]   Y.C. Li, Z. Yan, J. Hitt, R. Wycisk, P.N. Pintauro, T.E. Mallouk, Bipolar Membranes Inhibit Product Crossover in CO_2 Electrolysis Cells, Advanced Sustainable Systems, 2 (2018) 1700187.

[17]   S. Ma, M. Sadakiyo, R. Luo, M. Heima, M. Yamauchi, P.J.A. Kenis, One-step electrosynthesis of ethylene and ethanol from CO_2 in an alkaline electrolyzer, Journal of Power Sources, 301 (2016) 219-228.

[18]   X. Zhou, R. Liu, K. Sun, Y. Chen, E. Verlage, S.A. Francis, N.S. Lewis, C. Xiang, Solar-Driven Reduction of 1 atm of CO_2 to Formate at 10% Energy-Conversion Efficiency by Use of a TiO2-Protected III–V Tandem Photoanode in Conjunction with a Bipolar Membrane and a Pd/C Cathode, ACS Energy Letters, 1 (2016) 764-770.

[19]   M. Ramdin, A.R.T. Morrison, M. de Groen, R. van Haperen, R. de Kler, E. Irtem, A.T. Laitinen, L.J.P. van den Broeke, T. Breugelmans, J.P.M. Trusler, W.d. Jong, T.J.H. Vlugt, High-Pressure Electrochemical Reduction of CO_2 to Formic Acid/Formate: Effect of pH on the Downstream Separation Process and Economics, Industrial & Engineering Chemistry Research, 58 (2019) 22718-22740.

[20]   K.P. Kuhl, E.R. Cave, D.N. Abram, T.F. Jaramillo, New insights into the electrochemical reduction of carbon dioxide on metallic copper surfaces, Energy & Environmental Science, 5 (2012) 7050-7059.

[21]   C.-T. Dinh, T. Burdyny, M.G. Kibria, A. Seifitokaldani, C.M. Gabardo, F.P. García de Arquer, A. Kiani, J.P. Edwards, P. De Luna, O.S. Bushuyev, C. Zou, R. Quintero-Bermudez, Y. Pang, D. Sinton, E.H. Sargent, CO_2 electroreduction to ethylene via hydroxide-mediated copper catalysis at an abrupt interface, Science, 360 (2018) 783-787.

[22]   M. Ma, E.L. Clark, K.T. Therkildsen, S. Dalsgaard, I. Chorkendorff, B. Seger, Insights into the carbon balance for CO_2 electroreduction on Cu using gas diffusion electrode reactor designs, Energy & Environmental Science, 13 (2020) 977-985.

[23]   C.M. Gabardo, C.P. O'Brien, J.P. Edwards, C. McCallum, Y. Xu, C.-T. Dinh, J. Li, E.H. Sargent, D. Sinton, Continuous Carbon Dioxide Electroreduction to Concentrated Multi-carbon Products Using a Membrane Electrode Assembly, Joule, (2019).

[24]   W. Luc, B.H. Ko, S. Kattel, S. Li, D. Su, J.G. Chen, F. Jiao, SO_2-Induced Selectivity Change in CO_2 Electroreduction, Journal of the American Chemical Society, 141 (2019) 9902-9909.

[25]   S. Sen, S.M. Brown, M. Leonard, F.R. Brushett, Electroreduction of carbon dioxide to formate at high current densities using tin and tin oxide gas diffusion electrodes, Journal of Applied Electrochemistry, 49 (2019) 917-928.

5.7   Supporting information

Experimental sections

Chemicals

The copper (99.9%) target used in the sputter coater was purchased from Goodfellow. Sn particles (< 150 nm) and Cu_2O (< 350 nm) dispersion were purchased from Sigma Aldrich. Potassium hydroxide (KOH, 50wt% of solution) were purchased from Carl Roth. Carbon paper (Sigracet 39BC) purchased from Fuel Cell Store were used for prepared all GDEs in this work. The four types of anion exchange membrane used in this work were Sustainion® X37-5 (from Dioxide materials[TM]), Fumasep® FAA-3-50 (from FuMA-Tech) and AE< fro, Linzhang's lab[1] (from Hephas energy), and Selemion AMV (from AGC Engineering). All the chemicals were used without purification. Carbon dioxide (99.998%) was supplied by Carbagas. Deionized water (18.2 MΩ) produced by a Milipore system was used to prepare electrolyte.

Preparation of electrodes

Cu GDEs were prepared by sputter coating or drop casting. For sputter coating, 75 nm thick (measured by the quartz crystal microbalance) of Cu layer were deposited on the carbon paper by sputter coating at 60 mA with (Quorum Q150T ES). For drop casting, the commercial Cu_2O were firstly oxidized to be CuO in NH_3 H_2O solution (reference) and then the ink of CuO (2.7 mg cm^{-1}) was drop-casted on the carbon paper. To oxidize Cu_2O, 157 µl of 2.45 mM $NH_3 \bullet H_2O$ was added into 615 µl of 11.44 mg ml^{-1} Cu_2O dispersion in ethanol and then the mixture was stir for two hours and separated by centrifuge. The CuO catalyst ink were prepared by sonicating the mixture of 8 mg of CuO particles, 7 µL of Nafion solution (5 wt % in water and alcohol), and 1 mL of isopropanol.

Tin GDEs with tin loading of 0.4 mg cm^{-2} were prepared by drop-casting the tin catalyst ink on the carbon paper. The Tin catalyst ink was prepared by sonicating the mixture of 24 mg of metal particles, 21 µL of Nafion solution (5 wt % in water and alcohol), and 3 mL of isopropanol.

Evaluation of the performance for eCO$_2$RR

Collection of the liquid products

The design of the flow cell system is presented in the main text. The peristaltic pump (multi-channels) fed the anolyte and catholyte from their storage tank into the anolyte chamber and catholyte chamber of the flow reactor. The catholyte flowing out of the reactor was directly collected while the anolyte (10 ml) was circulated. After reaction, the catholyte chamber was rinsed with a few milliliters of flowing electrolyte to collect any liquid product that may remain. Before entering GC, the CO_2 off-gas was washed with a tube of water (5 ml of water, 100 mm long of bath and 100 mm long of headspace) to absorb the vapor liquid products in the CO_2 off-gas. This CO_2 washing liquid, catholyte, and the anolyte were analyzed by NMR. To confirm the CO_2 off-gas was completely washed, another tube of water was connected in series after the first one. It turned out that the liquid products in the second tube of water was less than 0.25% and could be neglected (Figure S5.2).

Electrochemical measurements

The GDEs were evaluated in the flow cell using constant current mode controlled by a galvanostat (Autolab PGSTAT302N). The FEs and potential at each current density were repeatedly measured on three electrodes from three different batches. The potential was post compensated by ohmic resistance that was determined by the electrochemical impedance spectroscopy (EIS). The value of the potential versus Ag/AgCl was converted to the scale of the reversible hydrogen electrode (RHE) using the equation: E (versus RHE) = E (versus Ag/AgCl (3 M KCl)) + 0.21 V + 0.059 * pH.

Quantification of products

Gas products

Gas products were analysed using a gas chromatography (GC, SRI Instrument 8610C) with the auto-sampling loop (1 ml) connected to CO_2 off-gas of the flow cell. H_2 was analyzed using thermal conductive detector (TCD) and CO, CH_4, C_2H_4, and C_2H_6 were analyzed using flame ionization detector (FID) with a methanizer. The eCO_2RR measurement on each electrode was about 20 minutes, during which the CO_2 off-gas was injected at least two times into the column of the GC. Thus, the Faradaic efficiencies of the gas products for each electrode were the average of these two injections. For liquid products, we collected and analyzed the catholyte, anolyte, and the CO_2 off-gas washing bath only after the 20-minute reaction. The error bars in the figures of the manuscript represent the standard deviation of three completely independent measurements with three different electrodes. Figure S5.15 shows the typical spectrum produced by GC and Figure S5.16 shows the calibration curves for each products analyzed by GC.

Liquid products

Quantification using NMR

Liquid products of all Cu-based GDEs and some tin-based GDEs were quantified using nuclear magnetic resonance (NMR, Bruker 400 MHz AVIIi HD). Figure S5.17 shows ta typical 1D ^1H NMR spectrum collected from a standard solution containing typical liquid products from eCO_2RR. The peak area ratio of a given product to that of the internal standard (Phenol or DMSO) was used to determine the concentration of the product. Identical NMR acquisition parameters were used for all measurements. In addition, the water peak was suppressed using solvent suppression function. The time of d1 was 5 seconds and the number of scan was 64. The peaks used for quantification are highlighted with green color in Figure S5.17. Products with peaks at the left side of the water peak were quantified using phenol peak as reference, and products with peaks at the right of the water peak were quantified using DMS peak as reference. Figure S5.18 shows the calibration curves for ethanol, acetate, acetone, methanol, n-propanol, and formate.

Quantification of acetaldehyde, propionaldehyde, allyl alcholol, and n-propanol

Acetaldehyde and propionaldehyde are too volatile to prepare an accurate standard solution. The peaks used for quantifying acetaldehyde were from their diol form derived from acetaldehyde. When calculating the concentration of acetaldehyde and propionaldehyde, we took into account that their diol and keto forms are present in 1:1 ratio in aqueous solution[2] as the equilibrium constant of hydration of acetaldehyde is one at room temperature.[3]

When calculating the concentration of n-propanol (Chemical shift at 0.77ppm), the signal from the idol form of propionaldehyde at 0.78 ppm was subtracted.

The average slopes of the calibration curves from the n-propanol, ethanol, acetate, and methanol were used to calculate the concentration of acetaldehyde and propionaldehyde because they have the same number of hydrogen used for quantification and had almost the same slope as shown in Figure S5.18.

The slopes of the calibration curves from the α hydrogen in n-propanol were used to quantify allyl alcohol because n-propanol and allyl alcohol have the same number of α hydrogen and have the same slope.[2]

Qantification using HPLC

The liquid products of tin-based GDE were quantified using high performance liquid chromatography (HPLC, Thermo Scientific Ultimate 3000 UHPLC Systems). Figure S5.19 shows a typical HPLC spectrum collected from a standard solution. Figure S5.20 shows the HPLC calibration curves for formate, acetate, ethanol, acetone, and n-propanol. Sigma Supelcogel 8H column was used with 8 mM H_2SO_4 solution as the effluent at a flow rate of 0.3 ml min^{-2} and operation temperature of 35 ℃. 20 µl of sample was injected using an auto-sampler for each HPLC measurement.

Calculation of Faradaic efficiency

The Faradaic efficiency was calculated for gas and liquid products, using FE $=\dfrac{nFC_ivP}{jRT}$ and FE $=\dfrac{nFC_iV}{Q}$, respectively, where n is the number of transferred electron to produce one molecule of the target product i, *F* is the Faradaic efficiency, C_i is the concentration of the target product i determined by GC or NMR or HPLC, *v* is the flow rate of CO_2 of the inlet, *P* and *T* are the pressure (101325 Pa) and temperature (22 ℃) of the gas sampled by the GC sample loop, respectively, *j* is the total current when sampling, *R* is the gas constant, *V* is the volume of the electrolyte, and *Q* is the total charge transfer to produce the target product.

Very recently, Larrazábal et al. reported the crossover of CO_2 through anion exchange membrane in the membrane-electrode assembly type electrolyzer, which led to a substantial overestimation of the Faradaic efficiency.[4] We here compared the inlet flow rate of CO_2 with the outlet flow rate from the flow cell by connecting another flow meter at the outlet line. No significant difference in our system was found between the inlet and outlet flow rate of CO_2 (Figure S5.12). Considering that the crossover of CO_2 is influenced by the cell design and GDE size, we recommend researchers to check the possible crossover of CO_2 through GDE, especially at low flow rates.

Material characterization

Scanning electron microscope (SEM) images were taken using an FEI Teneo SEM.

Calculation of the mass transfer coefficients
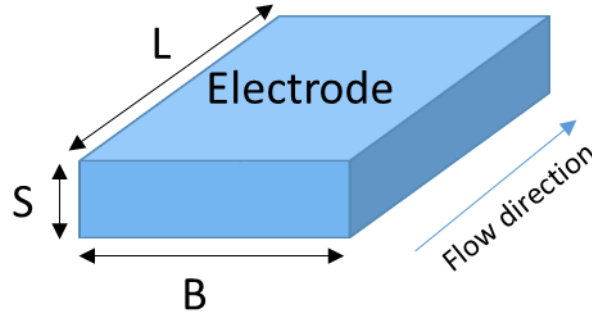
Scheme S5.1 Schematic of the catholyte chamber with the geometric parameters. L = 10 mm, S = 3 mm, and B = 5 mm for cathodic chamber, and L = 10 mm, S = 2 mm, and B = 5 mm for CO_2 chamber.

The local mass transfer coefficient of a species (k_y) in a parallel plate cell can be obtained by using a Leveque-type equation, as shown in equation (0.1), when the flow is fully developed and

$$Gz = \frac{\text{Re}\,Sc\,d_e}{y} > 200 \text{.}^{[5, 6]}$$

$$Sh = 0.978(\text{Re}\,Sc\,d_e/y)^{\frac{1}{3}}\left(\frac{2}{\gamma+1}\right)^{\frac{1}{3}} \tag{0.1}$$

where *Sh* is the Sherwood number defined as $k_y d_e/D$, k_y is the local mass transfer coefficient (m/s) at distance *y downstream away* from the starting point, d_e, the equivalent diameter (m) of cell, is equal to $2BS/(B+S)$ where *B* and *S* are the width and gap distance of the cell, respectively; *D* is the diffusion coefficient of the species in the electrolyte (m²/s), *Re* is the Reynolds number, defined as $\rho d_e U/\mu$ where *ρ* is the density of the electrolyte (kg/m³), *U* is mean electrolyte velocity (m/s), and *μ* viscosity of electrolyte (kg/m s), *Sc* is the Schmidt number, defined as $\mu/\rho D$, and *γ* is named the respect ratio, defined as *S/B*. The parameters used for the calculation are presents in Table S5.7.

The local mass transfer coefficient of the vapor of ethanol and n-propanol in the CO_2 flow could be obtained from another Leveque-type equation, equation(0.2), when *Gz* > 5.[7, 8]

$$Sh = 1.62(\text{Re}\,Sc\,d_e/y)^{\frac{1}{3}} \tag{0.2}$$

The diffusion coefficient of ethanol vapor and n-propanol vapor in CO_2 were calculated based on Fuller correlation, equation(0.3) [9, 10]:

$$D_{AB} = \frac{1.00\times10^{-3}T^{1.75}(\frac{1}{M_A}+\frac{1}{M_B})^{\frac{1}{2}}}{P[(\sum_A \upsilon_i)^{\frac{1}{3}}+(\sum_B \upsilon_i)^{\frac{1}{3}}]^2} \tag{0.3}$$

Where D_{AB} is the binary diffusion coefficient, cm² s⁻¹, M_A and M_B are the molecular mass, g mol⁻¹, $\Sigma \upsilon_i$ is the sum of the atomic diffusion volumes shown in Table S5.6. $\Sigma_{ethanol}\upsilon_i$=2x16.5+6x1.98+5.48=50.36, and $\Sigma_{n-propanol}\upsilon_i$=3x16.5+8x1.98+5.48=70.82. The other parameters used for the calculation are presents in Table S5.8.

The calculated mass transfer coefficient (k) is a function of the flux (U) and the location (y) in the channel and is thus expressed as $k = <k> (U/y)^{1/3}$. The obtained results are:

In the cathodic chamber	In CO_2 flow
$k_{ethanol} = 7.83 \times 10^{-6}(U/y)^{1/3}$	$k_{ethanol} = 5.33 \times 10^{-3}(U/y)^{1/3}$
$k_{n\text{-}propanol} = 6.87 \times 10^{-6}(U/y)^{1/3}$	$k_{n\text{-}propanol} = 4.70 \times 10^{-3}(U/y)^{1/3}$
$k_{formate} = 8.86 \times 10^{-6}(U/y)^{1/3}$	

The 3D plots in Figure S5.13and S5.14 show the profiles of the local mass transfer coefficient as the function of the flux and location.

Note that, the overall evaporation rate of ethanol and n-propanol from the surface of the catalyst is much more complicated because of the impact of the gas diffusion layer and the generation of gas bubbles.[11]
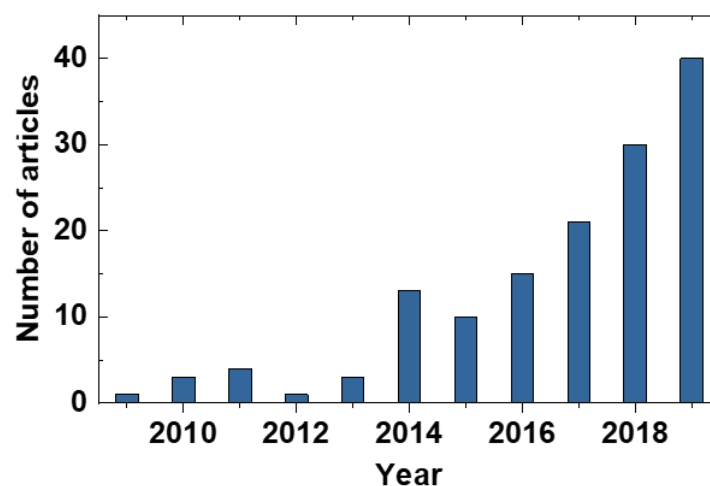
Figure S5.1 A literature survey on the published articles in which flow cells with gas diffusion electrode were used for evaluating the electrochemical CO_2/CO reduction.
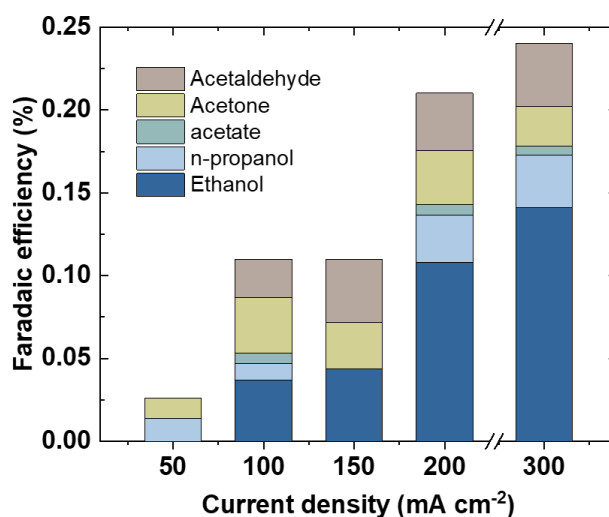
Figure S5.2 Faradaic efficiency of the liquid products collected from the second water bath for washing CO_2 off-gas. It can be seen that first water bath is sufficient to adsorb the liquid products in CO_2 off-gas and only traces left in the second water bath. eCO_2RR was catalyzed by Cu catalysts in 1.0 M KOH. CO_2 flow rate: 50 ml min^{-1}, and AEM: from LinZhuang's lab.
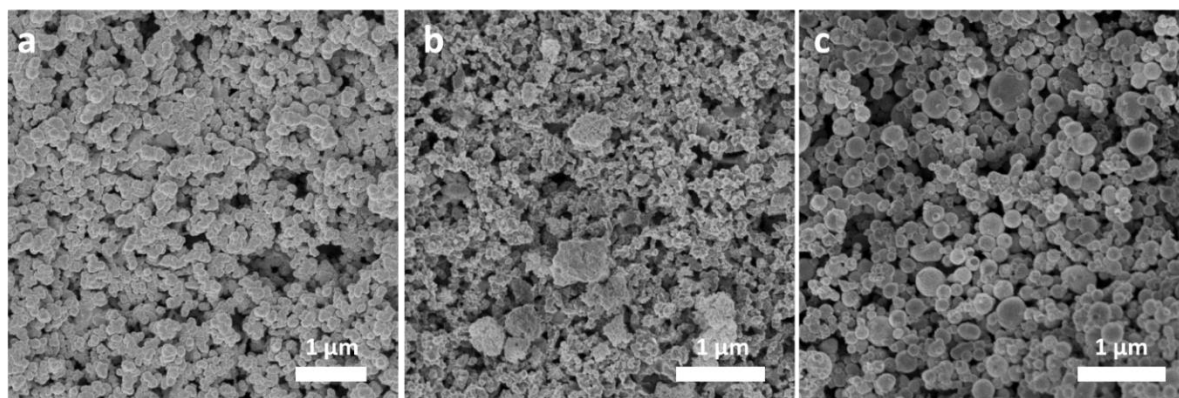
Figure S5.3 SEM images of (a) sputtered and (b) drop-casted Cu catalysts and (C) drop-casted Sn catalyst of the as-prepared gas diffusion electrode.
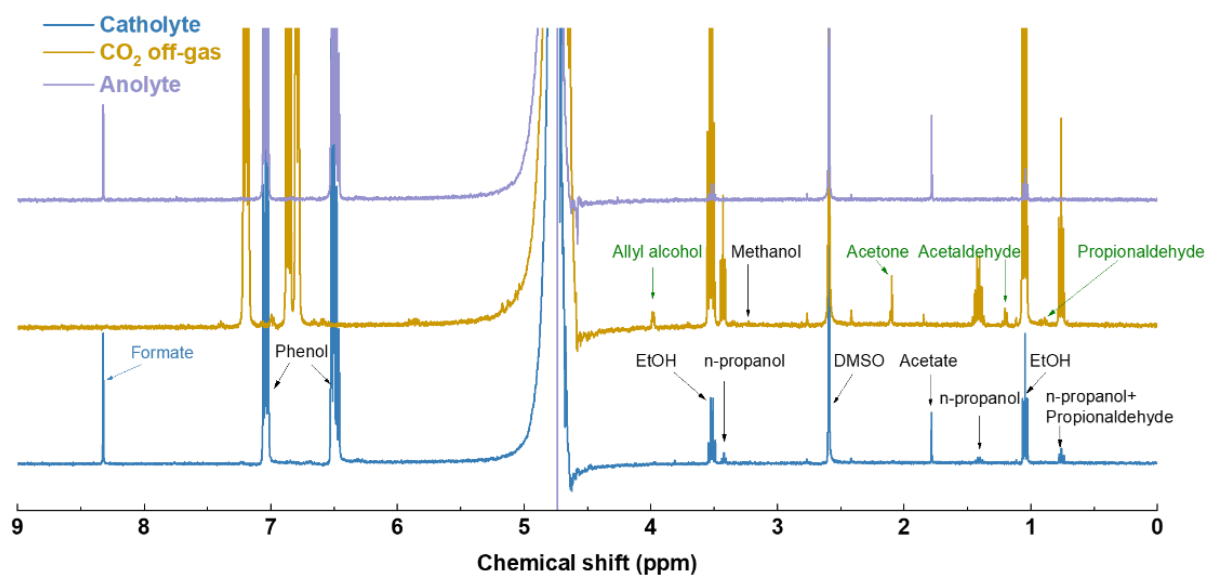
Figure S5.4 The typical ^{1}H NMR spectrum of the liquid products from eCO$_2$RR on Cu catalyst collected from catholyte, CO$_2$ off-gas, and anolyte, respectively. Electrolyte: 1.0 M KOH, CO$_2$ flow rate: 50 ml min^{-1}, and AEM: from LinZhuang's lab.
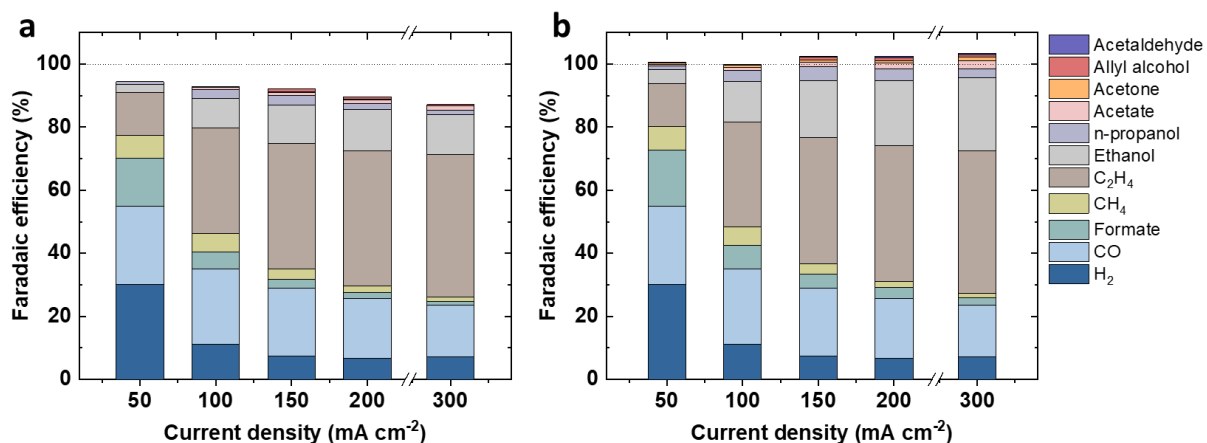
Figure S5.5 Faradaic efficiency, (a) excluding and (b) including the liquid products from the CO_2 off-gas and anolyte of the sputtered Cu catalysts in 1.0 M $KHCO_3$. CO_2 flow rate: 50 ml min^{-1}, and AEM: from LinZhuang's lab.
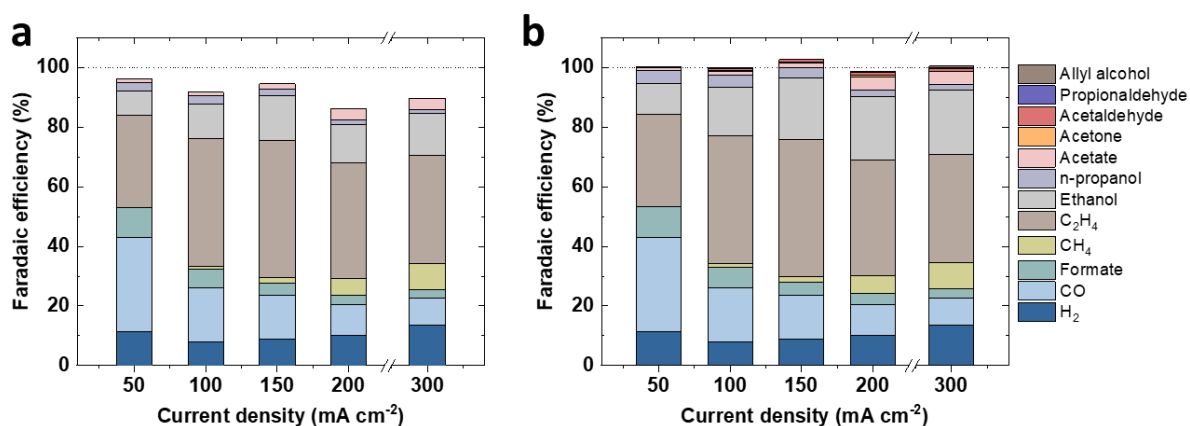
Figure S5.6 Faradaic efficiency, (a) excluding and (b) including the liquid products from the CO_2 off-gas and anolyte of the drop-coated CuO catalysts as a function of current density. Electrolyte: 1.0 M KOH, CO_2 flow rate: 50 ml min^{-1}, and AEM: from LinZhuang's lab.
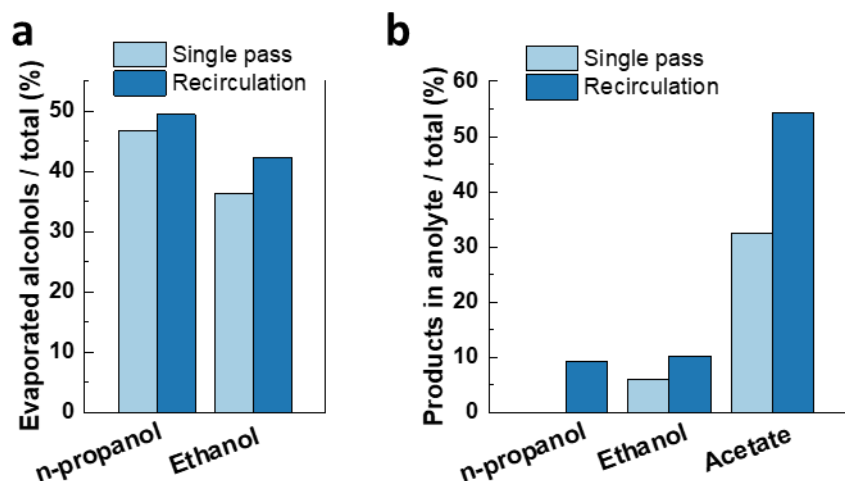
Figure S5.7 Comparison of the crossover through GDE (a) and AEM (b) of liquid products between systems with single-passed catholyte and recirculated catholyte (five times). Catalysts: sputtered Cu; Electrolyte: 1.0 M KOH; AEM: from LinZhuang's lab.
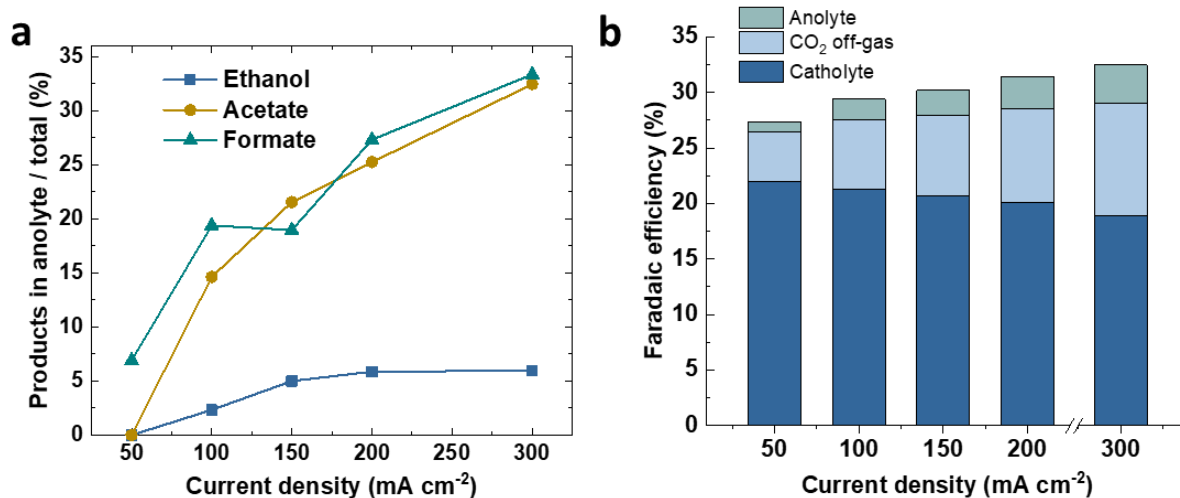
Figure S5.8 (a) the ratio of the products in the anolyte to total produced products. (b) the distribution of all produced liquid products in the three chambers of the flow cell. The data are corresponding to Figure 5.1.
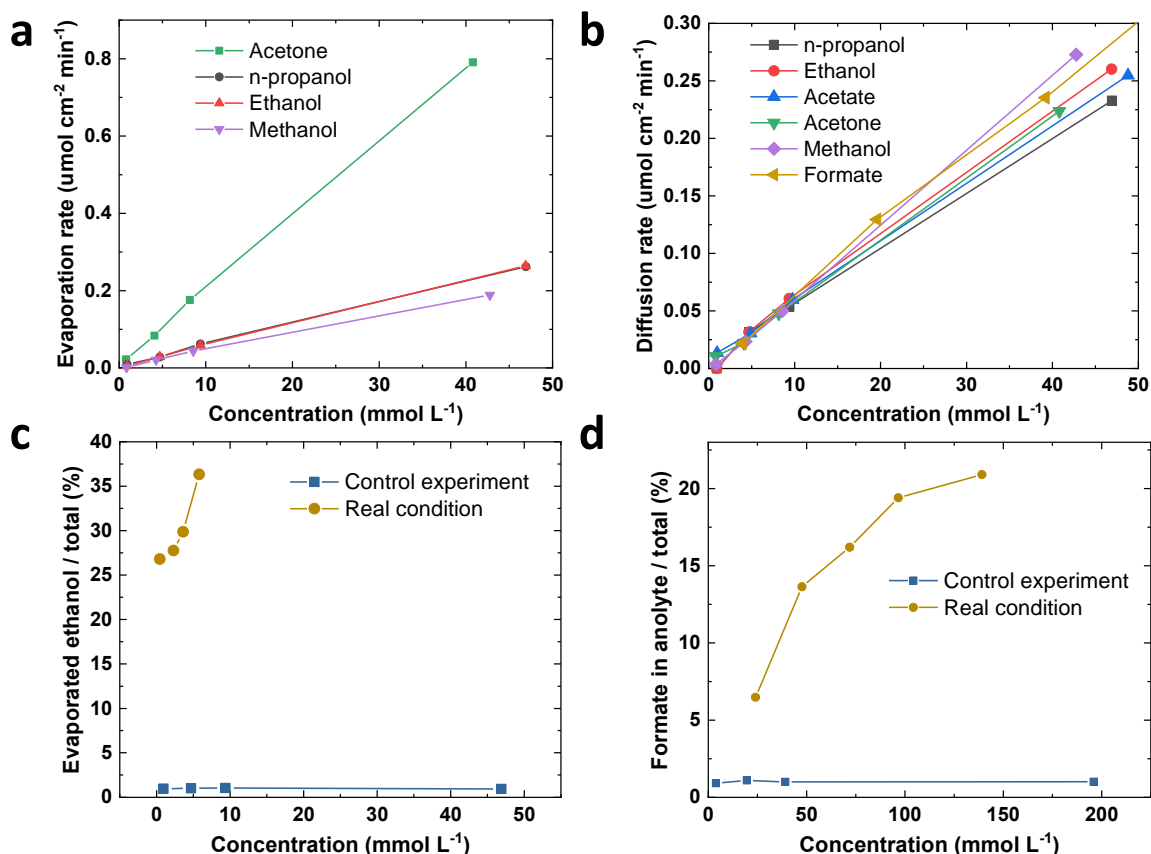
Figure S5.9 The evaporation rate through GDE (a) and the crossover rate through AEM of the liquid products as a function of their concentrations in the solution. No potential was applied. (c) Comparison of the ethanol-evaporation fraction between the control experiment and real reaction condition. (d) Comparison of the formate-crossover fraction between the control experiment and real reaction condition. CO_2 flow rate: 50 ml min^{-1} Catholyte flow rate: 0.3 mL min^{-1}. GDE: sputtered Cu. Solution: 1.0 M KOH. Membrane: Sustainion® X37-5.

This figure shows that the product-evaporation rates through GDE and diffusion rates through AEM in the control experiments are much smaller than that during the eCO_2RR reaction, even though the concentrations in control experiments are much higher than those produced during eCO_2RR. This is because CO_2 reduction products are produced on the surface of GDE, thus product concentrations near GDE are much higher than those in the bulk, and they evaporate into the gas phase more easily comparing with the dissolved ones in the control experiments. For the liquid products that cross the AEM, the crossover is also impacted by the electromigration for ionic products and electroosmotic drag for neutral products. Therefore, these results highlight the importance of understanding the crossover issue under real eCO_2RR conditions.
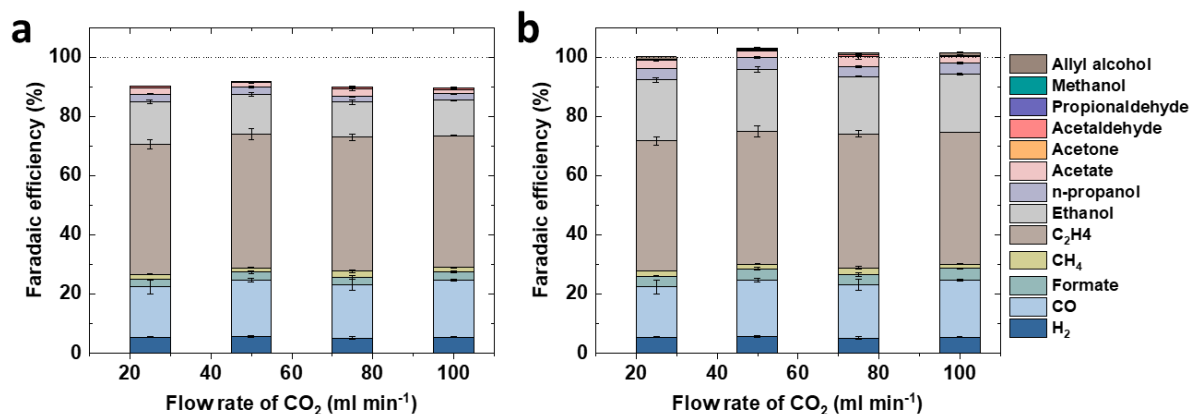
Figure S5.10 Faradaic efficiency, (a) excluding and (b) including the liquid products from the CO_2 off-gas and anolyte of the sputtered Cu catalysts as a function of CO_2 flow rate at 200 mA cm^{-2}. Electrolyte: 1.0 M KOH, and AEM: from LinZhuang's lab.
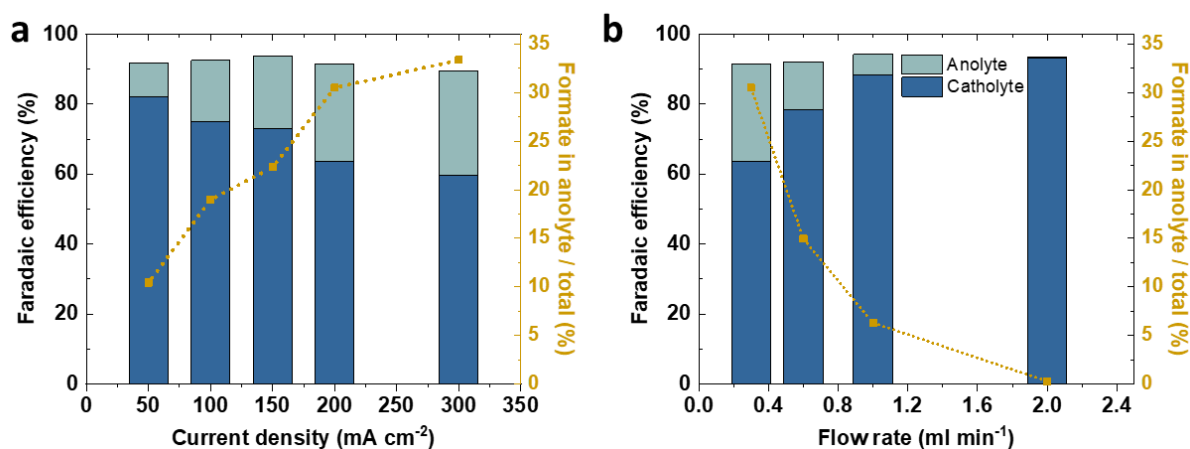
Figure S5.11 Comparison of the Faradaic efficiency of formate in the catholyte and anolyte from Sn catalyst. (a) Influence of the current density (at 0.3 mL min^{-1}), (b) Influence of catholyte flow rate (at 200 mA cm^{-2}). The AEM from LinZhuang's lab was used for collecting these data. Electrolyte was 1.0 M KOH.
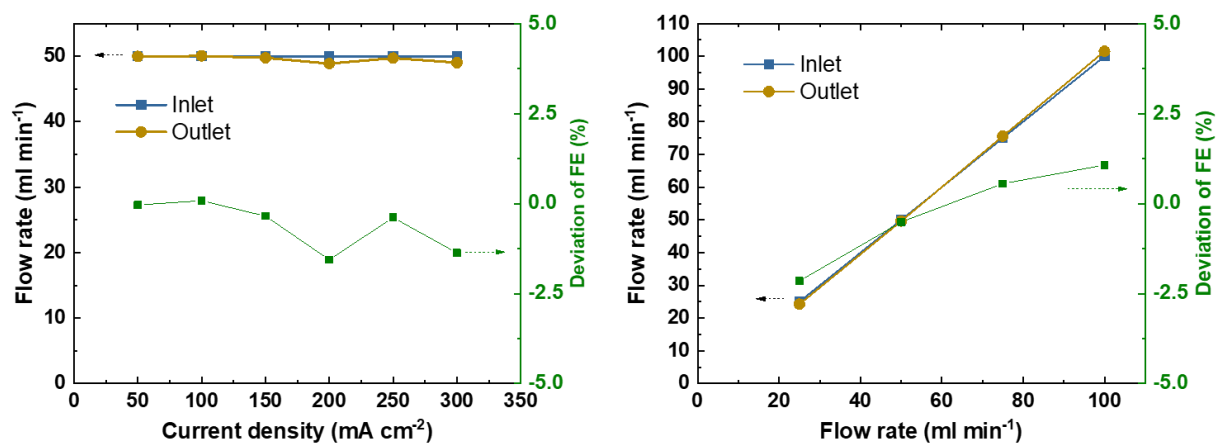
Figure S5.12 Comparison of the flow rates of CO_2 in the inlet and outlet lines of the flow cell at various current densities and CO_2 flow rates. The deviation of the FE is the deviation of Faradaic efficiency resulted in by the difference between inlet and outlet flow rates. Sputtered Cu was the catalyst and 1 M KOH was the electrolyte with the AEM from LinZhuang's lab.
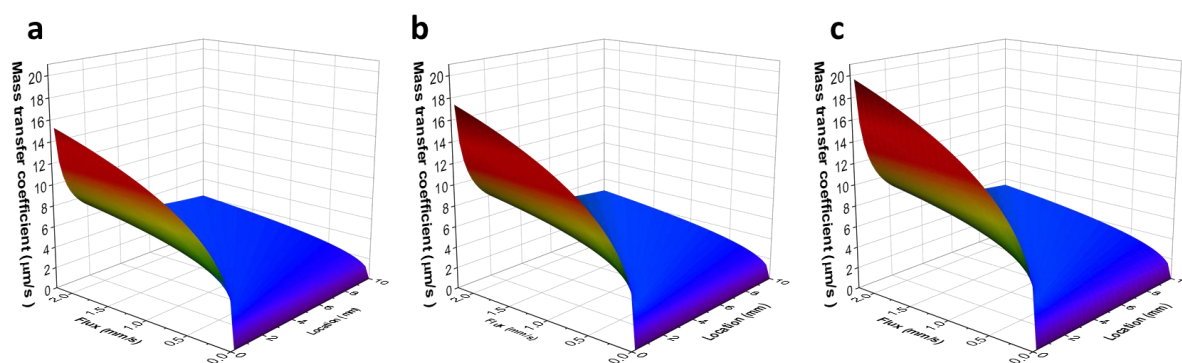
Figure S5.13 The calculated local mass transfer coefficient of n-propanol (a), ethanol (b), and formate (c) in 1 M KOH as the function of the flux of the catholyte and the location in the flow cell. Location is the distance y, downstream away from the starting point.

a

b
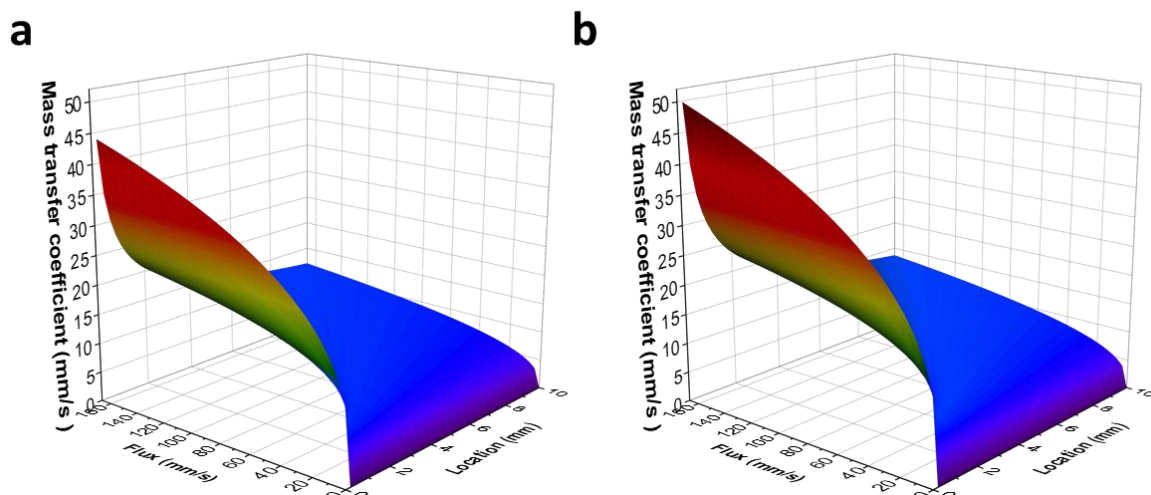
Figure S5.14 The calculated local mass transfer coefficient of ethanol vapor (a) and n-propanol vapor (b) in CO_2 as the function of the flux of the CO_2 and the location in the flow cell. Location is the distance y, downstream away from the starting point.

a

b
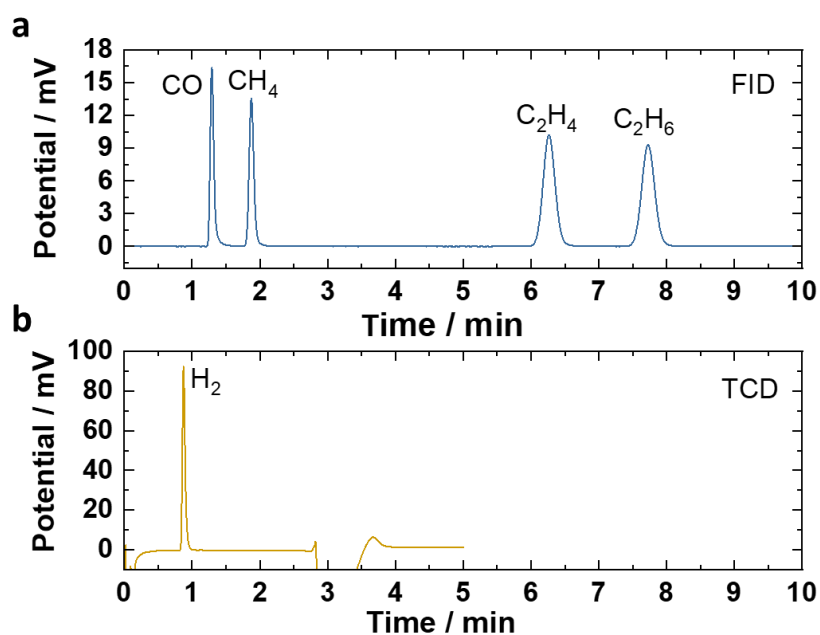
Figure S5.15 Typical spectra of gas products from the electrochemical CO_2 reduction detected using GC.
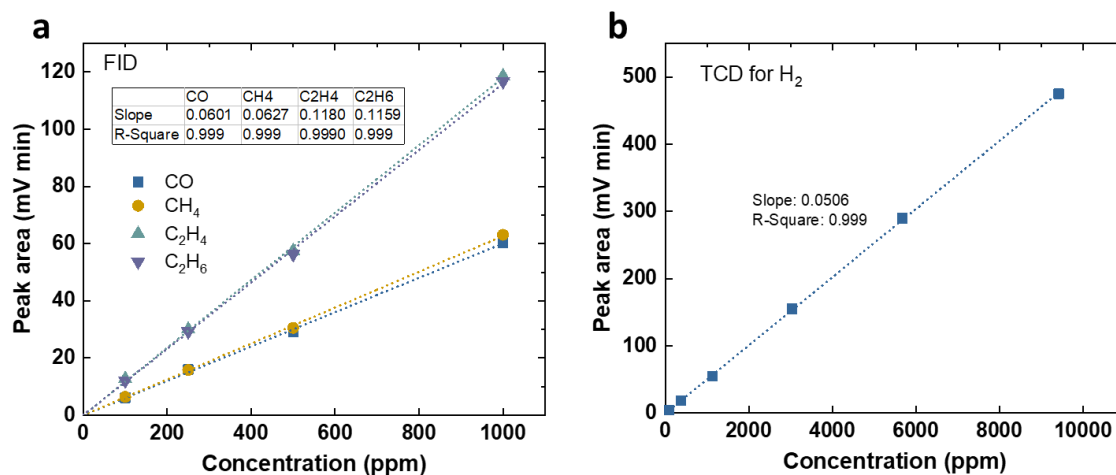
Figure S5.16 The calibration curves of the CO, CH₄, C₂H₄, C₂H₆ (from FID), and H₂ (from TCD) for the gas chromatography.
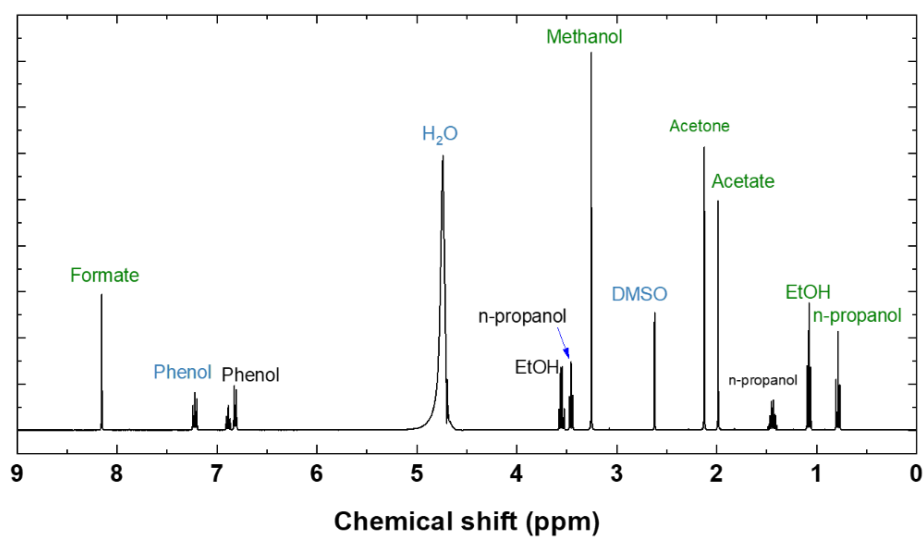
Figure S5.17 A typical NMR spectrum of the liquid products from eCO₂RR using.
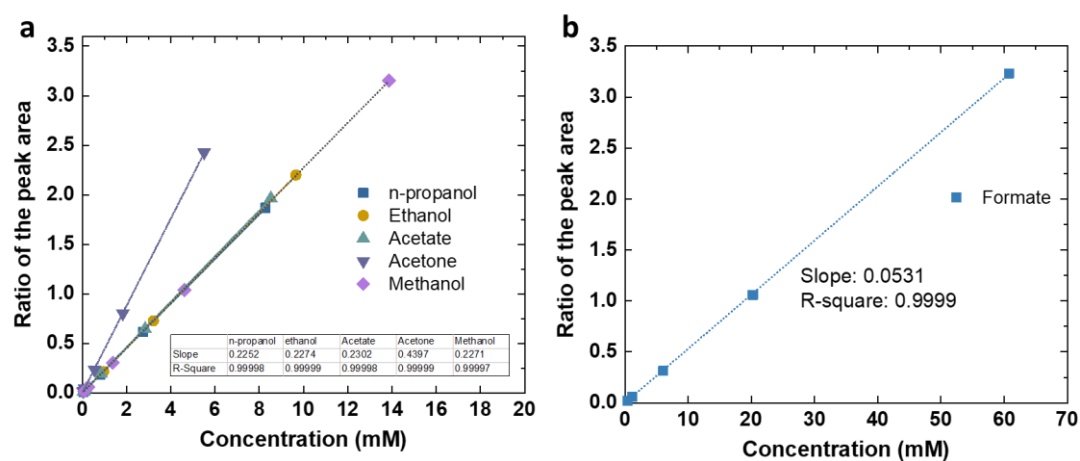
Figure S5.18 NMR calibration curves of the liquid products.
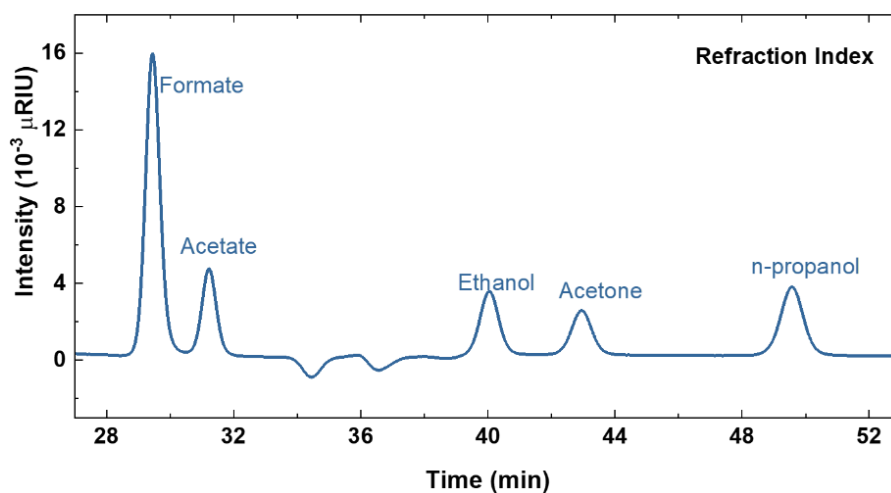
Figure S5.19 A typical HPLC spectrum for the liquid products from eCO$_2$RR.
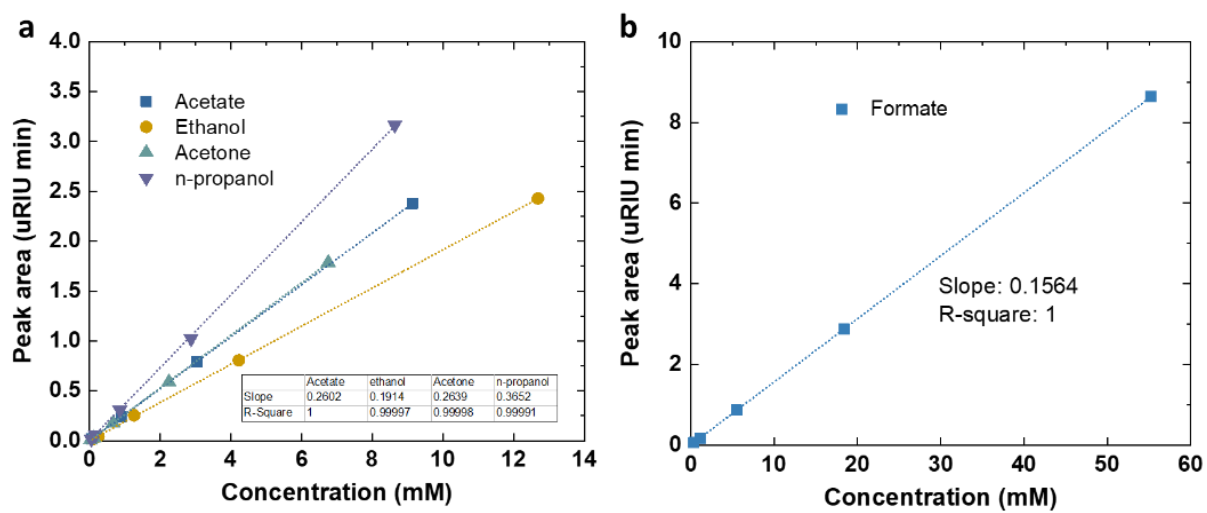
Figure S5.20 HPLC calibration curves of the liquid products.

Table S5.1 Faradaic efficiency as a function of current density for the products from eCO$_2$RR on sputtered Cu catalyst (corresponding to Figure 5.1).

Potential	Current density	Faradaic efficiency (%)											
V vs RHE	mA cm^{-2}	H$_2$	CO	CH$_4$	C$_2$H$_4$	n-propanol	Propionaldehyde	ethanol	Acetaldehyde	acetate	acetone	methanol	Allyl alcohol	formate
-0.55	50	11.10	35.30	0.67	26.86	4.91	-	10.22	0.01	1.22	0.19	0.01	0.01	11.25
-0.58	100	6.96	26.75	1.11	35.65	4.94	-	15.33	0.11	1.52	0.31	0.01	0.42	6.40
-0.59	150	6.34	23.45	1.15	40.52	4.47	-	17.75	0.24	1.93	0.26	0.03	0.78	4.93
-0.61	200	5.64	19.63	1.39	42.48	4.02	0.12	20.85	0.19	2.29	0.20	0.03	0.47	3.94
-0.63	300	5.98	16.30	1.71	44.84	2.96	0.04	22.38	0.31	3.44	0.15	0.02	0.51	2.63
Liquid products in the CO$_2$ off-gas														
-0.55	50					1.43	0.00	2.77	0.01	0.05	0.19	0.01	0.01	-
-0.58	100					1.63	0.00	4.05	0.11	0.08	0.31	0.00	0.07	-
-0.59	150					1.60	0.00	4.93	0.24	0.04	0.26	0.01	0.17	-
-0.61	200					1.49	0.12	6.23	0.19	0.03	0.20	0.00	0.22	-
-0.63	300					1.38	0.04	8.13	0.26	0.04	0.15	0.00	0.17	-
Liquid products in the catholyte														
-0.55	50					3.49	-	7.46	-	1.17	-	-	-	10.38
-0.58	100					3.31	-	10.95	-	1.24	-	0.01	0.35	5.08
-0.59	150					2.87	-	11.91	-	1.46	-	0.01	0.91	3.97
-0.61	200					2.53	-	13.44	-	1.65	-	0.03	0.25	2.83
-0.63	300					1.58	-	12.92	-	2.25	-	0.02	0.34	1.72
Liquid products in the anolyte														
-0.55	50					-	-	-	-	-	-	-	-	0.87
-0.58	100					-	-	0.33	-	0.19	-	-	-	1.31
-0.59	150					-	-	0.91	-	0.43	-	-	-	0.96
-0.61	200					-	-	1.19	-	0.61	-	-	-	1.11
-0.63	300					-	-	1.33	-	1.16	-	-	-	0.90

Table S5.2 Faradaic efficiency as a function of the flow rate from eCO$_2$RR on Cu catalyst at 200 mA cm^{-2} (corresponding to Figure 5.2 and Figure S5.5).

Flow rate	Potential					Faradaic efficiency (%)								
ml min^{-1}	V vs RHE	H2	CO	CH$_4$	C$_2$H$_4$	n-propanol	Propionaldehyde	ethanol	Acetaldehyde	acetate	acetone	methanol	Allyl alcohol	formate
25.00	-0.62	5.44	16.89	1.80	43.92	3.90	-	20.59	0.16	2.67	0.21	0.05	0.89	3.69
50.00	-0.62	5.64	18.97	1.43	45.03	4.10	0.04	20.85	0.19	2.29	0.20	0.03	0.47	3.94
75.00	-0.61	5.14	17.96	2.11	45.32	3.36	0.01	19.39	0.33	3.32	0.23	0.02	0.71	3.59
100.00	-0.60	5.46	19.21	1.45	44.63	3.72	-	19.76	0.20	2.16	0.23	0.01	0.83	3.92
Liquid products in the CO2 off-gas														
25.00	-0.62					1.26	-	5.09	0.16	0.03	0.21	0.01	0.22	-
50.00	-0.62					1.56	0.04	6.23	0.19	0.03	0.20	0.00	0.22	-
75.00	-0.61					1.47	0.01	6.29	0.33	0.06	0.23	0.01	0.24	-
100.00	-0.60					1.63	-	6.57	0.20	0.05	0.23	0.01	0.29	-
Liquid products in the catholyte														
25.00	-0.62					2.64	-	14.31	-	2.03	-	0.03	0.67	2.57
50.00	-0.62					2.53	-	13.44	-	1.65	-	0.03	0.25	2.83
75.00	-0.61					1.90	-	11.92	-	2.65	-	0.01	0.47	2.48
100.00	-0.60					2.09	-	12.00	-	1.51	-	0.01	0.54	2.80

Table S5.3 Faradaic efficiency as a function of the current density for the products from eCO$_2$RR on Tin catalyst in GDE (corresponding to Figure 5.3 and Figure S5.8).

		Faradaic efficiency (%)			
Potential	Current density			Formate	
V vs RHE	mA cm^{-2}	H$_2$	CO	Catholyte	Anolyte
Sustainion					
-0.61	50	1.75	7.76	86.89	5.99
-0.65	100	1.19	5.18	79.56	12.41
-0.69	150	2.28	5.22	77.56	14.99
-0.74	200	2.96	5.47	75.26	18.01
-0.79	250	5.17	3.74	75.32	18.01
-0.83	300	6.07	4.31	70.78	18.70
LinZhuang					
-0.65	50	1.09	5.89	82.2	9.58
-0.72	100	1.58	4.76	75.0	17.53
-0.78	150	3.89	4.20	72.9	20.95
-0.79	200	4.41	4.09	63.6	27.87
-0.79	300	7.36	3.65	59.7	29.87

Table S5.4 Faradaic efficiency as a function of the catholyte flow rate for the products from eCO$_2$RR on Tin based GDE at 200 mA cm^{-2} (corresponding to Figure 5.3 and Figure S5.8).

		Faradaic efficiency (%)			
Potential	CO$_2$ flow rate			Formate	
V vs RHE	ml min^{-1}	H$_2$	CO	Catholyte	Anolyte
Sustainion					
-0.74	0.30	2.96	5.47	75.26	18.01
-0.75	0.60	3.68	4.28	78.77	12.60
-0.75	1.00	2.81	4.78	88.97	2.51
-0.72	2.00	2.33	6.26	90.47	0.40
LinZhuang					
-0.79	0.30	4.41	4.09	63.57	27.9
-0.79	0.60	4.85	4.56	78.27	13.8
-0.76	1.00	5.20	4.25	88.29	5.93
-0.76	2.00	4.88	4.25	93.05	0.29

Table S5.5 ^{1}H NMR peaks of the standards.[2] Peaks used for quantification are green highlighted.

Assignment		Chemical shift	
Probed nucleus	Product name	^{1}H splitting	Chemical shift
CH$_3$H$_2$CH=O	Propionaldehyde	s	9.57
CH$_3$CH=O	Acetaldehyde	q	9.55
HCOO$^-$	Formate	s	8.33
Phenol	Internal standard	t	7.20
Phenol	Internal standard	t	6.86
Phenol	Internal standard	d	6.80
CH$_2$CHCH$_2$OH	Allyl Alcohol	dt	3.99
CH$_3$CH$_2$OH	Ethanol	q	3.53
CH$_3$CH$_2$CH$_2$OH	n-propanol	t	3.44
CH$_3$OH	Methanol	s	3.23
DMSO	Internal standard	s	2.60
CH$_3$H$_2$CH=O	Propionaldehyde	q	2.44
CH$_3$CH=O	Acetaldehyde	d	2.12
CH$_3$CH=OCH$_3$	Acetone	s	2.10
CH$_3$C(=O)O$^-$	Acetate	s	1.87
CH$_3$H$_2$CH=O	Propionaldehyde	dt	1.47
CH$_3$CH$_2$CH$_2$OH	n-propanol	sextet	1.42
CH$_3$CH(OH)$_2$	Acetaldehyde	d	1.2
CH$_3$CH$_2$OH	Ethanol	t	1.06
CH$_3$H$_2$CH=O	Propionaldehyde	t	0.92
CH$_3$H$_2$CH(OH)$_2$	Propionaldehyde	t	0.78
CH$_3$CH$_2$CH$_2$OH	n-propanol	t	0.77

Table S5.6 special atomic diffusion volume.

C	16.5
H	1.98
O	5.48
CO$_2$	26.9

Table S5.7 The parameters used to calculate the local mass transfer coefficients of ethanol, n-propanol, and formate in 1 M KOH in the flow cell.

Physical variable	Symbol	Condition	Unit	Value	Assumption	Ref
Pressure	P	Atmospheric	Pa	1.01×10^{-5}		
Temperature	T	Room temperature	K	298.15		
Density	ρ	1 M KOH	kg/m^3	1.04×10^3		
Viscosity	μ	1 M KOH	$kg/(m\ s)$	9.98×10^{-4}		Ref[12]
Diffusion coefficient	D	ethanol in water	m^2/s	1.24×10^{-9}	infinite dilute	Ref[13]
Diffusion coefficient	D	n-propanol in water	m^2/s	1.02×10^{-9}	infinite dilute	Ref[14]
Diffusion coefficient	D	formic acid in water	m^2/s	1.49×10^{-9}	infinite dilute	Ref[15]
Equivalent diameter of cell	d_e	Catholyte	m	3.75×10^{-3}		
Respect ratio	γ	Catholyte		0.60		
Geometry	$LxBxS$	Catholyte	mm	10 x 5 x 3		
Flow rate	$Volume$	Catholyte	m^3/s	5.00×10^{-9}		
Flux	U	Catholyte	m/s	3.33×10^{-4}		
Reynolds number	Re	Catholyte		1.31E+00		

Table S5.8 The hydrodynamic parameters related to the evaporation of ethanol and n-propanol in the CO_2 chamber of the flow cell.

Physical variable	Symbol	Condition	Unit	Value	
Pressure	P	Atmospheric	Pa	1.01×10^{-5}	
Temperature	T	Room temperature	K	298.15	
Density	ρ	CO_2	kg/m^3	1.8	Ref[16]
Viscosity	μ	CO_2	$kg/(m\ s)$	1.51×10^{-6}	Ref[16]
Diffusion coefficient	D	ethanol vapor in CO_2	m^2/s	1.01×10^{-5}	Calculated[10]
Diffusion coefficient	D	n-propanol vapor in CO_2	m^2/s	8.34×10^{-6}	Calculated[10]
Equivalent diameter	d_e	CO_2 chamber	m	2.86×10^{-3}	
respect ratio	γ	CO_2 chamber		0.40	
Geometry	$LxBxS$	CO_2 chamber	mm	10 x 5 x 2	
Flow rate	$volume$	CO_2	m^3/s	8.33×10^{-7}	
Flow rate	U	CO_2	m/s	0.083	
Carbon paper		Sigracet 39BC			

References

[1]   J. Pan, C. Chen, Y. Li, L. Wang, L. Tan, G. Li, X. Tang, L. Xiao, J. Lu, L. Zhuang, Constructing ionic highway in alkaline polymer electrolytes, Energy & Environmental Science, 7 (2014) 354-360.

[2]   K.P. Kuhl, E.R. Cave, D.N. Abram, T.F. Jaramillo, New insights into the electrochemical reduction of carbon dioxide on metallic copper surfaces, Energy & Environmental Science, 5 (2012) 7050-7059.

[3]   J.L. Kurz, Hydration of acetaldehyde. I. Equilibrium thermodynamic parameters, Journal of the American Chemical Society, 89 (1967) 3524-3528.

[4]   G.O. Larrazábal, P. Strøm-Hansen, J.P. Heli, K. Zeiter, K.T. Therkildsen, I. Chorkendorff, B. Seger, Analysis of Mass Flows and Membrane Cross-over in CO_2 Reduction at High Current Densities in an MEA-Type Electrolyzer, ACS Applied Materials & Interfaces, 11 (2019) 41281-41288.

[5]   J. Qi, R.F. Savinell, Mass transfer in a laminar-flow parallel plate electrolytic cell with simultaneous development of velocity and concentration boundary layers, Journal of Applied Electrochemistry, 20 (1990) 885-892.

[6]   D.J. Pickett, B.R. Stanmore, Ionic mass transfer in parallel plate electrochemical cells, Journal of Applied Electrochemistry, 2 (1972) 151-156.

[7]   S.R. Wickramasinghe, M.J. Semmens, E.L. Cussler, Mass transfer in various hollow fiber geometries, Journal of Membrane Science, 69 (1992) 235-250.

[8]   C.Y. Wang, E. Mercer, F. Kamranvand, L. Williams, A. Kolios, A. Parker, S. Tyrrel, E. Cartmell, E.J. McAdam, Tube-side mass transfer for hollow fibre membrane contactors operated in the low Graetz range, Journal of Membrane Science, 523 (2017) 235-246.

[9]   E.N. Fuller, P.D. Schettler, J.C. Giddings, NEW METHOD FOR PREDICTION OF BINARY GAS-PHASE DIFFUSION COEFFICIENTS, Industrial & Engineering Chemistry, 58 (1966) 18-27.

[10]   B.E. Poling, J.M. Prausnitz, J.P. O'Connell, The Properties of Gases and Liquids 5E, McGraw-Hill Education2000.

[11]   S. Lal, A. Lamibrac, J. Eller, F.N. Büchi, Determination of Water Evaporation Rates in Gas Diffusion Layers of Fuel Cells, Journal of The Electrochemical Society, 165 (2018) F652-F661.

Chapter 6   Conclusions and Perspectives

6.1   Conclusions

This thesis extends our understanding of the electrochemical CO_2 reduction (eCO_2RR) to C_{2+} products on copper-based catalysts from the following three aspects: (1) the active sites on monometallic copper and bimetallic silver-copper catalysts for C_{2+} products, (2) the effects of mass transfer and pH on the activity and selectivity of eCO_2RR regarding C_{2+} products, and (3) the crossover of the liquid products through the gas diffusion electrode and anion exchange membrane in a flow cell for eCO_2RR.

Firstly, Chapter 2 demonstrates that the copper phthalocyanine molecules under eCO_2RR are demetallized and release copper atoms that gather up to form clusters on the surface of the carbon support. These clusters further agglomerate into nanoparticles with rich grain boundaries. This bottom-up evolution of copper clusters is correlated with the selectivity of C_{2+} products, which reveals that the copper nanoparticles must be large enough to have sufficient grain boundaries as the active sites to allow the formation of C_{2+} products. The adsorbed intermediates, e.g., CO, accelerate the growth of copper clusters to large nanoparticles during eCO_2RR. These findings are of importance to the design of novel copper catalysts for eCO_2RR selectively to C_{2+} chemicals and highlight the role of the dynamic reconstruction of copper catalysts during eCO_2RR.

In Chapter 3 concerning the debate about the active sites (tandem or interface sites) in silver-copper bimetallic catalysts for C_{2+} products, we developed a method to synthesize Ag@C@Cu core-shell nanoparticles with a controllable formation of carbon layer between silver core and copper shell to control the existence of Ag-Cu interface. For the Ag@C@Cu core-shell nanoparticles where only tandem effect exists, a high local concentration of CO generated on the silver surface can make the Cu surface more selective towards ethanol than C_2H_4. Thus, the tandem effect between Cu and Ag can be used to tune the reaction pathways toward C_2H_4 and ethanol in order to control the selectivity.

Next, we developed a strategy in Chapter 4 that can be used to directly transform nanostructured Cu catalysts into self-supported gas diffusion electrodes, thus achieving a current density up to 300 mA cm^{-2} with a high selectivity of C_{2+} products (> 40%). The two types of copper nanowires still preserve their intrinsic catalytic properties in the flow cell – that is, the Cu nanowires formed by thermal annealing favor the production of C_{2+} products, while the Cu nanowires derived from wet chemical oxidation produce more C_1 products. The direct comparison of the same catalyst in a batch-type cell and a flow cell revealed that the activity of copper catalyst in the batch-type cell suffer from a mass transfer limitation and that a higher pH in the flow reaction favors production of the C_{2+} products from eCO_2RR. These findings highlight the importance of assessing the catalytic behaviors of eCO_2RR under industrially relevant conditions and open new avenues for the rational design of self-supported GDEs based on nanostructured materials.

In Chapter 5, we revealed that more than 30% of the liquid products can cross through the gas diffusion electrode and anion exchange membrane in a flow reactor at commercial current densities (from 50 mA cm^{-2} to 300 mA cm^{-2}), which should not but was always neglected in the prior reports. Volatile products (e.g., ethanol and propanol) pass through the gas diffusion electrode mainly by evaporation, and the migration rate increases proportionally with the current density and CO_2 flow rate. Non-volatile products (e.g., formate ions) prefer to pass through the anion exchange membrane through electromigration, and the migration rate is affected by the current density and the flow rate of the catholyte. These results led us to propose a strict protocol for the collection of the liquid products in a gas diffusion reactor and the findings may inspire the design of advanced CO_2 electrolysis systems.

6.2 Perspectives

In this work, we revealed the active sites and reconstruction of copper catalysts for eCO$_2$RR to C$_{2+}$ products and demonstrated the effects of the local reaction environments and the crossover of the liquid products in the gas diffusion electrode. During our research we also realized that there are several other issues that need to be addressed to advance the technology of eCO$_2$RR to C$_{2+}$ products toward industrialization.

6.2.1 Effect of carbon on the copper clusters from phthalocyanine

In Chapter 2, we observed the copper nanoparticles (up to 60 nm in diameter) derived from the decomposition of copper phthalocyanine during eCO$_2$RR. However, several other research groups have observed copper clusters (less than 10 atoms each) derived from copper phthalocyanine.[1-3] The difference between our results and the others may be due to the differences in the carbon materials used with copper phthalocyanine. Carbon black is mixed with copper phthalocyanine here to increase the conductivity of the catalysts. As most copper clusters grow on the carbon surface, the carbon's properties thus greatly affect the formation of these clusters. Therefore, it is essential to clarify the nucleation process of copper clusters derived from copper phthalocyanine on a carbon surface and which surface properties of carbon affect the nucleation process.

6.2.2 Stability of the copper catalyst

In Chapters 2 and 3, we revealed the reconstruction of copper catalysts during eCO$_2$RR, which previous studies have also addressed from a different angles.[4, 5] Therefore, future studies on the active sites and reaction mechanisms should also keep in mind that the surface of copper catalysts may be reconstructed during eCO$_2$RR. The reconstruction of the copper catalysts probably impacts the stability of the reaction, so a strategy for keeping these catalysts stable during eCO$_2$RR should be developed in future studies.

6.2.3 Flooding of the gas diffusion electrode in an alkaline electrolyte

The eCO$_2$RR consumes protons and thus produces the hydroxide ions that reacts further with the CO_2, producing the carbonate ions. This process results in the quick accumulation of carbonate salt in the gas diffusion electrode. The accumulated carbonate salt blocks the pores of the gas diffusion layer and thus prevents the CO_2 from transferring to the catalysts. Consequently, eCO$_2$RR in a gas diffusion electrode can only proceed for at most several hours. At the moment, most of the gas diffusion electrodes work in an alkaline electrolyte and a high current density, which enhances the accumulation of carbonate salt. Therefore, it is urgent that a strategy is developed to prevent the

accumulation of carbonate salt or make eCO_2RR well-performed in acidic electrolytes and thereby improve the long-term stability of the catalysts.

6.2.4   Catalysts for producing ethanol with a high selectivity

Even though the tandem effect in silver-copper bimetallic catalysts can improve the selectivity of ethanol from CO_2 reduction, C_2H_4 still competes with ethanol, limiting the further improvement of the ethanol selectivity. To completely solve the problem of low selectivity of ethanol, the active sites and reaction conditions exclusively valid for ethanol should be identified and then the corresponding catalysts should be developed. A recent report shows that the copper clusters stabilized by surface hydroxyl group and supported by carbon can produce ethanol without C_2H_4 and thus are quite promising to be a model catalyst to solve these problems.[6]

6.3   References

[1]   B. Mei, C. Liu, J. Li, S. Gu, X. Du, S. Lu, F. Song, W. Xu, Z. Jiang, Operando HERFD-XANES and surface sensitive Δμ analyses identify the structural evolution of copper(II) phthalocyanine for electroreduction of CO_2, Journal of Energy Chemistry, 64 (2022) 1-7.

[2]   Z. Weng, Y. Wu, M. Wang, J. Jiang, K. Yang, S. Huo, X.-F. Wang, Q. Ma, G.W. Brudvig, V.S. Batista, Y. Liang, Z. Feng, H. Wang, Active sites of copper-complex catalytic materials for electrochemical carbon dioxide reduction, Nature Communications, 9 (2018) 415.

[3]   Y. Xu, F. Li, A. Xu, J.P. Edwards, S.-F. Hung, C.M. Gabardo, C.P. O'Brien, S. Liu, X. Wang, Y. Li, J. Wicks, R.K. Miao, Y. Liu, J. Li, J.E. Huang, J. Abed, Y. Wang, E.H. Sargent, D. Sinton, Low coordination number copper catalysts for electrochemical CO_2 methanation in a membrane electrode assembly, Nature Communications, 12 (2021) 2932.

[4]   J. Huang, N. Hörmann, E. Oveisi, A. Loiudice, G.L. De Gregorio, O. Andreussi, N. Marzari, R. Buonsanti, Potential-induced nanoclustering of metallic catalysts during electrochemical CO_2 reduction, Nature Communications, 9 (2018) 3117.

[5]   P. Wilde, P.B. O'Mara, J.R.C. Junqueira, T. Tarnev, T.M. Benedetti, C. Andronescu, Y.-T. Chen, R.D. Tilley, W. Schuhmann, J.J. Gooding, Is Cu instability during the CO_2 reduction reaction governed by the applied potential or the local CO concentration?, Chemical Science, 12 (2021) 4028-4033.

[6]   H. Xu, D. Rebollar, H. He, L. Chong, Y. Liu, C. Liu, C.-J. Sun, T. Li, J.V. Muntean, R.E. Winans, D.-J. Liu, T. Xu, Highly selective electrocatalytic CO_2 reduction to ethanol by metallic clusters dynamically formed from atomically dispersed copper, Nature Energy, 5 (2020) 623-632.

Curriculum vitae

Jie Zhang
Chinese, born on 24.01.1989
ORCID 0000-0002-5449-9412
Google Scholar https://scholar.google.ch/citations?user=kSQ4dZ0AAAAJ&hl=en
Email: jie.zhang@epfl.ch

Education

01.2018 – 01.2022	**PhD** in Chemistry and Chemical Engineering
	École Polytechnique Fédérale de Lausanne – EPFL (Sion, Switzerland)
	Supervised by Prof. Andreas Züttel
09.2013 – 07.2015	**MSc** in Chemical Engineering
	Harbin Institute of Technology (Harbin, China)
	Supervised by Prof. Maozhong An
09.2009 – 07.2013	**BSc** in Chemical Engineering and Technology
	Harbin Institute of Technology (Harbin, China)

Employment history

01.2018 – now	**Doctoral Assistant**
	Department of Chemistry and Chemical Engineering
	École Polytechnique Fédérale de Lausanne – EPFL
	Advised by Prof. Andreas Züttel
11.2016 – 11.2017	**Research Assistant**
	Southern University of Science and Technology (Shenzhen, China)
	Advised by Prof. Baomin Xu
07.2015 – 06.2016	**Quality Engineer**
	TP-Link Technologies Co., Ltd (Shenzhen, China)

Teaching activities

I worked as a teaching assistant to help several professors teach courses in department of chemistry and chemical engineering of EPFL with a total teaching hours of around 500 hours. I participated to teach:

- Introduction to chemical engineering Laboratory Works (Lecture: Prof. Kevin Sivula, Spring of 2019, 2020, and 2021),
- Physical chemistry of interfaces (lecture: Dr. Rothenberger Guido, Autumn of 2018),
- Electrochemical engineering (Lecture: Prof. Comninellis Christos, Autumn of 2019).

Publications

1. **Jie Zhang**, Thi Ha My Pham, Mo Li, Youngdon Ko, Loris Lombardo, Wen Luo, Andreas Züttel, Bottom-up unveiling the size effect of copper nanoparticles on electrochemical CO_2 reduction to C_{2+} products by using phthalocyanine demetalation, *in preparation*.

2. **Jie Zhang**, Thi Ha My Pham, Youngdon Ko, Shuliang Yang, Wen Luo, Andreas Züttel, Ag@C@Cu core-shell nanoparticles reveal tandem effect for electrochemical CO_2 reduction, *in preparation*.

3. **Jie Zhang**, Wen Luo, Andreas Züttel, Crossover of liquid products from electrochemical CO_2 reduction through gas diffusion electrode and anion exchange membrane*, Journal of Catalysis* **2020**, 385 140.
    https://doi.org/10.1016/j.jcat.2020.03.013

4. **Jie Zhang**, Wen Luo, Andreas Züttel, Self-supported copper-based gas diffusion electrodes for CO_2 electrochemical reduction, *Journal of Materials Chemistry A* **2019**, 7, 26285 (cover highlighted)
    https://doi.org/10.1039/C9TA06736A

5. Shuliang Yang[#], **Jie Zhang**[#], Li Peng, Mehrdad Asgari, Dragos Stoian, Ilia Kochetygov, Wen Luo, Emad Oveisi, Olga Trukhina, Adam Hugh Clark, Daniel T Sun, Wendy Lee Queen, A metal-organic framework/polymer derived catalyst containing single-atom nickel species for electrocatalysis, *Chemical Science* **2020**, 11, 10991 (# equally contribute)
    https://doi.org/10.1039/D0SC04512H

6. Xin Zong[#], **Jie Zhang**[#], Jinqiu Zhang, Wen Luo, Andreas Züttel, Yueping Xiong, Synergistic Cu/CeO2 carbon nanofiber catalysts for efficient CO2 electroreduction, *Electrochemistry Communications* **2020**, 114, 106716 (# equally contribute)   https://doi.org/10.1016/j.elecom.2020.106716

7. Wen Luo, Qin Zhang, **Jie Zhang**, Emanuele Moioli, Kun Zhao, Andreas Züttel, Electrochemical reconstruction of ZnO for selective reduction of CO2 to CO*, Applied Catalysis B: Environmental* **2020**, 273, 119060.   https://doi.org/10.1016/j.apcatb.2020.119060

8. Wen Luo, **Jie Zhang**, Mo Li, Andreas Zuttel, Boosting CO production in electrocatalytic CO2 reduction on highly porous Zn catalysts, *ACS Catalysis* **2019**, 5, 3783.
    https://doi.org/10.1021/acscatal.8b05109

9. Wen Luo, Wei Xie, Mo Li, **Jie Zhang**, Andreas Züttel, 3D Hierarchical Porous Indium Catalyst for Highly Efficient Electroreduction of CO2, *Journal of Materials Chemistry A* **2019**, 7, 4505.
    https://doi.org/10.1039/C8TA11645H

10. Xiangnan Li[#], **Jie Zhang**[#], Qi Feng, Chunying Pu, Luozheng Zhang, Manman Hu, Xianyong Zhou, Xiongwei Zhong, Wendi Yi, Jun Tang, Zhiwei Li, Xingzhong Zhao, Hui Li, Baomin Xu, Redox inactive ion meliorated BaCo0.4Fe0.4Zr0.1Y0.1O3−δ perovskite oxides as efficient electrocatalysts for the oxygen evolution reaction*, Journal of Materials Chemistry A* **2018**, 6, 17288 (# equally contribute)
    https://doi.org/10.1039/C8TA05599H

11. **Jie Zhang**, Maozhong An, Anmin Liu, Shanshan Ji, Ye Lian, Xuefeng Ren, Communication—Octahedral Indium Particles Synthesized by Electrodeposition from 1-Butyl-3-methylimidazolium Trifluoromethanesulfonate Ionic Liquid. *Journal of the Electrochemical Society* **2016**, *163* (13), D707.
    https://doi.org/10.1149/2.1011613jes

12. **Jie Zhang**, Maozhong An, Qi Chen, Anmin Liu, Xiaobiao Jiang, Shanshan Ji, Ye Lian, Xiaoyu Wen, Electrochemical Study of the Diffusion and Nucleation of Gallium(III) in [Bmim][TfO] Ionic Liquid. *Electrochimica Acta* **2016**, *190*, 1066.   https://doi.org/10.1016/j.electacta.2016.01.027

13. **Jie Zhang**, Anmin Liu, Xuefeng Ren, Jinqiu Zhang, Peixia Yang, Maozhong An, Electrodeposit copper from alkaline cyanide-free baths containing 5,5'-dimethylhydantoin and citrate as complexing agents. *RSC Advances* **2014**, *4* (72), 38012.   https://doi.org/10.1039/C4RA06855F

14. Luozheng Zhang, Chang Liu, **Jie Zhang**, Xiangnan Li, Chun Cheng, Yanqing Tian, Alex K-Y Jen, Baomin Xu, Intensive Exposure of Functional Rings of a Polymeric Hole-Transporting Material Enables Efficient Perovskite Solar Cells, *Advanced Materials* **2018**, 30, 1804028.
    https://doi.org/10.1002/adma.201804028

15. Anmin Liu, Xuefeng Ren, **Jie Zhang**, Deyu Li, Maozhong An, Complexing agent study for environmentally friendly silver electrodeposition(ii): electrochemical behavior of silver complex. *RSC Advances* **2016,** *6* (9), 7348.   https://doi.org/10.1039/C5RA23766A

16. Peixia Yang, **Jie Zhang**, Lei Liu, Maozhong An, Electroless Deposition of Nickel Nanowire and Nanotube Arrays as Supports for Pt-Pd Catalyst for Ethanol Electrooxidation. *Chinese Journal of Chemical Physics* **2015,** *28* (2), 206.   https://doi.org/10.1063/1674-0068/28/cjcp1412204

132

17. Xuefeng Ren, Ying Song, Anmin Liu, **Jie Zhang**, Guohui Yuan, Peixia Yang, Jinqiu Zhang, Maozhong An, Daniel Matera, Gang Wu, Computational Chemistry and Electrochemical Studies of Adsorption Behavior of Organic Additives during Gold Deposition in Cyanide-free Electrolytes. *Electrochimica Acta* **2015,** *176*, 10. https://doi.org/10.1016/j.electacta.2015.06.147

18. Xuefeng Ren, Ying Song, Anmin Liu, **Jie Zhang**, Peixia Yang, Jinqiu Zhang, Guohui Yuan, Maozhong An, Hannah Osgood, Gang Wu, Role of polyethyleneimine as an additive in cyanide-free electrolytes for gold electrodeposition. *RSC Advances* **2015**.
https://doi.org/10.1039/C5RA12217A

19. Xuefeng Ren, Ying Song, Anmin Liu, **Jie Zhang**, Peixia Yang, Jinqiu Zhang, Maozhong An, Experimental and theoretical studies of DMH as a complexing agent for a cyanide-free gold electroplating electrolyte. *RSC Advances* **2015,** *5* (80), 64997.
https://doi.org/10.1039/C5RA13140E

20. Anmin Liu, Xuefeng Ren, **Jie Zhang**, Guohui Yuan, Peixia Yang, Jinqiu Zhang, Maozhong An, A composite additive used for an excellent new cyanide-free silver plating bath. *New Journal of Chemistry* **2015,** *39* (4), 2409. https://doi.org/10.1039/C4NJ02060J

21. Ye Lian, Shanshan Ji, Lei Zhao, **Jie Zhang**, Peixia Yang, Jinqiu Zhang, Maozhong An, One-step electrodeposition of CuInxGa1-xSe2 thin films from a mixture system of ionic liquid and ethanol. *New Journal of Chemistry* **2015**. https://doi.org/10.1039/C5NJ01395J

22. Shanshan Ji, Ye Lian, Jie Zhang, Peixia Yang, Jinqiu Zhang, Maozhong An, Electrodeposition of CuInxGa1−xSe2 thin films via pulse technique from Ionic liquid containing n-propyl alcohol. *Materials Letters* **2015,** *161*, 411. https://doi.org/10.1016/j.matlet.2015.08.094

23. Anmin Liu, Xuefeng Ren, Bo Wang, **Jie Zhang**, Peixia Yang, Jinqiu Zhang, Maozhong An, Complexing agent study via computational chemistry for environmentally friendly silver electrodeposition and the application of a silver deposit. *RSC Advances* **2014,** *4* (77), 40930.
https://doi.org/10.1039/C4RA05869K

24. Anmin Liu, Xuefeng Ren, **Jie Zhang**, Chong Wang, Peixia Yang, Jinqiu Zhang, Maozhong An, Drew Higgins, Qing Li, Gang Wu, Theoretical and experimental studies of the corrosion inhibition effect of nitrotetrazolium blue chloride on copper in 0.1 M H2SO4. *RSC Advances* **2014,** *4* (76), 40606.
https://doi.org/10.1039/C4RA05274A

25. Shanshan Ji, Peixia Yang, Jinqiu Zhang, Ye Lian, **Jie Zhang**, Maozhong An, Electrodeposition of CuInxGa1−xSe2 from a 1-butyl-3-methylimidazolium trifluoromethanesulfonate ionic liquid. *Materials Letters* **2014,** *133* (0), 14. https://doi.org/10.1016/j.matlet.2014.06.147

Conference Presentations

1. Self-Supported Copper-Based Gas Diffusion Electrodes for Electrochemical CO2 Reduction, 17th International Congress on Catalysis (ICC), San Diego, California, June 2020. (The abstract was accepted and an oral presentation was assigned while the conference is postponed to 2022)

2. Electrochemical reduction of CO2 using Cu based gas diffusion electrode, 13th International Hydrogen and Energy Symposium, January 2019, Incheon, South Korea. Oral presentation and poster.